HAL
open science

Thermal stability of potential fuel cell core materials La2Mo2-yWyO9 ($0 \leq y \leq 2.0$) under air and reductive atmospheres, and in contact with a Sr containing cathode material

Uday Krishna Ravella

To cite this version:

Uday Krishna Ravella. Thermal stability of potential fuel cell core materials La2Mo2-yWyO9 ($0 \leq y \leq 2.0$) under air and reductive atmospheres, and in contact with a Sr containing cathode material. Other. Le Mans Université, 2012. English. NNT : 2012LEMA1009 . tel-00743197

HAL Id: tel-00743197

https://theses.hal.science/tel-00743197v1

Submitted on 18 Oct 2012

HAL is a multi-disciplinary open access archive for the deposit and dissemination of scientific research documents, whether they are published or not. The documents may come from teaching and research institutions in France or abroad, or from public or private research centers.

L'archive ouverte pluridisciplinaire **HAL**, est destinée au dépôt et à la diffusion de documents scientifiques de niveau recherche, publiés ou non, émanant des établissements d'enseignement et de recherche français ou étrangers, des laboratoires publics ou privés.

THÈSE

Présentée en vue de l'obtention du titre de :

DOCTEUR de l'Université du Maine

Mention Chimie de l'État Solide

Par

Uday Krishna RAVELLA

Thermal stability of potential fuel cell core materials $La_2Mo_{2-y}W_yO_9$ ($0 \leq y \leq 2.0$) under air and reductive atmospheres, and in contact with a Sr containing cathode material.

Soutenue le 21 septembre 2012 devant la commission d'examen suivante:

Mme. R.-N. VANNIER	Professeur, ENS de Chimie de Lille	Président
Mme. M. BAHOUT	Maître de conférences, Université de Rennes 1	Rapporteur
Mr. W. PAULUS	Professeur, Université Montpellier 2	Rapporteur
Mr. P. LACORRE	Directeur de Recherche au CNRS, Le Mans	Directeur de thèse
Mr. G. CORBEL	Chargé de recherche au CNRS, Le Mans	Encadrant

2012

Département des Oxydes et Fluorures
IMMM-UMR 6283
Institut des Molécules et Matériaux du Mans

Ecole Doctorale 3MPL
Matière, Molécules, Matériaux en Pays de la Loire

Acknowledgments

It was nearly five years back I came to France and started my scientific career. I studied under guidance of some of the world renowned scientists and worked at some of the most famous laboratories. This thesis is the end of my PhD and I have seen both peaks and valleys in this journey. I am extremely indebted to all my colleagues, friends and family who have encouraged and supported me through this endeavor and made this a pleasant journey.

At first, I pay homage to my guide, Dr. Philippe Lacorre. This work would not have been possible without his guidance, support and encouragement. Under his guidance I successfully overcame many difficulties and learned a lot. Despite his busy schedule he supported me through his valuable suggestions and made corrections. I am grateful that he has given me many opportunities to attend training schools, conferences and workshops which were very important for this research work.

I am extremely thankful to my guide Dr. Gwenaël Corbel, for his expert guidance, professionalism and diplomacy. I am grateful for the time we spent on scientific discussions, which were useful in expanding my scientific knowledge and enabled me to finish my degree successfully.

I take this opportunity to sincerely acknowledge Dr. Stephen J Skinner, Imperial College, London, for our collaborative work on cationic diffusion studies. Several hours spent on meetings and scientific discussions were fruitful. His critical comments and suggestions on this thesis work are greatly appreciated.

I cordially express my gratitude to Prof. Alberto Caneiro, Centro Atomico Bariloche, Argentina, for the collaborative research work we have carried on reduction and conductivity studies. His ever friendly nature and cheerful enthusiasm helped us perform cutting edge research activities.

I am also very grateful to Mrs. A Mercier, Mr. C. Galven and Mr. J. Botquelen for their technical support which helped me carry out various measurements for this thesis work. I even thank Mr. R. Carter, Imperial College London, for his suggestions and discussions on our SIMS measurements.

I thank Dr. O. Bohnke, Dr. K. Adil and Dr. F. Goutenoire for their moral support and encouragement in this thesis work. My Sicnere thanks to my peers and research fellows Dr. J. Liu, Mr. J. Vega-Castillo, Dr. J. Jacquens and Dr. M. Chambrier for being patient with my questions and helping me understand several aspects of research activities. This helped me a lot to work for hours together tirelessly. I doubt that I will ever be able to convey my appreciation fully, but I owe my gratitude.

Last but not least, I would like to pay high regards to my beloved family for their sincere encouragement, inspiration and unconditional support throughout my research work and lifting me uphill to this phase of life. I owe everything to them. Besides this, several people have knowingly and unknowingly helped me in the successful completion of this project. I am very grateful to each and every one of them.

Uday Krishna Ravella

Index

General Introduction……..……1

Chapter 1: Bibliography

1.1Fast Oxide Ion Conductors..... 7

1.2 Solid Oxide Fuel Cells..... 8

1.2.1 Electrolytes..... 11

1.2.2 Electrodes 11

1.3 **$La_2Mo_2O_9$** 14

1.3.1 Phase Transition, Crystal Structure..... 16

1.3.1.1 High temperature form 16

1.3.1.2 Low temperature form 17

1.3.2 Limitations of $La_2Mo_2O_9$ as an electrolyte material 19

1.3.3 Chemical compatibility $La_2Mo_2O_9$ with electrode materials..... 20

1.3.3.1 Cationic diffusion studies of YSZ with cathode materials. 21

1.4 LAMOX family 23

1.4.1 Tungsten substituted $La_2Mo_2O_9$ and its stability in air. 26

1.5 Stability of $La_2Mo_2O_9$ and W-substituted $La_2Mo_2O_9$ in reducive Atmospheres..... 30

1.5.1 Stability of $La_2Mo_2O_9$ 30

1.5.2 Stability of W substituted $La_2Mo_2O_9$ 34

1.6 Summary and commitment to this thesis work..... 38

1.7 References..... 40

Chapter 2: Experimental and Methodology

2.1 Introduction 49

2.2 Synthesis of powder samples 49

2.3 Synthesis of Pellets 51

2.4 X-Ray Diffraction (XRD) and in-situ Temperature Controlled X-Ray Diffraction (TC-XRD) 54

2.5: Thermal Analysis 55

2.5.1: Thermogravimetric Analysis (TGA) 56

2.5.2: Differential Thermal Analysis (DTA) 57

2.6: Secondary Ion Mass Spectrometry (SIMS) 58

2.7: Electrical Conductivity Studies 62

2.8: References 64

Chapter 3: Thermal stability of W-substituted $La_2Mo_2O_9$

3.1Introduction 67

3.2 $La_2Mo_{2-y}W_yO_9$ with y = 1, 1.1, 1.2 68

3.3 $La_2Mo_{2-y}W_yO_9$ with y = 1.3-1.575 70

3.3.1 $La_2Mo_{0.7}W_{1.3}O_9$ (W 1.3) and $La_2Mo_{0.65}W_{1.35}O_9$ (W 1.35) 70

3.3.2 $La_2Mo_{2-y}W_yO_9$ with y = 1.4 - 1.575 75

3.4 $La_2Mo_{2-y}W_yO_9$ with y = 1.6-1.8 82

3.4.1 $La_2Mo_{0.4}W_{1.6}O_9$ (W1.6) 83

3.4.2 $La_2Mo_{2-y}W_yO_9$ with y = 1.65-1.8 87

3.5 $La_2Mo_{2-y}W_yO_9$ with y = 1.85 - 2.0 91

3.6 Phase Diagram of $La_2W_yMo_{2-y}O_9$ ($1.0 \leq y \leq 2.0$) 94

3.7 X-Ray Powder Diffraction Analyses 97

3.7.1 Raw powders 97

3.7.2 Powders post-annealed above 700°C 103

3.8 Conclusions 113

3.9 References 115

Chapter 4: Cationic diffusion studies in $La_2Mo_2O_9$

4.1: Introduction 119

4.2: Experimental Setup: 120

4.3 Results & Discussions: 122

4.3.1 Surface reactions on the solution deposited $La_2Mo_2O_9$ and $La_{0.8}Sr_{0.2}MnO_{3-\delta}$ pellets: ... 122

4.3.1. 1) $La_2Mo_2O_9$ with 5mg/cm^2 of $MnCl_2 \cdot 4H_2O$ solution deposition: 122

4.3.1.2: $La_2Mo_2O_9$ with 5mg/cm^2 of $Sr(NO_3)_2$ solution deposition: 128

4.3.1.3: $La_{0.8}Sr_{0.2}MnO_{3-\delta}$ with 5mg/cm^2 of $(NH_4)_6Mo_7O_{24}.4H_2O$ deposited solution: 138

4. 3.2: Cationic diffusion measurements on $La_2Mo_2O_9$ / $La_{0.8}Sr_{0.2}MnO_{3-\delta}$ pellet couples 146

4.3.2.1: XRD analysis and FIB-SIMS surface analysis on $La_2Mo_2O_9$ pellets: *146*

4.3.2.2: XRD analysis and FIB-SIMS surface analysis on $La_{0.8}Sr_{0.2}MnO_3$ pellets: *150*

4.3.2.3: FIB-SIMS depth profile analysis on $La_2Mo_2O_9$ / $La_{0.8}Sr_{0.2}MnO_3$ couples: *151*

4.3.2.4: Discussions 154

4.4: Conclusions 160

4.5: References 165

Chapter 5: LAMOX stability under Reductive Atmospheres

5.1: Introduction 169

5.2: Stability of $La_2Mo_2O_9$ under reductive atmospheres 171

5.3: Stability of $La_2Mo_2O_9$ and $La_2Mo_2O_{7-\delta}$ (amorphous 7-δ) under mild reductive conditions 179

5.4: Triggering and boosting of reduction process 184

5.5: Stability of W- substituted $La_2Mo_2O_9$ under reductive atmospheres 188

5.6: Thermodynamic stability of $La_2Mo_2O_9$ and W- substituted $La_2Mo_2O_9$ under pO_2 pressures 194

5.7: Conductivity experiments on reduced $La_2Mo_2O_9$ and reduced W-LAMOX materials 196

5.8: Conclusions 203

5.9: References 205

Summary and Conclusion 207

Perspectives 211

Annex 213

Abbreviations

Dx	Diffusion of element x
DTA	Differential Thermal Analysis
LAMOX	$La_2Mo_2O_9$ based materials
LMO	$La_2Mo_2O_9$
- α-LMO	Monoclinic α-$La_2Mo_2O_9$ type phase
- β-LMO	Cubic β -$La_2Mo_2O_9$ type phase
- α-LWO	Triclinic α-$La_2W_2O_9$ type phase
- W-LMO	W – substituted $La_2Mo_2O_9$
- W0.5	$La_2Mo_{1.5}W_{0.5}O_9$
- W1.0	La_2MoWO_9
- 7730	$La_7Mo_7O_{30}$
- 7-δ	Amorphous $La_2Mo_2O_{7-\delta}$
LPS	Lone Pair Substitution method
LSM	$La_{0.8}Sr_{0.2}MnO_{3-\delta}$
pO_2	Partial Oxygen pressures
R.T	Room temperature
SEM	Scanning Electron Microscope
SIMS	Secondary Ion Mass Spectrometry
- FIB-SIMS	Focused Ion Beam -SIMS
- TOF-SIMS	Time of Flight -SIMS
SOFC	Solid Oxide Fuel Cell
TEC	Thermal Expansion Coefficient
TGA	Thermogravimetric Analysis
TPB	Triple Phase Boundary
XRD	X-Ray Diffraction
- TC-XRD	Temperature Controlled X-Ray Diffraction
YSZ	Yttrium Stabilized Zirconia oxide
- 8 % -YSZ	8 mol% Y_2O_3 substituted ZrO_2

General Introduction

Progress of the modern society is marked by its increasing consumption of energy and it is a challenge for scientific community to discover new ways to meet the power requirements for ever-increasing population. Majority of the energy requirements are provided by the combustion of fossil fuels like coal and oil, since industrial revolution. Over consumption of such fuels increases air pollution thus causing global warming and such dependency on these fossil fuels spiked health and environmental concerns. Apart from that, steady depletion of world's fossil fuels reserves and its insufficiency for future generations raises alarm. Need to meet power requirements economically, efficiently with minimal or no pollutants call usage of renewable energy sources. Study for such unconventional sources of power lead to discovery of solar, wind, hydro, geothermal, ocean, nuclear and photovoltaic energies. All of these unconventional methods have multiple advantages and limitations over one another; however the efficient way for future could be optimal mixture of several methods. Fuel cells are also extensively studied for their high efficiencies, better portability and low pollution yield, and no pollutant is expected if hydrogen is used as a fuel source.

Solid oxide fuel cell (SOFC) is a type of fuel cell and is an inclined application for this study. SOFC use oxygen ion conductors for operation. Ionic conductors are compounds in which ions migrate carrying an electrical charge. Depending on the structure of the compounds, these ions could be monovalent (H^+, Li^+, Na^+, K^+, Ag^+) or divalent or trivalent (rare earth) cations or anions (F^- and O^{2-}). Li^+ batteries which are regularly used in electrical devices like cell phones, GPS units etc are examples of solid state ionic conductors.

Oxygen ion conductors are an interesting group of solid state ionic conductors, and are widely used for oxygen gas sensors, oxygen separating membranes and as electrolytes in SOFC. Oxygen ions are doubly charged big ions (radius ~1.4 Å) and they strongly interact with cationic network. Materials exhibiting oxygen ion conductivity would need specific structural network and such structural framework should provide ample space for the oxygen ion transport. Moreover such compounds should contain unoccupied positions equivalent to those of oxygen sites so that oxygen can migrate. The ionic conductivities in these compounds are comparable to liquid ionic conductors especially at elevated temperatures. One such compound is yttria stabilized zirconia (YSZ) and it is a widely used oxygen ion

conductor because of its high ionic conductivity. In most applications, high temperatures are required to achieve satisfactory ionic conductivities in YSZ and SOFC is one such application, where cell operation is around ~1000 ^{o}C. Use of such elevated temperatures for long duration affects the thermal behavior of SOFC components and leads to the premature deterioration of the cell. For economic and industrial application of SOFC, it is of vital importance to reduce operating temperatures to intermediate levels (~600 ^{o}C). Such intermediate temperature utilization of SOFC calls for discovery of new materials (electrolytes) for the SOFC.

A new fast oxide ion conductor $La_2Mo_2O_9$ (LMO) was reported by Lacorre *et al.* in 2000, which exhibits higher oxide ion conductivity (at temperatures above ~580 ^{o}C) compared to that of standard 8 mol % yttrium stabilized zirconia (YSZ8%). LMO undergoes a phase transition around 580 ^{o}C, from a low temperature α form (α-LMO) to high temperature and high conducting β form (β-LMO). Phase transition occurs with a significant increase in cell volume by ~0.46% and increase of conductivity by two orders of magnitude. Several studies were reported where substitutions were carried out on La or Mo or both sites to stabilize the high temperature cubic phase down to room temperature. Out of all of those studies, W substitution to Mo in LMO is considered a viable choice since little W substitution (~10 mol %) is sufficient to suppress the phase transition and the solubility limit of W in LMO is high (~80 mol %). However, little information is available on the stability of these W-substituted LMO compounds. Significant part of this thesis work is dedicated to study W substitution in LMO (W substitution ≥ 50 mol %), and stability and metastability of the resultant compounds.

Chemical inertness and mechanical compatibility of the electrolyte with the electrodes is crucial to avoid premature breakdown of the fuel cell. Undesired reaction of electrolyte with electrode can lead to the formation of new insulating phases, which would in turn lead to immediate drop in the cell performance, finally leading to the complete failure of total unit. Few studies were reported where the compatibility of LMO powders was tested against standard compounds used as SOFC cathode materials and observed that $La_{0.8}Sr_{0.2}MnO_3$ (LSM) is the less reactive compound, with $SrMoO_4$ as a reaction product above 700 ^{o}C. Apart from knowing the reaction products it is important to understand the diffusion process of these elements at the interface along with their diffusion coefficients, thereby evaluating its magnitude during fuel cell operation and possibly controlling it by appropriate method. In

this thesis work, cationic diffusion process in LMO and LSM compounds is studied along with the diffusion of individual elements Mn/Sr in LMO and Mo in LSM.

LMO is unstable under reducing conditions. When LMO is annealed in diluted H_2 atmospheres, Mo partially reduces from hexavalent to lower oxidation states leading to the formation of undesired reaction products and even amorphisation under extreme reducing conditions. Such reaction products induce electronic conductivity, making such reduced compound a mixed electronic and ionic conductor (MIEC) (LMO is an electrolyte material and is a pure oxide ion conductor). However use of reduced LMO as an MIEC anode material in SOFC was proposed and attempted with success. It was even found that reduced LMO material is sulfur tolerant till satisfactory level giving new opportunities to explore in LAMOX world. Few studies stated that W substitution in LMO can limit its reducibility, and even showed that W component in the LMO is not prone to any reduction. Not many studies were conducted to understand reduction behavior and its kinetics. The last part of my thesis work was devoted to study structural changes, reduction behavior, and reductive kinetics of LMO and W-LMO under different reducive atmospheres and parameters.

There are five chapters in this thesis work. Bibliographic survey carried on previous works on LMO, W-LMO and their stabilities under air and reducing conditions along with their chemical compatibilities with electrode materials will be presented in Chapter 1. Synthesis methods and general experimental methodology are described in Chapter 2. Synthesis and stability of W-LMO under air will be discussed in Chapter 3. Cationic diffusion studies carried on LMO and LSM pellets will be presented in Chapter 4. Reduction behavior of LMO and W-LMO along with their stability under different reducing conditions will be presented in Chapter 5. Finally highlights of the results are discussed and conclusions are summarized. Perspectives for future work which are important for successful realization of LAMOX materials as components for SOFC application will be proposed.

Chapter 1: Bibliography

1.1Fast Oxide Ion Conductors 7

1.2 Solid Oxide Fuel Cells 8

1.2.1 Electrolytes 11

1.2.2 Electrodes 11

1.3 **$La_2Mo_2O_9$** 14

1.3.1 Phase Transition, Crystal Structure 16

1.3.1.1 High temperature form 16

1.3.1.2 Low temperature form 17

1.3.2 Limitations of $La_2Mo_2O_9$ as an electrolyte material 19

1.3.3 Chemical compatibility $La_2Mo_2O_9$ with electrode materials 20

1.3.3.1 Cationic diffusion studies of YSZ with cathode materials. 21

1.4 LAMOX family 23

1.4.1 Tungsten substituted $La_2Mo_2O_9$ and its stability in air. 26

1.5 Stability of $La_2Mo_2O_9$ and W-substituted $La_2Mo_2O_9$ in reducive Atmospheres 30

1.5.1 Stability of $La_2Mo_2O_9$ 30

1.5.2 Stability of W substituted $La_2Mo_2O_9$ 34

1.6 Summary and commitment to this thesis work 38

1.7 References 41

Chapter 1
Bibliography

1.1Fast Oxide Ion Conductors*:*

Fast oxide ion conductors have attracted considerable attention in last few decades. Out of all the ionic conductors, oxide ion conductors are heavily studied for their increasing number of application domains. However their applications were confined to very few domains like oxygen sensors because of lack of higher performance materials (materials which can present higher current densities). Some of the major applications of these materials is as an electrolyte in Solid Oxide Fuel Cells (SOFC), oxygen separation membranes, dense membranes reactors for oxygen catalysis, etc. It was discovered by Nernst that some solids exhibit this specific property of oxide ion conduction [1]. Oxide ion is double charged with relatively big radius ~ 1.40 Å, and can interact with cationic network. High mobility of this species requires high operating temperatures and specific structural framework which can tolerate their conduction by providing sufficient open spacing for oxygen ion transport. It is suggested that, for a material to favor higher oxygen ion mobility there have to be equivalent crystallographic sites, which can support movement of oxygen ions [2]. Therefore, most of the electrolytes have cubic or nearly cubic structures. However, in some materials with non-cubic symmetry, oxide ion conduction occurs in conducting planes exhibiting higher anisotropic conductivity (bidimensional).[2]

For a material to be designated as a fast oxide ion conductor, it should exhibit high oxide ion conductivity and must contain unoccupied positions equivalent to those oxygen sites so that oxygen can migrate in the material [2]. In other words, there should be enough vacancies (intrinsic vacancies) in the material for O^{2-} ions to migrate. There are two methods to introduce oxygen vacancies in the material to improve their conductivity: one way is to opt for the materials with satisfactory intrinsic vacancies, while the other is to substitute aliovalent cations into the structure and create extrinsic oxygen vacancies [3].

1.2 Solid Oxide Fuel Cells:

Like any electrochemical device, Solid Oxide Fuel Cells (SOFC) has an anode, electrolyte and a cathode. SOFC operate at high temperature converting fuel directly into electrical energy, heat and rendering theoretical efficiency significantly higher than conventional methods like internal combustion engines. The system can reach efficiency about 80% (efficiency of Internal combustion engine is < 40%), when coupled with heat recovering system for cogeneration (heating applications and electric power). When pure hydrogen is used as fuel, the reaction product is water apart from desired electric power, making system eco-friendly. A schematic representation of SOFC is shown in Fig.1.1. Cathode takes e^- and reacts with the O_2 from air reducing it to O^{2-} ions.

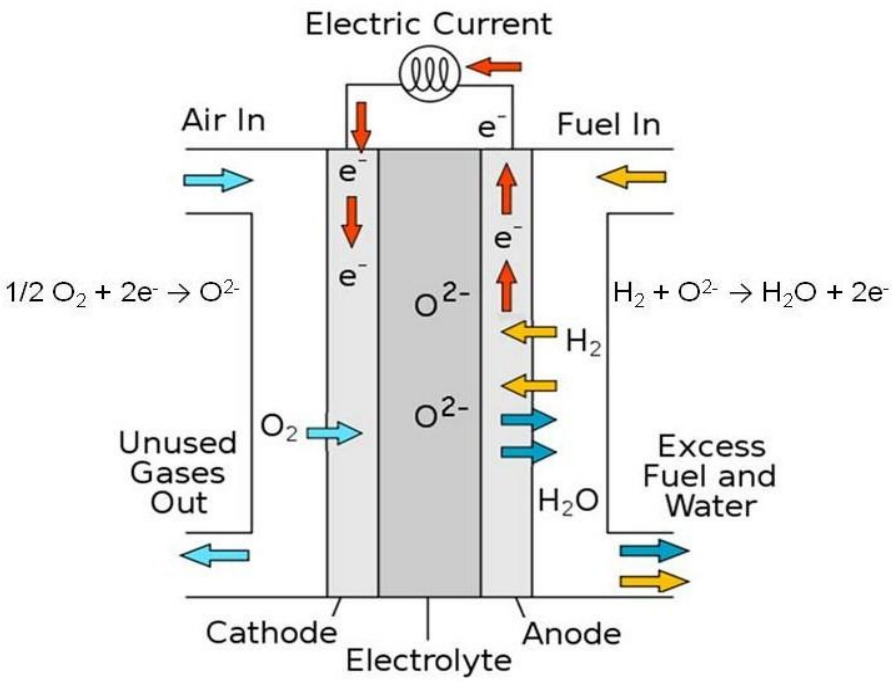

Figure 1.1: Schematic representation of SOFC working principle.

These O^{2-} ions from the cathode diffuse into the electrolyte and are collected at the anode. Fuel at anode (hydrogen or hydrocarbons) reacts with these O^{2-} ions (oxidation of H_2 to H_2O)

and form water, giving out e-. These electrons flow to the external circuit generating electricity. Oxidation of H_2 to H_2O is an exothermic reaction, which produces heat energy. When the fuel cell is used for stationary applications, this generated heat can be used for domestic heating applications. The total reaction mechanism can be stated as following equations:

$$1/2\ O_2 + 2e^- \rightarrow O^{2-} \text{ (cathode)}$$

$$H_2 + O^{2-} \rightarrow H_2O + 2e^- \text{ (anode)}$$

$$\text{With overall reaction: } H_2 + 1/2\ O_2 \rightarrow H_2O$$

Although the operating principle of SOFC is rather simple, material selection process for individual components is a challenge. All the materials are supposed to exhibit required ionic and electronic conductivity properties to function in a cell. Good chemical and mechanical stability to endure fabrication and its high temperature operation have to be ensured. In order to achieve required current densities and power output, SOFC runs at high temperature (~ 800-1000 ^oC). Any chemical reactivity or interdiffusion between components is considered fatal for the cell. The thermal expansion coefficients of the components must be close to each other, to ensure minimal thermal stresses, which could lead to mechanical failure of the total cell. One end of the cell must work in air, and the other in reducing atmosphere sustaining any chemical toxicity from the current environment. For industrial applications, materials selected, processing and fabrication are to be cost effective. The total cell is expected to run continuously for a long time (nearly 40,000 hours) ensuring chemical and mechanical stability [4]. This is a current challenge, which demands novel materials with properties to meet requirements of SOFC and ability to work at intermediate temperatures with an increased efficiency.

This conventional SOFC setup is also known as double-chamber SOFC, since two different chambers are used for anode and cathode separately, where fuel and air are pumped respectively. Another SOFC setup called single chamber SOFC was proposed by Eyraud *et al.*, where the total setup of anode, electrolyte and cathode are placed in a single chamber and mixture of fuel and oxidation gas are supplied [5]. The working principle is based on the difference in catalytic activity of the electrodes for the respective cathode and anode reactions. The resulting difference in the oxygen partial pressure (pO_2) between the electrodes leads to the generation of an open circuit voltage. Progress in single chamber technology has enabled the

generation of power outputs comparable to those of conventional SOFC's [6]. Various hydrocarbons like ethane, methane, propane and LPG are used along with air for SC-SOFC operation [7, 8]. Fig.1.2 shows the schematic representation of single chamber SOFC.

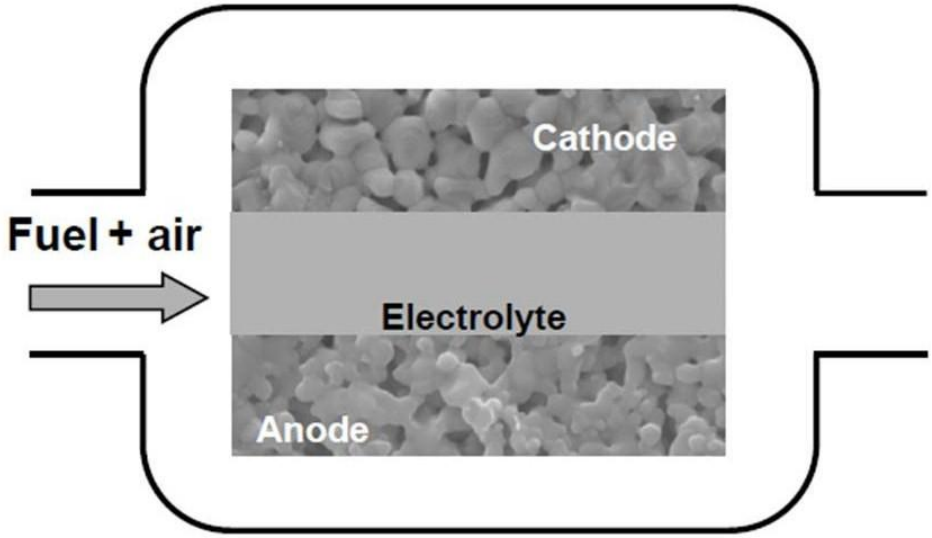

Figure 1.2: Schematic representation of Single Chamber SOFC setup.[6]

Single chamber fuel cells have few advantages over conventional SOFC's. The setup is free of sealing (which is a problem in double chamber SOFC, where there is a risk of fuel escape towards cathode or air escape towards anode). It has increased thermo-mechanical stability. Easier stack assembly and fabrication are possible along with compact and simplified designs. However single chamber setup faces few challenges. There is always a risk of explosion for fuel-air mixtures at high temperatures. Highly selective and catalytically active materials are necessary. Since the oxidation reaction is exothermic in nature, such heat created will be well distributed throughout the system. SC-SOFC tends to have low efficiency due to parasitic non-electrochemical reactions. Hibino *et al.* was the first to operate SC-SOFC in a methane and air mixture at 950 ^{o}C and these SC-SOFC's are still subject to further studies for amplified advantages and applications [6, 7, 9-12].

1.2.1 Electrolytes:

Once the O_2 from air is converted to O^{2-} ions at the cathode, they must migrate through the electrolyte towards the anode. For such migration to occur, the electrolyte must possess high oxygen ion conductivity with negligible amount (less than 0.01%) or no electronic conductivity [13]. It is expected to be as thin as possible to minimize resistive losses and supposed to be highly dense to ensure high ionic conductivity and to prevent short circuit of any gas passing through it. It is expected to be chemically, mechanically and thermally stable over a wide range of temperatures (800 – 1000 ^{o}C).

Fluorite and Fluorite type oxides are widely investigated materials for solid state electrolytes. Most commonly used 8%YSZ (8 mol% Y_2O_3 substituted ZrO_2) belongs to this category [14]. Gadolinium doped Ceria oxide (CGO) is also a widely used fluorite material [15-17]. Isovalent and aliovalent doped Bi_2O_3 are also studied for their improved oxide ion conductivity [2, 16, 18, 19]. Some other materials which have attracted significant attention include perovskites and perovskite based oxides [20, 21]; Layered aurivillius type oxides [22-24]. Silicates and germinates based apatite oxides [2, 25-27]. Few studies suggested pyrochlores and scheelites for their possible application as O^{2-} ion conductors. Currently huge research for suitable electrolyte is still going on; for now, 8%YSZ is accepted as default electrolyte for standard SOFC applications.

1.2.2 Electrodes:

An ideal electrode for SOFC applications needs to possess good ionic and electronic conduction. Electrode materials should contribute to the diffusion of gasses, adsorption of reactants and desorption of reactant products. To promote diffusion of gas, electrodes are expected to be porous preserving mechanical, chemical and thermal stability and compatibility with electrolyte materials. To ensure sufficient electrocatalytic activity, and ion and electronic conductivity, two different types of material groups are considered: composite materials and materials exhibiting mixed ionic and electronic conductivity (MIEC).

Porous composite electrodes are used for their extended area useful for electrochemical activity which improves the current output of an electrode. Performance of these electrodes

depends mostly on mass-transfer process, electrocatalytic activity, surface area available for electrochemical reaction and the ionic and electronic conductivity of the material. Electrochemical activity happens here at the triple phase boundary (TPB). TPB is the interface where the ion conducting electrolyte, electron conducting metal part and gas (fuel for anode and air for cathode) meet together. Length of the TPB enhances the catalytic activity and therefore , the current densities and overall activity of the fuel cell rely on the TPB length [28]. Ionic conductive part can also improve electronic conductivity part by increasing TPB area [29-35]. Failure of one component in TPB can compromise SOFC operation, which leads to the development of materials exhibiting MIEC properties.

Most of the MIEC materials are cathodes; however some these MIEC materials can be used as anode for SOFC applications. Few metallic oxides demonstrate both electronic and ionic conductivities (which can be even possible by doping with selective elements). Metal oxides are very poor reforming catalysts. They do not form carbon fibers unless they are reduced to their respective metallic forms. They have high melting points and very low surface energies (which prevent them from forming clusters and blocking gas pathways; also help them to preserve their porosity under extreme operating conditions). For this to happen the electrode (anode) should be of a single material; single phase, for the electrocatalytic oxidation to happen all over the anode. Since the electrode is porous, and the entire electrode is in solid and single phase, it increases the surface of the electrode exposed to the gases, i.e. more area for electrochemical activity. Unlike in TPB which exist at single line in cermets, electrocatalytic activity happens in these materials all over the surface (in other words, TPB = lines and MIEC = total surface). Such electrochemical activity occurring all over the surface increases the efficiency of the cell; and cracks or mechanical failure in small region of component does not compromise the operation of the total unit.

The preliminary function of the cathode is to furnish enough reaction sites for the electrochemical reduction of oxygen (normally oxygen from air in SOFC). It should be stable in oxidizing environment retaining adequate electronic conductivity and electrocatalytic activity towards oxidation of gas at higher operating conditions of SOFC. The cathode must have ample electrocatalytic activity, hence low polarization for the electrochemical oxidation of air [36]. Perovskite (ABO_3) type $LaMnO_3$, $La_{0.8}Sr_{0.2}MnO_{3-\delta}$ (LSM), $La_{1-x}Sr_xCo_{1-y}Fe_yO_{3-\delta}$,

$Gd_{0.8}Sr_{0.2}CoO_3$ [37] and perovskite based ABO_3 (AO) type $La_2NiO_{4+\delta}$ are studied for MIEC cathode materials [38-40]. Whereas LSM cermets (LSM mixed with noble metals) and Pt/Ag - $Zr(Sc)O_2$ cermets are suggested as cathode materials [41].

The electrochemical oxidation of fuels is the important function of an anode in a SOFC. Basic requirements for anode include high catalytic activity towards oxidation of fuels, good chemical and thermal stability (in reducive atmospheres); high electronic conductivity all over the exposed surface, tolerance towards carbon decomposition (coking) and sulfur poisoning. Platinum, cobalt, iron, nickel and graphite were studied earlier as materials for anode. Nickel was assumed as the best material considering its availability, low cost, chemical and thermal stability and good electrocatalytic activity towards reforming of hydrocarbon fuels and oxidation of hydrogen. Considering YSZ as a standard industrial electrolyte, pure nickel is not tolerated because of its huge thermal expansion coefficient mismatch, poor adhering with the electrolyte and coarsening while operation of SOFC. To overcome these unlikely parameters, Ni was mixed with YSZ, resulting in a new hybrid material called cermet, Ni-YSZ. Ni metal induces electronic conductivity and YSZ induces ionic conductivity. Ni-YSZ cermets minimize the effect of thermal expansion coefficient mismatch, and Ni is prevented from aggregation and coarsening maintaining internal porosity and conduction path for O^{2-} ions, which preserves the active surface area for electrocatalytic activity. Ni-YSZ cermet met most of the general requirements for a SOFC anode material and is still used as an anode for SOFC. However Ni-YSZ suffers from coking and sulfur poisoning. Many studies to overcome these limitations were not successful [42-54] leading to the study of Cu based cermet materials. Cu was immune to sulfur problem and even limited coking, but was instable thermally at temperatures over 700 ^{o}C because of its low melting point and low surface energy [35, 55-59]. It has been stated in a review by Atkinson, that an alternative anode for Ni-YSZ should exhibit conductivity 1 S/cm at 10^{-20} atm pO_2 [60]. Although there are oxides which exhibit this conductivity value, it has been difficult to identify an oxide which is both chemically and mechanically (thermal expansion) compatible with YSZ along with tolerance towards coking and sulfur poisoning.

For MIEC anode materials, chemically stable $Sr_{0.85}Y_{0.10}Ti_{0.095}Co_{0.05}O_3$ was proposed and the compound exhibited the highest conductivity values (higher that 60 S/cm @ 800 ^{o}C and 10^{-19} atm). It showed good resistance towards oxidation (O^{2-} ions from electrolyte) and sulfur

poisoning as well[4]. These samples are still subject to further studies in establishing irreversibility of the redox mechanism. Few other compounds studied are $La_{0.75}Sr_{0.25}Cr_{0.5}Mn_{0.5}O_3$, $Sr_2MoMgO_{6-\delta}$, $Gd_2Ti_{1.4}Mo_{0.6}O_7$ [61-64], however each of these compounds lack one requirement at least and therefore have to be improved.

Recently the amorphous phase sample resulting from the reduction of $La_2Mo_2O_9$ was proposed as sulfur tolerating anode material for SOFC applications [65] by X. C. Lu and J. H. Zhu. It is of interest to study the stabilization and properties of the reduced form of $La_2Mo_2O_9$ in order to probe their use as anode material for SOFC.

1.3 $La_2Mo_2O_9$:

A new fast oxide ion conductor $La_2Mo_2O_9$ (LMO) was reported by Lacorre *et al.* in 2000 [66], which exhibits higher oxide ion conductivity (at temperatures above 600 ^oC) compared to that of standard 8 mol% yttrium stabilized zirconia (YSZ8%). See Fig. 1.3. The conductivity of the compound was found to be 6 x 10^{-2} S/cm at 800 ^oC. When the compound was synthesized by nanocrystalline powder, significant improvement in conductivity (12 x 10^{-2} S/cm) is found at 750 ^oC [67]. Such a conductivity value was reached in YSZ at 970 ^oC, showing that LMO was able to lower the operating temperatures of SOFC by ~200 ^oC. This group of materials was considered as possible substitute to YSZ and CGO and has dragged considerable attention.

LMO undergoes a phase transition around 580 ^oC, from a low temperature α- form (α-LMO) to a high temperature β-form (β-LMO). The phase transition occurs with a significant increase in cell volume by ~0.46%.

Post analysis for the possible origin of the conductivity in this compound lead to a new concept called Lone Pair Substitution (LPS) method, which was proposed by the same team [68]. LPS concept is expected to provide an original way to discover new families of oxide ion conductors, by appropriate substitution in specific oxides.

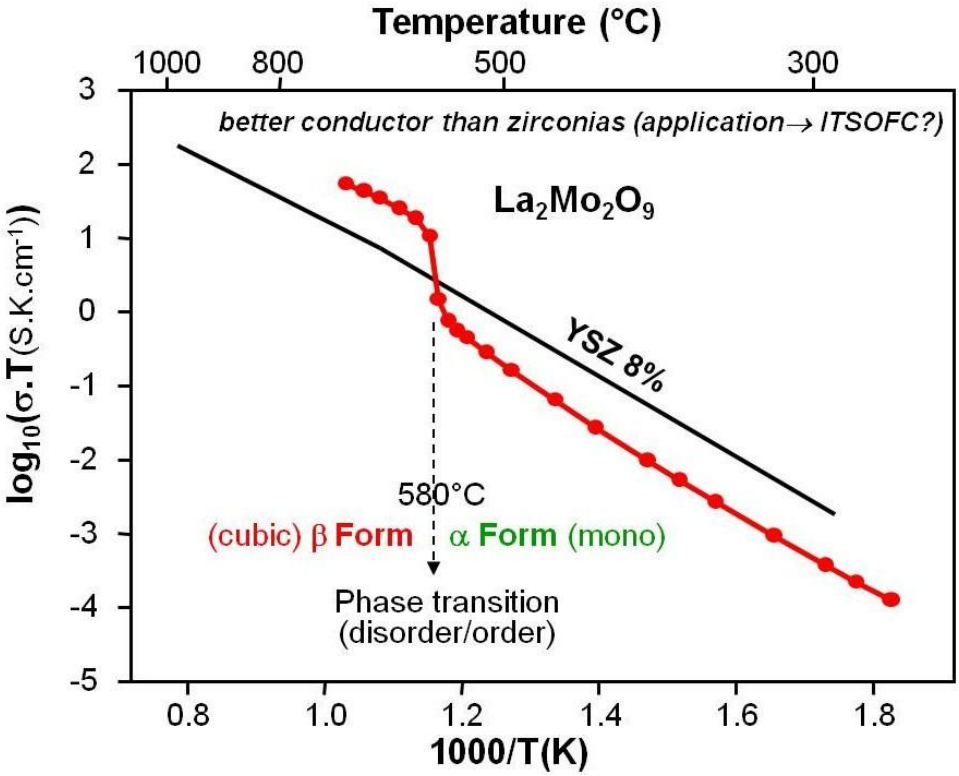

Figure 1.3: Conductivity of LMO compared to that of YSZ8%. [66]

It is known that in some elements, valence shell has a lone pair of electrons, occupying a position normally occupied by a ligand in the element without a lone pair. Because of the similarity in size between a lone pair (denoted as E) and an oxide ion, when the element is replaced by one without a lone pair, the same structure would be kept while leaving a vacancy (represented as □) through which oxygen can migrate. In β-$SnWO_4$, Sn^{2+} is a cation with a lone pair, so it can be formulated as $Sn_2W_2O_8E_2$. When Sn^{2+} is substituted by La^{3+} (which has no lone pair and with a charge +1) and W^{6+} by Mo^{6+}, it results $La_2Mo_2O_{8+1}\square$, with a vacancy and an oxygen atom added to compensate the loss of two lone pairs and for the change in cationic valence state. This vacancy in LMO helps mobility of O^{2-} ions. See Fig.1.4 for such illustration. Based on this concept, a series of possible lone pair substitutions were proposed [68].

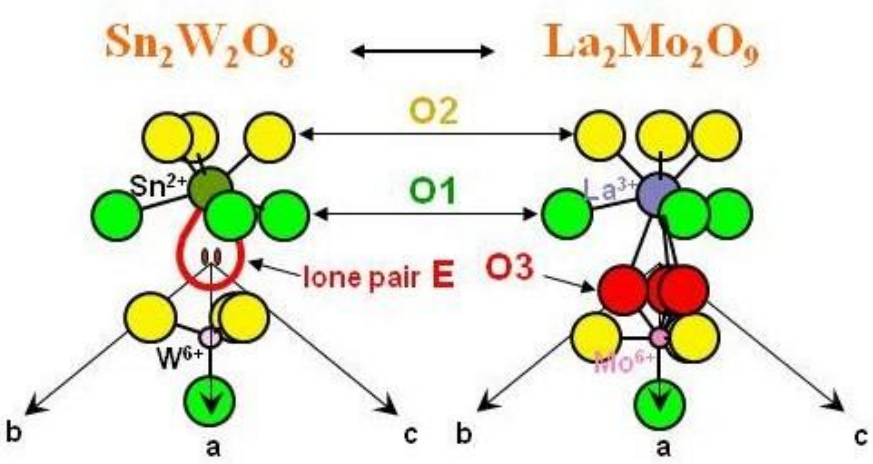

Figure 1.4: Illustration of LPS concept by $La_2Mo_2O_9$ and isostructural β-$SnWO_4$. [69]

1.3.1 Phase Transition, Crystal Structure:

1.3.1.1 High temperature form:

β-LMO is a high temperature phase, with cubic cell (space group $P2_13$). At 617 ^oC, cell parameters are found by both Neutron and X-ray diffraction patterns as a = b = c = 7.2014 Å. La and Mo occupy 4a positions. Oxygen O1 (4a) position is completely occupied; whereas O2 and O3 (12b) positions are partially occupied (about 78% and 38% respectively), leaving vacancies [70]. These oxygen vacancies form a path for oxide ion transport (migration). Thermal factors of oxygen atoms are large, suggesting three dimensional oxygen conduction through channels created by oxygen vacancies [69]. See Fig.1.5 and Table 1.1 for structure and cell parameters of the β-LMO phase.

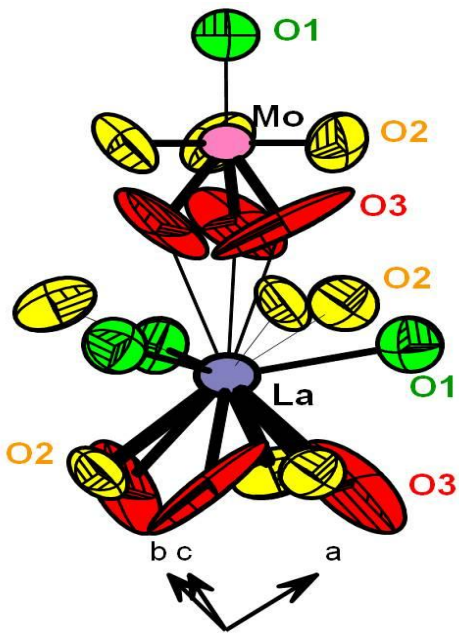

Figure 1.5: Environment of La^{3+}, Mo^{6+} and coordinating O1, O2, and O3 positions in β-LMO (left)(69).

Atome (site)	La (4a)	Mo (4a)	O(1) (4a)	O(2) (12b)	O(3) (12b)
x	0.8528(3)	0.1697(5)	0.3165(6)	0.9928(7)	0.911(3)
y	0.8528(3)	0.1697(5)	0.3165(6)	0.181(2)	0.642(5)
z	0.8528(3)	0.1697(5)	0.3165(6)	0.336(2)	0.551(2)
Occ	1	1	1	0.78(2)	0.38(2)
$B_{eq.}$ (Å^2)	5.6(2)	4.5(1)	6.9(2)	7.7(4)	19(2)

La-O1 (×3)	2.701(5)	Mo-O1 (×1)	1.840(6)
La-O2 (×3)	2.517(9)	Mo-O2 (×3)	1.760(9)
(×3)	2.799(9)	Mo-O3 (×3)	1.71(3)
La-O3 (×3)	2.68(3)		
(×3)	2.80(3)		

Table1.1: (on the top) showing crystallographic information of β-LMO structure, along with Occ (site occupation factor) and $B_{eq.}$ (Thermal factors). Table on the bottom showing inter-atomic distances in β-LMO (in Å) at 670 °C. [70]

1.3.1.2 Low temperature form:

Low temperature α-form represented as α-LMO has a monoclinic symmetry with 2x3x4 superstructure, unlike the β-LMO form, as observed by X-ray neutron and electron diffraction [69]. Space group $P2_1$, and cell parameters are: a = 14.325 Å, b = 21.482 Å, c = 28.585 Å, V = 8796 Å^3 and β = 90.40°. Evans *et al.* determined the structure and it has a total of 312 crstallographically independent atoms with 48 La, 48 Mo and 216 O. In this superstructure, La^{3+} have lower coordination numbers (with 6 and 12 O atoms), where 30 La atoms being nine coordinated. Whereas Mo exhibits three different types of coordinates; 15 tetrahedral, 15 trigonal bipyramidal and 18 octahedral [71]. See Fig. 1.6 for α-LMO structure.

It was suggested that order-disorder phase transition at α ←→ β phase transition is the key for increase in conductivity in LMO [72]. When probed by neutron atomic pair distribution analysis it was found that the local structure of the high temperature phase is very similar to that of the low temperature phase, implying that α ←→ β phase transition is because of the change in the distribution of the oxygen defects creating order and disorder in structures [73].

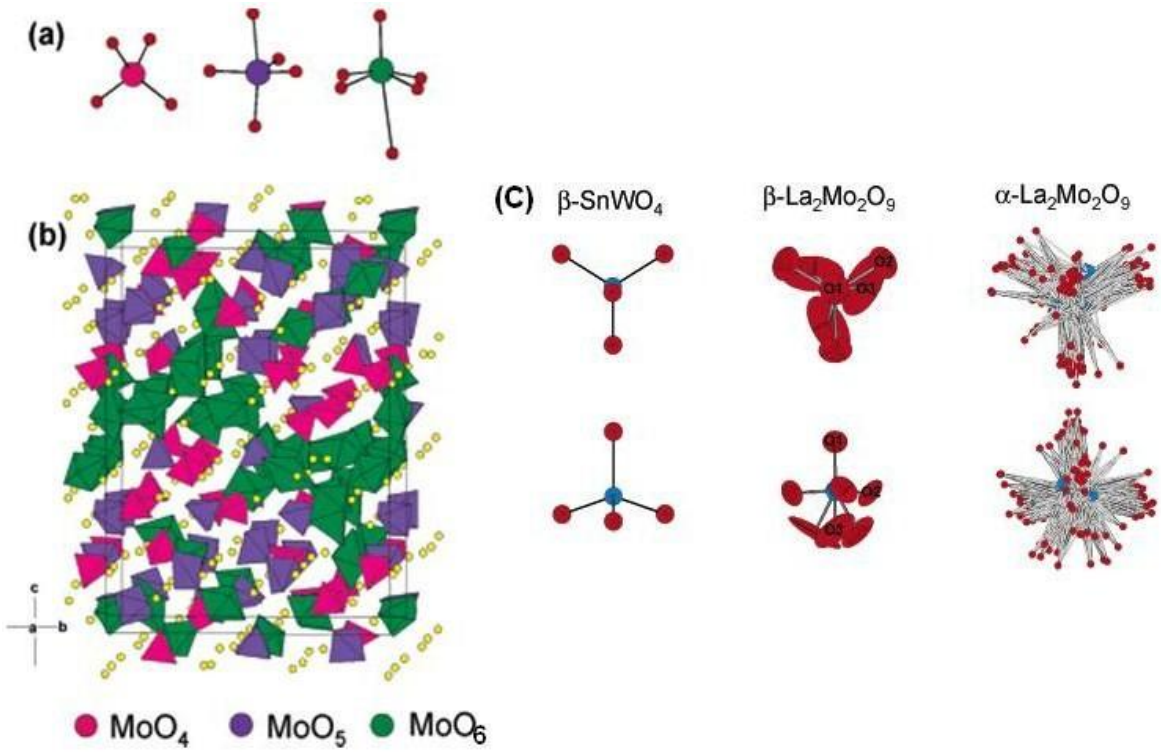

Fig. 1.6: (a) Coordination environment of Mo observed in α-LMO. (b) Polyhedral representation of α-LMO: tetrahedral groups shown in pink, trigonal bipyramidal in purple, octahedral in green and yellow spheres represent La atoms. (c) Comparison of B site coordination in β-$SnWO_4$, β-LMO and α-LMO. [71]

In thermal analysis performed on LMO, a hysteresis was observed at the transition during heating and cooling, and such transition is first order [66, 74, 75]. On the contrary, Hayward *et al.* have mentioned that α-LMO is sensitive to the thermal history of the material [76]. It was reported that when a sample which was in β-LMO was quenched from 950 ^{o}C, the progressive phase transition was of second order; however after subsequent annealing and cooling (slow cooling) 1st order phase transition occurs. The 2nd order transition is because of the replacement of the high temperature dynamic disordered structure by static disorder (because of quenching). See Fig. 1.7 for evolution of cell parameters with the increase in temperature.

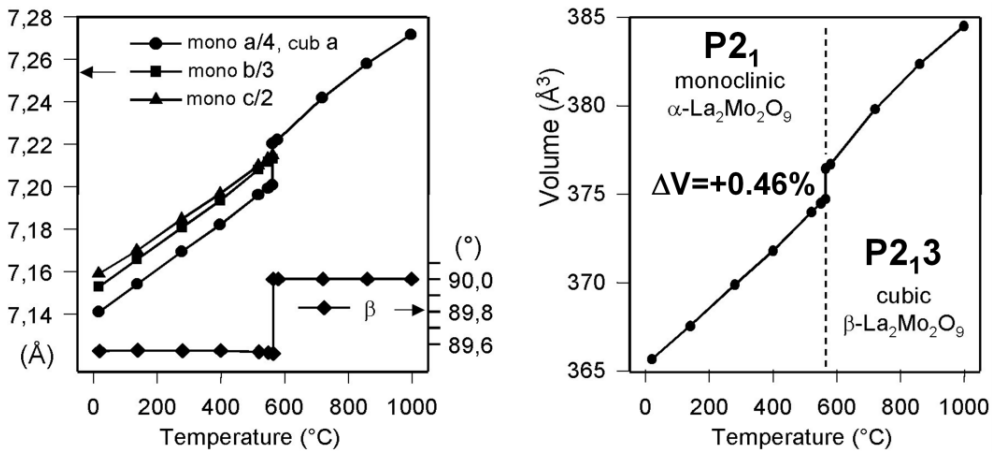

Figure 1.7: Evolution of LMO cell parameters as a function of temperature (left), Evolution of volume over monoclinic/cubic phase transition (right).[77]

1.3.2 Limitations of $La_2Mo_2O_9$ as an electrolyte material:

Although LMO exhibits considerable O^{2-} conductivity compared to standard electrolyte materials like YSZ, it is subject to some limitations. First major drawback is its instability in reducing atmospheres. When LMO comes in contact with H_2 or even diluted H_2 at SOFC operating temperatures, Mo^{6+} tends to reduce to lower valence states. It was shown by Goutenoire *et al.* that when LMO is heated at 760 °C in presence of diluted H_2 (6%H_2 + 94% N_2), the compound reduces to $La_7Mo_7O_{30}$ phase with part of Mo^{6+} reduced to Mo^{5+} or even Mo^{4+} [78]. Marrero-Lopez *et al.* found the same result after annealing LMO at 650 °C for 24 hours in a flux of 5%H_2 + 95% Ar. If LMO should be used as an SOFC electrolyte, stability in reducing atmospheres is vital, although less reducive gases are used in a single chamber fuel cell.

Another drawback is the phase transition around 580 °C from α ←→ β, which leads to an abrupt volume increase (thermal expansion) of 0.46%. This undesired behavior can induce mechanical stress at the electrode interfaces and in extreme cases could lead to fracture of the membrane. Most isovalent and aliovalent substitutions were able to stabilize the high temperature form down to room temperature (these possibilities will be discussed later in this chapter). Although the high thermal expansion coefficient (TEC) of LMO could lead to the formation of cracks at the interface with the electrodes, appropriate substitution is likely to reduce the TEC.

1.3.3 Chemical compatibility $La_2Mo_2O_9$ with electrode materials:

Chemical inertness and mechanical compatibility of the electrolyte with the electrodes is crucial to avoid premature breakdown of the fuel cell. Undesired reaction of electrolyte with electrode can lead to the formation of new isolating phases, which would in turn lead to immediate drop in the cell performance, changing essential parameters for cell operation and finally leading to the complete failure of total unit.

When powders of LMO and $Ce_{0.9}Gd_{0.1}O_{1.95}$ (CGO, which can be used as diffusion barrier /interconnect) were annealed together at 600 ^oC, 700 ^oC, 800 ^oC and 1000 ^oC even for 72 hours no reaction products were observed. No Inter-diffusion/reaction of either of cationic species into other compounds was evidenced, showing that CGO is chemically compatible with LMO [79].

NiO or NiO based cermets like Ni-YSZ are some of the standard anode materials used in SOFC. When chemical inertness of NiO was tested with LMO, no reaction between Ni or NiO and LMO was observed even at 1000 ^oC. Now it is known that Ni-CGO cermets do not react with LMO and could be potential anode materials compatible with LMO electrolyte [80]. Contrary to this results when W 75 mol% substituted LMO annealed with NiO, it was shown that the β-LMO/ β-LWO tend to form α-LWO (which is a poor conductor) [81]. However this result was contradicted by another study carried on mixture of 70% W substituted LMO and NiO, stating that NiO is stable with W-LMO compounds [82]. In another study it was shown that the potential cathode material $La_2NiO_{4+\delta}$ reacts with LMO readily at 600 ^oC resulting in the formation of La_2MoO_6 which on further annealings at 900 ^oC showed appearance of new NiO phase [79].

Studies carried out on LMO with cathode material $La_{0.6}Sr_{0.4}Co_{0.2}Fe_{0.8}O_{3-\delta}$ (LSCF) showed appearance of impurity phases La_2MoO_6 and scheelite $SrMoO_4$ already at 600 ^oC. It is clearly evident that Sr from LSCF reacts with Mo in LMO and forms $SrMoO_4$, leaving Mo deficient LMO to form La_2MoO_6. In other terms it is explained as alkaline earth cation Sr^{2+} from LSCF diffuses in LMO and reaction leads to the formation of two new phases. A complex mechanism was realized when mixture of $La_{0.85}Ca_{0.15}FeO_{3-\delta}$ (LCF) was annealed with $La_2Mo_{0.6}W_{1.4}O_9$ (70 mol% W substitution in LMO). When the same mixture is annealed at 1100 ^oC, appearance of $La_{14}W_8O_{45}$ and $CaMoO_4$ are observed, showing cross cationic diffusion of all elements in the system into each other, making LCF unsuitable cathode for LMO [82]. When

$La_{0.8}Sr_{0.2}MnO_{3-\delta}$ (LSM) powders are mixed with the monoclinic phased LMO annealed at temperatures more than 700 ^{o}C, formation of $SrMoO_4$ is observed, leaving Sr deficient LSM to form $LaMnO_3$ phase. It was found that Sr^{2+} was stabilizing high temperature β-LMO phase to room temperature. See Table 1.2 for the reactivity and the reaction products when LMO was annealed with some of the well known cathode materials.

Cathode	500 °C	600 °C	700 °C	1000 °C
$(La_{0.85}Ca_{0.15})FeO_3$	***Stable***			+ $CaMoO_4$ if T ≥ 1000°C
$(La_{0.75}Ca_{0.25})(Co_{0.8}Fe_{0.2})O_3$	***Stable***			+ $CaMoO_4$ + La_2MoO_6 if T ≥ 1000°C
$(La_{0.8}Sr_{0.2})MnO_3$ (LSM)	***Stable***		+ $SrMoO_4$ if T ≥ 700°C	
$(La_{0.6}Sr_{0.4})(Co_{0.2}Fe_{0.8})O_3$	***Stable***	+ $SrMoO_4$ + La_2MoO_6 if T ≥ 600°C		
La_2NiO_{4+d}	***Stable***	+ NiO + La_2MoO_6 if T ≥ 600°C		

Table 1.2: Stability range and reaction products observed as a function of temperature, when LMO is annealed with various cathode materials.[10, 79, 80]

1.3.3.1 Cationic diffusion studies of YSZ with cathode materials.

Apart from knowing the reaction products, it is important to understand the diffusion process of these elements at the interfaces. Diffusivity behavior of each element has to be studied precisely along with the possible cross-cationic diffusion and their coefficients. This kind of studies were performed on zirconias in contact with $La_{0.8}Sr_{0.2}CoO_3$, $La_{0.8}Sr_{0.2}FeO_3$, (La, Ca)CrO_3 and LSM e.t.c.[83-89]. When LSM is sputtered on a YSZ8% pellet and annealed at 1200 ^{o}C for two hours, new undesired phases of $La_2Zr_2O_7$ and $SrZrO_3$ are observed [90].

Kilo *et al.* [84] coupled pellets of LSM-YSZ and annealed the samples at 900 ^{o}C for 1000 hours and observed interdiffusion of elemental species from one pellet to other when analyzed by secondary ion mass spectrometry technique (SIMS; SIMS is briefly discussed in the next chapter). Undesired chemical reactions with dynamic chemical potential made it hard for investigating the mechanism. Diffusion coefficient of Sr^{+} in YSZ was observed ranging between 1 x 10^{-16} to 10^{-15} cm^2 s^{-1} at 1600 K to 1750 K. Diffusion coefficient of Mn in YSZ was estimated between 1 x 10^{-17} to 10^{-14} cm^2 s^{-1} at 1350 K to 1750 K respectively. See Fig. 1.8 for the diffusion profiles.

In a study carried by Horita *et al.*, a $Sr(NO_3)_2$ solution was applied on $La_{0.75}Ca_{0.25}CrO_3$ (LCC) pellet and diffusion was probed by annealing the sample at 900, 1000 and 1100 ^{o}C, which resulted in the formation of $SrCrO_4$, $Ca_5(CrO_4)_3O_{0.5}$, $(La_{1-x}Ca_x)CrO_3$ and few other minor phases. Alkaline earth Sr cationic diffusivity was than studied with SIMS; diffusion profile along the diffusion path was measured and diffusion coefficient of Sr in this compound was calculated. Diffusion coefficient of Sr in LCC pellet was distributed from 1 x 10^{-17} to 10^{-13} cm^2 s^{-1} ranging between 900 to 1100 ^{o}C. Activation energy of 318 kJ mol^{-1} was calculated from the slope of the line used for fitting the diffusion profile. The same type of study was carried by coupling pellets of two different compositions ($(La,Ca)CrO_3$ and $(La,Sr)CrO_3$) and cross cationic diffusion mechanism of elements from one pellet to other was studied along with diffusion coefficients. In the measurements performed on a pellet couple, diffusion coefficient of both Sr and Ca was calculated as 2.8 x 10^{-12} cm^2 s^{-1}. It was observed that diffusion coefficients are higher in solution deposited measurements compared to measurements involving coupling of pellets.[87]

Studies related to reaction mechanisms, diffusion mechanisms and cationic diffusion have to be realized to better understand the compatibility and the chemical stability of LMO and W-LMO with other electrode materials.

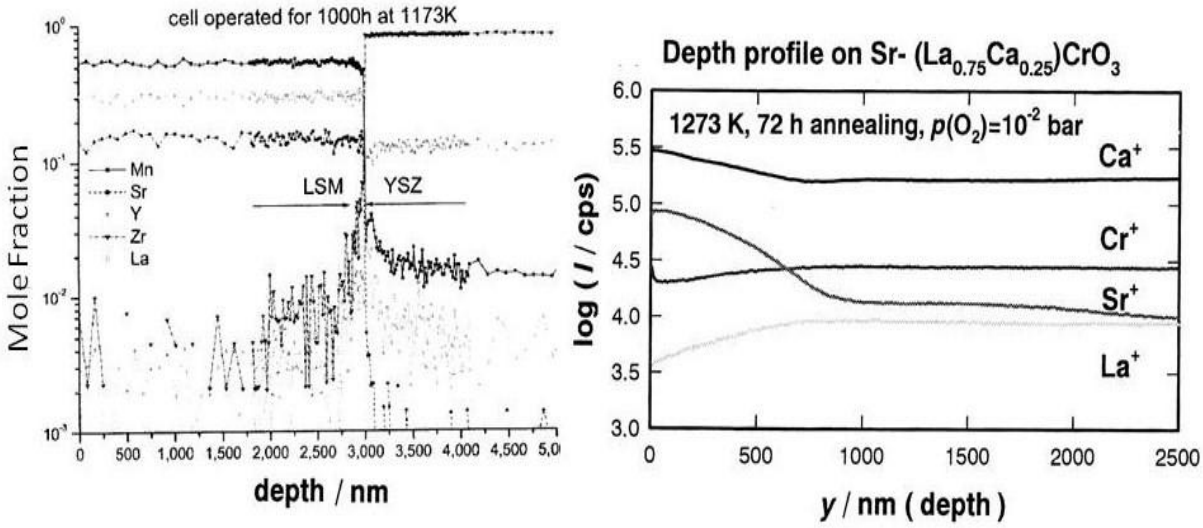

Figure 1.8: SIMS depth profile on: LSM-YSZ coupled pellets after annealing (left) [84] *, LCC compound annealed after deposition of $Sr(NO_3)_2$ (right).* [87]

1.4 LAMOX family:

Efforts to stabilize the high temperature β-phase at room temperature, improvement in conductivity, tolerability towards reducive atmospheres were observed by doping or substitution on La or Mo or on both sites. All these compounds which were derived this way are known as LAMOX family. Substitutions made to $(La_{2-x}A_x)(Mo_{2-y}B_y)O_{9-\delta}$ included alkaline, alkali, rare earth and Bi^{3+} on A site, where as B site was substituted with transition metals. Attempts to substitute oxygen by fluorine were also carried out [13, 70, 75, 91-135]. Oxygen tracer diffusion experiments carried on LAMOX family demonstrated that these materials are the best oxide ions conductors so far with higher tracer diffusion coefficient than stabilized zirconia and substituted gallate materials [136]. These results keep encouraging evaluation of the properties and development of LAMOX materials.

In an attempt to substitute oxide ion by fluorine ion, $La_2Mo_2O_{9-0.5z}F_z$ (z = 0.02 to 0.3) samples were synthesized [119]. The phase transition was not suppressed; but the transition temperature was reduced by 40 ^oC. The role of F^- ions in conductivity is uncertain. By F substitution, one O^{2-} ion is replaced by two F^- ion, modifying the vacancy present in the

Substituted Element	*Solubility Limit*	*Reference*
Bi^{3+}	3 – 15%	115, 123
Pr^{3+}	10-35%	115
Nd^{3+}	65-75%	87
Sm^{3+}	10% - ?	94
Eu^{3+}	12.5 – 20%	90
Gd^{3+}	10 – 25%	110
Dy^{3+}	-	118
Er^{3+}	-	118
Y^{3+}	5 – 10%	110
Ca^{2+}	~2%	18, 127
Sr^{2+}	-	124
Ba^{2+}	-	18
K^{+}	~2 – 3%	126, 127
Rb^{+}	-	126
W^{6+}	12.5 – 70%	85
Re^{6+}	-	125
Cr^{6+}	5 – 25%	125
V^{5+}	-	123
Dy^{3+} & W^{6+}	-	114

Table 1.3: Substitutions carried on La site (blue); Mo site (green) and double substitutions (red) along with their solubility limits

parent material which results in different super structure with tripling of cubic cell parameters. [92]. However the decrease in phase transition temperature promises improvement in anionic conductivity, but the compound is not stable since fluorine (all the samples with fluorine substitutes) tends to evolve upon heating. Some attempts to stabilize the high temperature form to room temperature by substitutions at the La site, Mo site and double substitutions along with their solubility limits are summarized in table 1.3.

V^{5+} doping at the Mo site is shown to suppress the phase transition, but no change in conductivity is reported [113, 137]. Al^{3+} substitution at the Mo site has a positive effect on its stability in reduced atmospheres [114]. Partial substitution of sulfur suppressed totally the phase transition, but conductivity is nearly half of that of LMO. See Fig. 1.9.

Few studies were reported where both La and Mo sites are substituted. Gd & W; Sr & Cr; Ba & W; Dy & W; Sm & W were doped on both A and B sites together. In these compounds, improved stability in reducing atmospheres, total suppression of the low temperature phase and improvements in conductivity at high temperature were reported [114, 120, 124, 130, 131].

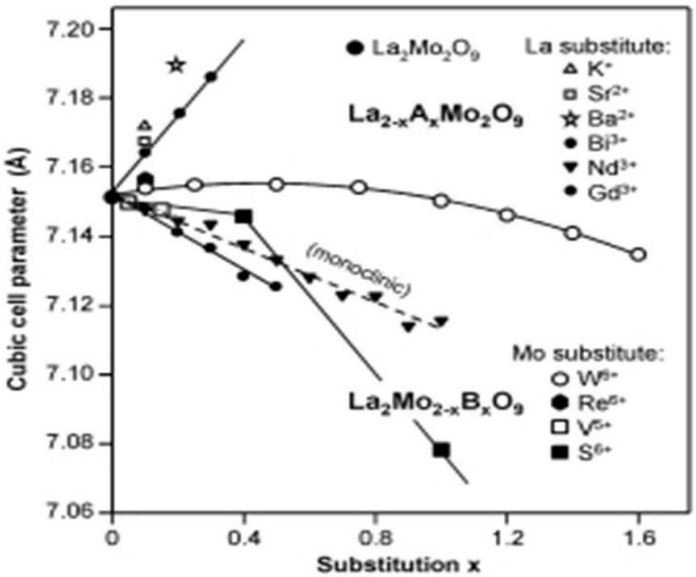

Figure 1.9: Evolution of cubic cell parameters with different substitutions. [136]

Unusual metastability is observed in Ca substituted LMO compounds. Abnormal demixion/recombination behavior is observed in these samples and a narrow window for stabilizing the β-phase is reported. See Fig. 1.10. This phenomenon has been identified as originating from a temperature dependent solid solution limit of alkali and alkaline-earth (for La) in LAMOX compounds, with higher solubility at higher limits. Many factors such as the synthesis temperature, cooling and heating rates, and the nature of the substituting element, sample shaping and sintering should be controlled to obtain pure β-phase LMO compounds which were however metastable [91, 138]. Metastable β-phase at room temperature was also observed in Eu substituted LMO compounds. It was stated that in compounds $La_{2-x}Eu_xMoO_9$, till the x = 0.2 limit, the compound can be obtained in stable β-phase; further increase of x content exhibits metastable phase with release of metastability (successive β-α-β phase transitions) during heating [100].

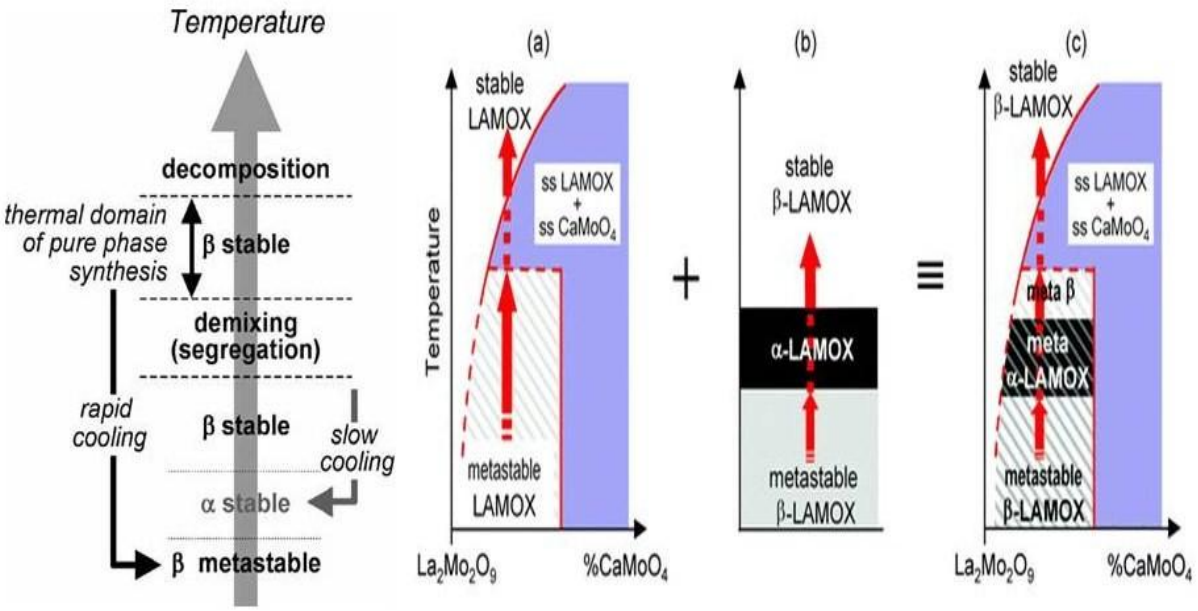

Figure 1.10: Complex successive phase transitions observed when heating and cooling LMO samples with 3mol% and 4mol% Ca substitute (extreme left). [13]*; Complex phase transformations observed when LMO sample with 4mol% Ca substitute (right). When cationic dimixing triggered by thermal stabilization at high temperature (a) and anionic vacancy ordering at intermediate temperature (b) are superimposed, complex metastability is observed (c).* [91]

1.4.1 Tungsten substituted $La_2Mo_2O_9$ and its stability in air.

One of the principle limitations of LMO is its vulnerability in reducing atmospheres. W substitution to Mo in LMO has shown to be successful to limit its stability in H_2 atmospheres. A significant amount of this thesis work is dedicated to stability of LMO and W-LMO in reductive atmospheres, next session will be focused on this point. W substitution showed strong influence on the synthesis and sintering behavior of LAMOX compounds, leading to higher sintering temperatures to obtain pure compounds with the same relative density. The solubility limit of W in β-LMO was found to be 80 mol% above which the stable α-$La_2W_2O_9$ (LWO) structure was obtained. The substitution range could be due to the similar ionic radius of W^{6+} (0.60 Å) and Mo^{6+} (0.59 Å) [109, 126, 139]. Substitution of W and its effects on conductivity and redox stability properties were very widely studied [81, 95, 96, 109, 115, 124, 140, 141].

LWO, the tungsten counterpart of LMO, has a similar structural arrangement at high temperature, only above ~1077 ^{o}C. Low temperature form α-LWO is significantly different from its high temperature form, with triclinic crystal structure bearing space group $P\bar{1}$ (cell parameters a = 7.2489 Å, b = 7.2878 Å, c = 7.0435 Å, α = 96.367^{o}, β = 94.715^{o} and γ = 70.286^{o}) [142, 143]. With the increase in W content, cell parameters of its cubic LAMOX phase increases till certain limit, and surprisingly after this limit of substitution (50 mol% W in LMO), the cell parameters decreases, the reason for which is not clear [92, 94, 109].

Collado *et al.* studied the phase stability of W substituted LMO and showed its stability range. In the series of $La_2Mo_{2-y}W_yO_9$, (y = 0, 0.2, 0.4, 0.6, 0.8, 1.0, 1.1, 1.2, 1.3, 1.4, 1.5, 1.6, 1.7 1.8, 1.9, 2.0) it was shown that when x = 1.8 and 2.0, the resulted compound is triclinic LWO phase at room temperature [109].

While y = 1.5 to 1.7, compounds can be prepared as pure phase: when quenched into liquid nitrogen from high temperature; the compounds will be mixture of α-LWO and β-LWO/ β-LMO when cooled slowly in the furnace. Attempts to quench compounds with y = 1.8 and 1.9 from high temperature to liquid nitrogen for obtaining pure β-LWO went unsuccessful leading to mixed α and β-LWO phases. Compounds with y = 1.3 and 1.4 were already β-LWO phase by slow cooling of furnace, although few impurities from α-LWO were found. For all compounds from y ≤ 1.3, pure β-LWO was obtained. In the case of y = 0.2 and 0.4, differential thermal analysis (DTA) has not shown the presence of any phase transition. Below y ≥ 0.2, the monoclinic α-LMO is stable at room temperature (RT). Schematic representation is given in fig. 1.11.

Apart from the synthesis by conventional solid state route, synthesis by microwave is also reported. It is shown that W series compounds can be obtained in pure phase easily and economically by microwave within 5 minutes [82, 109]. DTA performed on compounds with y ≥ 1.3 revealed an endothermic event above 950 ^{o}C, which can be ascribed to α-LWO (triclinic) to β-LMO/LWO (cubic) phase transition. See Fig. 1.12 for DTA curves. Comprehensive study on phase stability of W-LAMOX is due, for any industrial application.

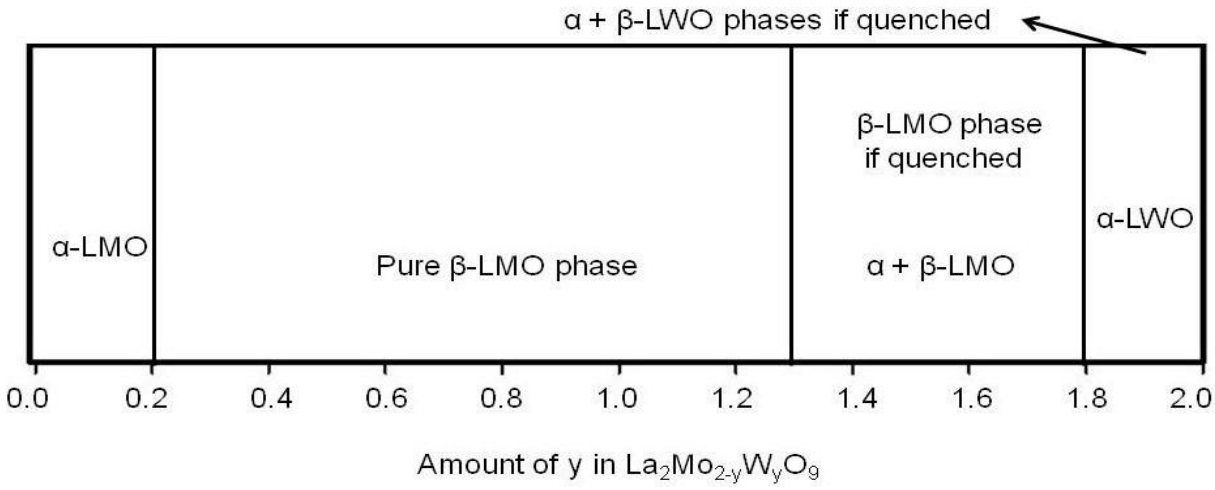

Figure 1.11: Change of phases with increase in W-content (y) in $La_2Mo_{2-y}W_yO_9$ at RT [109].

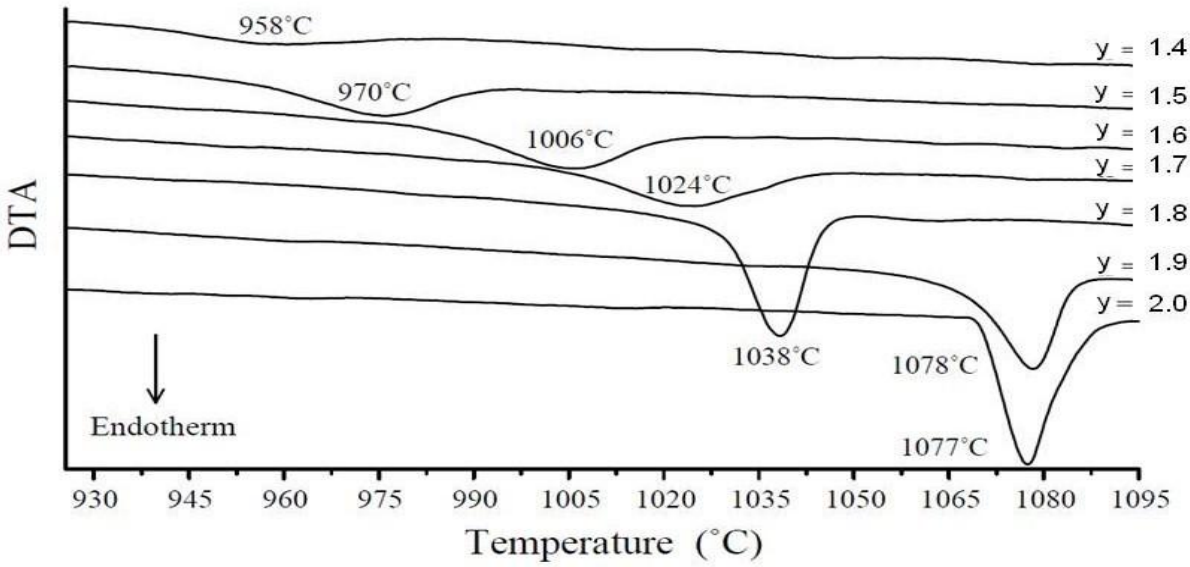

Figure 1.12: DTA curves for y in $La_2Mo_{2-y}W_yO_9$; α → β-LWO phase transition is observed. [109]

Georges *et al.* measured the electrical properties of $La_2Mo_{2-y}W_yO_9$ (y = 0.25, 0.5, 0.75, 1.0, 1.2 and 1.4) pellets (which were in pure β-LMO phase at room temperature) and derived Arrhenius plots, see Fig. 1.13 for such Arrhenius plots. Because of the suppression of the α/β

phase transition, no abrupt jump in conductivity is noticed. The evolution of log (σT) vs 1/T was linear at low temperature (typical Arrhenius type behavior with thermal activated ionic mobility). High temperature evolution is more complex, with a deviation from Arrhenius behavior (increase in conductivity at first, then leveling off). This behavior is explained to be originated from variation in the conduction mechanism from Arrhenius type at low temperature (thermally activated ionic mobility in solids) to VTF-type (Vogel-Tammann-Fulcher model) at high temperature (mobility thermally assisted by the local environment).

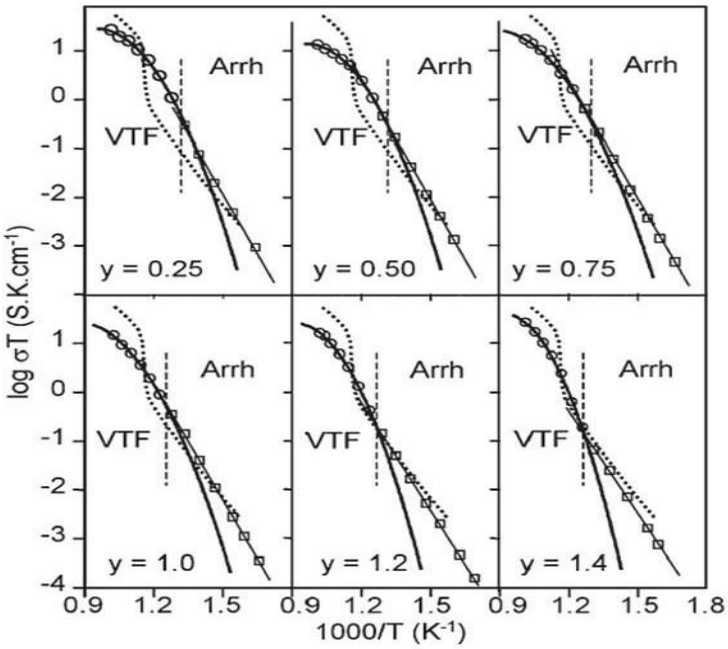

Figure 1.13: Arrhenius plots of the conductivity curves of high density pellets of the series $La_2Mo_{2-y}W_yO_9$, fitted with a conventional Arrhenius model on the linear part at low temperature (thin lines), and with a VTF model when departure from linearity is observed at high temperature (thick lines). The conductivity of LMO is added as a dotted line for reference.[93]

In β-LMO the formation of 3D rigid framework by anti-tetrahedral units of [1OLa_3Mo] creates tunnels through which oxygen ions can migrate, introducing anionic conductivity in this sample. W substitution in LMO has a complex influence on the β-LMO structure, which is explained as a combination of two effects: a smooth, regular evolution (re-equilibration) of O2/O3 sites occupancy balance, and a non-linear variation in the geometry of the [1OLa3Mo] anti-tetrahedral units. This could result in unusual evolution in cell volume parameters. It was found that La_2MoWO9 (50 mol% W substitution) represents the highest degree of disorder on the hexavalant sublattice (the largest entropy), and such disorder is favorable for oxide ion mobility.[93]

In double substituted system, W substitution compensates the negative effect of rare earth substitution on reducibility[144] and stabilizes the high temperature phase to room temperature; retaining or even improving the conductivity values compared to the parent compound. Along with the substitution of W at the Mo site; La site was substituted by Gd, Nd, Y, Dy, Ba, Ca, K [120, 136, 144-146]. Generally, W in LMO improves its stability in reductive atmospheres (discussed later) and even reduces the TEC. Previous studies provide guidance for the development and enhancement of desired properties in these materials.

1.5 Stability of $La_2Mo_2O_9$ and W-substituted $La_2Mo_2O_9$ in reductive Atmospheres

1.5.1 Stability of $La_2Mo_2O_9$:

It is mentioned in earlier discussion that LMO is vulnerable in reductive atmosphere. Prior to use LMO as core material (either electrolyte or electrode) in SOFC, it is mandatory to understand and control its reduction mechanism. Once understood, this phenomenon can possibly be limited by appropriate substitution, or once we have a wide spectrum of its reduction limitations, composition tuning for a given application is more possible.

Goutenoire *et al.* in 1999 found that the partial reduction of LMO under diluted H_2 (6%H_2 + 94% N_2) at 700 ^oC leads to the formation of $La_7Mo_7O_{30}$ (7730) phase (a perovskite related compound). A 1.5% weight loss (see Fig. 1.14) was observed and reoxidization in air at lower temperature leads back to $La_2Mo_2O_9$. However, its electrical conductivity properties were not explored [78]. These reductions of Mo^{6+} in LMO, lead to the formation of the 7730 phase where mixture of Mo^{5+} and Mo^{6+} can be observed. Further reduction of LMO above 700 ^oC leads to the amorphous phase [95]. Surprisingly, attempts to reduce LMO pellets with temperature less than 700 ^oC (under 5 % H_2 + 95 % Ar), revealed no change in the crystal structure but pellets broke easily. Degradation of the microstructure was also observed [95].

The oxygen stoichiometry of the amorphous LMO was found close to 7 (i.e. 9-δ = ~7 in $La_2Mo_2O_{9-\delta}$), suggesting that the possible oxidation state of Mo was +4. When the sample is oxidized back in the TGA apparatus, oxygen stoichiometry of 9 is gained back swiftly (see fig. 1.15).

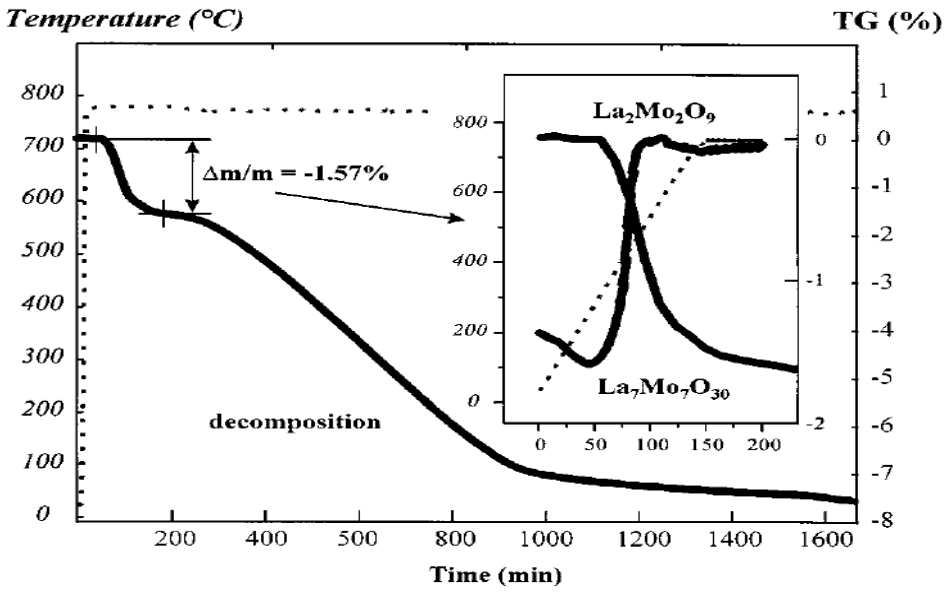

Figure 1.14: TGA curve of the reduction of LMO under 5% H_2 + 95% N_2 at 700 °C. In inset: Detail of the same TGA curve along with its oxidation behavior from LM 7-7-30 to LMO phase.[78]

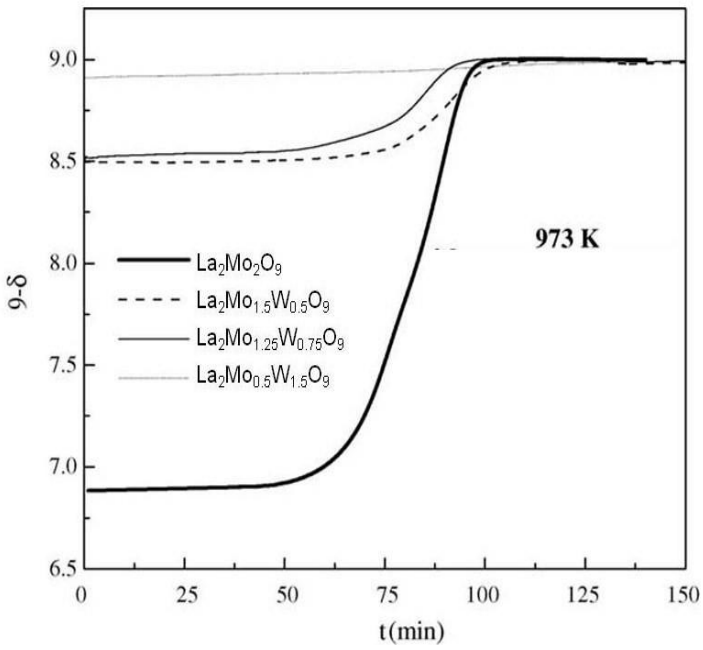

Figure 1.15: TGA curves of LMO and W-LMO reduced samples, showing the oxygen gain (9- δ) when annealed in air. [95]

Further studies carried out on LMO reduction showed that it is able to get amorphous (i.e. LMO reduced down to amorphous phase $La_2Mo_2O_{7-\delta}$) at temperature as low as 608 ^oC under high Ar + 10% H_2 flow (contrary to earlier belief of its stability around 700 ^oC) [147]. XRD pattern of amorphous $La_2Mo_2O_{7-\delta}$ and LMO, and TGA curve showing loss of oxygen as a function of time can be seen in fig. 1.16.

The amorphous phase $La_2Mo_2O_{6.88}$ (reduced LMO) is stable at temperatures less than 900 ^oC in Ar–H_2 atmosphere, further annealing lead to the crystallization in an unknown phase. Reducibility of LMO has been studied in different pO_2 pressures. Annealing carried in different pO_2 atmospheres at 1000 ^oC (see Fig. 1.17) demonstrated that LMO is stable down to pO_2 of 10^{-7} Pa. Once the pO_2 is further reduced down to 10^{-8} Pa, oxygen loss has started stabilizing sample with oxygen stoichiometry 7.71; which on further drop in pO_2 under 10^{-10} Pa leads to more oxygen loss down till 6.4. It is shown that LMO when annealed at 10^{-9} Pa pO_2, decomposes into a mixture of partially reduced molybdates: $La_5Mo_3O_{16}$ ($La_5Mo_2^{VI}Mo^{V}O_{16}$) and $La_5Mo_6O_{21}$ ($La_5Mo_3^{V}Mo_3^{IV}O_{21}$). When annealed at a pO_2 of 10^{-11} Pa, it decomposes in a mixture of two different molybdates: $La_4Mo_2O_{11}$ and $La_{16}Mo_{21}O_{56}$ ($La_{16}Mo_{20}^{III}Mo^{IV}O_{56}$).

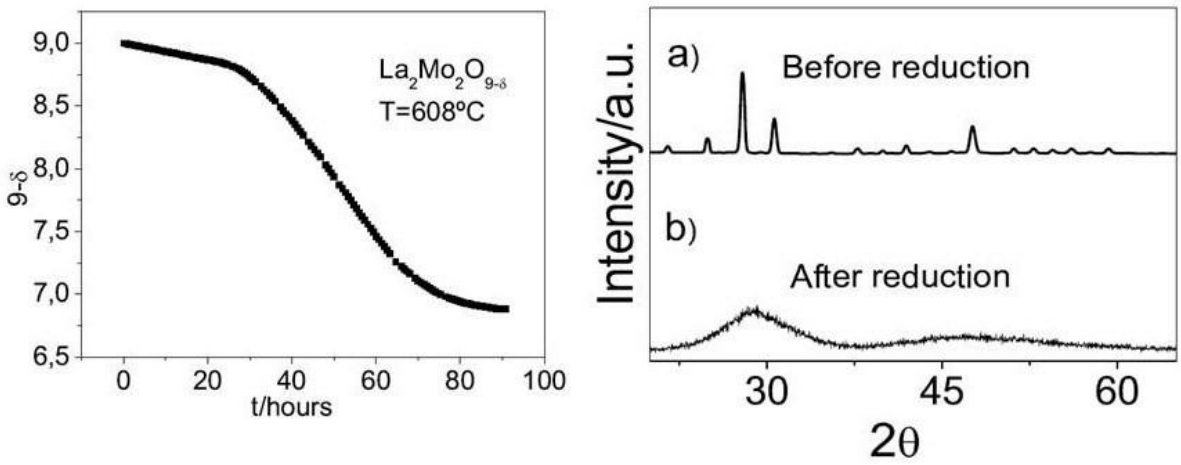

Figure 1.16: TGA curve showing oxygen stoichiometry 9-δ *in reduced LMO as a function of time when reduced under 10% H_2 + 90% Ar at 608 ^oC (left); XRD patterns of a) LMO and b) amorphous reduced phase* $La_2Mo_2O_{7-\delta}$ *(right)* [147].

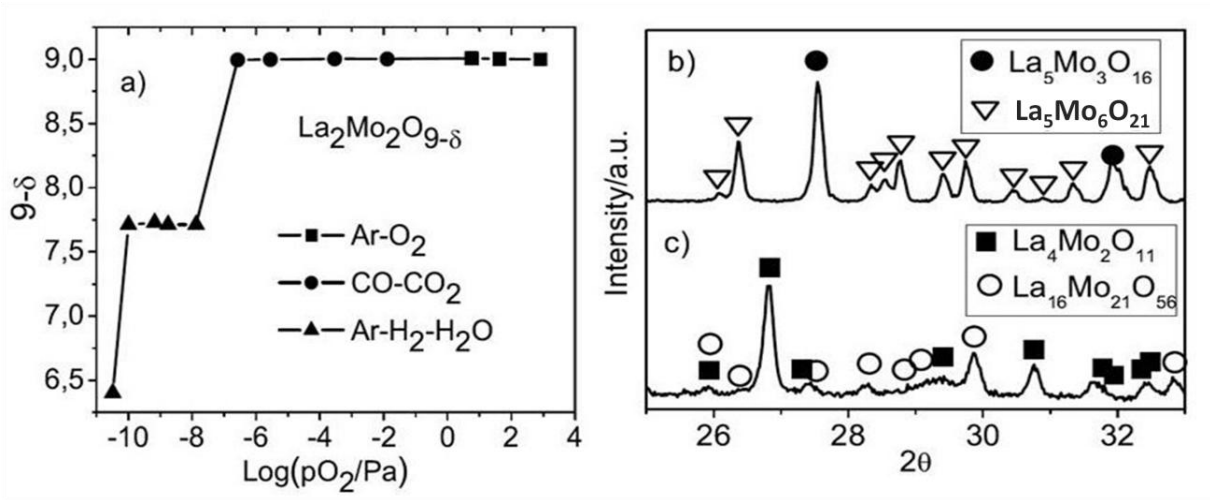

Figure 1.17: a) pO_2 dependence of the overall oxygen content determined by isothermal TGA at 1000 ^oC LMO powders; b) and c) showing the resultant XRD patterns with their crystallographic phases at 10^{-9} Pa and 10^{-11}Pa after annealing at 1000 ^oC. [147]

Conductivity measurements carried out on reduced LMO (amorphous phase) and reduced W-substituted LMO showed enhanced total conductivity values [95]. It is explained that Mo^{6+} in LMO, reduces into a mixture of Mo^{5+} and Mo^{6+} states (at 7730 phase). It is stated that once molybdenum loses oxygen from its lattice, this gives rise to n-type conductivity, suggesting that the reduced $La_2Mo_2O_9$ compounds display electronic conductivity. The same possibility was suggested by Vega Castillo *et al.* [147] when they have observed SEM images of a reduced LMO material. On a pellet of LMO without any gold layer sputtering, they were able to explore the surface of the pellet (SEM technique is limited only to conductive materials: when an insulating material (non electronic conductive material) like LMO is observed, no electron image will be constructed); in other words, the surface of a reduced LMO pellet is electronically conductive. As we have seen above, the electrolyte in a SOFC should not exhibit electronic conductivity, if not the performance and stability of SOFC is affected and it gradually leads to the failure of the total unit. This observation of electronic conduction now raises question about the possible utilization of LMO and the LAMOX family materials as electrodes in SOFC.

Considering the increase in total conductivity is attributed to the electronic part, recently the amorphous reduced LMO phase was proposed as an anode material in SOFC. Porous amorphous LMO anode is synthesized and coupled with $La_{0.8}Sr_{0.2}Ga_{0.83}Mg_{0.17}O_{3-\delta}$ electrolyte

material and discovered to have satisfactory performance. LMO reduced anode has shown significant tolerance towards sulfur (performance was tested against H_2; H_2 + 5ppm H_2S; H_2 + 10 ppm H_2S) [65].

1.5.2 Stability of W substituted $La_2Mo_2O_9$:

Vulnerability in reducing atmospheres is a crucial problem with molybdates. It has been showed that W-substitution to Mo in LMO can minimize the oxygen losses caused by partial reduction of hexavalant Mo (see Fig. 1.18), while stabilizing high conductive β-phase down to room temperature and improving its conductivity and its abrupt thermal expansion behavior. In H_2 atmospheres, Mo^{6+}reduces partially to a mixture of Mo^{6+} and Mo^{5+} (happens at 7730 phase and this reduction of Mo^{6+} leads to the appearance of electronic conductivity) and its partial substitution by hexavalent W^{6+} helped to stabilize the same in reductive atmospheres.

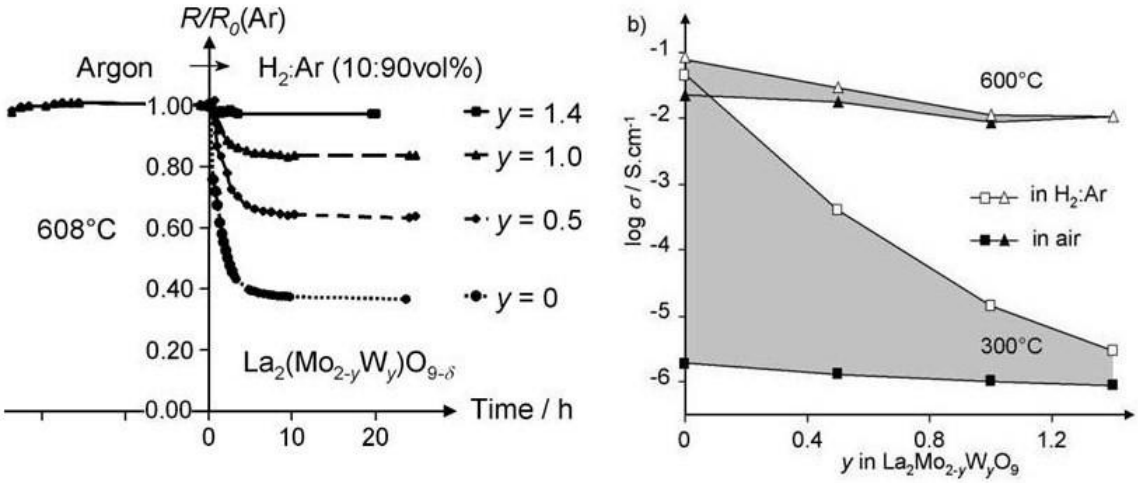

Figure 1.18: Time dependency of W-LMO relative resistivity at 608 °C under diluted H_2 (left); Total conductivity of the same compounds at 300 °C and 600 °C in air and diluted H_2 as a function of W content, grey colored area is assumed to represent the electronic contributions (right) [140].

In a study which included W-LMO compounds (y = 0, 0.5, 1.0 and 1.4), it was suggested that the compound with y = 1.4 is a suitable candidate as an electrolyte because of its resistance towards reductive atmospheres and good total conductivity (assuming that the lesser the sample

is reduced, the lower will be its electronic contribution; overall good ionic conductor). On the other hand, compounds with low tungsten content are suggested to be suitable candidates for anode applications [140]. Since W component in these compounds is less reduced, the sample still shows sufficient ionic conductivity, whereas reduced Mo component contributes to electronic part. It was found that reduction depends on time and temperature as well. Considering other dopants at the Mo site, W exhibited superior stability in terms of oxygen loss. During reduction, once LMO loses 0.43 oxygen per formula unit, the structure changes to $La_7Mo_7O_{30}$; but when Mo is substituted by 12.5 mol% W, even after oxygen loss of 1.13 per formulae unit, no change in the structural type is noticed [144] (see Fig. 1.19 and 1.20).

An XPS study carried by Jin *et al.* concluded that only Mo component in LMO is prone to reduction. When 10 mol% of Dy is substituted to La in LMO and annealed in diluted H_2 atmospheres, oxygen loss attributed to Mo reduction is observed. Similarly, when 10 mol% Dy to La site and 50 mol% of W to Mo site are substituted, the reductive behavior in the sample was controlled and it is shown that only Mo is susceptible to reduction [124].

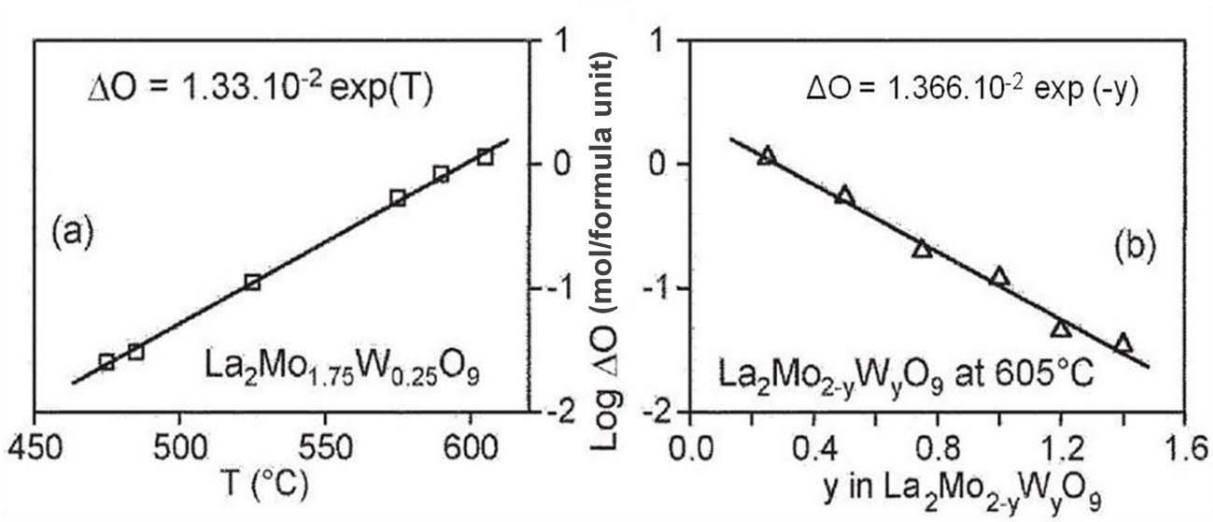

Figure 1.19: Evolution of oxygen loss (ΔO) under reducing conditions (16 hours in dilute H_2 flow) for W-LMO compounds: as a function of temperature for 12.5 mol% W substitution in LMO (left), as a function of composition at fixed 605 °C (right).[144]

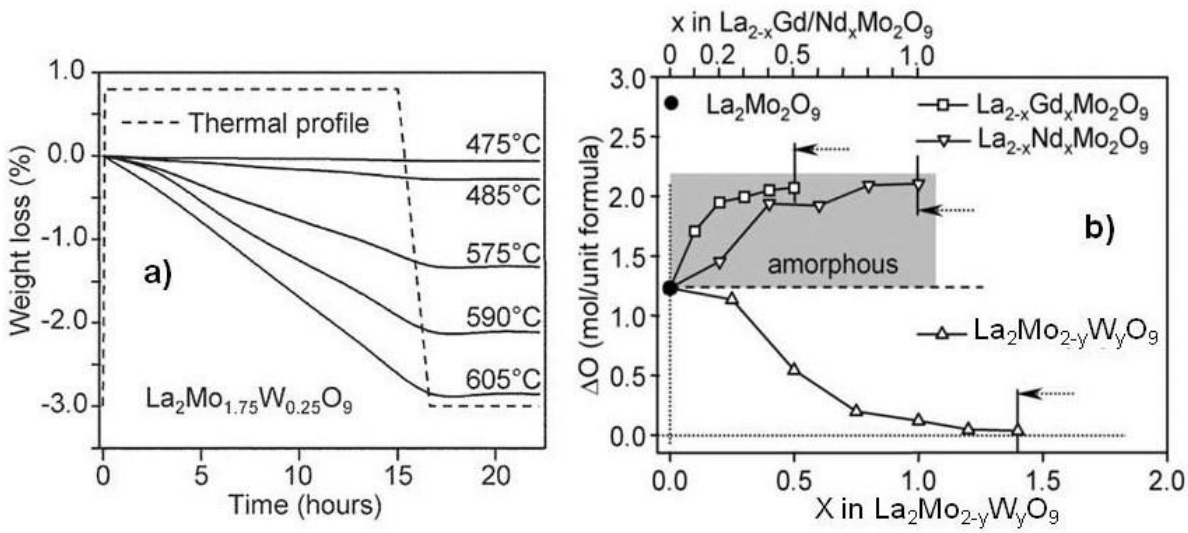

Figure 1.20: a) TGA curves showing Wt loss (%) on 12.5 mol% W substituted LMO as a function of time and temperature. b) Evolution of oxygen loss (ΔO) under diluted H_2 as a function of composition at 605 ^oC: bottom scale = y in $La_2Mo_{2-y}W_yO_9$; top scale = x in $La_{2-x}Gd_xMo_2O_9$ and $La_{2-x}Nd_xMo_2O_9$. [144]

A Spanish team has conducted similar type of experiments on LMO pellets with W substitution of 0 mol %, 25 mol %, 33.33 mol % and 75 mol % which were reduced in 5%H_2+ 95%Ar flow for 24 hours at 700 ^oC [95]. They have obtained amorphous pellets (7-δ) (initially LMO), whereas pellets with 25 and 33.33 mol % W substitute were obtained as isostructural $La_7Mo_7O_{30}$ phase; however on pellet with 75 mol % W-substitute, no change in the β-LMO structure was noticed (nevertheless when the annealing temperature was increased from 700 ^oC to 900 ^oC, the pellet had partially decomposed into $La_7Mo_7O_{30}$ phase). The oxygen stoichiometry of the reduced amorphous sample (initially LMO) was close to 7 (9-δ = ~7, where δ is oxygen loss), showing that the oxidation state of Mo was +4. These samples have been oxidized back in air in TGA recording the Wt. gain (amount of O_2 took back by reduced compounds to retain their stable state). Such TGA curves were shown in Fig. 1.15 (in section 1.5.1). This study has shown a non-linear behavior of the thermal expansion coefficients with increase in W-content. In another study carried on $La_2Mo_{0.8}W_{1.2}O_9$, the thermal expansion coefficient was found to 9.7 x 10^{-6} $^oC^{-1}$, which was a significant improvement compared to parent material LMO[109]. Another study reported TEC in $La_2Mo_{2-y}W_yO_9$ with $0.5 \leq y \leq 1.5$ range from 13.5 - 16.0 x 10^{-6} K^{-1}

between 298 and 773 K and TEC would range from 19.4 to 21 x 10^{-6} K^{-1} between 823 to 1073 K [95]. Details are given in Table1.4. TEC of some other standard electrode and electrolyte materials are given in Table 1.5.

It can be concluded that the partial reduction of LMO or W-LMO compounds can induce mixed electronic and ionic conductivity in these samples. W substitution in LMO reduces the oxygen loss and increases its potential as a suitable anode material in SOFC. However more research is needed to explore appropriate composition, thermal stability, reduction temperatures and atmospheres to have a complete understanding of the system.

Composition	**Thermal expansion coefficients**	
	Temperature (K)	**TEC (10^{-6} K^{-1})**
$La_2Mo_2O_9$	298–823	13.5
	898–1073	16.8
$La_2Mo_{1.5}W_{0.5}O_9$	298–723	15.2
	823–1073	19.9
$La_2Mo_{1.25}W_{0.75}O_9$	298–773	16.0
	823–1073	19.4
$La_2Mo_1W_1O_9$	298–773	15.4
	823–1073	20.7
$La_2Mo_{0.5}W_{1.5}O_9$	298–773	13.9
	823–1073	21.0

Table 1.4: TEC of LMO and W-LMO compounds evaluated by Dilatometry [95].

Composition	Thermal expansion coefficients		Reference
	Temperature (^{o}C)	TEC (10^{-6} $^{o}C^{-1}$)	
$La_{0.9}Sr_{0.1}MnO_{3-\delta}$	50-1000	11.2	148
$La_{0.8}Sr_{0.2}MnO_{3-\delta}$	50-1000	11.4	148
$La_{0.6}Sr_{0.4}MnO_{3-\delta}$	50-1000	12.3 (1)	149
$La_{0.6}Sr_{0.4}Co_{0.2}Fe_{0.8}O_{3-\delta}$	100-600	15.3	150
CeO_2	50-1000	12.3	151
$Ce_{0.9}Gd_{0.1}O_{1.95}$	RT-800	11.9	79
$Ce_{0.8}Gd_{0.2}O_{1.9}$	50-1000	12.5	149
$Ce_{0.6}Gd_{0.4}O_{1.8}$	50-1000	12.1	149

Table 1.5: TEC of some standard electrode and electrolyte materials used in SOFC applications.

1.6 Summary and commitment to this thesis work:

LMO is considered to be competitive to the industrially appreciated 8%YSZ. Its conductivity in intermediate temperature range around 600 ^{o}C makes it a potential candidate as an electrolyte material in SOFC. However, application of LMO is limited because of its instability in reductive atmospheres; abrupt volume expansion because of a phase transition from monoclinic α to cubic β around 580 ^{o}C; high thermal expansion; and chemical reactivity towards other components (electrodes) in SOFC.

Various studies carried by doping / substitution of La and Mo site by other transition and rare earth elements were able to suppress the phase transition making thermal expansion continuous and lower its high thermal expansion coefficient. Out of all substitutions, only W-substitution was able to limit the instability of LMO in reductive atmospheres and W-substitution is considered a viable candidate because of its high solubility allowance (~80 %). It was shown that the more the W-substitution, the more is its stability in reductive atmospheres; however

conductivity requirements for overall performance of SOFC were met better than 8% YSZ, but the compound is still vulnerable to reduction. First part of my thesis work presented in chapter-3, deals with studying the phase stability of W-substituted LMO compounds with W-content 50 mol% and more. Since high W-content in LMO can result in the appearance of less conducting α- $La_2W_2O_9$ (α- LWO) and appearance of unusual metastable behavior, there is need to evaluate its phase stability. Selection and optimization of the suitable composition for SOFC application is important. Temperature controlled XRD, DTA were employed to study the thermal stability and phase diagram of W-LMO in precise.

Many studies related to the compatibility of LMO and W-LMO with traditionally used cathode materials, electrolytes and anode were performed. LMO is considered to be chemically stable with the anode material NiO and the electrolyte CGO; raising hopes for possible use of Ni-CGO cermets as possible anode materials for LMO electrolyte. However exploration of suitable cathode material is still in progress. Experiments carried with many standard cathode materials lead to appearance of undesired reaction products at the interface (which are considered to be hazardous for SOFC operation); thus indicating that cross cationic diffusion took place. In my thesis work, I attempt to probe the diffusion mechanism and to study the cationic diffusion behavior, cross cation diffusion, diffusion length, effect of time and temperature on diffusion. SIMS technique and XRD are used for this study to gain deeper insight into diffusion process. These details are discussed in chapter 4.

As already discussed, LMO is vulnerable to reductive atmospheres. LMO in diluted H_2 atmospheres or any reductive atmospheres first reduces to $La_7Mo_7O_{30}$ phase and on further reduction lead to the amorphisation of the sample. Overall the increase in conductivity is observed and it is attributed to the electronic contribution which was caused by partial reduction of hexavalent Mo to a mixture of Mo^{5+} and Mo^{6+}, making these samples MIEC (behavior which makes LMO inapplicable as electrolyte in SOFC). However use of the reduced LMO as an anode material in SOFC was proposed and attempted with success. It is even found that reduced LMO material is sulfur tolerant till satisfactory level, giving new opportunities to explore in LMO world. Few studies stated that W substitution in LMO can limit its reducibility, and even showed that W part in the LMO is not prone to any reduction. Not many studies were conducted to understand the reduction behavior and its kinetics. In my thesis work I study the structural

changes, reduction behavior, and reduction kinetics of LMO in different reductive atmospheres and parameters. This part of the work is discussed in chapter 5.

In summary, in this current thesis, possible use of LMO and W-LMO materials as electrolyte and anode materials for SOFC is studied and evaluated. Chemical compatibility of LMO with cathode materials was examined by studying the cationic diffusion mechanism.

1.7 References:

1. W. Nernst, *Z. Elektrochem* **1899,** 6:41.
2. J. C. Boivin; G. Mairesse, *Chemistry of Materials* **1998,** 10, (10), 2870-2888.
3. J. B. Goodenough, *Nature* **2000,** 404, (6780), 821-823.
4. S. Basu, *Recent Trends in Fuel Cell Science and Technology*. Springer: 2007.
5. C. Eyraud; J. Lenoir; M. Gery, *Comptes Rendus de l'Academie des sciences* **1961,** 252, 1599.
6. M. Kuhn; T. Napporn, *Energies* **2010,** 3, (1), 57-134.
7. I. Riess, *Journal of Power Sources* **2008,** 175, (1), 325-337.
8. T. Hibino; A. Hashimoto; T. Inoue; J. Tokuno; S. Yoshida; M. Sano, *Journal of the Electrochemical Society* **2000,** 147, (8), 2888-2892.
9. T. Hibijo; H. Iwahara, *Chemistry Letters* **1993,** 7, 1131-1134.
10. J. Jacquens. Stabilite, reactivite et Performances de conducteurs par ions oxyde de la famille LAMOX comme elements de coeur de pile a combustible SOFC mono-chamber. Universite du Maine, Le Mans, 2010.
11. T. Hibino; S. Q. Wang; S. Kakimoto; M. Sano, *Solid State Ionics* **2000,** 127, (1-2), 89-98.
12. T. Hibino; H. Tsunekawa; S. Tanimoto; M. Sano, *Journal of the Electrochemical Society* **2000,** 147, (4), 1338-1343.
13. A. Selmi. Synthese et caracterisation de nouvelles ceramiques conductrices par ions O2- derivees de La2Mo2O9 par substitutions aliovalentes. Universite du Maine, Le Mans, France, 2007.
14. A. Lashtabeg; S. J. Skinner, *Journal of Materials Chemistry* **2006,** 16, (31), 3161-3170.
15. H. Inaba; H. Tagawa, *Solid State Ionics* **1996,** 83, (1-2), 1-16.
16. V. V. Kharton; F. M. B. Marques; A. Atkinson, *Solid State Ionics* **2004,** 174, (1-4), 135-149.
17. M. Mogensen; N. M. Sammes; G. A. Tompsett, *Solid State Ionics* **2000,** 129, (1-4), 63-94.
18. T. Takahashi; H. Iwahara; Y. Nagai, *Journal of Applied Electrochemistry* **1972,** 2, (2), 97-104.
19. P. Shuk; H. D. Wiemhofer; U. Guth; W. Gopel; M. Greenblatt, *Solid State Ionics* **1996,** 89, (3-4), 179-196.
20. J. B. Goodenough; J. E. Ruiz-Diaz; Y. S. Zhen, *Solid State Ionics* **1990,** 44, (1-2), 21-31.
21. M. Feng; J. B. Goodenough, *European Journal of Solid State and Inorganic Chemistry* **1994,** 31, (8-9), 663-672.
22. F. Abraham; J. C. Boivin; G. Mairesse; G. Nowogrocki, *Solid State Ionics* **1990,** 40-41, Part 2, (0), 934-937.
23. S. Lazure; C. Vernochet; R. N. Vannier; G. Nowogrocki; G. Mairesse, *Solid State Ionics* **1996,** 90, (1-4), 117-123.
24. F. Abraham; M. F. Debreuille-Gresse; G. Mairesse; G. Nowogrocki, *Solid State Ionics* **1988,** 28-30, Part 1, (0), 529-532.
25. H. Arikawa; H. Nishiguchi; T. Ishihara; Y. Takita, *Solid State Ionics* **2000,** 136, 31-37.
26. L. Leon-Reina; M. C. Martin-Sedeno; E. R. Losilla; A. Cabeza; M. Martinez-Lara; S. Bruque; F. M. B. Marques; D. V. Sheptyakov; M. A. G. Aranda, *Chemistry of Materials* **2003,** 15, (10), 2099-2108.
27. E. J. Abram; D. C. Sinclair; A. R. West, *Journal of Materials Chemistry* **2001,** 11, (8), 1978-1979.
28. R. H. J. W. Fergus, X. Li, D. P. Wilkinson, J. Zhang, *Solid Oxide Fuel Cells Material Properties and Performance*. CRC Press: 2009.
29. E. P. Murray; S. A. Barnett, *Solid State Ionics* **2001,** 143, (3-4), 265-273.
30. J. M. Ralph; A. C. Schoeler; M. Krumpelt, *Journal of Materials Science* **2001,** 36, (5), 1161-1172.
31. N. T. Hart; N. P. Brandon; M. J. Day; N. Lapena-Rey, *Journal of Power Sources* **2002,** 106, (1-2), 42-50.
32. M. T. Colomer; B. C. H. Steele; J. A. Kilner, *Solid State Ionics* **2002,** 147, (1-2), 41-48.

33. Y. Y. Huang; J. M. Vohs; R. J. Gorte, *Journal of the Electrochemical Society* **2004,** 151, (4), A646-A651.
34. S. P. Simner; J. R. Bonnett; N. L. Canfield; K. D. Meinhardt; J. P. Shelton; V. L. Sprenkle; J. W. Stevenson, *Journal of Power Sources* **2003,** 113, (1), 1-10.
35. S. McIntosh; R. J. Gorte, *Chemical Reviews* **2004,** 104, (10), 4845-4865.
36. N. Q. Minh; T. Takahashi, *Science and Technology of Ceramic Fuel Cells*. Elsevier: 1995.
37. S. P. Jiang; W. Wang, *Journal of the Electrochemical Society* **2005,** 152, (7), A1398-A1408.
38. A. Chroneos; D. Parfitt; J. A. Kilner; R. W. Grimes, *Journal of Materials Chemistry* **2010,** 20, (2), 266-270.
39. S. J. Skinner, *Solid State Sciences* **2003,** 5, (3), 419-426.
40. E. V. Tsipis; V. V. Kharton, *Journal of Solid State Electrochemistry* **2008,** 12, (9), 1039-1060.
41. L. S. Wang; S. A. Barnett, *Solid State Ionics* **1995,** 76, (1-2), 103-113.
42. T. Misono; K. Murata; T. Fukui; J. Chaichanawong; K. Sato; H. Abe; M. Naito, *Journal of Power Sources* **2006,** 157, (2), 754-757.
43. S. Lee; Y. Lim; E. A. Lee; H. J. Hwang; J. W. Moon, *Journal of Power Sources* **2006,** 157, (2), 848-854.
44. Q. Li; Y. Fan; H. Zhao; L.-P. Sun; L.-H. Huo, *Journal of Power Sources* **2007,** 167, (1), 64-68.
45. R. Hui; Z. Wang; S. Yick; R. Maric; D. Ghosh, *Journal of Power Sources* **2007,** 172, (2), 840-844.
46. T. L. Nguyen; K. Kobayashi; T. Honda; Y. Iimura; K. Kato; A. Neghisi; K. Nozaki; F. Tappero; K. Sasaki; H. Shirahama; K. Ota; M. Dokiya; T. Kato, *Solid State Ionics* **2004,** 174, (1-4), 163-174.
47. C. Fu; K. Sun; N. Zhang; X. Chen; D. Zhou, *Electrochimica Acta* **2007,** 52, (13), 4589-4594.
48. Q. Li; H. Zhao; L. Huo; L. Sun; X. Cheng; J.-C. Grenier, *Electrochemistry Communications* **2007,** 9, (7), 1508-1512.
49. B. C. H. Steele; I. Kelly; H. Middleton; R. Rudkin, *Solid State Ionics* **1988,** 28-30, Part 2, (0), 1547-1552.
50. A. Subramania; T. Saradha; S. Muzhumathi, *Journal of Power Sources* **2007,** 165, (2), 728-732.
51. Y. S. Wang; H. W. Nie; S. R. Wang; T. L. Wen; U. Guth; V. Valshook, *Materials Letters* **2006,** 60, (9-10), 1174-1178.
52. Z. Wang; J. Qian; H. Cao; S. Wang; T. Wen, *Journal of Alloys and Compounds* **2007,** 437, (1-2), 264-268.
53. Y. Yin; S. Li; C. Xia; G. Meng, *Journal of Power Sources* **2007,** 167, (1), 90-93.
54. K. T. Lee; A. Manthiram, *Journal of Power Sources* **2006,** 158, (2), 1202-1208.
55. M. D. Gross; J. M. Vohs; R. J. Gorte, *Journal of the Electrochemical Society* **2006,** 153, (7), A1386-A1390.
56. H. P. He; R. J. Gorte; J. M. Vohs, *Electrochemical and Solid State Letters* **2005,** 8, (6), A279-A280.
57. S. Jung; M. D. Gross; R. J. Gorte; J. M. Vohs, *Journal of the Electrochemical Society* **2006,** 153, (8), A1539-A1543.
58. H. Kim; S. Park; J. M. Vohs; R. J. Gorte, *Journal of the Electrochemical Society* **2001,** 148, (7), A693-A695.
59. S. D. Park; J. M. Vohs; R. J. Gorte, *Nature* **2000,** 404, (6775), 265-267.
60. A. Atkinson; S. Barnett; R. J. Gorte; J. T. S. Irvine; A. J. McEvoy; M. Mogensen; S. C. Singhal; J. Vohs, *Nat Mater* **2004,** 3, (1), 17-27.
61. M. Gong; X. Liu; J. Trembly; C. Johnson, *Journal of Power Sources* **2007,** 168, (2), 289-298.
62. Y. H. Huang; R. I. Dass; Z. L. Xing; J. B. Goodenough, *Science* **2006,** 312, (5771), 254-257.
63. C. Sun; U. Stimming, *Journal of Power Sources* **2007,** 171, (2), 247-260.
64. S. W. Zha; Z. Cheng; M. L. Liu, *Electrochemical and Solid State Letters* **2005,** 8, (8), A406-A408.
65. X. C. Lu; J. H. Zhu, *Journal of the Electrochemical Society* **2008,** 155, (10), B1053-B1057.
66. P. Lacorre; F. Goutenoire; O. Bohnke; R. Retoux; Y. Laligant, *Nature* **2000,** 404, (6780), 856-858.

67. D. Marrero-Lopez; J. Canales-Vazquez; J. C. Ruiz-Morales; A. Rodriguez; J. T. S. Irvine; P. Nunez, *Solid State Ionics* **2005,** 176, (23-24), 1807-1816.
68. P. Lacorre, *Solid State Sciences* **2000,** 2, (8), 755-758.
69. F. Goutenoire; O. Isnard; R. Retoux; P. Lacorre, *Chemistry of Materials* **2000,** 12, (9), 2575-2580.
70. S. Georges; F. Goutenoire; F. Altorfer; D. Sheptyakov; F. Fauth; E. Suard; P. Lacorre, *Solid State Ionics* **2003,** 161, (3-4), 231-241.
71. I. R. Evans; J. A. K. Howard; J. S. O. Evans, *Chemistry of Materials* **2005,** 17, (16), 4074-4077.
72. J. Emery; D. Massiot; P. Lacorre; Y. Laligant; K. Conder, *Magnetic Resonance in Chemistry* **2005,** 43, (5), 366-371.
73. L. Malavasi; H. Kim; S. J. L. Billinge; T. Proffen; C. Tealdi; G. Flor, *Journal of the American Chemical Society* **2007,** 129, (21), 6903-6907.
74. X. P. Wang; Q. F. Fang, *Journal of Physics-Condensed Matter* **2001,** 13, (8), 1641-1651.
75. Z. S. Khadasheva; N. U. Venskovskii; M. G. Safronenko; A. V. Mosunov; E. D. Politova; S. Y. Stefanovich, *Inorganic Materials* **2002,** 38, (11), 1168-1171.
76. S. A. Hayward; S. A. T. Redfern, *Journal of Physics-Condensed Matter* **2004,** 16, (21), 3571-3583.
77. F. G. P. Lacorre, F. Altorfer, D. Sheptyakov, F. Fauth, E, Suard, *Advances in Science and Technology* **2003,** 33, (10th International Ceramic Congress-part C), 10.
78. F. Goutenoire; R. Retoux; E. Suard; P. Lacorre, *Journal of Solid State Chemistry* **1999,** 142, (1), 228-235.
79. G. Corbel; S. Mestiri; P. Lacorre, *Solid State Sciences* **2005,** 7, (10), 1216-1224.
80. G. Corbel; P. Lacorre, *Journal of Solid State Chemistry* **2006,** 179, (5), 1339-1344.
81. D. Marrero-Lopez; J. Pena-Martinez; J. C. Ruiz-Morales; D. Perez-Coll; M. C. Martin-Sedeno; P. Nunez, *Solid State Ionics* **2007,** 178, (23-24), 1366-1378.
82. C. Tealdi; G. Chiodelli; G. Flor; S. Leonardi, *Solid State Ionics* **2010,** 181, (31-32), 1456-1461.
83. S. Fearn; J. Rossiny; J. Kilner, *Solid State Ionics* **2008,** 179, (21-26), 811-815.
84. M. Kilo, *Defects and Diffusion in Ceramics: an Annual Retrospective Vii* **2005,** 242-244, 185-253.
85. H. Kishimoto; N. Sakai; T. Horita; K. Yamaji; M. E. Brito; H. Yokokawa, *Solid State Ionics* **2007,** 178, (21-22), 1317-1325.
86. I. Waernhus; N. Sakai; H. Yokokawa; T. Grande; M.-A. Einarsrud; K. Wiik, *Solid State Ionics* **2007,** 178, (13-14), 907-914.
87. T. Horita; M. Ishikawa; K. Yamaji; N. Sakai; H. Yokokawa; M. Dokiya, *Solid State Ionics* **1998,** 108, (1-4), 383-390.
88. T. Horita; N. Sakai; T. Kawada; H. Yokokawa; M. Dokiya, *Journal of the American Ceramic Society* **1998,** 81, (2), 315-320.
89. T. Horita; K. Yamaji; M. Ishikawa; N. Sakai; H. Yokokawa; T. Kawada; T. Kato, *Journal of the Electrochemical Society* **1998,** 145, (9), 3196-3202.
90. H. Taimatsu; K. Wada; H. Kaneko; H. Yamamura, *Journal of the American Ceramic Society* **1992,** 75, (2), 401-405.
91. A. Selmi; C. Galven; G. Corbel; P. Lacorre, *Dalton Trans* **2010**, (1), 93-102.
92. F. Goutenoire; O. Isnard; E. Suard; O. Bohnke; Y. Laligant; R. Retoux; P. Lacorre, *Journal of Materials Chemistry* **2001,** 11, (1), 119-124.
93. S. Georges; O. Bohnke; F. Goutenoire; Y. Laligant; J. Fouletier; P. Lacorre, *Solid State Ionics* **2006,** 177, (19-25), 1715-1720.
94. G. Corbel; Y. Laligant; F. Goutenoire; E. Suard; P. Lacorre, *Chemistry of Materials* **2005,** 17, (18), 4678-4684.
95. D. Marrero-Lopez; J. Canales-Vazquez; J. C. Ruiz-Morales; J. T. S. Irvine; P. Nunez, *Electrochimica Acta* **2005,** 50, (22), 4385-4395.

96. D. Marrero-Lopez; J. Canales-Vazquez; W. Z. Zhou; J. T. S. Irvine; P. Nunez, *Journal of Solid State Chemistry* **2006,** 179, (1), 278-288.
97. G. Corbel; P. Durand; P. Lacorre, *Journal of Solid State Chemistry* **2009,** 182, (5), 1009-1016.
98. S. Basu; P. S. Devi; H. S. Maiti, *Applied Physics Letters* **2004,** 85, (16), 3486-3488.
99. D. Marrero-Lopez; D. Perez-Coll; J. C. Ruiz-Morales; J. Canales-Vazquez; M. C. Martin-Sedeno; P. Nunez, *Electrochimica Acta* **2007,** 52, (16), 5219-5231.
100. G. Corbel; E. Chevereau; S. Kodjikian; P. Lacorre, *Inorganic Chemistry* **2007,** 46, 6395-6404.
101. A. Selmi; G. Corbel; P. Lacorre, *Solid State Ionics* **2006,** 177, (35-36), 3051-3055.
102. X. P. Wang; Z. J. Cheng; Q. F. Fang, *Solid State Ionics* **2005,** 176, (7-8), 761-765.
103. Q. F. Fang; X. R. Wang; Z. S. Li; G. G. Zhang; Z. G. Yi, *Materials Science and Engineering a-Structural Materials Properties Microstructure and Processing* **2004,** 370, (1-2), 365-369.
104. D. Marrero-Lopez; P. Nunez; M. Abril; V. Lavin; U. R. Rodriguez-Mendoza; V. D. Rodriguez, *Journal of Non-Crystalline Solids* **2004,** 345, 377-381.
105. Q. F. Fang; X. P. Wang; G. G. Zhang; Z. G. Yi, *Journal of Alloys and Compounds* **2003,** 355, (1-2), 177-182.
106. Q. F. Fang; Z. Zhuang; X. P. Wang; D. Li; J. X. Wang, *Chinese Journal of Chemical Physics* **2008,** 21, (3), 270-274.
107. X. P. Wang; D. Li; Q. F. Fang; Z. J. Cheng; G. Corbel; P. Lacorre, *Applied Physics Letters* **2006,** 89, (2).
108. F. J. Liang; X. P. Wang; Q. F. Fang; J. X. Wang; C. Li; D. Li; Z. Zhuang, *Physical Review B* **2006,** 74, (1).
109. J. A. Collado; M. A. G. Aranda; A. Cabeza; P. Olivera-Pastor; S. Bruque, *Journal of Solid State Chemistry* **2002,** 167, (1), 80-85.
110. S. Basu; P. S. Devi; H. S. Maiti, *Journal of the Electrochemical Society* **2005,** 152, (11), A2143-A2147.
111. S. Basu; P. S. Devi; H. S. Maiti; Y. Lee; J. C. Hanson, *Journal of Materials Research* **2006,** 21, (5), 1133-1140.
112. S. Basu; H. S. Maiti, *Journal of Solid State Electrochemistry* **2010,** 14, (6), 1021-1025.
113. C. Li; X. P. Wang; J. X. Wang; D. Li; Z. Zhuang; Q. F. Fang, *Materials Research Bulletin* **2007,** 42, (6), 1077-1084.
114. D. Li; X. P. Wang; Z. Zhuang; J. X. Wang; C. Li; Q. F. Fang, *Materials Research Bulletin* **2009,** 44, (2), 446-450.
115. D. Li; X. P. Wang; Q. F. Fang; J. X. Wang; C. Li; Z. Zhuang, *Physica Status Solidi a-Applications and Materials Science* **2007,** 204, (7), 2270-2278.
116. D. Li; X. P. Wang; Z. Zhuang; Q. F. Fang, *Physica B-Condensed Matter* **2009,** 404, (12-13), 1757-1760.
117. M. R. Li; X. J. Kuang; S. Y. Chong; Z. L. Xu; C. I. Thomas; H. J. Niu; J. B. Claridge; M. J. Rosseinsky, *Angewandte Chemie-International Edition* **2010,** 49, (13), 2362-2366.
118. X. Li; Z. P. Yang; L. Guan; C. Liu; P. L. Li, *Journal of Crystal Growth* **2008,** 310, (12), 3117-3120.
119. A. Arulraj; F. Goutenoire; M. Tabellout; O. Bohnke; P. Lacorre, *Chemistry of Materials* **2002,** 14, (6), 2492-2498.
120. S. Georges; F. Goutenoire; P. Lacorre; M. C. Steil, *Journal of the European Ceramic Society* **2005,** 25, (16), 3619-3627.
121. S. Basu; H. S. Maiti, *Journal of the Electrochemical Society* **2009,** 156, (7), P114-P116.
122. Q. B. Bo; J. Feng; H. Y. Wang; J. Meng, *Chinese Chemical Letters* **2003,** 14, (2), 197-200.
123. T. M. He; Y. L. Huang; Q. He; Y. Ji; L. Pei; J. Liu; Z. Lu, *Journal of Alloys and Compounds* **2005,** 388, (1), 145-152.

124. T.-Y. Jin; M. V. M. Rao; C.-L. Cheng; D.-S. Tsai; M.-H. Hung, *Solid State Ionics* **2007,** 178, (5-6), 367-374.
125. I. P. Marozau; A. L. Shaula; V. V. Kharton; N. P. Vyshatko; A. P. Viskup; J. R. Frade; F. M. B. Marques, *Materials Research Bulletin* **2005,** 40, (2), 361-371.
126. P. Pinet; J. Fouletier; S. Georges, *Materials Research Bulletin* **2007,** 42, (5), 935-942.
127. R. Subasri; D. Matusch; H. Nafe; F. Aldinger, *Journal of the European Ceramic Society* **2004,** 24, (1), 129-137.
128. D. S. Tsai; M. J. Hsieh; J. C. Tseng; H. Y. Lee, *Journal of the European Ceramic Society* **2005,** 25, (4), 481-487.
129. X. P. Wang; Q. F. Fang, *Solid State Ionics* **2002,** 146, (1-2), 185-193.
130. J. H. Yang; Z. H. Gu; Z. Y. Wen; D. S. Yan, *Solid State Ionics* **2005,** 176, (5-6), 523-530.
131. K. S. Yoo; A. J. Jacobson, *Journal of Materials Science* **2005,** 40, (16), 4431-4434.
132. G. G. Zhang; Q. F. Fang; X. P. Wang; Z. G. Yi, *Physica Status Solidi a-Applied Research* **2003,** 199, (2), 329-334.
133. V. Voronkova; E. Kharitonova; A. Krasilnikova, *physica status solidi (a)* **2009,** 206, (11), 2564-2568.
134. P. Lacorre; A. Selmi; G. Corbel; B. Boulard, *Inorganic Chemistry* **2006,** 45, (2), 627-635.
135. C. Tealdi; G. Chiodelli; L. Malavasi; G. Flor, *Journal of Materials Chemistry* **2004,** 14, (24), 3553-3557.
136. S. Georges; F. Goutenoire; O. Bohnke; M. C. Steil; S. J. Skinner; H. D. Wiemhofer; P. Lacorre, *Journal of New Materials for Electrochemical Systems* **2004,** 7, (1), 51-57.
137. V. I. Voronkova; E. P. Kharitonova; A. E. Krasil'nikova, *Crystallography Reports* **2010,** 55, (2), 276-282.
138. A. Selmi; G. Corbel; S. Kojikian; V. Voronkova; E. Kharitonova; P. Lacorre, *European Journal of Inorganic Chemistry* **2008**, (11), 1813-1821.
139. D. Marrero-Lopez; J. C. Ruiz-Morales; J. Pena-Martinez; J. Canales-Vazquez; P. Nunez, *Journal of Solid State Chemistry* **2008,** 181, (4), 685-692.
140. J. Jacquens; D. Farrusseng; S. Georges; J. P. Viricelle; C. Gaudillere; G. Corbel; P. Lacorre, *Fuel Cells* **2010,** 10, (3), 433-439.
141. Z. Zhuang; X. P. Wang; D. Li; T. Zhang; Q. F. Fang, *Journal of the American Ceramic Society* **2009,** 92, (4), 839-844.
142. Y. Laligant; A. Le Bail; F. Goutenoire, *Journal of Solid State Chemistry* **2001,** 159, (1), 223-227.
143. D. Marrero-Lopez; J. Pena-Martinez; J. C. Ruiz-Morales; P. Nunez, *Journal of Solid State Chemistry* **2008,** 181, (2), 253-262.
144. S. Georges; F. Goutenoire; Y. Laligant; P. Lacorre, *Journal of Materials Chemistry* **2003,** 13, (9), 2317-2321.
145. S. Georges; M. Salaun, *Solid State Ionics* **2008,** 178, (37-38), 1898-1906.
146. A. Selmi; C. Galven; G. Corbel; P. Lacorre, *Dalton Transactions* **2010,** 39, (1), 93-102.
147. J. Vega-Castillo; L. Mogni; G. Corbel; P. Lacorre; A. Caneiro, *International Journal of Hydrogen Energy* **2010,** 35, (11), 5890-5894.
148. M. Mori; Y. Hiei; N. M. Sammes; G. A. Tompsett, *Journal of the Electrochemical Society* **2000,** 147, (4), 1295-1302.
149. M. Mori; N. M. Sammes; E. Suda; Y. Takeda, *Solid State Ionics* **2003,** 164, (1-2), 1-15.
150. L. W. Tai; M. M. Nasrallah; H. U. Anderson; D. M. Sparlin; S. R. Sehlin, *Solid State Ionics* **1995,** 76, (3â€“4), 273-283.
151. M. Mogens; L. Thomas; H. Uffe Rud; M. Gurli, *Journal of the Electrochemical Society* **1994,** 141, (8), 2122-2128.

Chapter 2: Experimental and Methodology

2.1 Introduction 49

2.2 Synthesis of powder samples 49

2.3 Synthesis of Pellets 51

2.4 X-Ray Diffraction (XRD) and in-situ Temperature Controlled X-Ray Diffraction (TC-XRD) 54

2.5: Thermal Analysis 55

2.5.1: Thermogravimetric Analysis (TGA) 56

2.5.2: Differential Thermal Analysis (DTA) 57

2.6: Secondary Ion Mass Spectrometry (SIMS) 58

2.7: Electrical Conductivity Studies 62

2.8: References 64

Chapter 2
Experimental and Methodology:

2.1 Introduction:

Current materials utilized for high end applications are result of years of research, application of different experimental synthesis and analysis process. Advanced ceramic materials come under this group, which were designed for their unique and exceptional properties. Materials and methods designated for these properties also come through extreme experimental approvals and scrutinization. The properties of these designed breed of new materials are determined by their composition, synthesis route, microstructure, particle size and purity e.t.c. Optimization of synthesis, different processing stages, analysis methods, characterization techniques also play a vital role for proper governance of time, man power and cost induced.

In this chapter we will discuss synthesis and processing of $La_2Mo_2O_9$, W-substituted LMO powders. We will be even discussing how these powders were pelletized and densified. How these samples were analyzed by different experimental techniques like differential thermal analysis (DTA), thermo gravimetric analysis (TGA), X-ray diffraction (XRD), in-situ temperature controlled X-ray diffraction (TC-XRD) and secondary ion mass spectrometry (SIMS). We will be discussing how electrical conductivity experiments were performed on chosen samples and how their respective stabilities in different reductive atmospheres were studied.

2.2 Synthesis of powder samples:

Synthesis of LMO is a well studied process. Till date, different synthesis process like traditional solid state synthesis route, Pechini method, sol-gel process, precipitation method, microwave synthesis, chemical or physical vapour deposition methods; are available. It is well known that synthesis process employed can determine the grain size and microstructure of the final product; which in turn govern the properties of the materials. Few synthesis processes were able to derive final products at low temperature, but can take significant amount of time and man

power. Moreover it is already known that LMO if synthesized in smaller grain sizes, can drastically boost its electrical conductive properties.

We have employed traditional synthesis route for all of our LAMOX compounds, because of its simplicity and easiness. As of LMO: La_2O_3 is first dehydrated by calcining at 1000 ^oC for 3 hours. Then, stoichiometric quantities of commercial La_2O_3 (99.99 % pure, Chempur) and MoO_3 (99.99 % pure, Chempur) are mixed in agate jar and ground by hand. This mixture is than heated at 500 ^oC for 12 hours (@ 2^oC /min heating and cooling rates) to ensure homogeneity in the mixture. The product later goes for two other annealings at 900 ^oC for 12 hours each (@ 5^oC /min heating and cooling rates) followed by groundings in agate jar at the end of each heat treatment process. The final product is then confirmed by XRD before further experimentation.

W-LMO powders ($La_2Mo_{2-x}W_xO_9$, x = 0.5, 1, 1.1, 1.2, 1.3, 1.35, 1.4, 1.45, 1.5, 1.525, 1.550, 1.575, 1.60, 1.65, 1.7, 1.75, 1.8, 1.85, 1.9, 1.95, 2.0) were also synthesized by conventional solid state synthesis route. For convenience we will code W-substituted LMO compounds with their W-stoichiometry (Wx, where x is the stoichiometry of W, for example W1.3 is the sample where 65% of W substituted to Mo in LMO i.e. $La_2Mo_{0.7}W_{1.3}O_9$). Different W-LMO compounds were synthesized at different synthesis temperatures; final temperatures applied depend on the amount of W, substituted in the sample. We have realized that more the amount of W-substituted, high are the final annealing temperatures required. Stoichiometric quantities of La_2O_3 (preheated at 1000 ^oC for 3 hours for dehydration), MoO_3 and WO_3 (99.9% pure, Riedel-de Heen) are mixed in agate jar and ground well. The mixture is first annealed at 500 ^oC for 12 hours (@ 2 ^oC /min heating and cooling rate) for a homogenous distribution of the compounds in the mixture. Later on, multiple annealing stages are employed on each sample with variation in annealing temperature and time of annealing. Grinding of the product is carried for every stage and phase purity is also verified. The different annealing stages employed are mentioned in the fig. 2.1. Samples till $x \leq 1.575$ were annealed with final temperature 1150 ^oC, and remaining samples were annealed at 1250 ^oC.

As already discussed in chapter-1, phase purity of W-LMO compounds tend to vary with the amount of W substitution. For availability of pure phase, some compounds were quenched from high temperature into a mixture of ice and water (these details will be discussed in the next

chapter). For quenching experiments, the samples were annealed in closed Pt tubes (Pt is very inert towards LMO compounds and Pt can sustain thermal shock caused by quenching), where as for traditional solid state synthesis route Al_2O_3 crucibles (Al_2O_3 crucibles are stable at high temperature used for synthesis and completely inert towards LMO compounds) were utilized. However, the phase purity of all the samples at all the stages from 900 ^oC was examined by XRD. We can see the XRD patterns of LMO and W-LMO in the next chapter.

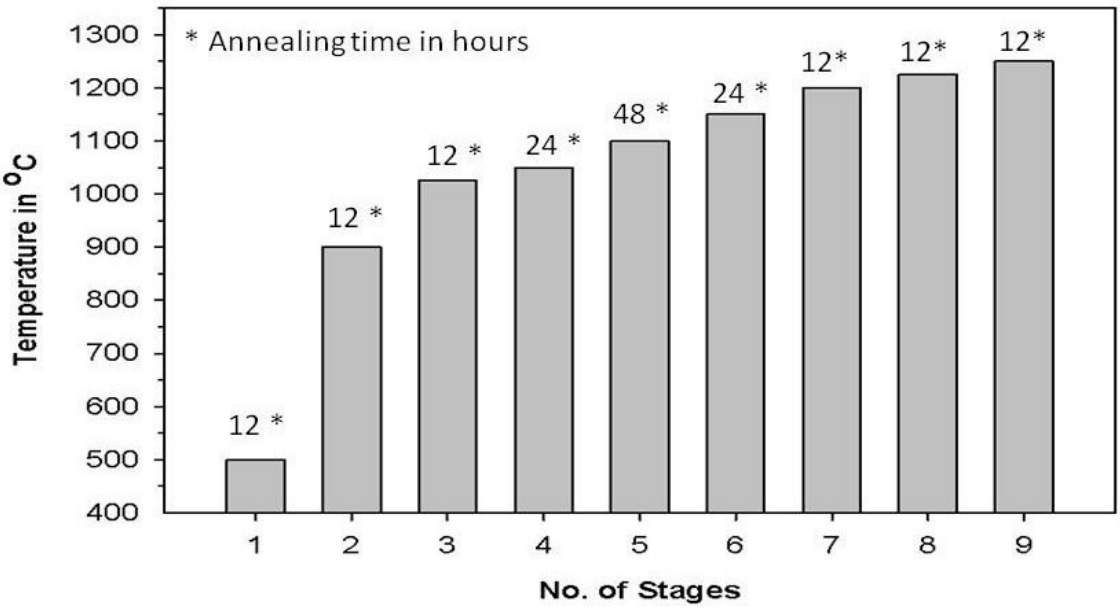

Figure 2.1: Bar Diagram showing different stages used in W-LMO synthesis along with the annealing temperature and annealing time per stage.

2.3 Synthesis of Pellets:

Most of the analysis techniques need the samples to be in defined geometry and as pellets. Conductive measurements, diffusion experiments which were the part of these studies, can be carried only on highly densified samples; where porosity is well controlled. The synthesis of the pellets is normally done in 4 stages: 1) Ball Milling, 2) Moulding and uni-axial pressing, 3) Iso-static pressing and 4) Sintering. Relative densities in pellets as high as ~97% can be achieved by this process.

Ball milling is a stage where, the powders synthesized by conventional way are milled down to fine grains with uniform grain size. This uniformity in grain size helps to increase relative density in green pellet and eases formation of coarse grains while sintering, leading final product to achieve higher relative density. In this stage, ~ 4 – 5 grams of LMO or W-LMO powders are taken in an agate jar adapted to "Ball Milling Fritsch®" (a planetary ball milling apparatus) equipment along with 5 ml of ethanol or acetone and 20 agate balls of diameter 6 mm. Then the powders are milled in the apparatus at speed no. 8 on the instrument (1532 rpm of agate jar and 766 rpm of the platform) for 15 minutes. The powders are crushed inside the jar (agate jar of 45ml volume) with the help of agate ball used, give uniform and fine grained final product. Thus obtained powder is collected from agate jar and heated at 100 ^{o}C for alcohol to evaporate. It was found in the literature LMO reacts with Zr; when Zr based milling jar is used, forming impurity $La_2Zr_2O_7$ [1]. Figure 2.2 shows the ball mill setup.

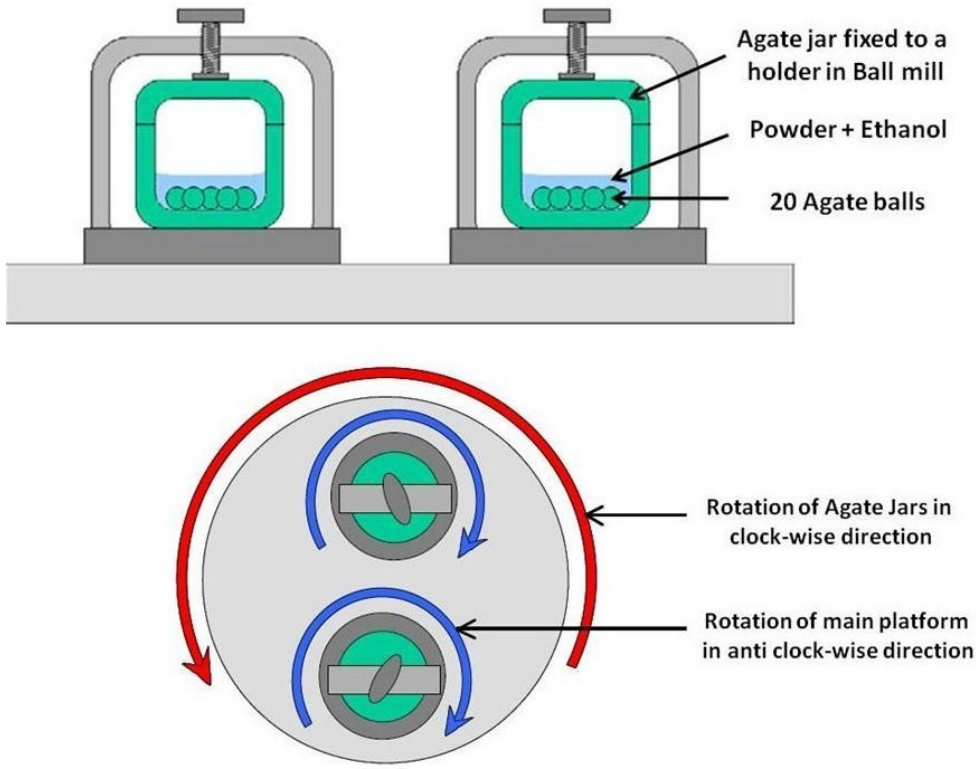

Figure 2.2: Cross section of Ball Mill showing its setup (top figure). Top view of ball mill showing the rotation sense of agate jar, when operating (bottom figure). [2]

Fine powders obtained from ball mill, are than moulded into desired shape (generally into pellets). In our study, we have moulded powders into pellets ranging in diameter from 5-13 mm. Inner walls of die and punches were coated with Vaseline to reduce friction when pressing. Required amount of sample (calculated in accordance to thickness and diameter of desired pellet) is taken into the die. If the sample cannot cohere well under pressure, a binder (commercially available polyvinyl alcohol) is used. On a rough approximation, a droplet of binder is used for every 300 mg of sample; however once the sample is annealed for sintering, binder evaporates. The sample along with die is pressed uniaxially at 4~5 MPa. The powder formed in to pellet than put sealed into a balloon and pressed (4~5 MPa) into water controlled iso-static press. Iso-static press is equipment, where one can apply equal and high pressure in all directions, making green pellet even denser.

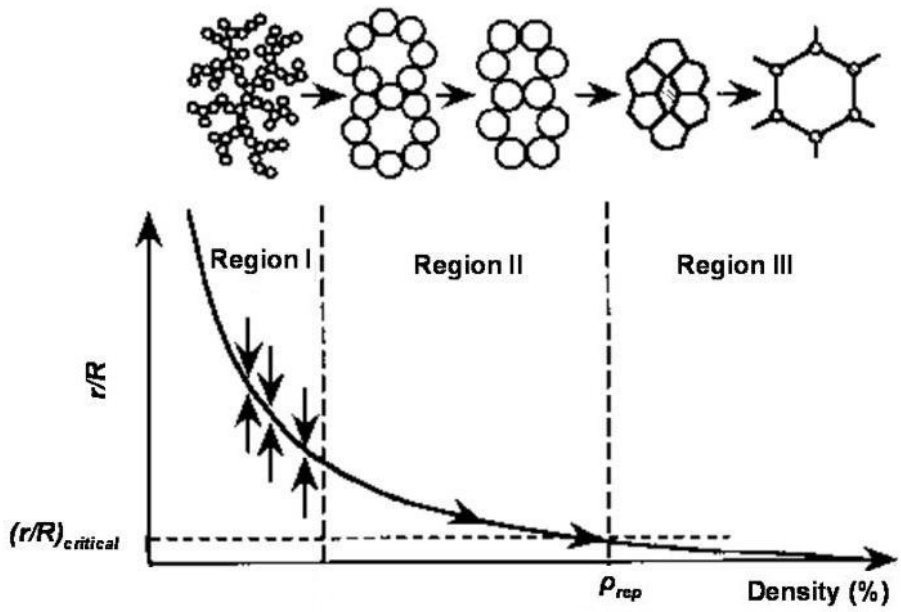

Figure 2.3: Schematic diagram for different sintering stages (adapted) [3, 4]), R- particle radius, r-pore radius, ρ_{rep} – the density of random close packing of spheres of an identical size, $(r/R)_{critical}$ is the boundary below which the pores in the sample become subcritical and shrink with grain boundary diffusion.

Thus obtained green pellet is than sintered to achieve pellet with higher relative density. Sintering is a vital step in ceramic processing which will define the ceramic's microstructure and its relative properties. The sintering process can be broadly divided into three stages, 1) where the particles will have little thermal expansion but do not lose their individuality, 2) Particles tend to shrink and adhere to each other leading to densification, 3) Grains will grow slightly, but the densification will halt with the display of flat shrinkage curve [5]. In Fig. 3.5, shown above region I is a area where density of the sample approaches to 40% through homogenization and stochastic particle relocation. In region II, the density is approaching to 63% by particle repacking and coarsening by surface diffusion. In the final region, the densification is controlled through grain boundary diffusion or lattice diffusion.[6-8].

Coming back to LMO, pellets are sintered at 1050 ^{o}C for 12 hours with heating and cooling rate 5 ^{o}C/min. The relative density thus obtained varies from 98~95 % depending on the diameter. For W-LMO samples, pellets with Wx ($x \leq 1.3$) are sintered; and sintering temperature applied was 1150 ^{o}C for 12 hours and standard heating and cooling rates of 5 ^{o}C/ min are applied. For diffusion studies (discussed in chapter 4), pellets of LSM were synthesized, where fine powders of LSM (99.9 % pure, Praxair, particle size dispersion d_{50} = 1.3 μm) were commercially available. In this case step of ball milling is skipped (since the powders are already of fine size), and remaining 3 steps were carried, with sintering temperature being 1400 ^{o}C (for 12 hours, with 5 ^{o}C/ min rate of heating and cooling).

2.4 X-Ray Diffraction (XRD) and insitu Temperature Controlled X-Ray Diffraction (TC-XRD):

X-ray diffraction (XRD) is a typical analysis method used to derive composition of a compound. This is a most convenient tool to check phase purity and to define possible impurities in a sample. When X-rays hit the sample (powder or a single crystal sample), monochromatic light of X-rays are diffracted back by crystal lattices. This involves the occurrence of interferences of the waves scattered at the successive planes, which are described by Bragg's law. If θ is the angle of incident beam that is made by lattice planes, d is the spacing between

crystal lattices, λ is the wavelength of incident beam (X-ray) and n is the integer, than Bragg's equation is stated as:

$$n\,\lambda = 2d\,sin\theta$$

Most commonly used types of X-ray diffraction are powder X-ray diffraction (XRD) and single crystal X-ray diffraction. A diffraction pattern is collected by exposing the sample to X-rays, which is then compared to a standard database (PCPDF, JCPDS e.t.c) to determine the unknown materials (if certain compound is already known and was analyzed by XRD and if its pattern is submitted to these standard data bases). Apart from that for regular laboratory usage, it is very helpful in determining purity of the samples (XRD pattern of desired compound is already known), crystal structure or possibility of crystal orientation e.t.c. Regular XRD analysis software include X-pert High Score, X-pert Data Viewer, EVA e.t.c. When combined with other techniques like Le Bail fitting [9] or Rietveld refinement [10], more information about the crystal structure can be obtained.

For this current study, we have used "Philips® X'pert MPD PRO" powder diffractometer, with dichromatic light Cu Kα1+2 at 40 kV/35 mA. Qualitative parameters like 2θ range, step size, time per step etc were varied as of the requirement.

For high temperature stability studies of W-LMO and reducibility studies on LMO, we have used in-situ temperature controlled X-ray diffractometer (TC-XRD). This instrument is equipped with a furnace, where one can study the crystal structure variations or phase stability of a given sample at high temperature. The sample can be placed in the atmospheres of Air or Ar or N_2 and can be heated anywhere from 25 ^{o}C to 1200 ^{o}C. This HT unit is very useful in characterizing phase stability or thermal behavior of the sample.

2.5: Thermal Analysis:

Thermal analysis can be defined as the measurement of physical and chemical properties of materials as a function of temperature. Some of these properties include enthalpy, heat capacity, mass and coefficient of thermal expansion. One of the main usage of these techniques is measurement of weight loss when oxides or hydrates, decompose while heating. Uses of

thermal analysis in solid state science are many and varied, which include study of solid state reactions, thermal decompositions and phase transitions and the determination of phase diagrams. Most of the solids are thermally active in one way or other, and can be studied by thermal analysis. There are four main types of thermal analysis: 1) Thermogravimetry, 2) Differential thermal analysis, 3) Differential scanning calorimetry and 4) Dilatometry. For our studies on LMO and W-LMO, for phase transition/stability studies, thermal behavior study, studies carried to examine stability of LAMOX compounds in reductive atmospheres, we have used TGA and DTA, details of which can be seen below. Data from DTA or TGA when coupled and analyzed with XRD data will reveal significant information.

2.5.1: Thermogravimetric Analysis (TGA):

TGA is a technique for measuring the change in weight of a material as a function of temperature or time. The results usually appear as a continuous chart record. The sample usually a few milligrams in weight, is heated at a constant rate (1 to 30 ^{o}C/min). It is usually to check the moisture content, presence of volatile components in samples, or to check amount of any released gases in the sample. In this instrument annealing can be done in different atmospheres like Ar or N_2 or air, or O_2 or diluted H_2.

In our case we use this instrument to check the stability of the LAMOX materials under different reductive conditions. LMO or W-LMO compound will be taken in Quartz crucible [unlike Pt (Pt does not reduce or oxidize in presence of H_2, but it is known that H_2 can enter in Pt cellmatrix), quartz is quite stable in reductive atmospheres and can withstand thermal shocks]. The compound is then placed in the flow of the gas to fill the respective chamber with the desired gas. (TGA instrument we use has a chamber capacity of 3 liters). Once the balance (weight of sample has to balanced by counter weights) is stabilized, and sample is heated, we can see the amount weight loss occurring in the samples as a function of time (in case of isothermal annealing), or temperature and time together. O_2 in LMO reacts with H_2 from the supplied gas forming H_2O and flows away from the unit. The loss of this O_2 can be attributed to the weight loss observed in the sample. So far, quantity of weight loss is the only tool to calculate the oxygen stoichiometry in LMO. On vice versa, when reduced LMO is heated in presence of air or

O_2, weight gain is observed, revealing amount of O_2 absorbed by the sample to oxidize to it stable state.

We have used two different equipments for our experiments. First one, commercially available "Setaram® TGA92". Different gas mixtures we used include Air Liquide® RH_4 (6%H_2 + 94% N_2); Air liquid® Arcal 15 – Noxal 3 (5% H_2 + 95% Ar). We have observed that, the reduction rate of the sample depends on the quantity of sample used, gas used, flow rate, temperature, time e.t.c. Particular parameters governing reduction reaction will be furnished along with the experiments (discussed in chapter 5).

Second TGA setup is a home built TGA instrument "symmetric Cahn 1000 electro-balance". This instrument has a sensitivity of 0.5 µg, with electrical and mechanical tares of 10 and 100 g respectively. Configuration used in this setup reduces undesired thermal segregation effects, which is of primary importance when working with mixture of different gases having different densities [11]. Total unit is maintained at controlled temperature of 25 ^{o}C. On this instrument, we have studied the stability behavior of LMO and W-LMO compounds under different partial oxygen pressures. Same as earlier, reducibility of LMO and its derivates tend to depend on parameters varied on instrument. Details like temperature, gas flow e.t.c will be provided along with the results.

Studies on stability of LMO and W-LMO compounds were carried in different pO_2 pressures. Electrochemical pump which helps in controlling desired pO_2 is used for this study. Electrochemical pump together with an electrochemical gauge allows the continuous measurement and regulation of pO_2 in a flowing gaseous atmosphere. pO_2 pressures ranging from 10^{-5} to 10^{-27} atm were employed using different gas mixtures (Ar-O_2; CO_2 – CO and H_2O-H_2). [12]

2.5.2: Differential Thermal Analysis (DTA):

DTA is a technique in which the temperature of a sample is compared with that of an inert reference material during a programmed change of temperature. The temperature of samples and reference should be the same until some thermal event, such melting, decomposition or change in crystal structure, occurs in the sample, in which case the sample temperature lags

behind (if the change is endothermic) or leads (in the case of exothermic) the reference temperature. One of the main uses of this instrument is "method of cooling curves" which is used to determine phase diagram. The sample temperature was recorded on cooling rather than on heating; since the heat effects associated with solidification and crystallization are usually large, they could be detected by this method.

Normally in a DTA, sample and reference are placed side by side in a heating block which is either cooled or heated at a constant rate. Identical thermocouples are placed in each and are connected back to back. When the sample and reference are at the same temperature, the net output of this pair will be zero, but when a thermal event occurs in the sample, a temperature difference "ΔT", exists between the sample and the reference which is detected by the net voltage of the thermocouples. A third thermocouple is used to monitor the temperature of heating unit and the results are presented as a function of ΔT against temperature. This is much sensitive and can give precise information in case of phase transitions. [13]

For this study, we used sample of ~100 mg against reference of similar weight of Al_2O_3. Commercially available "TA-SDI Q600" DTA instrument is used for the study. Our study is conducted over steady flow of 100 ml/min air. Rates of heating and cooling are the crucial parameters governing these experiments and will be discussed in details along with results.

2.6: Secondary Ion Mass Spectrometry (SIMS):

Secondary Ion Mass Spectrometry is a widely used mass spectrometric technique to study surfaces of the inorganic materials in 2D and 3D. It is the process where a high energy beam of ions are bombarded with the surface of the sample; portion of the energy from this collision cascade is redirected towards the surface, thus promoting the release (breaking) of molecules, atoms, photons, electrons and molecular fragments in to the vacuum system of the SIMS instrument, creating irreversible bombardment experience to the sample surface. This process of releasing surface material is termed as sputtering process. Thus, sputtered material (secondary ions) emerged from the sample is either positive or negative in charge. These secondary ions are then extracted to mass spectrometer, where ions are separated on the basis of their respective mass/charge ratio. Mass spectrometers used generally are Quadrupole analyzer, magnetic sector

analyzer or time of flight (TOF) analyzer. Each of the current analyzer designs collects about 50% of the emitted ions and can provide a mass analysis with an ultrahigh mass resolution. SIMS can determine trace levels of all elements in the periodic table. [14, 15]

Primary ions sources can be classified into two types: plasma sources and liquid metal sources. When gas atoms are ionized, plasma is formed and these ions are than collected into optical column, Several gas sources like O_2^+, Ar^+, N_2^+ and Xe^+ are used [16]. These ion beams are normally used for depth profiling applications. Whereas, for the applications where high lateral resolution is required, ion beams from liquid metal is used. These beams are normally very fine and have small beam widths. Beams such as Au_2^+, Au_3^+ and Bi_3^+ are used for these applications.[3]

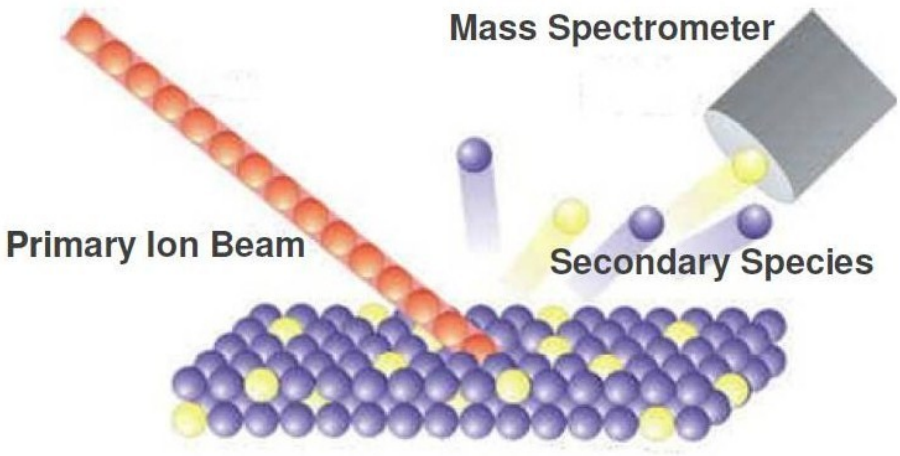

Figure 2.4: Schematic representation of SIMS operating principle. [3]

SIMS surface analysis is mainly classified into two modes of operation: static SIMS and dynamic SIMS. Static SIMS, is a process where low ion beam currents are applied, leading to low sputtering rates, i.e. low secondary ion yield. This is normally done when low sputtering rate is needed, for example, to study only top few atomic layers of a given material. This method is normally used to make surface image analysis and to collect mass spectrogram. This is normally done over a wide area to cover a large surface area of interest. Dynamic SIMS is a process where high energy ion beam is sputtered over the surface, to increase higher secondary ion yield and to sputter away material in large quantities. The primary ion beam is rastered over a typical area about 0.1~0.5 mm^2, eroding a certain depth per each scan and producing a flat-bottomed crater.

A profile of concentration as a function of depth is obtained by recording the variation in intensity of a restricted number species as a function of ion dose. SIMS analysis can be presented in three different ways: 1) Image analysis 2) Surface Mass spectrogram and 3) Depth profile. First two methods come under static SIMS, where as the last one under dynamic SIMS. Mass spectrum is plotted with concentration against amu.

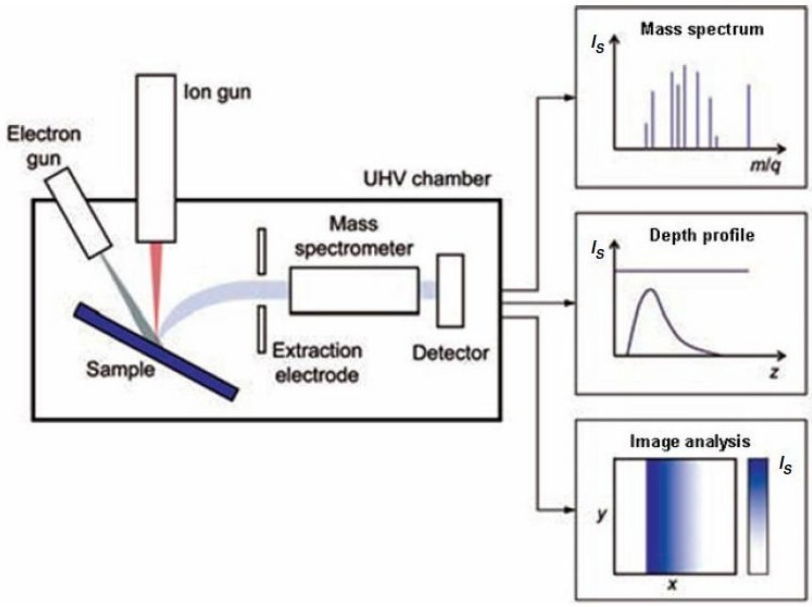

Figure 2.5: Schematic representation of three different modes of analysis possible by SIMS instrument.[17]

For the cationic diffusion studies mentioned in chapter 4, we have used this technique on LMO and $La_{0.8}Sr_{0.2}MnO_{3+\delta}$ samples to check the diffusion profiles (process and results are explained well in chapter 5). For these experiments, we have used focused ion beam – secondary ion mass spectrometry (FIB-SIMS) instrument. In this technique of FIB: an ion source is focused on an area of concentration, where sputtering is carried out generating secondary ions. In our case we used high brightness gallium liquid-metal ion source to generate the ion beam. As these ions are large, heavy and slow, it is easier to control the beam to remove material locally down to nanometer scale [18]. Like most of the SIMS instrument, with FIB SIMS, it is possible to mill the sample in the desired geometry (crater with top view as a square, rectangle or a circle e.t.c). When milling is being done, all the sputtered material from sample (secondary ions) are transferred to a mass spectrometry and analyzed. Surface imaging, mass spectrogram and depth

profiles were collected. The instrument used was a FEI FIB200-SIMS, with a Ga^+ ion beam with beam spot size around 10 nm.

In SIMS experiment, sample also plays a significant role. Sample has to be well polished and cleaned to have flat crater during profiling. If the sample has a insulating surface, during sputtering, there will be a surface charge build up. Sample charging can diffuse the primary beam and divert it from the analytical area and then reducing the secondary ion yield and affect their transmissions. The most common way to overcome this problem is to flood the surface with electron beam to compensate the surface charge. It is even possible to coat the surface of examining sample by gold (thin nanolayer (25~75 nm) of gold is sputtered). In our diffusion studies, we have sputtered gold on the surface of LMO and LSM pellets aswell.

For data processing of SIMS depth profile measurement, rate of sputtering has to be determined. This rate is calculated by time spent on sputtering and the depth of crater after sputtering. Crater depth can be calculated by the tilting the sample directly in the instrument and measuring the distance between the actual surface and bottom surface of the crater (see the procedure in Fig. 2.6). Sputtering depth is again verified by white light scanning interferometry. For this purpose, "ZYGO NewView 200" white-light microscope based interferometer is used which can have depth resolution of 2 nm, a lateral resolution of 0.2–20 µm.

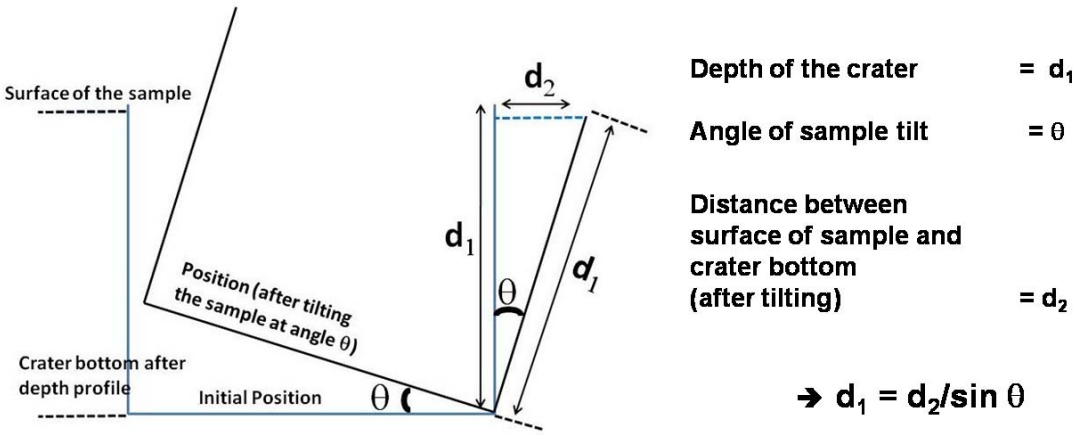

Figure 2.6: Schematic representation of crater depth measurement while performing SIMS depth profiling measurements.

2.7: Electrical Conductivity Studies:

Electrical conductivity measurements were carried on LMO, W0.5 and amorphous phased $La_2Mo_2O_{7-\delta}$ bars with approximate dimensions of 1 x 1 x 10mm. Resistivity measurements were carried by four wires method. Four Pt electrodes were first deposited on the bar by sputtering on one of the rectangular faces and Pt wire was glued on each electrode with Pt paste (see Fig. 2.7). The bar along with the Pt contacts was then annealed at 800 ^{o}C in static air for a hour to ensure maximum adherence of Pt paste. DC current variable (10 µA to 1mA) was applied between the external electrodes whilst the DC voltage between the internal electrodes was measured for the resistivity measurements.

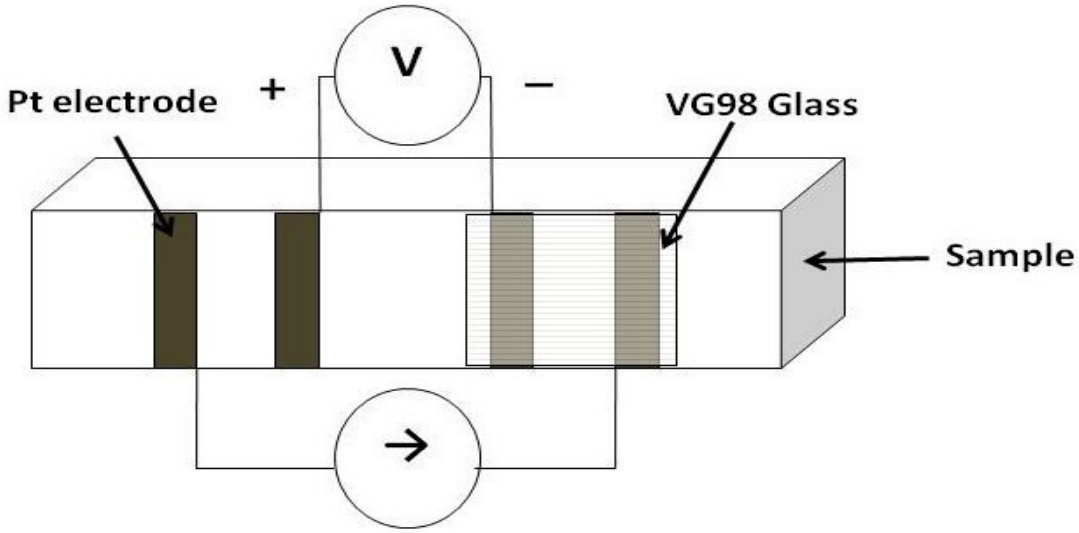

Figure 2.7: Schematic representation of 4 wire setup used for electronic conductivity measurements on LMO, W-LMO and amorphous phasedLa$_2$Mo$_2$O$_{7-\delta}$ bars.

As seen in earlier sections, LMO sample when reduced turns from pure ionic conductor to MIEC. Four point Hebb-Wagners polarization method was used to determine the electronic conductivity in reduced MIEC W-LMO and LMO materials. [19-22]. Powdered VG98 was suspended in a solution of polyvinyl-butyral and isoproponal; thus obtained viscous solution was used to paint over the two Pt electrodes on the bar. Two of the four electrodes were covered by VG98 glass to avoid oxygen exchange with the atmosphere and therefore block ionic

conductivity (ion-blocking). This setup was again fired for 15 minutes at 800 ^{o}C to decompose organic material and to ensure proper deposition of glass on the Pt electrodes.

The total setup is then put in a tubular furnace under reductive atmosphere (diluted H_2, UHV (ultra high vacuum) or low pO_2 pressures). Samples with different relative densities (98 – 75% relative dense) were used. Activation energy of sample is determined under given experimental conditions (discussed along with results in Chapter 5).

The resistivity obtained at ideal conditions was set as a reference for further experimentation. The behavior of the conductivity σ(T) as a function of temperature T was fitted with a thermally activated model:

$$\sigma(T) = \frac{\sigma_0}{T} e^{-\frac{Ea}{K_B T}}$$

Whereas σ_o is a pre-exponential factor, K_B is the Boltzmann constant and Ea is the activation energy. Activation energy was calculated and provided in accordance with the experimental parameters and setups.

Note: Experimental details, methods and materials used for regular laboratory experimentation were mentioned here. However experimental parameters cannot be standardized since they have to be varied in accordance with the requirement, which will be discussed along with their results further in this thesis report in their relative chapters.

2.8: References:

1. S. Georges; F. Goutenoire; P. Lacorre; M. C. Steil, *Journal of the European Ceramic Society* **2005,** 25, (16), 3619-3627.
2. J. Jacquens. Stabilite, reactivite et Performances de conducteurs par ions oxyde de la famille LAMOX comme elements de coeur de pile a combustible SOFC mono-chamber. Universite du Maine, Le Mans, 2010.
3. J. Liu. Mass Transport and Electrochemical Properties of La2Mo2O9 as a Fast Ionic COnductor. Imperial College London, London, 2011.
4. P. L. Chen; I. W. Chen, *Journal of the American Ceramic Society* **1997,** 80, (3), 637-645.
5. M. N. Rahman, *Ceramic Processing and Sintering. 2nd ed.* . M. Dekker: New York, 2003.
6. Z. Munir; U. Anselmi-Tamburini; M. Ohyanagi, *Journal of Materials Science* **2006,** 41, (3), 763-777.
7. I. W. Chen; X. H. Wang, *Nature* **2000,** 404, (6774), 168-171.
8. P. L. Chen; I. W. Chen, *Journal of the American Ceramic Society* **1996,** 79, (12), 3129-3141.
9. A. Le Bail; H. Duroy; J. L. Fourquet, *Materials Research Bulletin* **1988,** 23, (3), 447-452.
10. H. Rietveld, *Journal of Applied Crystallography* **1969,** 2, (2), 65-71.
11. A. Caneiro; M. Bonnat; J. Fouletier, *Journal of Applied Electrochemistry* **1981,** 11, (1), 83-90.
12. A. Caneiro; P. Bavdaz; J. Fouletier; J. P. Abriata, *Review Scientific Instruments* **1983,** 53, (7).
13. A. R. West, *Basic Solid State Chemistry*. John Wiely & Sons, Ltd. : Chichester, England:, 1999.
14. M. Setou, *Imaging Mass Spectrometry: Protocols for Mass Spectrometry*. Springer: 2010.
15. J. H. Gross, *Mass Spectrometry*. Springer: 2011; Vol. 2.
16. J. C. Vickerman; A. Brown; N. M. Reed, *Secondary Ion Mass Spectrometry: Principles and Applications*. Oxford: Clarendon Press: 1989.
17. R. A. D. Souza; M. Martin, *Bunsen-Magazin* **2006,** 8, 11.
18. D. Brandon; W. D. Kaplan, *Microstructural Characterization of Materials 2nd ed.* . John Wiely & Sons, Ltd. : Chichester, England:, 2008.
19. I. Riess, *Solid State Ionics* **1992,** 51, (3-4), 219-229.
20. M. H. Hebb, *The Journal of Chemical Physics* **1952,** 20, (1), 185-190.
21. I. Riess; D. S. Tannhauser, *Solid State Ionics* **1982,** 7, (4), 307-315.
22. L. J. V. d. PAUW, *Philips Research Reports* **1958,** 13, (1), 9.

Chapter 3: Thermal stability of W-substituted $La_2Mo_2O_9$

3.1Introduction 67

3.2 $La_2Mo_{2-y}W_yO_9$ with y = 1, 1.1, 1.2 68

3.3 $La_2Mo_{2-y}W_yO_9$ with y = 1.3-1.575 70

3.3.1 $La_2Mo_{0.7}W_{1.3}O_9$ (W 1.3) and $La_2Mo_{0.65}W_{1.35}O_9$ (W 1.35) 70

3.3.2 $La_2Mo_{2-y}W_yO_9$ with y = 1.4 - 1.575 75

3.4 $La_2Mo_{2-y}W_yO_9$ with y = 1.6-1.8 82

3.4.1 $La_2Mo_{0.4}W_{1.6}O_9$ (W1.6) 83

3.4.2 $La_2Mo_{2-y}W_yO_9$ with y = 1.65-1.8 87

3.5 $La_2Mo_{2-y}W_yO_9$ with y = 1.85 - 2.0 91

3.6 Phase Diagram of $La_2W_yMo_{2-y}O_9$ ($1.0 \leq y \leq 2.0$) 94

3.7 X-Ray Powder Diffraction Analyses 97

3.7.1 Raw powders 97

3.7.2 Powders post-annealed above 700°C 103

3.8 Conclusions 113

3.9 References 115

Chapter 3:

Thermal stability of W-substituted $La_2Mo_2O_9$

3.1Introduction

From the literature it seems clear that W substitution to Mo in $La_2Mo_2O_9$ (LMO) suppresses undesired phase transition from monoclinic α-phase to cubic β-phase while limiting its instability under reducive atmospheres [1-13]. The solubility of W in LMO is around 80% and W substitution in LMO also shows improvement in its thermal expansion behavior. LMO is monoclinic in symmetry (represented as α-LMO) and W substitution stabilizes the highly conducting β–form (cubic structure) represented as β-LMO. However compound with 100 mol% W substitute to Mo in LMO has a different structure at room temperature (R.T). At R.T $La_2W_2O_9$ is triclinic (α –LWO) in symmetry, which changes to β-LWO cubic form at temperature around 1077 ^{o}C. Both β –L**W**O and β –L**M**O have cubic symmetry. Fig 3.1 shows the XRD patterns of all the three α-LMO, β-LMO and α-LWO phases. W substituted LMO have undergone significant amount of research, however some of the properties of these compounds and their stability and metastable behavior are still not clear [1-13].

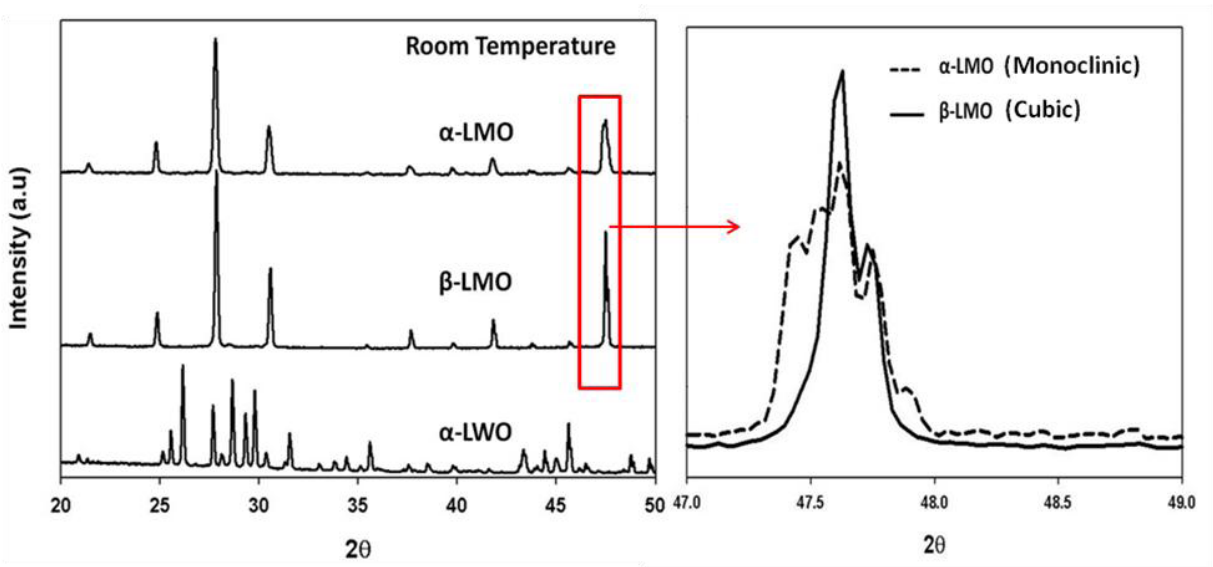

Figure 3.1: XRD patterns of α-$La_2Mo_2O_9$ (α-LMO), β –La_2WMoO_9 (β –LMO) and α-$La_2W_2O_9$ (α-LWO) phases (left). Enlargement of the 2 θ region showing splitting of the cubic (231) peak characteristics of the monoclinic α-LMO form (right).

In this part of work, we have synthesized various LMO compounds with W substitution (W-LMO) ranging from 50 mol% to 100 mol% ($La_2Mo_{2-y}W_yO_9$, y = 1, 1.1, 1.2, 1.3, 1.35, 1.4, 1.45, 1.5, 1.525, 1.550, 1.575, 1.60, 1.65, 1.7, 1.75, 1.8, 1.85, 1.9, 1.95, 2.0). In order to simplify the composition terminology, we will use the following nomenclature: a W-LMO compound with formula $La_2Mo_{2-y}W_yO_9$ will be named Wy. Compound with W 50 mol% i.e. La_2MoWO_9; (y = 1.0) will be called W1.0; and compound with y =1.1 is called as W1.1.

3.2 $La_2Mo_{2-y}W_yO_9$ with y = 1, 1.1, 1.2

The three compounds were synthesized by conventional solid state synthesis route (SSS) with final synthesis temperature being 1150 ^oC and were cooled to R.T at 5 ^oC/min (synthesis procedure along with various annealing temperatures and time are mentioned in section 2.2, of chapter 2). In agreement with the literature, complete stabilization of the β-form was observed. No phase transitions were detected by DTA performed on these samples (with ~100 mg of sample under air flow of 100 ml/min, with rate of heating 5 ^oC/min and rate of cooling 2 ^oC/min) (see Fig. 3.2). On the DTA curves slight perturbation was noticed around ~ 900 ^oC, which was confirmed as artifact (DTA was performed on empty crucibles and similar events were observed, results of this experiment are discussed in Annex-I).

In Ca and Eu substituted $La_2Mo_2O_9$[14, 15], depending upon the Ca/Eu substitution amount it was understood that some compounds were metastable and these compounds have to be heat treated to obtain respective thermodynamic stable products. In Ca and Eu substituted LMO compounds, the ordering and disordering of the structure at high temperature is caused by oxide ion migration. Since in W-LMO cationic migration is expected in the structure to achieve a thermodynamic stable state, W substituted compounds may have to be heat treated for longer periods of time. Accordingly, in this study to obtain thermodynamically stable compounds, all three samples were annealed at 700 ^oC for 60 days in a tubular furnace in static air. XRD patterns collected on these heat treated samples show no change in the structure type (see Fig. 3.3). However little variation in the peak shape and intensity were noticed. Le Bail fitting was performed on the XRD patterns of heat treated samples and slight decrease in cell volume was observed.

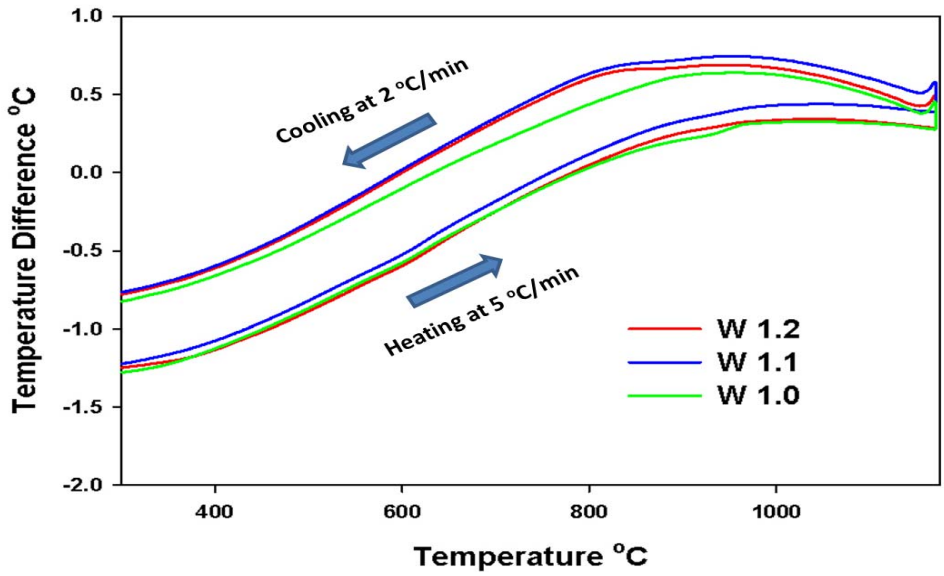

Figure 3.2: DTA curves of samples with y = 1.0, 1.1 and 1.2, showing no phase transformations.

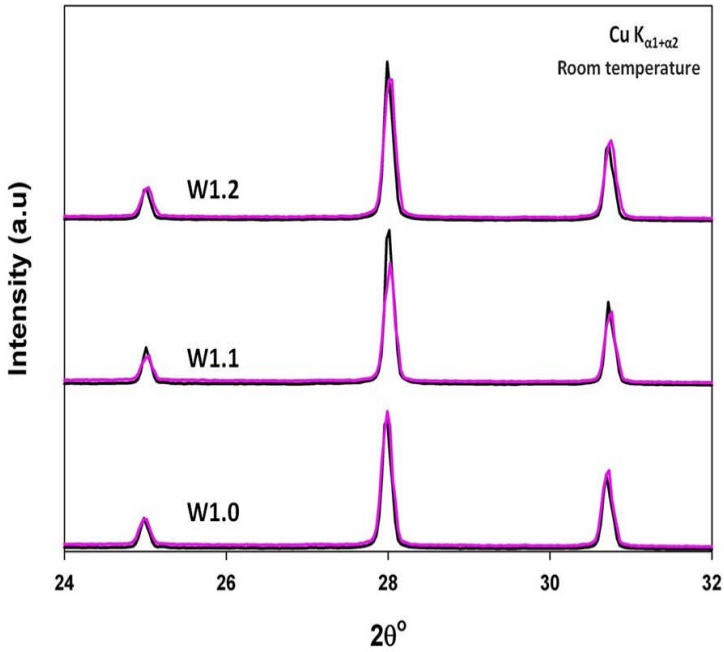

Sample		Cubic cell parameter '*a*'
W1.0	Before Annealing	7.1527(1)
	After Annealing	7.1503(1)
W1.1	Before Annealing	7.1502(1)
	After Annealing	7.1477(2)
W1.2	Before Annealing	7.1474(1)
	After Annealing	7.1452(2)

Figure 3.3: XRD patterns of $La_2Mo_{2-y}W_yO_9$ *samples with y = 1.0, 1.1 and 1.2 (left), before (in black color) and after annealing at 700 °C for 60 days (in pink color). Table (right) showing the variation in the cubic unit cell parameter of β-LMO phase compounds before and after heat treatments.*

3.3 $La_2Mo_{2-y}W_yO_9$ with y = 1.3-1.575

3.3.1 $La_2Mo_{0.7}W_{1.3}O_9$ (W 1.3) and $La_2Mo_{0.65}W_{1.35}O_9$ (W 1.35)

Within the synthesis conditions, the samples W1.3 and W1.35 behave the same way as samples W1.0-1.2 and stabilization of the β-form is noticed (see Fig. 3.4) TC-XRD patterns were collected on both samples. On W1.3 two different TC-XRD setups were used where data was collected from room temperature to 900 ^oC on 1st setup and from 900 ^oC to 1100 ^oC on another setup. On W1.35 TC-XRD was collected from 600 ^oC to 900 ^oC (see Chapter 2 for description of TC-XRD process and setups). TC-XRD patterns collected on W1.3 and W1.35 do not show any phase transitions even at elevated temperatures, suggesting that β-form might be a stable state (see Fig. 3.5). DTA analysis was performed on W1.3 by heating the powder from room temperature till 1175 ^oC at 10 ^oC/min and cooling back to room temperature at 10 ^oC/min cooling rate. Once again, neither endothermic nor exothermic events were noticed (except a perturbation around ~980 ^oC) and this observation is in agreement with TC-XRD analysis (see Fig. 3.5). The perturbation was confirmed by TC-XRD to be an instrumental anomaly (Fig 3.5b).

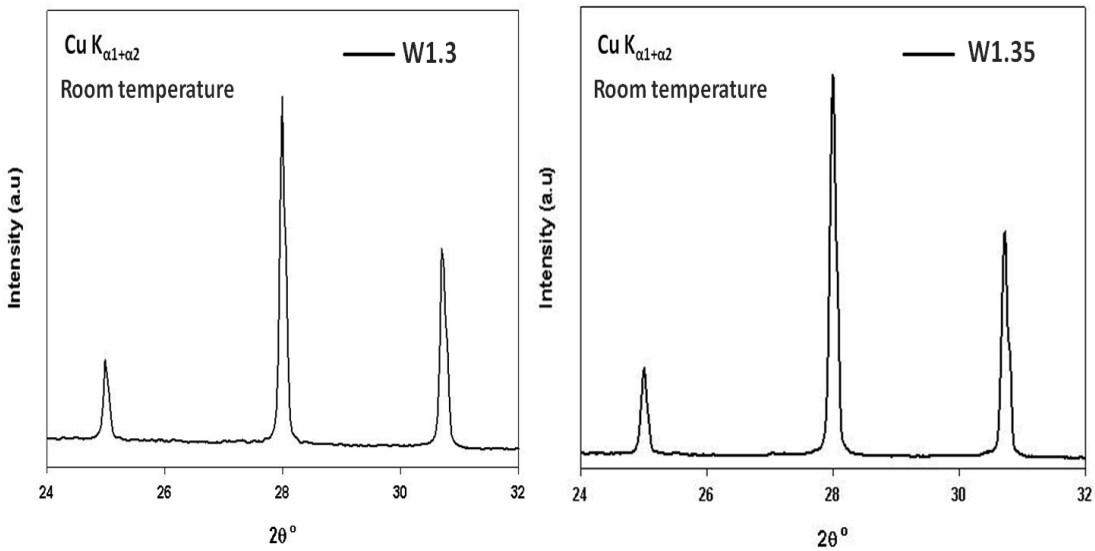

Figure 3.4: XRD patterns of W1.3 (left) and W1.35 (right) raw powders (synthesized at 1150 ^oC with a cooling rate 5 ^oC/min) showing the cubic β-LMO phase.

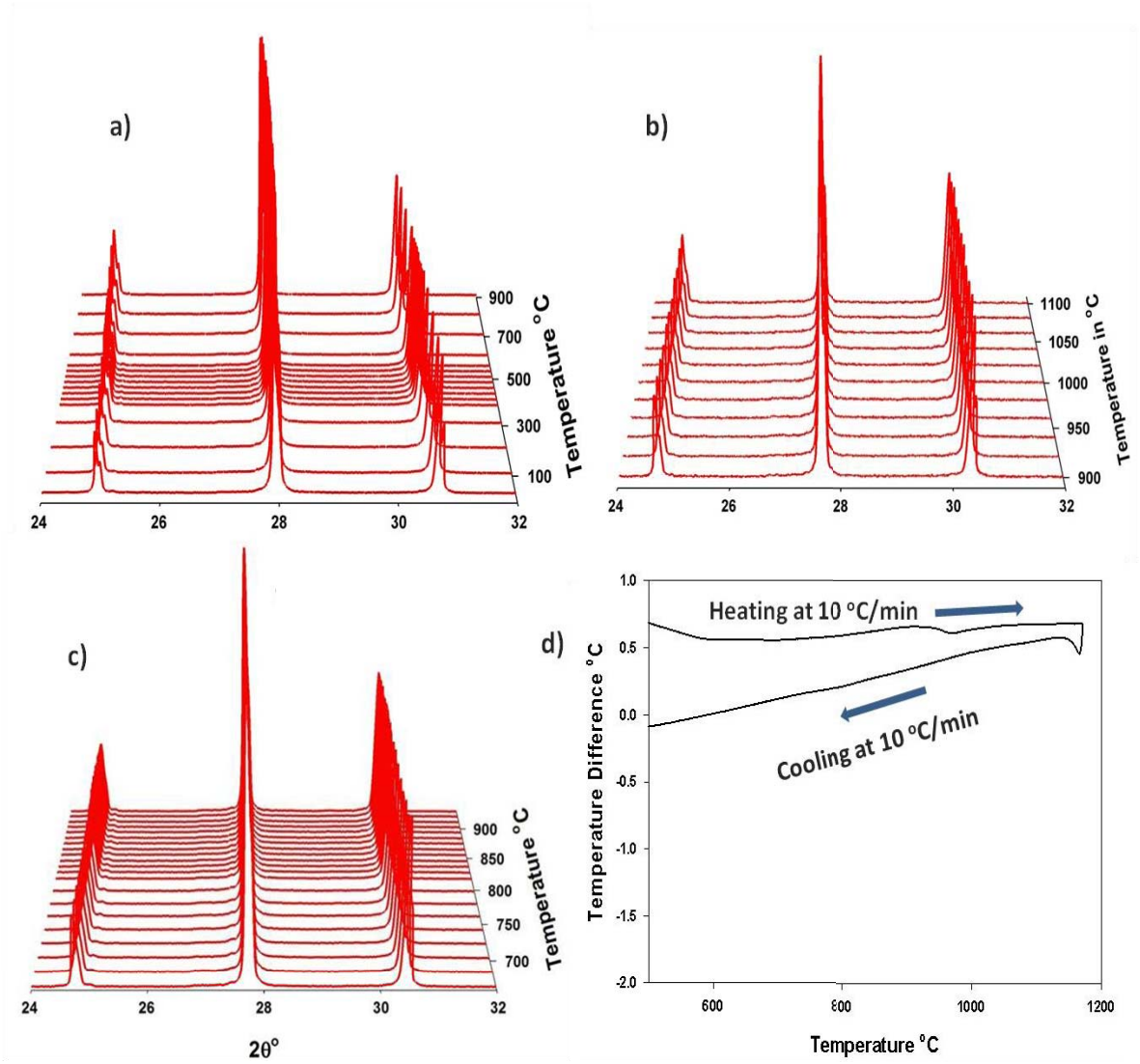

Figure 3.5: TC-XRD patterns collected on W1.3 (R.T to 900 °C in fig 'a', and 900 °C to 1100 °C in fig. 'b') and W1.35 (600 – 950 °C) in Fig. 'c'. DTA curve of W1.3 is shown in Fig. 'd'.

On TC-XRD patterns of W1.3 sample, Le Bail fits were carried out in the cubic cell and space group $P2_13$ with the FullProf program. The thermal evolution of the unit cell volume is plotted in Fig. 3.6. As observed for the cubic members of the LAMOX family, two thermal domains with linear dependences of volume are observed, corresponding to an increase (upon heating) of the thermal expansion coefficient (TEC) [14, 16]. The TEC was calculated from the linear regressions of the two thermal domains as 15.6 x 10^{-6} $^{o}C^{-1}$ and 22.3 x 10^{-6} $^{o}C^{-1}$ in the

temperature range 25 - 350 °C and 350 - 900 °C, respectively. These TEC values of W1.3 are comparable to the TEC values of W1.4 (13.9 x 10^{-6} °C^{-1} and 21.0 x 10^{-6} °C^{-1} in the temperature range R.T to 500 °C and 550 °C - 800 °C respectively)[17] and TEC values of W1.5 (15.4 x 10^{-6} °C^{-1} and 21.1 x 10^{-6} °C^{-1} in the temperature range R.T - 350 °C and 350 °C - 900 °C respectively)[9].

Temperature (°C)	a = b = c (Å)	Volume (Å³)
25	7.1444(1)	364.68(1)
100	7.1510(1)	365.69(1)
200	7.1616(1)	367.30(1)
300	7.1737(1)	369.18(1)
350	7.1805(1)	370.22(1)
375	7.1842(1)	370.79(1)
400	7.1878(1)	371.36(1)
425	7.1912(1)	371.89(1)
450	7.1947(1)	372.42(1)
475	7.1981(1)	372.95(1)
500	7.2018(1)	373.53(1)
525	7.2055(1)	374.10(1)
550	7.2100(1)	374.80(1)
600	7.2145(1)	375.52(1)
700	7.2337(1)	378.51(1)
800	7.2502(1)	381.11(1)
900	7.2649(1)	383.43(1)

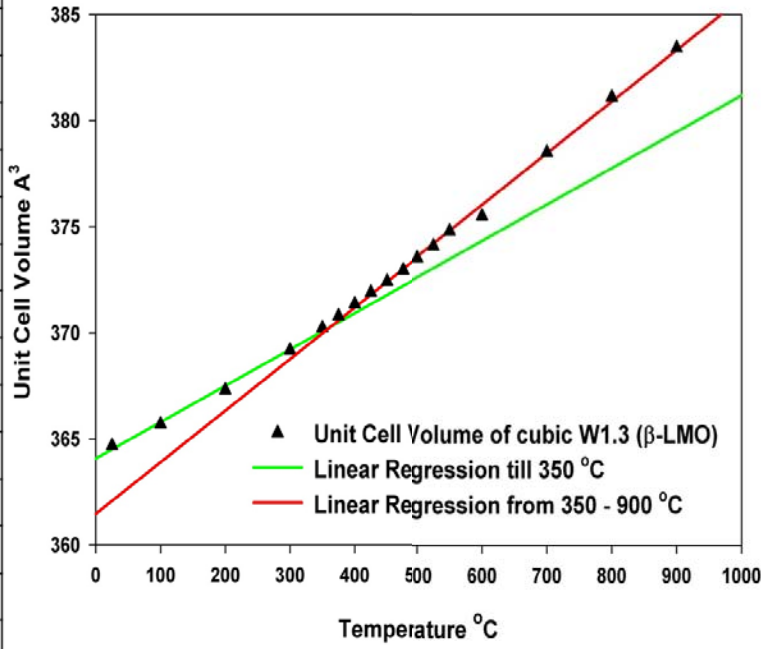

Figure 3.6: Temperature dependence of the cubic cell parameters of W1.3 determined by Le Bail fitting of TC-XRD (left). TEC (calculated from linear regression) are 15.6 x 10^{-6} °C^{-1} and 22.3 x 10^{-6} °C^{-1} in the temperature range 25 - 350 °C and 350 - 900 °C respectively (right). Note that error scale is within the thickness of the symbols (triangles).

To probe the long term stability of the compound, raw W1.3 powder was annealed at intermediate temperatures for different periods of time (at 700 °C and 750 °C for 45 days and 800 °C for 96 hours). Fresh batch of raw powder was used for each heat treatment and the same cooling rate of 5 °C/min used for synthesis was applied. All annealing were performed in a

tubular furnace and in static air. While raw W1.3 sample is cubic, heat treated sample turned into a mixture of β-LMO and α-LWO type phases (whatever the annealing temperature 700, 750 or 800 °C) (see Fig. 3.7). Similar heat treatment was performed on W1.35 (annealing at 800 °C for 96 hours), and the W1.35 also behaves the same as W1.3 (see Fig. 3.8). These measurements show that thermodynamic stable state of W1.3 and W1.35 compounds is bi-phasic in nature.

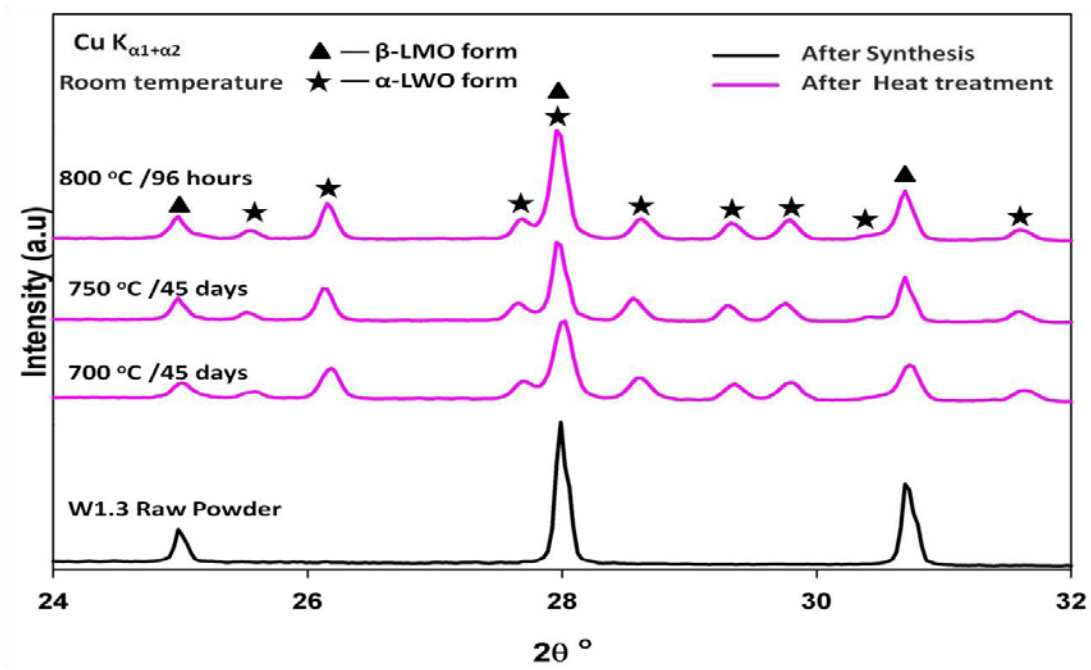

Figure 3.7: XRD patterns of W1.3 before (Black) and after long term heat treatment (Pink).

On W1.3 powder sample which was annealed for 96 hours at 800 °C, DTA and TC-XRD were performed (see Fig. 3.9). The sample was a mixture of β-LMO and α-LWO type phases before the DTA experiment, while a pure β-LMO type phase was noticed after the experiment. During TC-XRD upon heating, XRD patterns show that the W1.3 sample remains bi-phasic till 950 °C and after this temperature, the sample undergoes a phase transition to a single β-LMO phase. This phase is retained when the sample is cooled back to R.T at an average of 400 °C/min in the TC-XRD unit. An annealing for 96 h at 800 °C was necessary to re-obtain the mixture of β-LMO and α-LWO type phases. TC-XRD analysis was carried on the W1.3 sample (mixed phase sample) at room temperature and at 700 °C. Details will be discussed in section 3.7 of this chapter for convenience.

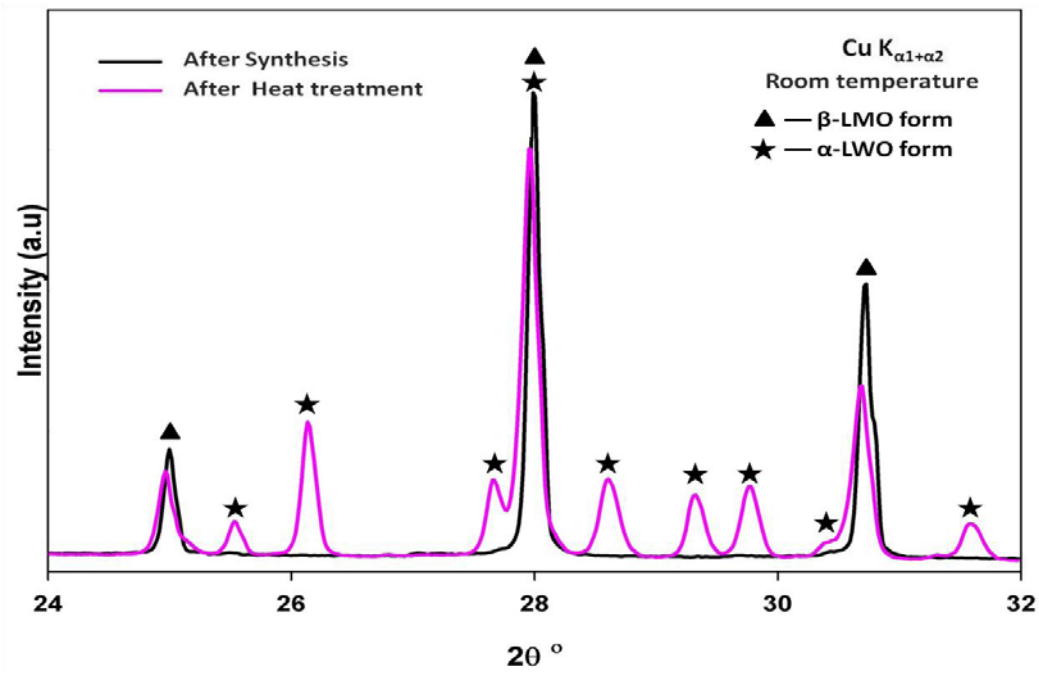

Figure 3.8: XRD patterns of W1.35 before (Black color) and after long term heat treatment (Pink color).

This unique thermal behavior of the W1.3 sample was never reported before. We have already shown that samples y = 1.0, 1.1 and 1.2 were stable after long annealing. The single β-LMO phase is preserved in these three samples after annealing (even for longer annealing duration ~60 days). Considering the results obtained from long annealing/heat treatment measurements carried on samples from y = 1.0 to 1.3; one can assume that thermal instability occurs for compositions having W content higher than 60 mol %. It is now possible to suggest that samples with W substitution higher than 60 mol % are not recommended for SOFC applications, since low conducting triclinic α-LWO phase appears when annealed at SOFC operating temperatures for periods longer than 4 days. More information about the structural analysis is given in section 3.7 of this chapter.

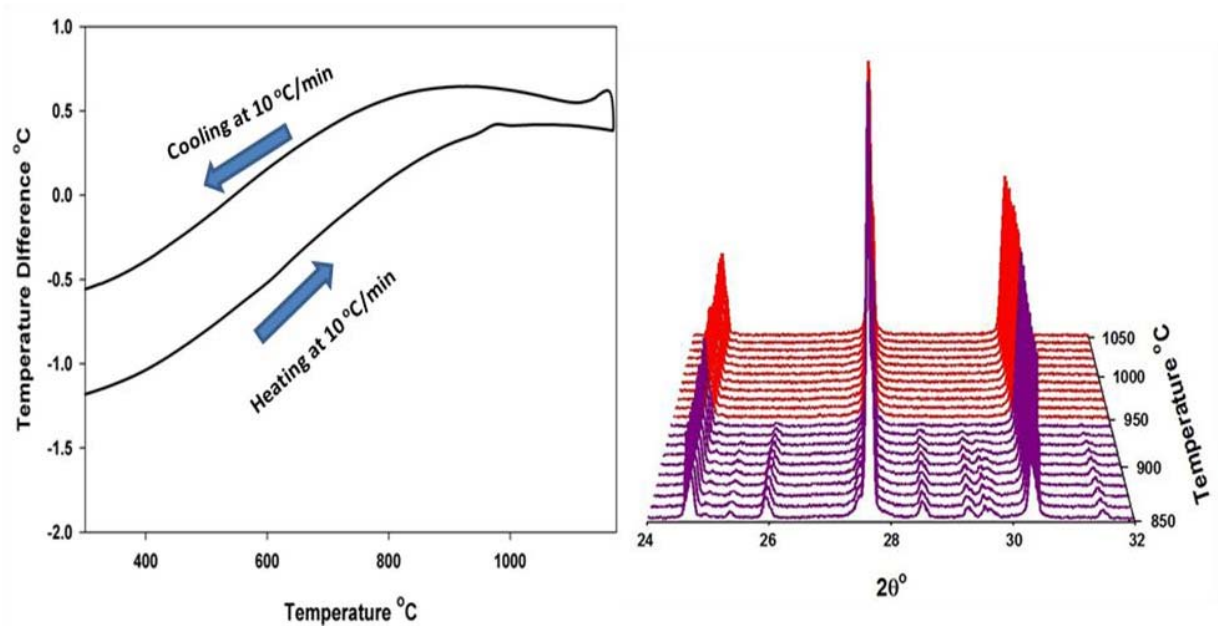

Figure 3.9: DTA curve of W1.3 sample which was annealed for 96 hours at 800 °C (~100 mg of sample under air flow of 100ml/min) (left). TC-XRD patterns on similar W1.3 sample from 850 to 1050 °C, patterns in violet showing the sample in a mixture of β-LMO and α-LWO phases and patterns in red showing the β –LMO phase. Please note the phase transition at 950 °C.

3.3.2 $La_2Mo_{2-y}W_yO_9$ with y = 1.4 - 1.575

Single β-LMO type phase compositions ranging from W1.4 to W1.575 were obtained when synthesized at 1150 °C by cooling down to R.T at 5 °C/min. In order to study the thermal stability of these raw powders, two successive DTA measurements were performed on raw W1.4 and W1.5 powders (see Fig. 3.10). As observed for lightly W-substituted LMO compounds, DTA diagrams of W1.4 and W1.5 did not show any endothermic /exothermic events. XRD patterns of W1.4 and W1.5 show pure β-LMO type phase after DTA (see Fig. 3.11).

These compounds (y = 1.4, 1.5, 1.525, 1.550, 1.575) were studied by TC-XRD. All the samples exhibit multiple phase transitions upon heating (Fig. 3.12). When heated above 730 °C, a partial conversion of the β-LMO phase into α-LWO phase starts, which turns back to pure β-LMO phase around 940 – 990 °C (depending on the composition) (see Table 3.1). It is surprising to observe this metastability in the TC-XRD measurements, since DTA did not exhibit

any such events. All the samples mentioned above were obtained in pure β-LMO phase when cooled down to room temperature at 400 ^{o}C/min. It must be noted that release of metastability was not observed in-situ by TC-XRD for W1.3 and W1.35 and starts from W1.4.

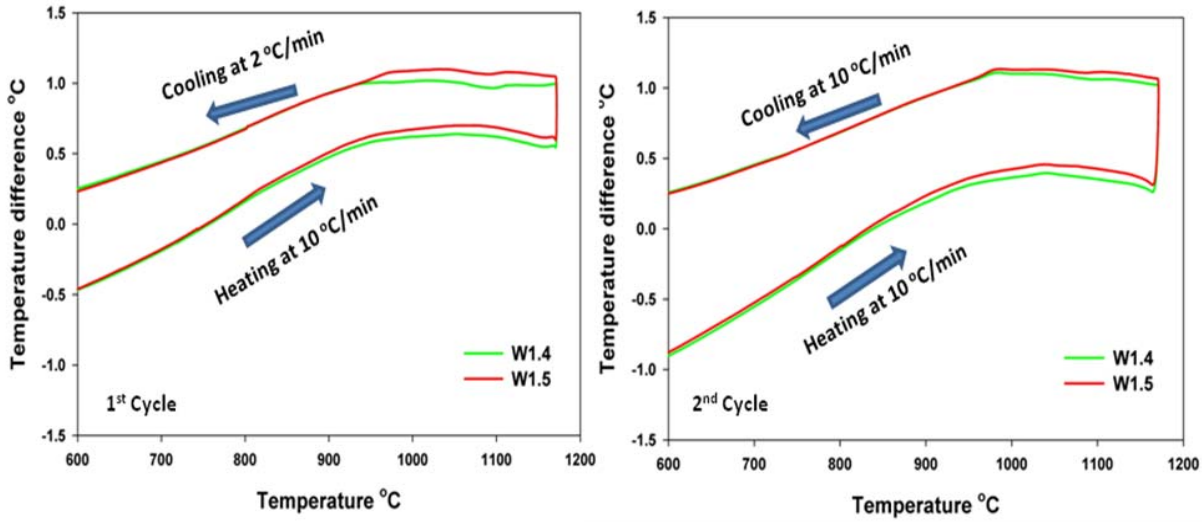

Figure 3.10: DTA curves of W1.4 and W1.5 samples (synthesized at 1150 ^{o}C with a cooling rate of 5 ^{o}C/min) (DTA conditions: ~100 mg of sample in air flow of 100 ml/min).

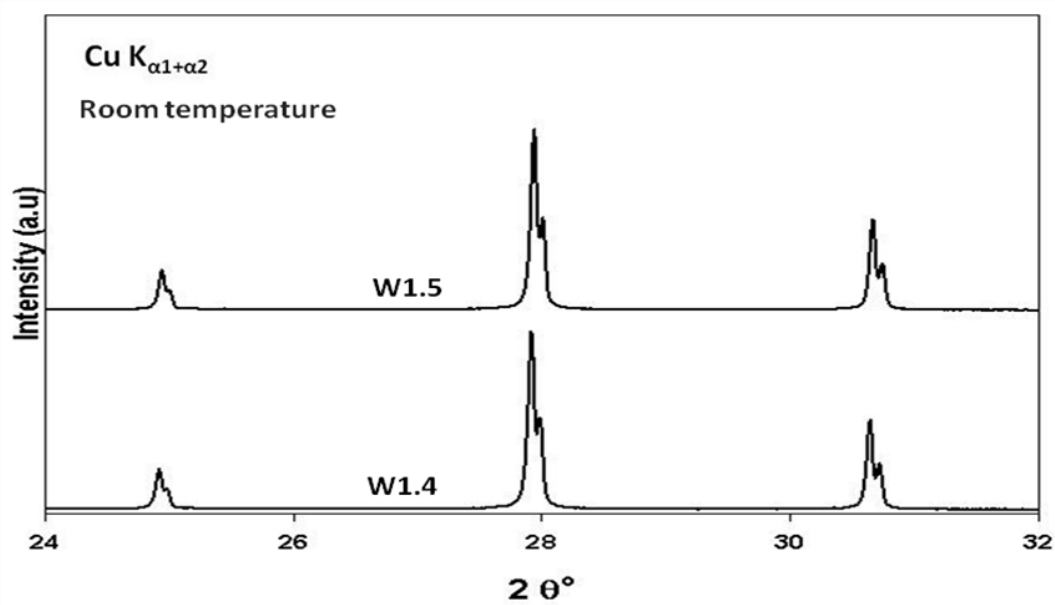

Figure 3.11: XRD patterns of W1.4 and W1.5 samples (synthesized at 1150 ^{o}C with a cooling rate of 5 ^{o}C/min) after DTA showing β-LMO type phase.

W - Composition (y) in $La_2W_yMo_{2-y}O_9$	Phase transition temperature to α–LWO + β-LMO phases (°C)	Phase transition temperature back to β-LMO (°C)
1.3	No Phase Transition	No Phase Transition
1.35	No Phase Transition	No Phase Transition
1.4	757	940
1.45	776	955
1.5	740	965
1.525	740	970
1.550	740	980
1.575	730	990

Table 3.1: Table showing the phase transition occurring in W-LMO samples with y = 1.3 to 1.575. All these phase transitions were determined by TC-XRD analysis. Note that all compounds were in β-LMO (cubic) phase before and after TC-XRD analysis.

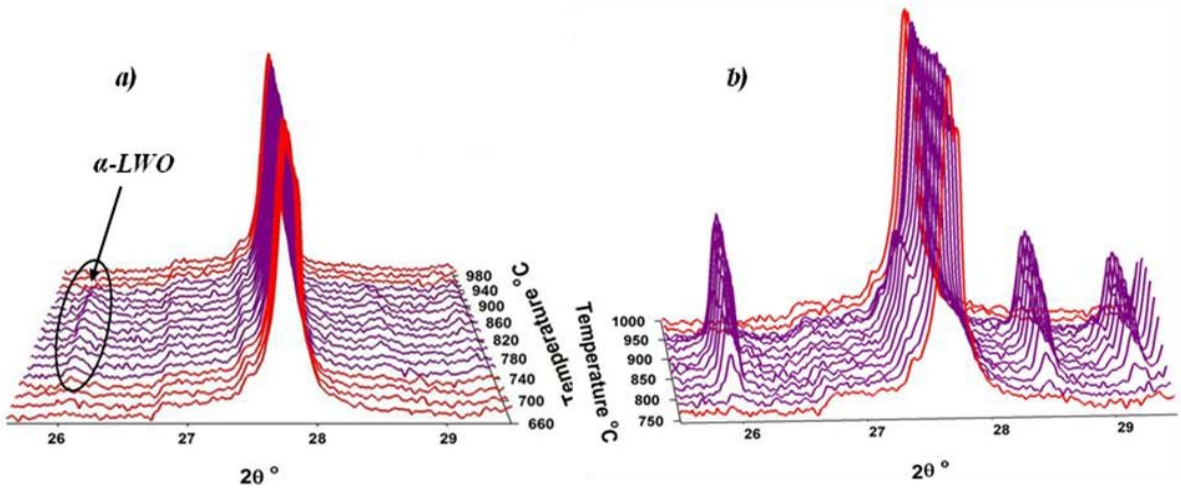

Figure 3.12.a & b: TC-XRD pattern collected on W1.4 (left) and W1.45 (right). Phase transitions from β-LMO (red) to a mixture of β-LMO + α-LWO (violet color) can be seen. W1.4 is the origin of this metastable behavior and the concentration of α-LWO is less; limited 2θ range is shown for clarity. Peaks matching α-LWO phases are highlighted.

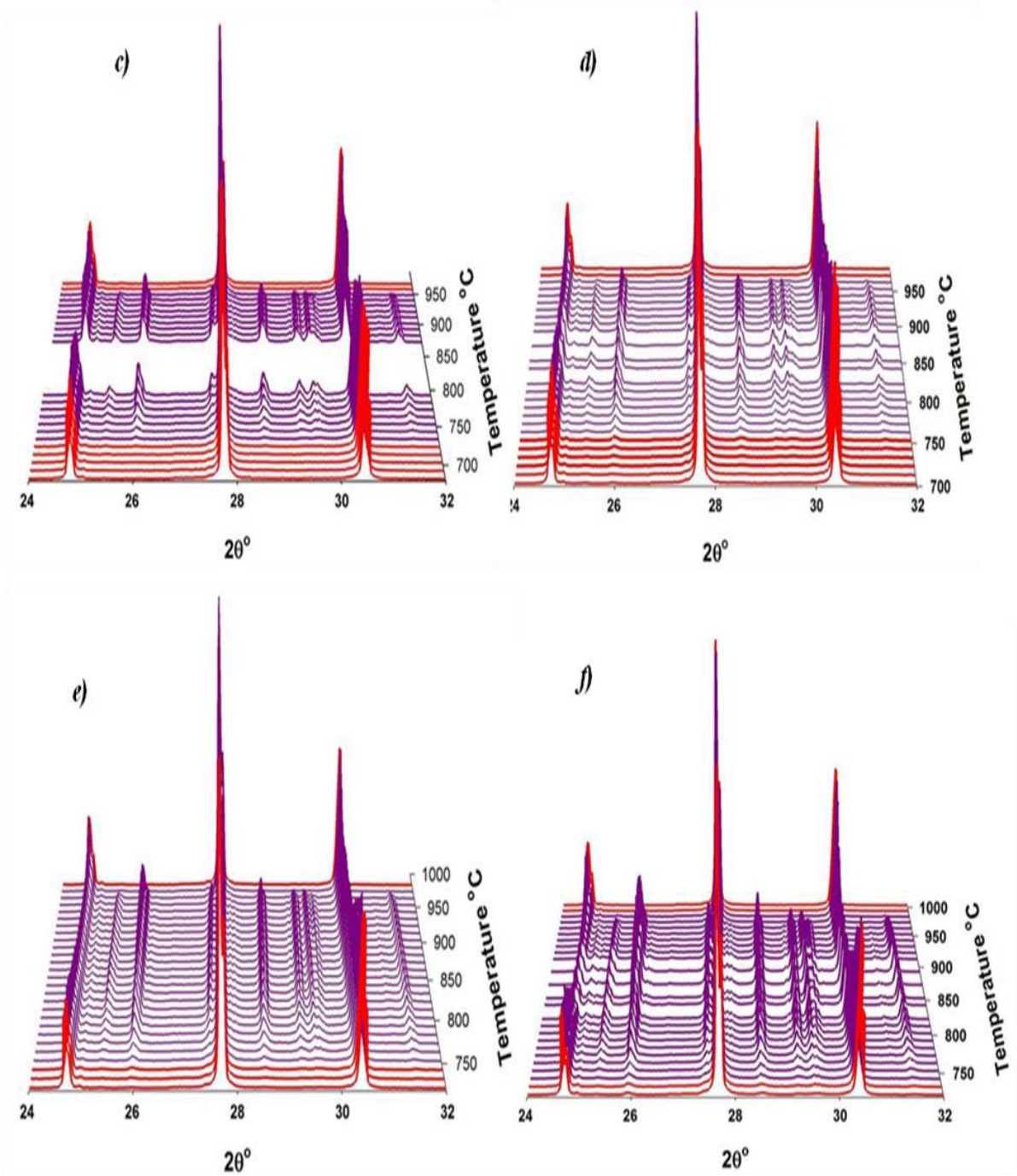

Figure 3.12.c, d, e &f: TC-XRD patterns collected on W1.5 (in 'c'), W1.525 (in 'd'), W1.550 (in 'e') and W1.575 (in 'f'). Phase transitions from β-LMO (red) to a mixture of β-LMO + α-LWO (violet) can be seen.

As expected from TC-XRD studies, long annealing of W1.4 and W1.5 raw powders for 96 hours at 700 ^{o}C or 800 ^{o}C in static air leads to a mixture of β-LMO + α-LWO type phases (see 3.13). However, the amount of α-LWO type phase is higher in W1.5 than in W1.4 (see Rietveld refinements reported in section 3.7 of this chapter).

Two successive DTA measurements were performed on ~100 mg of these biphasic W1.4 and W1.5 samples in 100 ml/min air flow. The first measurement was carried at a cooling rate lower than the second measurement. One can clearly observe a structural transition while heating in 1st cycle (Fig. 3.14). Note that both samples after the DTA study were in β-LMO phase. TC-XRD measurements were also performed on the bi-phasic W1.4 and W1.5 samples to determine the nature of the phase involved in the transition (see Fig. 3.15). The transition temperatures determined by DTA are similar to those determined by TC-XRD. From the TC-XRD study it is clear that, the endothermic event observed in the DT diagram upon heating is ascribed to the conversion of the bi-phasic sample into a β-LMO type phase.

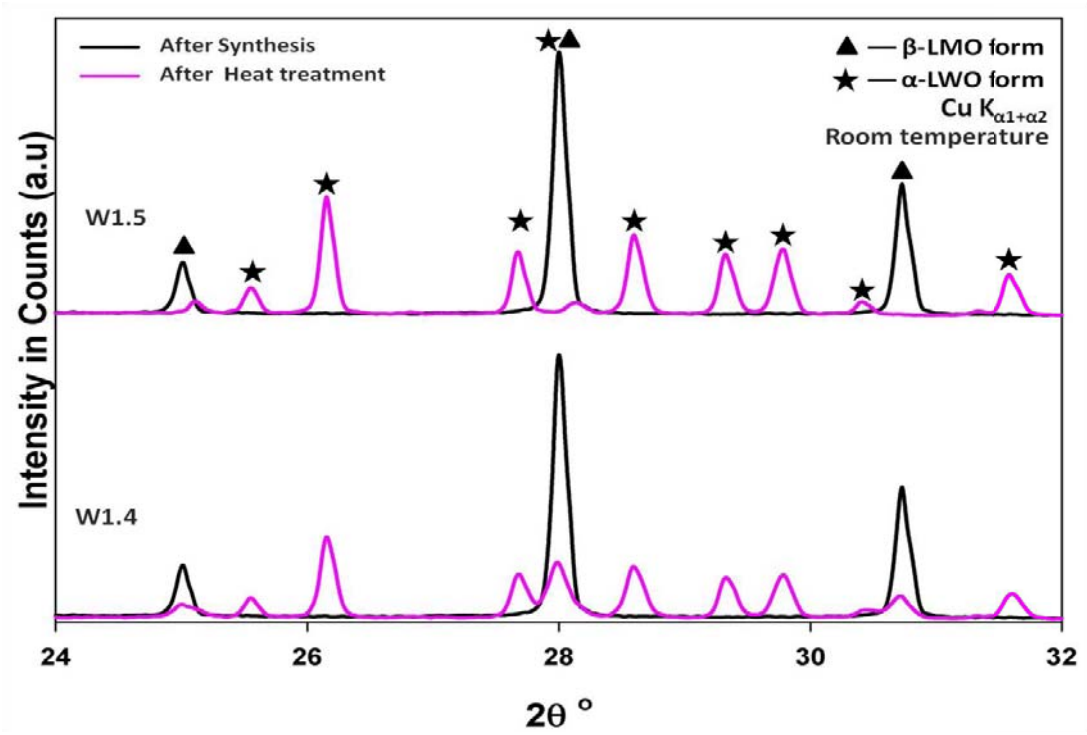

Figure 3.13: XRD patterns of W1.4 and W1.5 raw powder before (black) and after a heat treatment (at 700 ^{o}C for 96 hours) (pink).

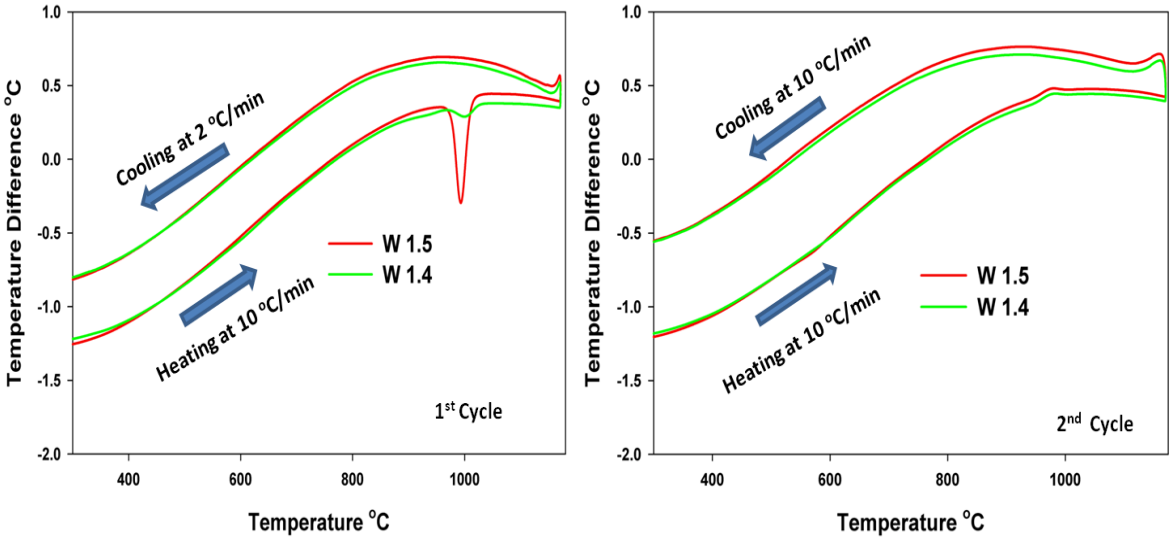

Figure 3.14: DTA curves of W1.4 and W1.5 samples (annealed at 800 °C for 96 hours) (DTA conditions: ~100 mg of sample in air flow of 100 ml/min).

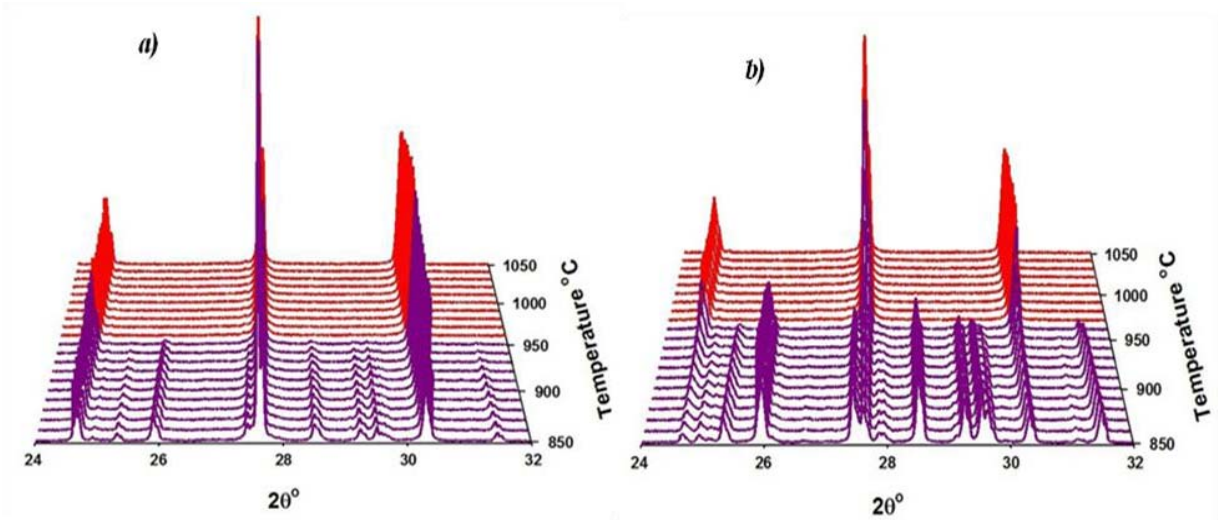

Figure 3.15.a & b: TC-XRD patterns collected on W1.4 (left 'a') and W1.5 (right 'b') which were heat treated at 800 °C for 96 hours. Phase transitions from a mixture of β-LMO + α-LWO (violet) to β-LMO (red) can be seen.

During cooling at 2°C/min and in the next heating/cooling cycle, no phase transitions were observed. XRD patterns reveal that samples were in pure cubic β-LMO phase after the DTA measurements. Another two successive DTA measurements were performed, with a cooling rate of 10 °C/min in 1st cycle and 2 °C/min in the 2nd cycle (data not shown). For both

cycles, the heating rate was fixed at 10°C/min. The DTA curves were similar to those reported in Fig. 3.14, where only the α/β transition is observed upon the first heating. It indicates that a cooling rate of 2°C/min is high enough to quench the high temperature β-form. In order to recover the thermodynamically stable bi-phasic state, only re-annealing for several hours at high temperature (at 800 ^{o}C for 96 hours) is necessary, thus suggesting that the kinetic is slow

The structure of α-LWO significantly differs from the structure of its high temperature form (β-LWO or β-LMO). The structure of α-LWO is built up from isolated four-member ring with $[W_4O_{18}]^{12-}$ formulation. In the structure of β-LMO, the coordinating polyhedra of the hexavalent Mo cations, share each of its oxygen corners with coordinating polyhedral of La. Thereby, the transition from β-LMO to α-LWO type structures or vice versa implies a cationic migration. In pure LWO sample, the structural transition from β-α is systematically observed on cooling whatever the cooling rate. What is surprising here is that no release of metastability (β-α transition) was observed for W1.4 and W1.5 upon the next heating at 10°C/min. This suggests that the cationic migration when molybdenum partly replaces tungsten in $La_2W_2O_9$ is slower than in pure $La_2W_2O_9$. Only a heat treatment for a longer period of time allows recovering a fraction of α–$La_2W_2O_9$. Because of this instability towards heat treatments (at working temperatures of SOFC ~800 ^{o}C), W1.3, W.14 and W1.5 oxides are not suitable materials either as electrolyte or in association with Ni within a cermet anode.

In was reported that LMO [18] and W-LMO [19] are inert towards NiO. However, Marrero-Lopez *et al.* have studied the thermal stability of NiO/W1.5 mixture under 5% H_2-Ar atmosphere at 650 ^{o}C. After the heat treatment, the XRD patterns revealed the presence of peaks of α -LWO type phase in addition to the peaks of NiO and a major β-LMO type phase [9]. The presence of the LWO type phase was ascribed by these authors to a reaction between NiO and W1.5 oxides. In this work it was demonstrated that this composition (W1.5) is metastable. In order to check that the segregation of α-LWO phase arise from a release of metastability rather than from a reaction, a mixture of Ni/W1.5 (50 Wt.% /50 Wt.%) was annealed at 1000 ^{o}C which is a temperature above the α- β phase transition and was cooled at 5 ^{o}C/min. Note that in these conditions of annealing and cooling, W1.5 was always obtained as a pure cubic β-phase. For the sake of comparison, the same experiment was carried out on the W1.2 composition which is thermodynamically stable. XRD patterns collected on the mixtures after annealing reveals that

no reaction between NiO and W1.5 or W1.2 occurs even at 1000 °C (see Fig. 3.16) Thereby, the occurrence of α -LWO phase observed by Marrrero *et al.* [9] for a mixture NiO/W1.5 arises from the release of metastability of this W-composition rather than from an undesired reaction.

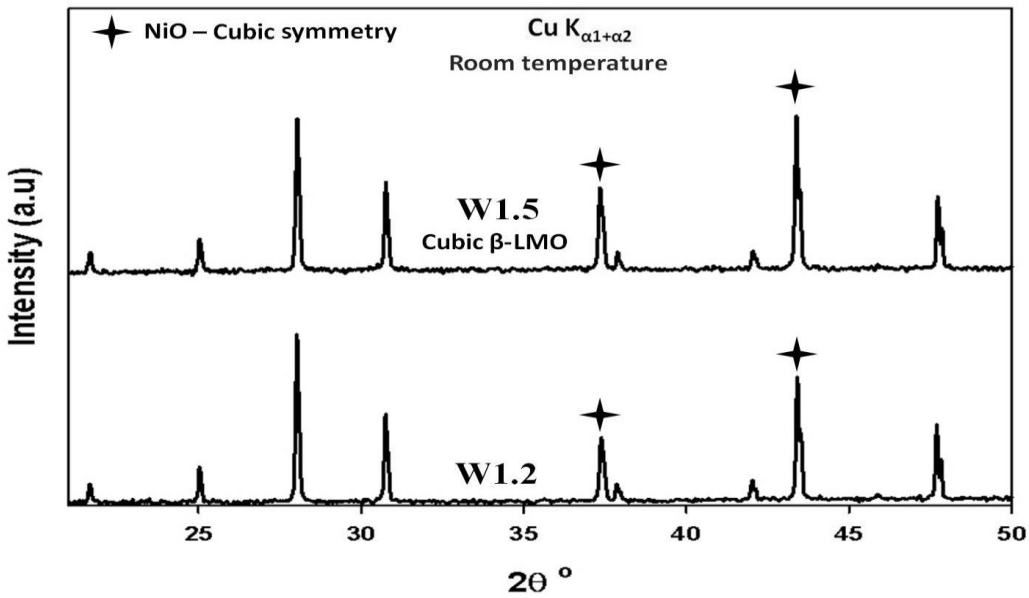

Figure 3.16: XRD patterns of W1.2 and W1.5 after annealing (for 60 Hrs at 1000 °C) with 50 – 50 Wt.% with NiO. Peaks attributed to NiO are marked with a star.

3.4 $La_2Mo_{2-y}W_yO_9$ with y = 1.6-1.8

The increase of W-amount in LMO above y = 1.575 necessitates an increase of the synthesis temperature up to 1250 °C in order to obtain raw powders exempt from impurity. Contrary to what has been observed for y ≤ 1.575, cooling from the synthesis temperatures at 5 °C/min is not enough to metastabilize the whole sample into β-form at room temperature. A mixture of α-LWO and β-LMO is obtained. Only a quenching into water – ice mixture allows to get a single β-phase at room temperature. The thermal study of these β-phase samples was probed by DTA and TC-XRD. From these analyses, it appears that W1.6 composition stands apart from the remaining ones W1.65 - W1.8.

3.4.1 $La_2Mo_{0.4}W_{1.6}O_9$ (W1.6)

DTA was carried out in the temperature range RT-1175°C with a heating/cooling rate of 10°C/min on the y = 1.6 compound which was quenched from 1250°C into a water-ice mixture. The curve is displayed in Fig. 3.17. Surprisingly, DTA revealed the appearance of multiple phase transitions in this sample upon heating and no transition while cooling. This behavior is not seen in any compound with y ≤ 1.575. DTA curves shows two exothermic peaks and an endothermic peak. The sample was in β-LMO phase before DTA and was a mixture of α-LWO and β-LMO phases after DT analysis. TC-XRD was carried on such sample to determine the nature of the phases involved in these transitions. The transition around ~ 475 ^{o}C, corresponds to the transition from β-LMO to a mixture of α-LWO and β-LMO (see Fig. 3.17). These two phases coexist till 750 ^{o}C, above which complete conversion into pure α-LWO takes place. Appearance of exothermic peak at 1008 ^{o}C (in DTA) can be then attributed to change of the compound from α-LWO to β-LMO phase.

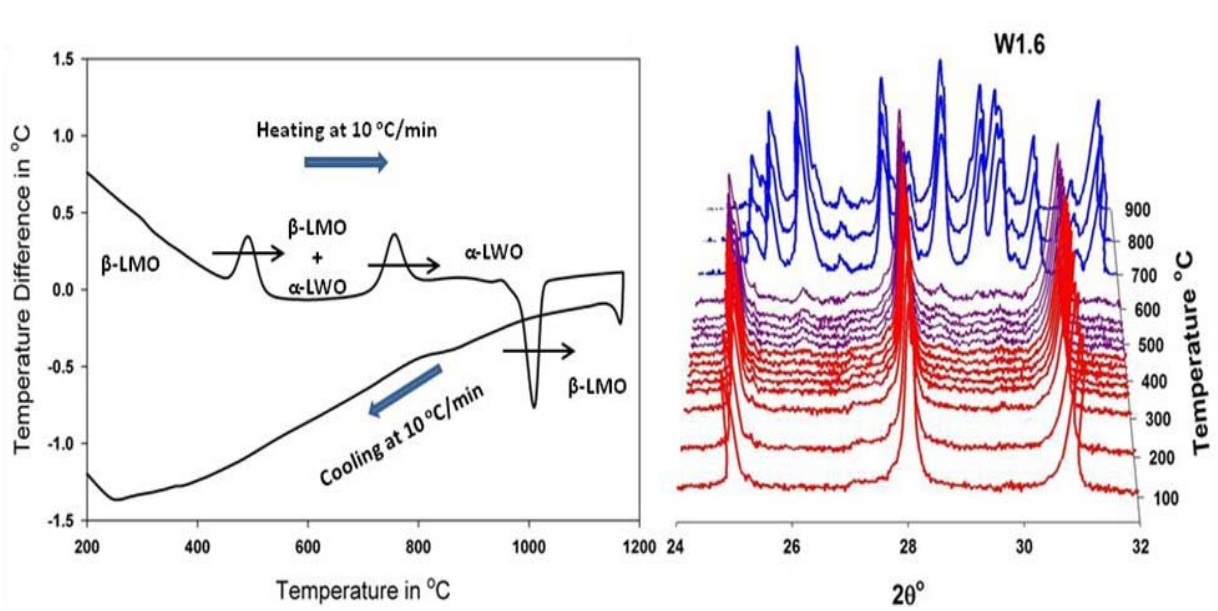

Figure 3.17: DTA curve of W1.6 sample showing multiple phase transitions (left). TC-XRD patterns of W1.6 (right) from room temperature to 960 ^{o}C, where phase transitions from β-LMO (red) to a mixture of α-LWO + β-LMO (violet) and another transition to α-LWO (blue) can be clearly seen. Note that the initial sample is quenched into a mixture of water and ice.

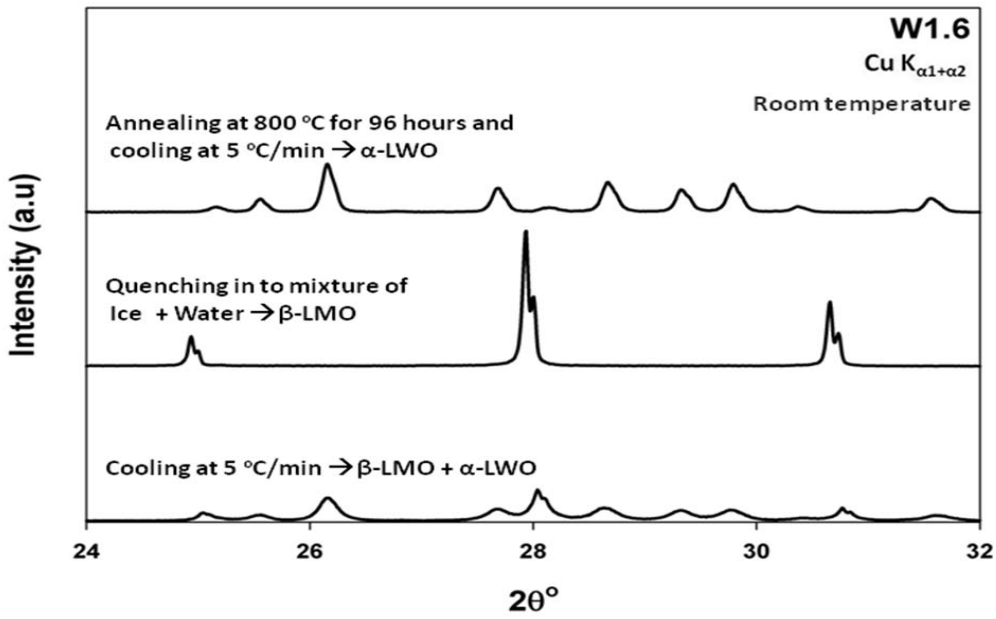

Figure 3.18: XRD patterns of W1.6 after annealing at 1250 °C and cooling down to room temperature at 5 °C/min (bottom), cooling into a mixture of water and ice (middle) and W1.6 after heat treatment at 800 °C for 96 hours (top).

To determine the nature of the thermodynamically stable phase below 1008 °C, short or long annealing followed by quenching into a mixture of ice and water were performed on a biphasic W1.6 sample synthesized by annealing the sample till 1250 °C and cooling down to R.T at 5 °C/min. Quenching experiments were performed after annealing the sample in Pt capsule at 800 °C, 750 °C, 700 °C, 650 °C, 600 °C for 12 hours; and 500 °C for 96 hours and 400 °C for 48 hours. All samples after annealing were obtained in α-LWO type phase. A single α-LWO type phase is also obtained when biphasic raw powder of W1.6 sample is annealed at 800°C for 96 hours and cooled at 5°C/min thus indicating the α-LWO form is the thermodynamically stable state of W1.6 composition below 1008 °C (see Fig. 3.18).

TC-XRD patterns and DTA curves were collected on such heat treated (800 °C for 96 hours) W1.6 sample. Two successive DTA measurements were performed. The sample was first heated to 1175 °C and cooled at 2 °C/min (1st cycle), reannealed to 1175 °C and cooled at 10 °C/min (2nd cycle). DTA analysis was performed over ~100 mg of sample in 100 ml/min of air

flow (see Figure 3.19). An endothermic event associated to a phase transition was observed upon heating for both cycles (see Fig. 3.19) while an exothermic event was only noted on cooling at 2 ^{o}C/min in the first cycle. XRD analysis performed on sample after the second cycle of DTA measurement has shown pure β-LMO phase. Since a single β-LMO phase was obtained when the sample was quenched from 1250°C into water-ice mixture, the above result shows that a cooling rate of 10°C/min is fast enough to metastabilize at room temperature the whole sample in the β-form, thus acting as quenching effect.

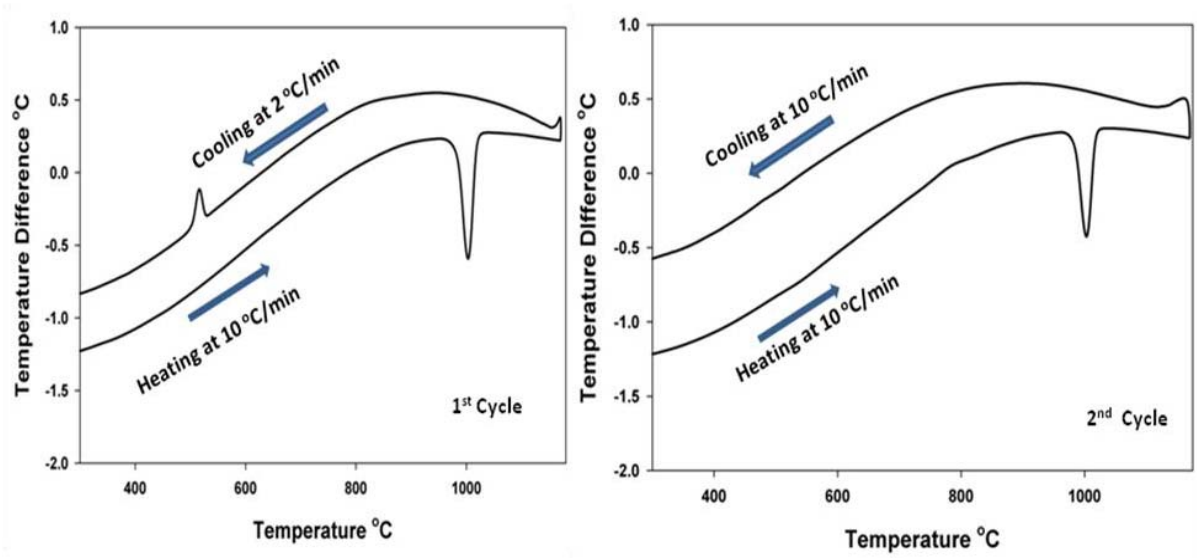

Figure 3.19: DTA curves of W1.6 (which was previously heat treated at 800 ^{o}C for 96 hours)

To determine the nature of the phases observed by DTA on heating and cooling, TC-XRD analysis was performed on similar W1.6 sample which was annealed for 96 hours at 800 ^{o}C. The thermal evolution of XRD patterns while heating and cooling is displayed in Fig. 3.20. W1.6 which is in α-LWO phase at room temperature has a phase transition to a mixture of cubic and triclinic phases at 890 ^{o}C, which changes back to β-LMO phase around 980 ^{o}C and remain unchanged till 1150 ^{o}C. While cooling the sample back to R.T., XRD patterns were collected where β-LMO phase was seen till 500 ^{o}C. Between 500 ^{o}C to 450 ^{o}C, a transition of β-LMO phase to bi-phasic domain occurs and W1.6 remains bi-phasic upon further cooling down to room temperature. The average rate of cooling in TC-XRD was calculated to be ~1.8 ^{o}C/min

(calculated by considering time took for each data collection at each temperature and time needed for cooling the sample down to the next temperature and the temperature difference). Since both α-LWO and β-LMO phases coexist at room temperature when the sample is cooled at 1.8 °C/min during TC-XRD measurements, it indicates that the conversion into α-LWO detected by DTA in the first cooling at 2°C/min is partial in nature and explain the occurrence of the α/β transition upon the next heating at 10°C/min.

Considering the DT and XRD analyses, synthesis under different cooling rates (including quenching) and long term annealing measurements, it is possible to tell that α-LWO is the thermodynamic stable phase for this compound at room temperature. However above 980 ^{o}C, β-LMO is the stable phase. Depending on the cooling rates applied during synthesis and post heat treatments, W1.6 can be obtained as a single cubic or triclinic phase or a mixture of both phases. When a fraction of β-LMO phase or a single β-LMO phase is obtained at room temperature, a release of metastability occurs on heating.

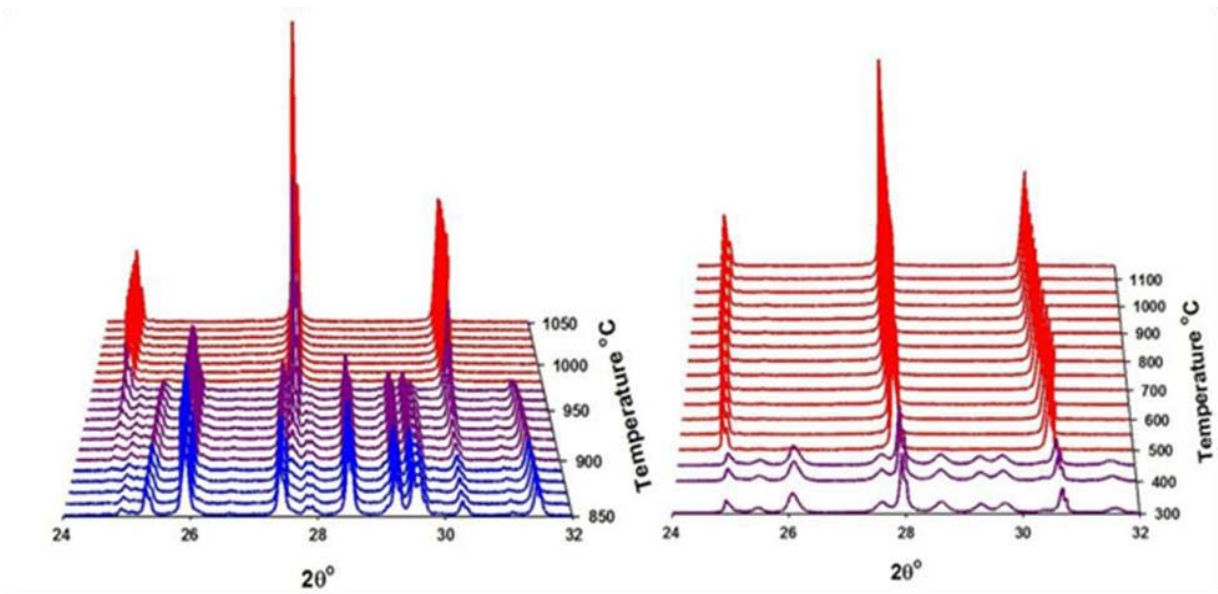

Figure 3.20: TC-XRD patterns collected on W1.6 upon heating (left) and cooling (right) (previously heat treated at 800 ^{o}C for 96 hours). Phase transitions can be clearly identified in the above patterns where β-LMO (red); α-LWO + β-LMO (violet) and α-LWO (blue).

3.4.2 $La_2Mo_{2-y}W_yO_9$ with y = 1.65-1.8

DTA curves and TC-XRD patterns were collected on the y = 1.65 to 1.8 compounds which were quenched from 1250 °C into a water-ice mixture (see Fig. 3.21 and Fig. 3.22). Upon heating, DTA curves exhibit one intense exothermic peak at around ~435-464 °C (peak maximum) and one intense endothermic at around ~1020-1048°C (peak maximum). Note that the difference in temperature between these two thermal events increases as the W content in the sample increases. The thermal evolution of the patterns collected on heating for the W1.7 sample (Fig. 3.22) reveals that a fraction of the β-LMO phase is converted into α-LWO phase upon heating around ~ 400 °C which turns back to a pure β-LMO phase above 1030°C. The transition temperatures determined by both DTA and XRD are in good agreement (see Fig. 3.23). Contrary to the W1.6 composition in similar data collection conditions, successive DT analyses show that the α/β phase transition taking place at high temperature upon heating is here reversible on cooling whatever the compositions: an intense exothermic peak is measured at around ~549-653 °C (peak maximum). However this reversibility is partial since all samples with y = 1.65 to 1.8 are bi-phasic (β-LMO + α-LWO) after DTA measurement.

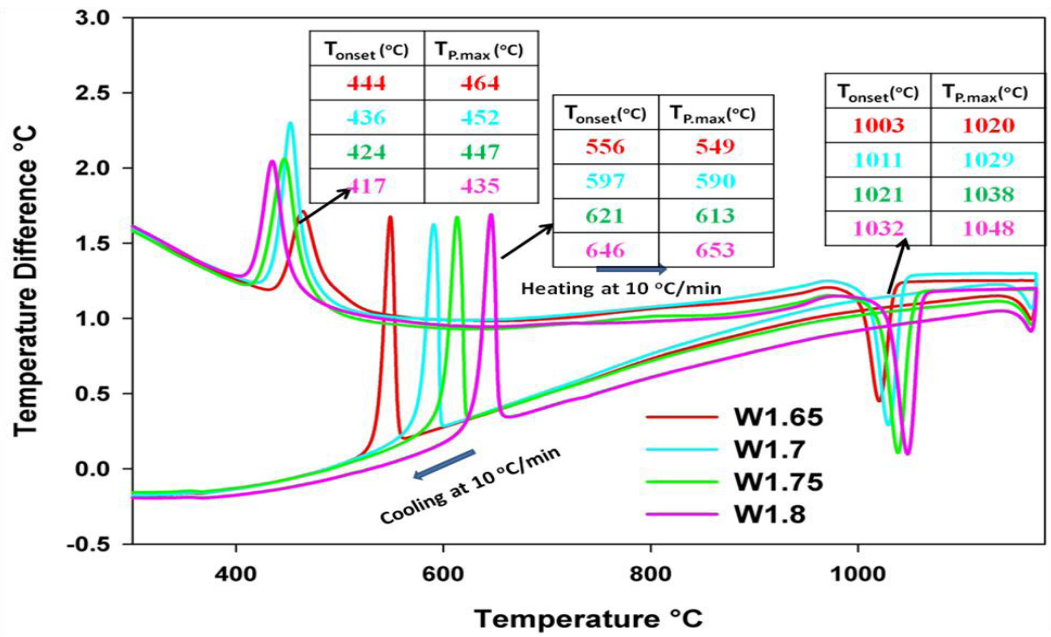

Figure 3.21: DTA curves of samples with y = 1.65 to 1.8 (quenched into mixture of ice and water). Transition temperatures: Onset (T_{onset}) and Peak max ($T_{p.max}$) are given in inset.

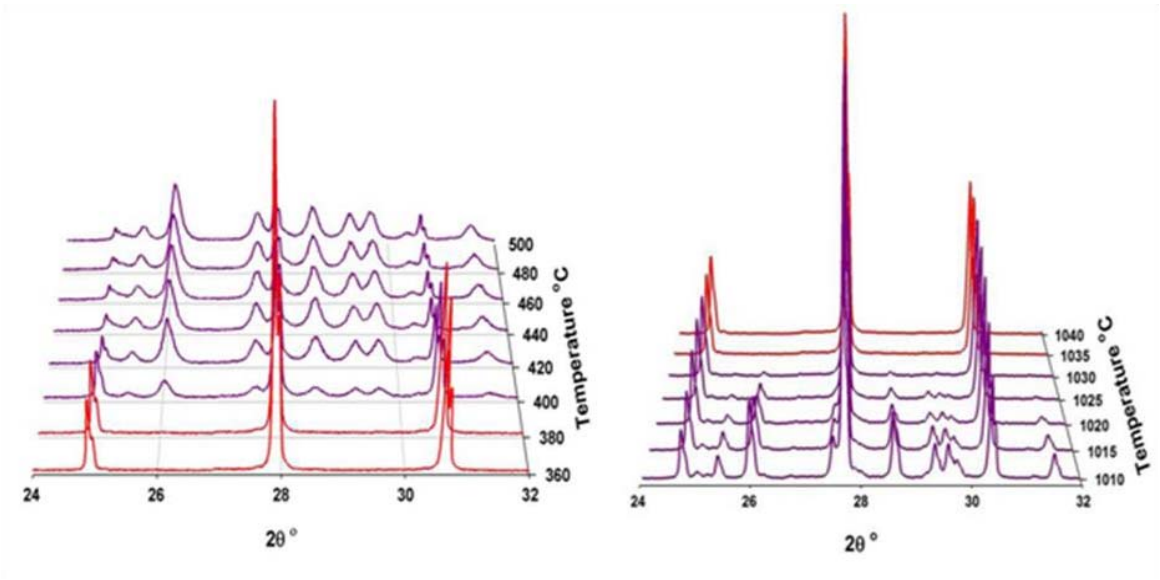

Figure 3.22: TC-XRD patterns collected upon heating the *W1.7 sample which was previously quenched from 1250 °C into a mixture of ice and water. Phase transitions from mixture of β-LMO + α-LWO (violet) to β-LMO (red) and vice versa can be seen.*

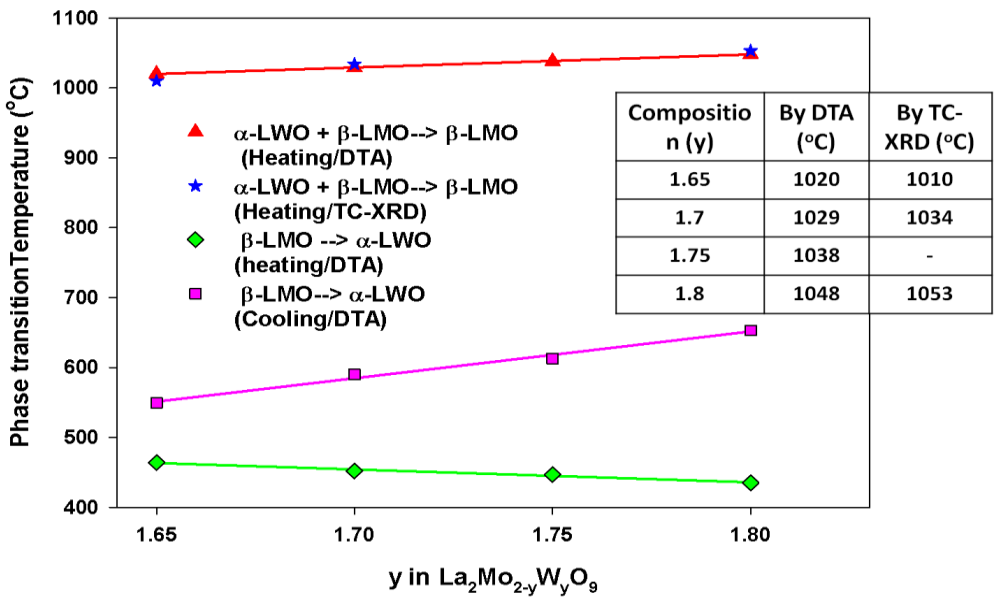

Composition (y)	By DTA (°C)	By TC-XRD (°C)
1.65	1020	1010
1.7	1029	1034
1.75	1038	-
1.8	1048	1053

Figure 3.23: Evolution of phase transition temperatures in W1.65 to W1.8 oxides. Note multiple phase transitions mentioned in Fig 3.21. H.T α→β phase transition temp determined by TC-XRD and DTA are given in inset.

To determine the nature of the thermodynamically stable phase below 1000 °C, short or long annealing followed by quenching into a mixture of ice and water were performed on biphasic W1.65, W1.7 samples (synthesized at 1250 °C and cooled to R.T. at 5 °C/min). Quenching experiments were performed after annealing the sample in Pt capsule at 800 °C, 750 °C, 700 °C, 650 °C, 600 °C for 12 hours; and 500 °C for 96 hours and 400 °C for 48 hours. All samples after annealing were obtained in an α-LWO type phase. A single α-LWO type phase is also obtained when biphasic raw powder of W1.7 and W1.8 samples is annealed at 800 °C for 96 hours and cooled at 5°C/min thus indicating the α-LWO form is the thermodynamically stable state of all these compositions below 1000 °C.

TC-XRD patterns and DTA curves were collected on such W1.7 and W1.8 samples. Two successive DTA measurements were performed. The sample was first heated to 1175 °C and cooled at 2 °C/min (1st cycle), re-annealed to 1175 °C and cooled back at 10 °C/min (2nd cycle). The DTA curves and TC-XRD are displayed in Fig. 3.24 and Fig. 3.25 respectively.

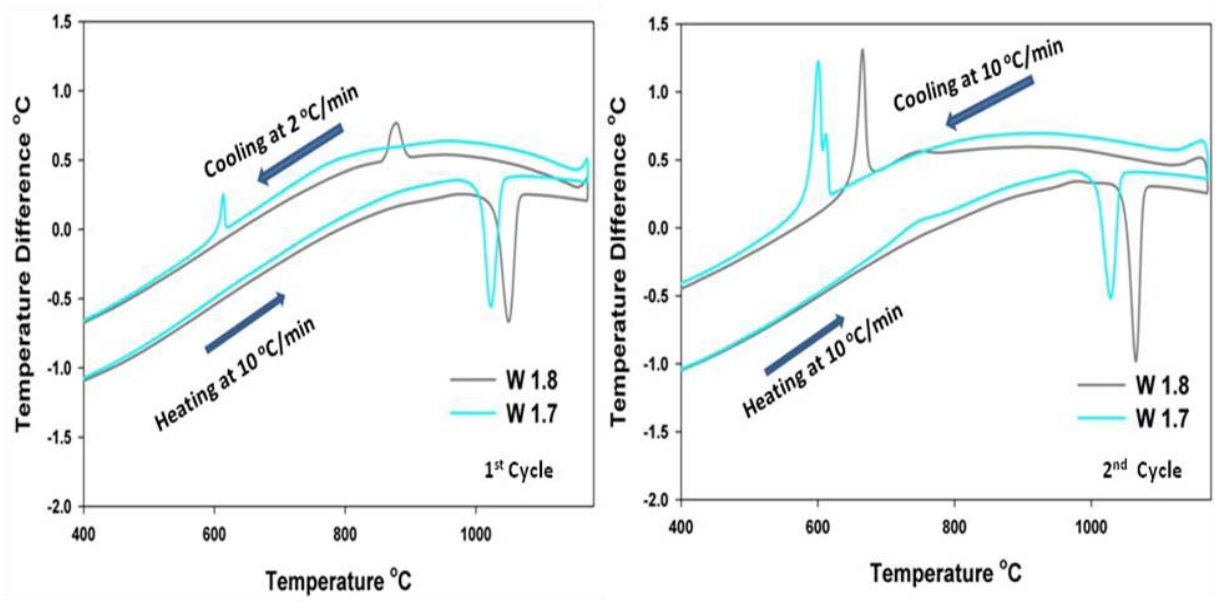

Figure 3.24: DTA curves of W1.7 and W1.8 samples which were annealed at 800 °C for 96 hours before measurement (DTA conditions: ~100 mg of sample with 100 ml/min air flow).

Contrary to what has been observed for W1.6 composition in similar data collection conditions, successive DT analyses show that the α/β phase transition is reversible whatever the compositions considered and the cooling rates used. However, the TC-XRD patterns collected on

cooling reveal that the reversibility of the phase transition is partial and complete in nature for W1.7 and W1.8 samples, respectively. Indeed, both α–LWO and β–LMO phases coexist when the W1.7 sample is cooled below 700°C while the XRD patterns for W1.8 sample show a pure α–LWO phase on cooling below 900°C.

Between the W1.7 and 1.8 samples, a significant difference of 200 °C in the β/α transition temperature is determined from TC-XRD measurements on cooling at ~2 °C/min. It is consistent with DT analysis performed on cooling at 2 °C/min since the average cooling rate during TC-XRD is similar. In DTA curve of quenched W1.7 sample reported in Fig. 3.24, a splitting of the exothermic peak while cooling was observed. Since a mixture of α–LWO and β–LMO phases is obtained after cooling the W1.7 sample at 10 °C/min, the peak splitting cannot arise from successive β-LMO→ α-LWO + β-LMO→ α-LWO phase transitions. In that way, one can interpret this peak splitting as originating from a non-uniform distribution of W/Mo within the sample which leads to several β/α phase transitions at very close temperatures depending on the W content and such a possibility was reported in literature [1]. Phase transition temperatures and nature of phases are discussed in Section 3.6.

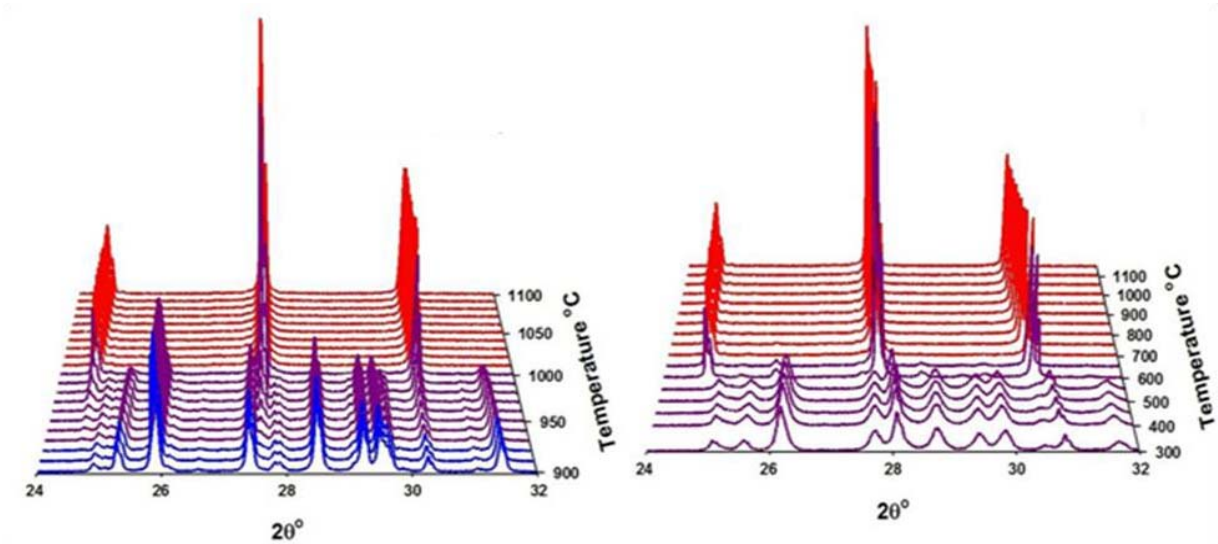

Figure 3.25.a: TC-XRD patterns of W1.7 sample upon heating (left) and cooling (right) which was previously heat treated by annealing at 800 °C for 96 hours. Patterns with β-LMO (red); β-LMO+ α-LWO (violet) and α-LWO (blue) can be noticed.

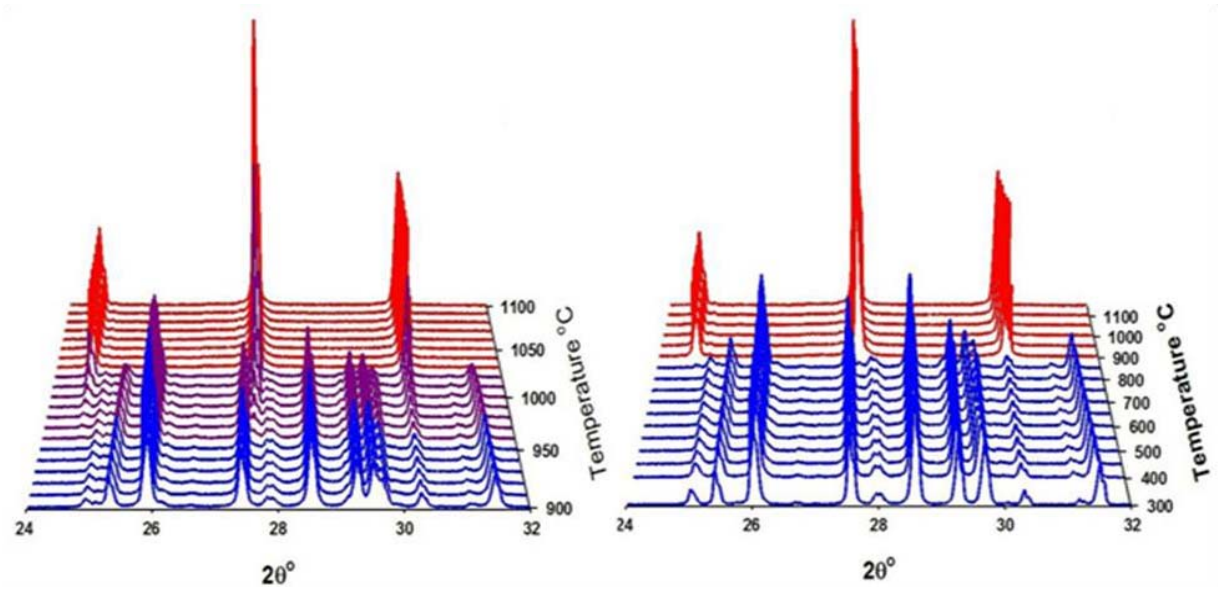

Figure 3.25.b: TC-XRD patterns of W1.8 sample upon heating (left) and cooling (right) which was previously heat treated by annealing at 800 °C for 96 hours. Patterns with β-LMO (red); β-LMO+ α-LWO (violet) and α-LWO (blue) can be noticed.

3.5 $La_2Mo_{2-y}W_yO_9$ with y = 1.85 - 2.0

All four samples (y = 1.85, 1.9, 1.95 and 2.0) were always obtained in pure α-LWO phase irrespective of the cooling rate applied while synthesis. Several synthesis attempts to obtain β-LMO phased samples (from y = 1.85 to 2.0) were unsuccessful. The thermal study of the α-LWO phases was probed by DTA and TC-XRD. DTA performed on W1.9 and W2.0 samples exhibits one endothermic peak on heating and one exothermic peak on cooling. The XRD patterns collected on the samples after DT analysis show a pure α-LWO phase. From TC-XRD patterns collected on the samples of 1.85, 1.9, 1.95 and 2.0, the thermal events on heating and on cooling are associated to α/β and β/α phase transitions, respectively (see Fig. 3.26). The transition from α-LMO phase to β-LWO phase undergoes through a transient mixture of both phases in the temperature range 1010-1060 °C and 1080-1090 °C for W1.9 and W2.0 samples, respectively (see Fig. 3.27).

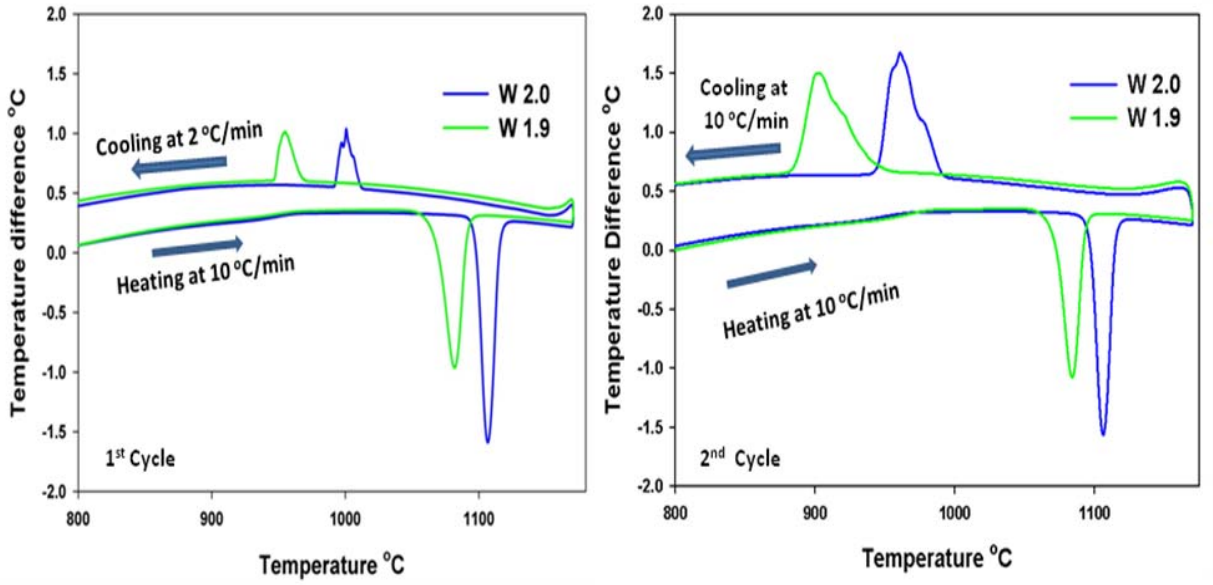

Figure. 3.26: DTA curves of W1.9 and W2.0 samples. These samples were synthesized at 1250 °C by cooling at 5 °C/min.

Although the TC-XRD patterns were collected only every 50 °C on cooling, a mixture α-LWO and β-LMO phases can be also noticed in the XRD pattern of the W2.0 sample at 1000 °C on cooling. On cooling at 10°C/min, the exothermic peak in DTA curves for both samples is broader than the endothermic peak measured on heating and exhibits a shoulder on the high temperature side. Since the transition from the β-LMO phase into α-LWO phase implies a cationic migration which decreases as the temperature decreases, a high cooling rate of 10 °C/min is likely to induce a non-uniform distribution of W/Mo within the sample. It leads to successive β/α phase transitions at temperatures dependent on the W content which explains the peak broadening and/or the occurrence of shoulders.

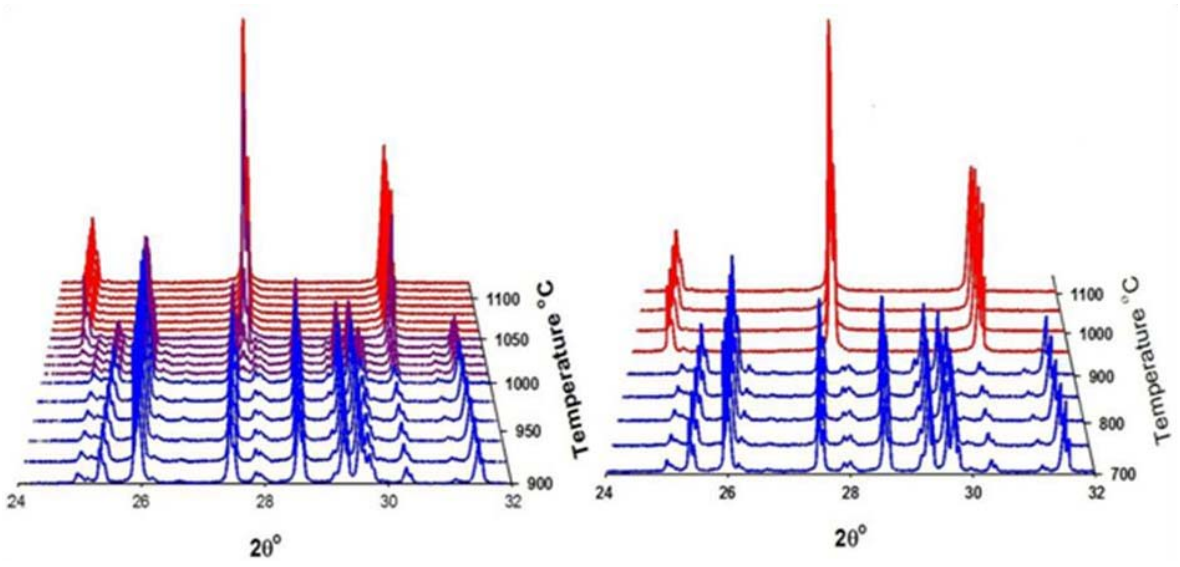

Figure 3.27.a: TC-XRD patterns of W1.9 sample while heating (left) and cooling (right) which was synthesized at 1250 ^{o}C and cooling at 5 ^{o}C/min. Patterns with β-LMO (red); β-LMO+ α-LWO (violet) and α-LWO (blue) can be identified.

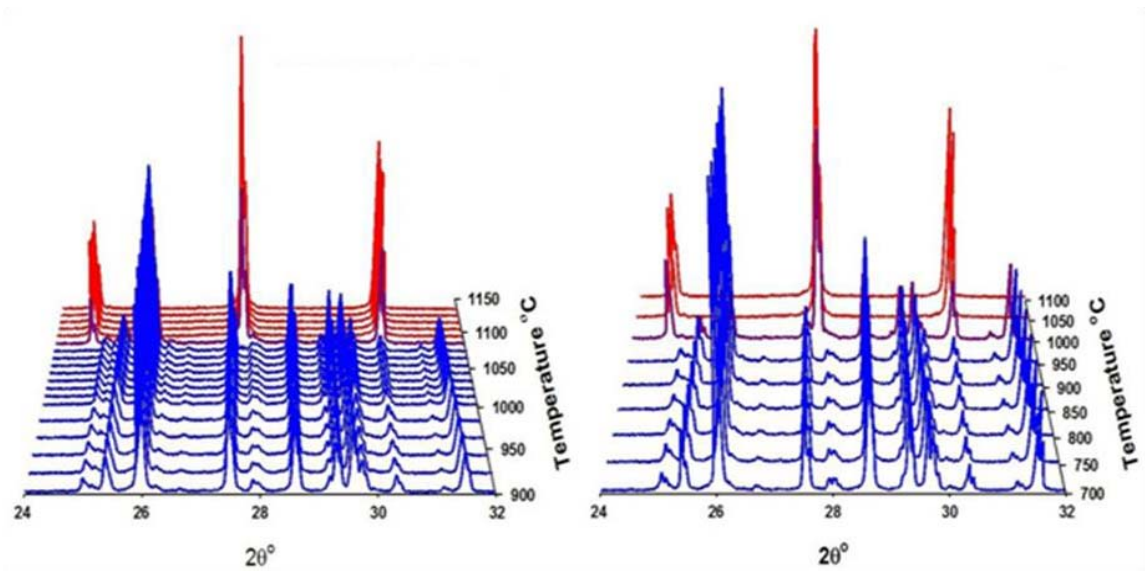

Figure. 3.27.b: TC-XRD patterns of W 2.0 sample while heating (left) and cooling (right) which was synthesized at 1250 ^{o}C and cooling at 5 ^{o}C/min. Patterns with β-LMO (red); β-LMO+ α-LWO (violet) and α-LWO (blue) can be identified.

3.6 Phase Diagram of $La_2W_yMo_{2-y}O_9$ ($1.0 \leq y \leq 2.0$)

It was observed that variation in the synthesis conditions of W-LMO compounds can have effect on final phase purity of the compounds and accordingly samples with single phase (either cubic or triclinic) and bi-phasic were synthesized. Here overview of all the final phase purity of samples and their synthesis conditions will be taken into consideration. Results of DTA, XRD analysis and TC-XRD analysis will be considered and a phase diagram of the series with y = 1.0 to 2.0 will be proposed.

W1.0, W1.1 and W1.2 oxides when synthesized by cooling at 5 ^{o}C/min, were in cubic β-LMO phase. Even though long heat treatments were performed, these samples were always in β-LMO phase. DTA measurements carried on these samples showed neither endothermic nor exothermic events suggesting that β-LMO form is a thermodynamic stable state.

Samples from W1.3 to W1.575 when synthesized by cooling at 5 ^{o}C/min were cubic β-LMO form. DTA performed on these samples did not show any phase transition. TC-XRD performed on W1.3 and W1.35 also did not reveal any phase transitions. However samples W1.4 to W1.575, when annealed in TC-XRD unit, revealed partial transition from β-LMO to α-LWO phase at intermediate temperatures which transits back to β-LMO phase at elevated temperatures. The samples W1.3 to W1.5, when heat treated at 800 ^{o}C for 96 hours, resulted in bi-phasic products, sustaining that a mixture of the β-LMO + α-LWO forms is their thermodynamically stable state. DTA analyses on heat treated samples show phase transition while heating but no such events while cooling. TC-XRD performed on these samples show phase transition at elevated temperatures (above 950 ^{o}C), however the samples once cooled irrespective of their cooling rates, theese are always in β-LMO phase. They have to be again heat treated to achieve their thermodynamic stable states (β-LMO + α-LWO). DTA and TC-XRD results are consistent. Samples W1.3 and W1.5 are the end members of this metastable domain. The phase transition temperatures are listed in Table 3.2.

Samples from W1.6 to W1.8 synthesized by cooling at 5 ^{o}C/min lead to the formation of biphasic compounds at room temperature. DTA analysis show phase transition events while heating and cooling. When these samples are quenched from elevated temperatures into a mixture of ice and water, pure cubic β-LMO phase compounds can be obtained. In this case β-

LMO phase is metastable and metastability releases upon annealing, around ~400 ^{o}C depending on W-content. DTA performed on these samples show multiple phase transition, which are consistent with the TC-XRD results. These compounds once annealed transit into α-LWO phase, supporting α-LWO phase as their stable state. Such compounds which are in α-LWO phase show phase transition to biphasic domain first which gradually forms β-LMO phase at elevated temperatures (≥ 980 ^{o}C). Transition temperatures are listed in Table 3.2.

Irrespective of the cooling rates and heat treatments, compounds from W1.85 to W2.0 are always in α-LWO phase at room temperature. These compounds if annealed go through short bi-phasic domain first, which on further increase in temperature change to β-LMO phase (> 1050 ^{o}C). The temperature limits of this bi-phasic domain increases with increase in W-content (see transition temperatures in Table 3.2).

Considering the results of DTA, XRD, TC-XRD and heat treatment measurements it was possible to differentiate stable and metastable domains in this series of samples (see Fig. 3.28). A phase diagram is proposed for the samples from y = 1.0 to 2.0 (see Fig. 3.29).

Y in $La_2W_yMo_{2-y}O_9$	*Stable phase at R.T*	*Phase Transition Temperature to β-LMO + α-LWO phases (°C)*	*Phase Transition Temperature to β-LMO phase (°C)*
1.0	β-LMO	---	---
1.1	β-LMO	---	---
1.2	β-LMO	---	---
1.3	β-LMO + α-LWO	---	950
1.4	β-LMO + α-LWO	---	960
1.5	β-LMO + α-LWO	---	970
1.6	α-LWO	890	980
1.7	α-LWO	930	1010
1.8	α-LWO	960	1030
1.9	α-LWO	1010	1060
2.0	α-LWO	1080	1090

Table 3.2: Phase Transition temperatures of all compounds from y = 1.0 to 2.0 (determined by TC-XRD).

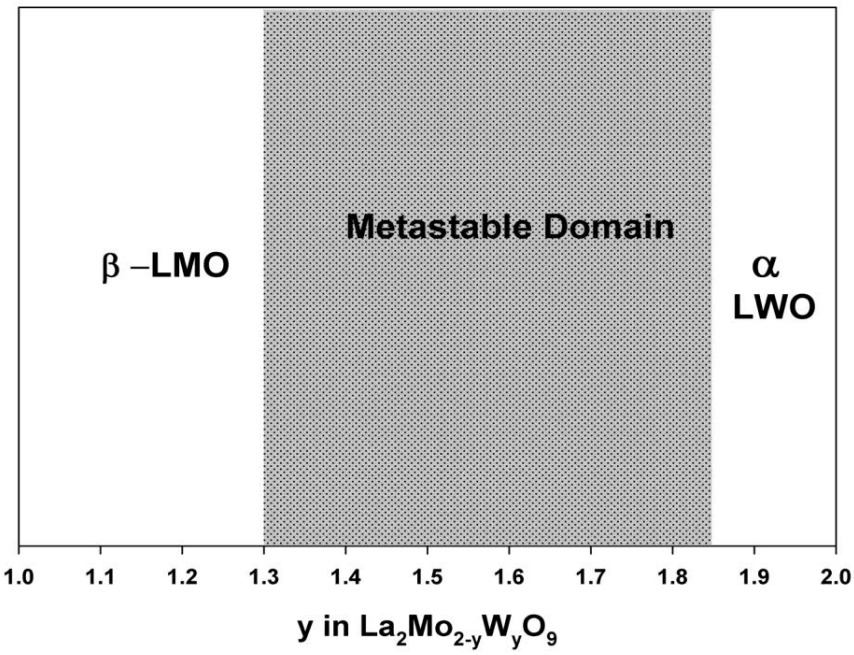

Fig. 3 .28: Compounds in W-LMO series exhibiting metastable behavior at room temperature.

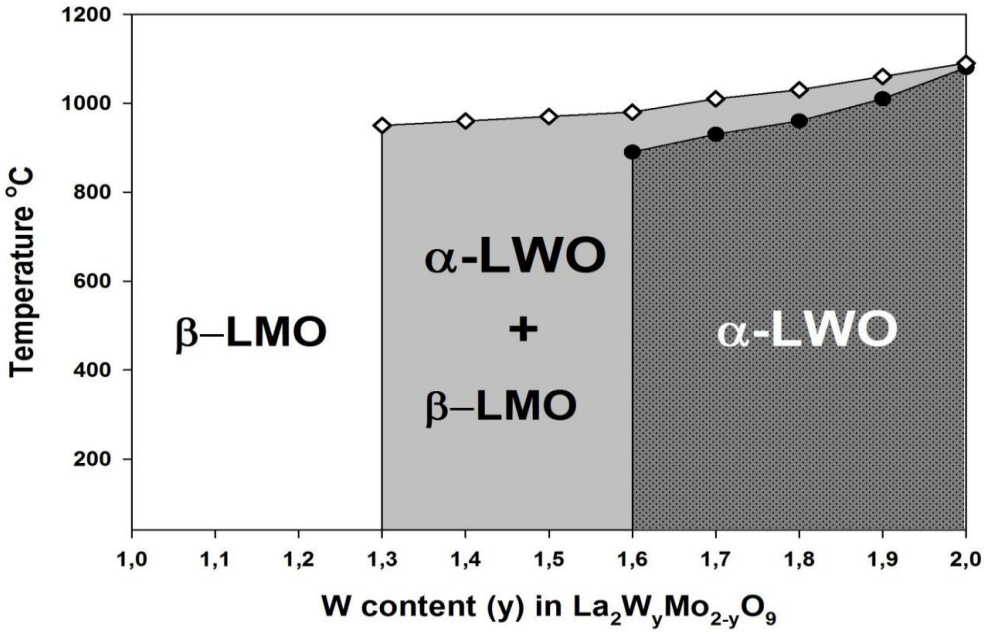

Fig. 3.29: Proposed phase diagram for W-LMO compounds with W substitution ≥ 50 mol%. Note that all compounds used for proposing this phase diagram were in their respective thermodynamically stable states.

3.7 X-Ray Powder Diffraction Analyses

The aim of this section is to determine the evolution of the unit cell volumes as a function of the W amount for raw powders and heat treated samples at R.T and at 700 ^{o}C. Evolution of weight fractions of each phase present in bi-phasic raw and heat treated samples are also studied. A new Nomenclature is proposed for ease of comprehension, and this nomenclature is provided according to the thermal history of the sample and the XRD data collecting conditions. XRD patterns collected on raw powders at room temperature which were synthesized at 1150 ^{o}C/1250 ^{o}C are called ***RP-1200-RT*** (R*aw powder – Synthesis temperature/1200 – Room temperature*). XRD patterns collected on heat treated samples (annealed for 800 ^{o}C for 96 hours) at room temperature are called ***HT-800-RT*** (*Heat treated – Annealing Temperature/800 ^{o}C – Room temperature*). As mentioned earlier, heat treated samples from y = 1.3 to 1.8, TC-XRD is performed at 700 ^{o}C; and XRD patterns collected on these pre-heat treated samples at 700 ^{o}C are called ***HT-800-700***.

The crystal structures have been refined from X-ray powder diffraction patterns by the Rietveld method using the structures of β-$La_2Mo_{0.6}W_{1.4}O_9$ (by Corbel *et al.*[20]) and β-$La_2W_2O_9$ (by Laligant *et al.*[6]) as starting structural models. Since the X-ray scattering factor of oxygen is lower than that of La, Mo and W, the atomic positions and Site Occupation Factors (SOF) of the oxygen atoms were kept fixed at the values of the structural models determined from neutron diffraction data. θ-zero shift, parameters of the profile shape function, unit cell parameters, atomic positions for cations were refined step by step together. In a first step, the site occupation factors for Mo and W were kept fixed at the values of the nominal content of the composition and refined later.

3.7.1 Raw powders

Unit cell parameters of all compositions as well as the weight fractions of the phases present in the bi-phasic samples are reported in Table 3.3. Representative observed, calculated, and difference diffraction patterns for samples exhibiting a single cubic phase, a single triclinic phase and a mixture of both phases are displayed in Fig. 3.30 and Fig. 3.31.

(y) in $La_2W_yMo_{2-y}O_9$	Phase	Cell Parameters						Single Cell Volume V [Å]^3	Wt. Fraction of phases (%)
		a [Å]	b [Å]	c [Å]	α°	β°	γ°		
1.0	β-LMO	7.1527(1)	7.1527(1)	7.1527(1)	90	90	90	365.947(3)	-
1.1	β-LMO	7.1502(1)	7.1502(1)	7.1502(1)	90	90	90	365.561(2)	-
1.2	β-LMO	7.1474(1)	7.1474(1)	7.1474(1)	90	90	90	365.128(3)	-
1.3	β-LMO	7.1447(1)	7.1447(1)	7.1447(1)	90	90	90	364.721(3)	-
1.4	β-LMO	7.1404(1)	7.1404(1)	7.1404(1)	90	90	90	364.064(6)	-
1.5	β-LMO	7.1370(1)	7.1370(1)	7.1370(1)	90	90	90	363.549(5)	-
1.55	β-LMO	7.1380(1)	7.1380(1)	7.1380(1)	90	90	90	363.696(3)	-
1.6	β-LMO	7.1341(2)	7.1341(2)	7.1341(2)	90	90	90	363.09(1)	27.7(1)
	α-LWO	7.2533(2)	7.2816(2)	7.0504(2)	96.349(2)	94.626(2)	70.483(2)	348.45(2)	72.3(1)
1.7	β-LMO	7.1309(2)	7.1309(2)	7.1309(2)	90	90	90	362.61(1)	30.6(1)
	α-LWO	7.2537(2)	7.2831(2)	7.0515(2)	96.365(2)	94.625(2)	70.460(2)	348.54(2)	69.4(1)
1.8	β-LMO	7.1197(4)	7.1197(4)	7.1197(4)	90	90	90	360.90(3)	15.9(1)
	α-LWO	7.2522(2)	7.2823(2)	7.0465(2)	96.369(2)	94.658(2)	70.429(1)	348.10(2)	84.1(3)
1.85	α-LWO	7.2533(1)	7.2888(1)	7.0470(1)	96.3779(6)	94.7162(6)	70.3547(6)	348.309(9)	-
1.9	α-LWO	7.2516(1)	7.2906(1)	7.0480(1)	96.3769(6)	94.7131(5)	70.3372(5)	348.415(7)	-
1.95	α-LWO	7.2528(1)	7.2905(1)	7.0475(1)	96.3734(4)	94.7124(4)	70.3127(3)	348. 307 (5)	-
2.0	α-LWO	7.2516(1)	7.2910(1)	7.0469(1)	96.3710(4)	94.7121(4)	70.2869(3)	348.354(3)	-

Table 3.3: Unit cell parameters of phases present in y = 1.0 - 2.0 samples ***(RP-1200-RT)****.*

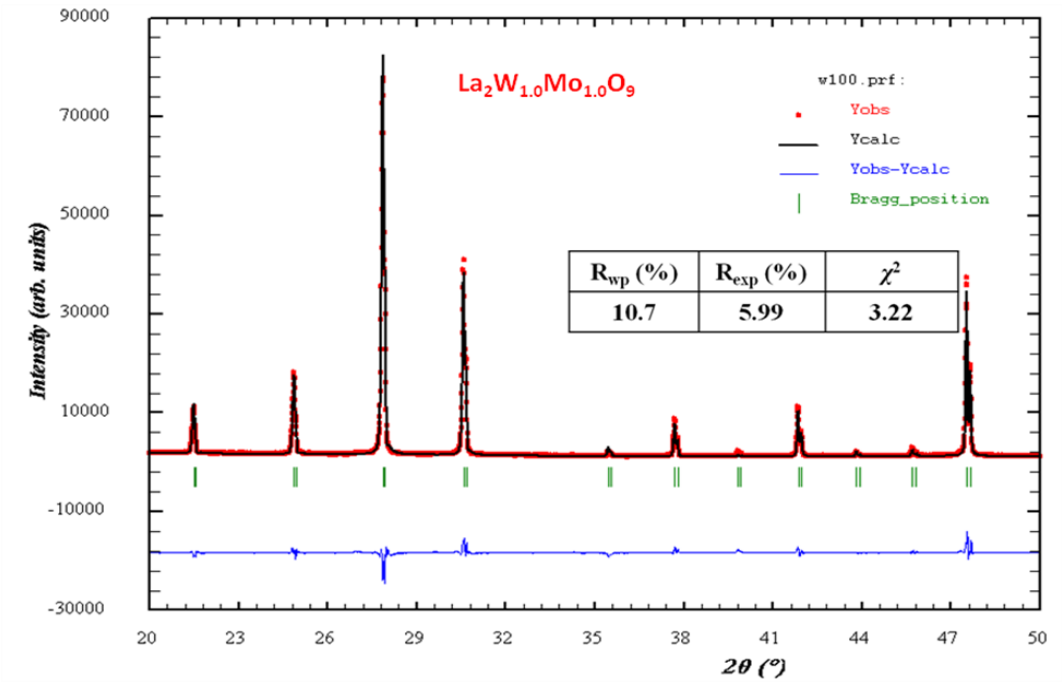

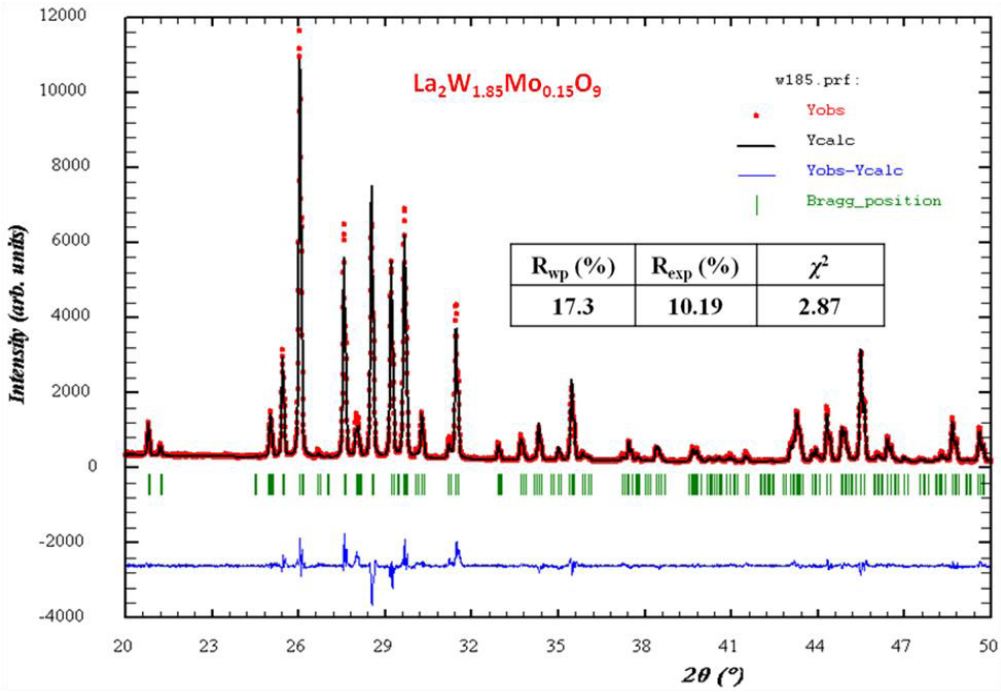

Figure 3.30. : Observed (red dots), calculated (black lines), and difference (blue, below) patterns of β–La_2WMoO_9 and α–$La_2W_{1.85}Mo_{0.15}O_9$ ***(RP-1200-RT)****. Vertical markers give Bragg peak positions of space group $P2_13$ or P-1, respectively. Reliability factors of the refinement were given in inset.*

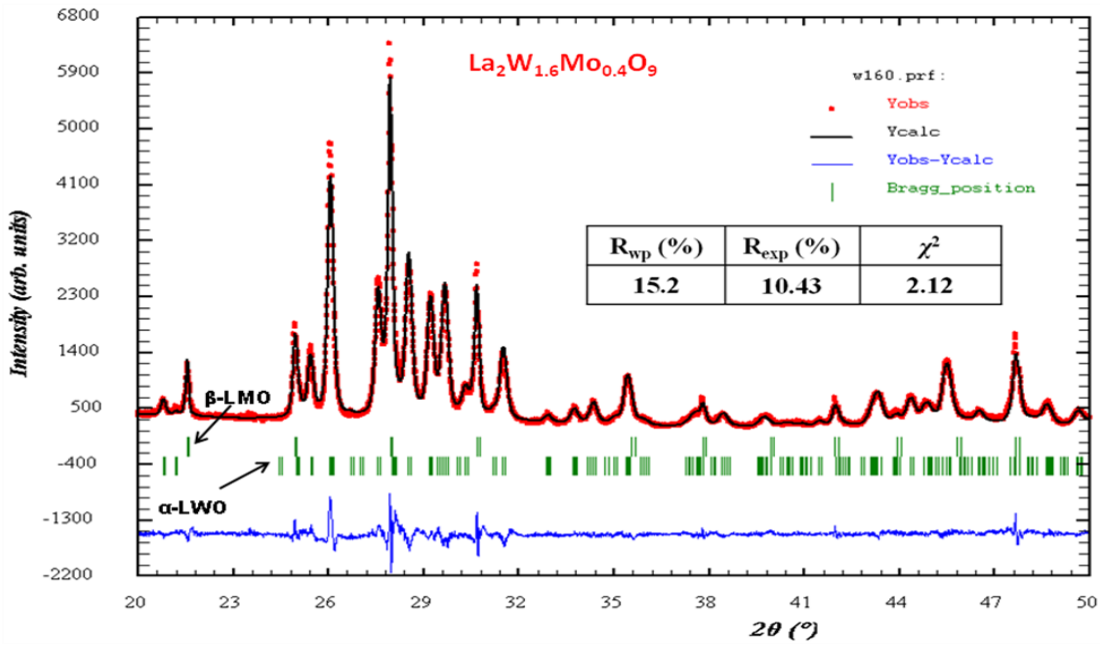

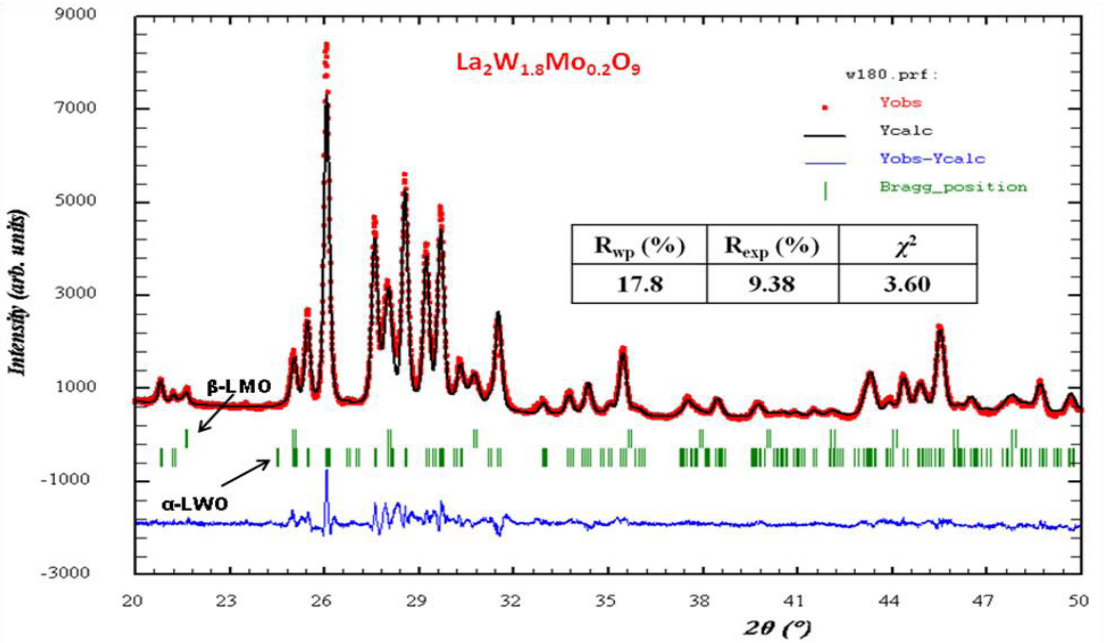

Fig 3.31. : Observed (dots), calculated (lines), and difference (below) patterns of bi-phasic $La_2W_{1.7}Mo_{0.3}O_9$ and $La_2W_{1.8}Mo_{0.2}O_9$ ***(RP-1200-RT)****. Vertical markers give Bragg peak positions of space group $P2_13$ (β–form) and P-1 (α–form), respectively. Reliability factors of the refinement were given in inset.*

As shown in Figure 3.32, the cubic unit cell volume of $La_2Mo_{2-y}W_yO_9$ samples decreases linearly (Volume (Å^3): V = 370.791 – 4.7572 (y), where y is the W content) as the tungsten content y increases from y =1 to 1.55. This evolution is in good agreement with previous studies reported by our group[20] and by Collado *et al.*[1]. Since W^{6+} ionic radius is slightly larger than that of hexavalent molybdenum, one would have expected the cell parameter to slightly increase upon W substitution. Previous thorough neutron diffraction study has revealed that this singular evolution is correlated with nonlinear changes in the O1 site cationic surrounding and with a variation in O2/O3 site occupation resulting in/from a decrease of the coordination number of tungsten ions [20]. For tungsten content higher than y = 1.85, all compositions crystallize in a triclinic α-LWO type structure. Surprisingly, no significant evolutions of the cell parameters are noticed as the tungsten amount increases (in Fig. 3.33).

In the compositional range $1.6 \leq y \leq 1.8$, all samples are bi-phasic in nature thus implying to carry out Rietveld refinements with both β-LMO and α-LWO structural models. The cubic unit cell parameter of β-LMO type phase still decreases between y = 1.6 and 1.7 following the previous linear dependence on y, determined for $1 \leq y \leq 1.55$ compositions (V = 370.791 – 4.7572 (y)). For the latter composition y =1.8, the cubic unit cell volume is much lower than that expected from the previous linear regression. In addition, the weight fraction of β-LMO type phase close to one third for y = 1.6 and 1.7 compositions decreases by a factor 2 for y =1.8. When compared in Fig.3.34 the diffraction patterns of these bi-phasic samples with those of mono-phasic specimens for either y<1.6 or y>1.8, one can note that diffraction lines of both phases are strongly broadened for compositions ranging from y = 1.6 to 1.8. In our series of samples, the difficulty to obtain satisfactory calculated patterns and then the low reliability factors for the Rietveld refinements, in particular for y = 1.8 composition, were ascribed to a non perfect simulation of the line broadening for both phases. In a previous study performed by Collado *et al.*[1], it has been suggested that the coexisting α-LWO and β-LMO type phases in the compositional range $1.3 \leq y \leq 1.7$ could have different fixed W/Mo ratios. However, one can interpret the line broadening (severe for y = 1.8, Figure 3.34) observed as a trace of the existence of a concentration gradient for both phases. This gradient, being probably dependent on the way the cooling to room temperature occurs, has a direct incidence on the stabilization or not of the β-LMO type phase and on its weight fraction within the sample.

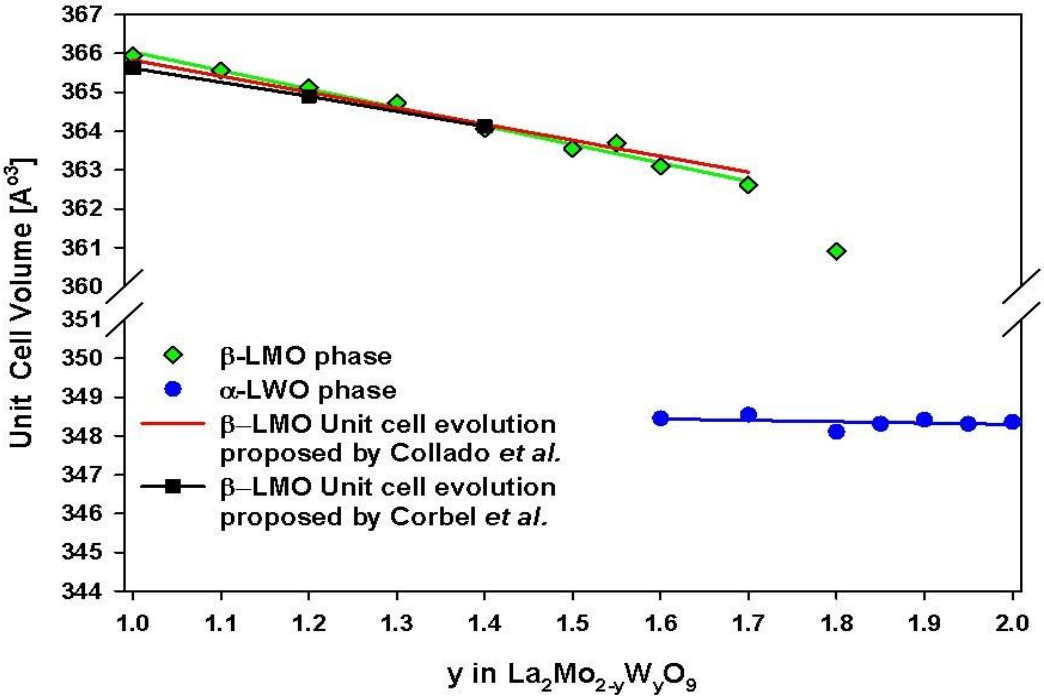

Figure. 3.32: Evolution of unit cell volume of compounds from W 1.0 to W 2.0 ***(RP-1200-RT)****. Unit cell volume of β-LMO is compared against the model proposed by Corbel et al.*[20] *and Collado et al.*[1]

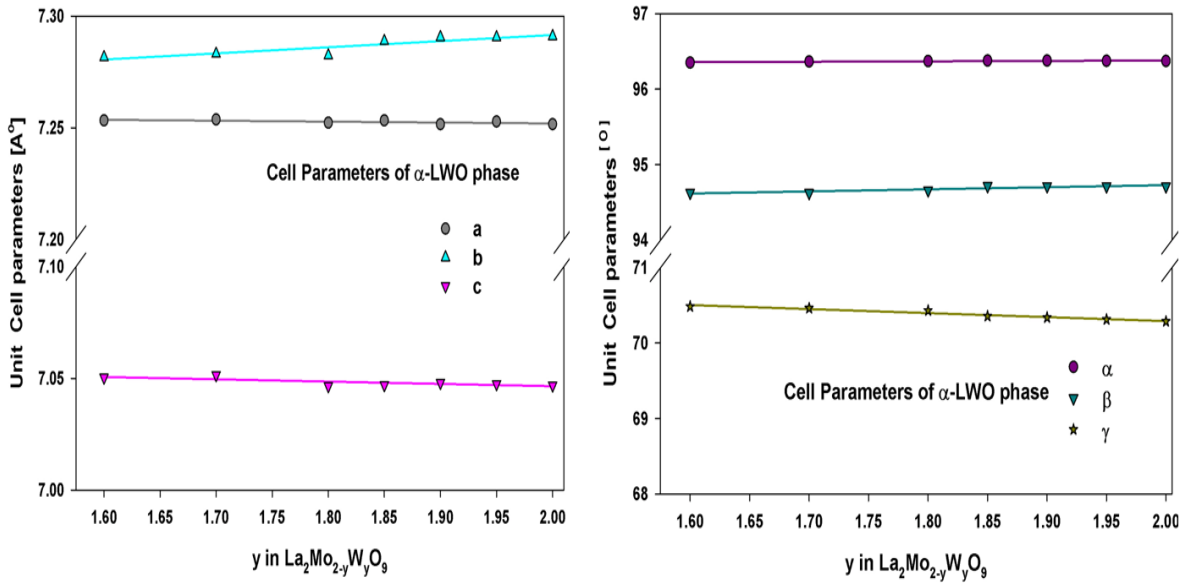

Fig. 3. 33: Evolution of triclinic unit cell parameters (a, b and c) (left) and (α, β and γ) (right) of compounds W1.6 to W2.0 compounds ***(RP-1200-RT)****.*

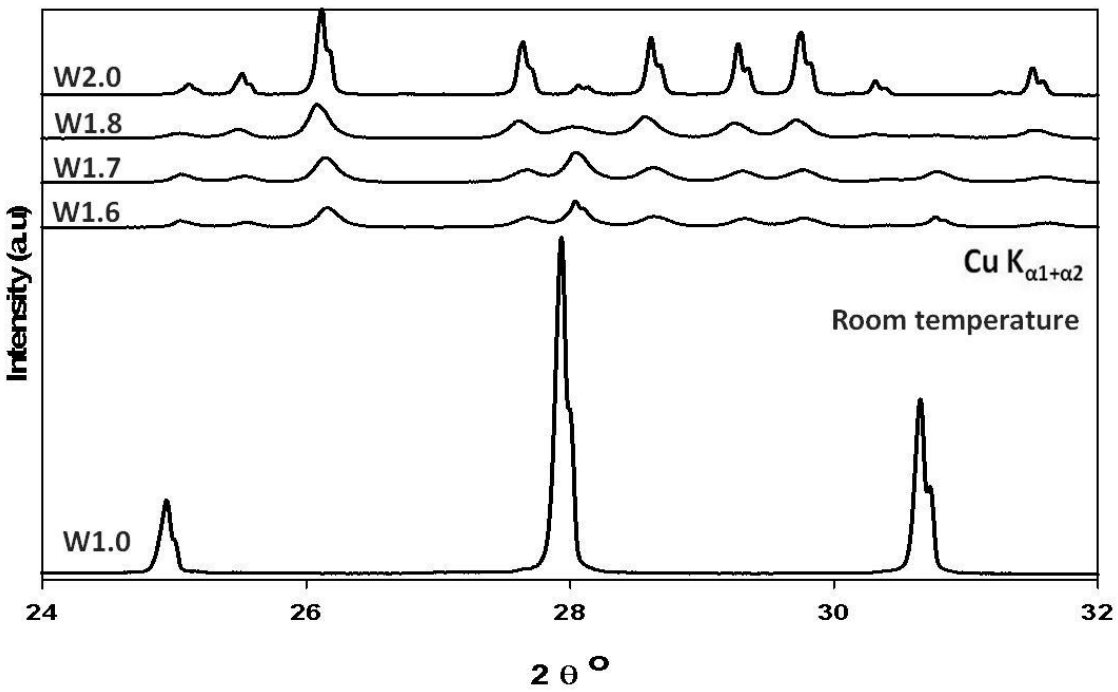

Figure 3.34: XRD patterns of W1.0, W1.6 – W1.85 and W2.0 oxides ***(RP-1200-RT)****. Notice the change in the peak width.*

3.7.2 Powders post-annealed above 700°C

When the raw powders of compositions ranging from y = 1.3 to 1.8 were post annealed at temperatures above 700°C, release of metastability of the β-form has been highlighted thanks to temperature-controlled X-ray diffraction. Two series of X-ray diffraction patterns were collected on these samples with the aim to determine the weight fraction of each phase when samples are in stable bi-phasic states ($1.3 \leq y \leq 1.5$). The first series was recorded at room temperature on raw powder post-annealed at 800 °C for 96 h and cooled down at 5°C/min, while the second data collection was carried out *in-situ* at 700 °C on the previous post-annealed powders. For both series of X-ray diffraction patterns, Rietveld refinements were performed. At first only the nominal content was used to calculate the occupation factors for Mo and W sites. Unit cell parameters and weight fractions are reported in tables 3.4 and 3.5. Observed, calculated, and difference diffraction patterns for all the samples are displayed in Figures 3.35 to 3.38. Besides y = 1.5 at room temperature, the cell parameters of β-LMO or α-LWO type phase follow the previous dependences on y of the cell parameters determined on raw powders as shown in Fig.

3.39. The evolution of unit cell parameters of these heat treated compounds at 700 °C is plotted in Fig. 3.40. In a previous study performed by Collado *et al.*[1], it has been suggested that the coexisting α-LWO and β-LMO type phases in the compositional range $1.3 \leq y \leq 1.7$ could have different fixed W/Mo ratios.

(y) in $La_2W_yMo_{2-y}O_9$	Phase	Cell Parameters						Single Cell Volume V [Å]³	Wt. Fraction of phases (%)
		a [Å]	b [Å]	c [Å]	α °	β°	γ°		
1.3	β-LMO	7.1457(1)	7.1457(1)	7.1457(1)	90	90	90	364.870(5)	88.5(3)
	α-LWO	7.2492(4)	7.2808(3)	7.0448(3)	96.384(5)	94.681(4)	70.512(4)	347.96(3)	11.5(1)
1.4	β-LMO	7.1432(1)	7.1432(1)	7.1432(1)	90	90	90	364.488(6)	78.1(2)
	α-LWO	7.2403(2)	7.2856(2)	7.0460(2)	96. 385(2)	94.692(1)	70.483(2)	347.75(1)	21.9(1)
1.5	β-LMO	7.1598(3)	7.1598(3)	7.1598(3)	90	90	90	367.04(2)	11.0(1)
	α-LWO	7.2514(1)	7.2797(1)	7.0456(1)	96.3833(7)	94.7257(7)	70.4995(6)	348.01(1)	89.0(2)
16	α-LWO	7.2511(1)	7.2819(1)	7.0475(1)	96.3814(8)	94.7161(7)	70.4721(7)	348.14(1)	-
1.7	α-LWO	7.2498(1)	7.2850(1)	7.0485(1)	96.3782(9)	94.7105(8)	70.4287(8)	348.19(1)	-
1.8	α-LWO	7.2472(1)	7.2884(1)	7.0494(1)	96.3811(9)	94.6971(8)	70.3919(8)	348.19 (1)	-

Table 3.4: Unit cell parameters of phases present in y = 1.3 – 1.8 oxides ***(HT-800-RT)****.*

(y) in $La_2W_yMo_{2-y}O_9$	Phase	Cell Parameters						Single Cell Volume V [Å]³	Wt. Fraction of phases (%)
		a [Å]	b [Å]	c [Å]	α °	β°	γ°		
1.3	β-LMO	7.2447(1)	7.2447(1)	7.2447(1)	90	90	90	380.252(6)	85.6(4)
	α-LWO	7.2789(3)	7.3445(3)	7.1155(3)	96.387(4)	94.750(4)	70.607(4)	356.16(3)	14.4(3)
1.4	β-LMO	7.2428(1)	7.2428(1)	7.2428(1)	90	90	90	379.951(7)	74.7(3)
	α-LWO	7.2725(2)	7.3460(2)	7.1151(2)	96.371(2)	94.731(2)	70.609(2)	355.92(2)	25.3(3)
1.5	β-LMO	7.2522(2)	7.2522(2)	7.2522(2)	90	90	90	381.42(2)	8.7(1)
	α-LWO	7.2825(1)	7.3458(1)	7.1175(1)	96.3658(9)	94.7566(8)	70.6211(7)	356.54(1)	91.3(9)
16	α-LWO	7.2784(1)	7.3435(1)	7.1139(1)	96.3638(8)	94.7447(7)	70.6031(7)	356.01(1)	-
1.7	α-LWO	7.2774(1)	7.3455(2)	7.1140(2)	96.365(1)	94.7437(9)	70.5683(8)	355.99(1)	-
1.8	α-LWO	7.2751(2)	7.3489(2)	7.1152(2)	96.373(1)	94.7356(9)	70.5405(9)	356.04(2)	-

Table 3.5: Unit cell parameters of phases present in y = 1.3 – 1.8 oxides specimens at 700 °C ***(HT-800-700)****.*

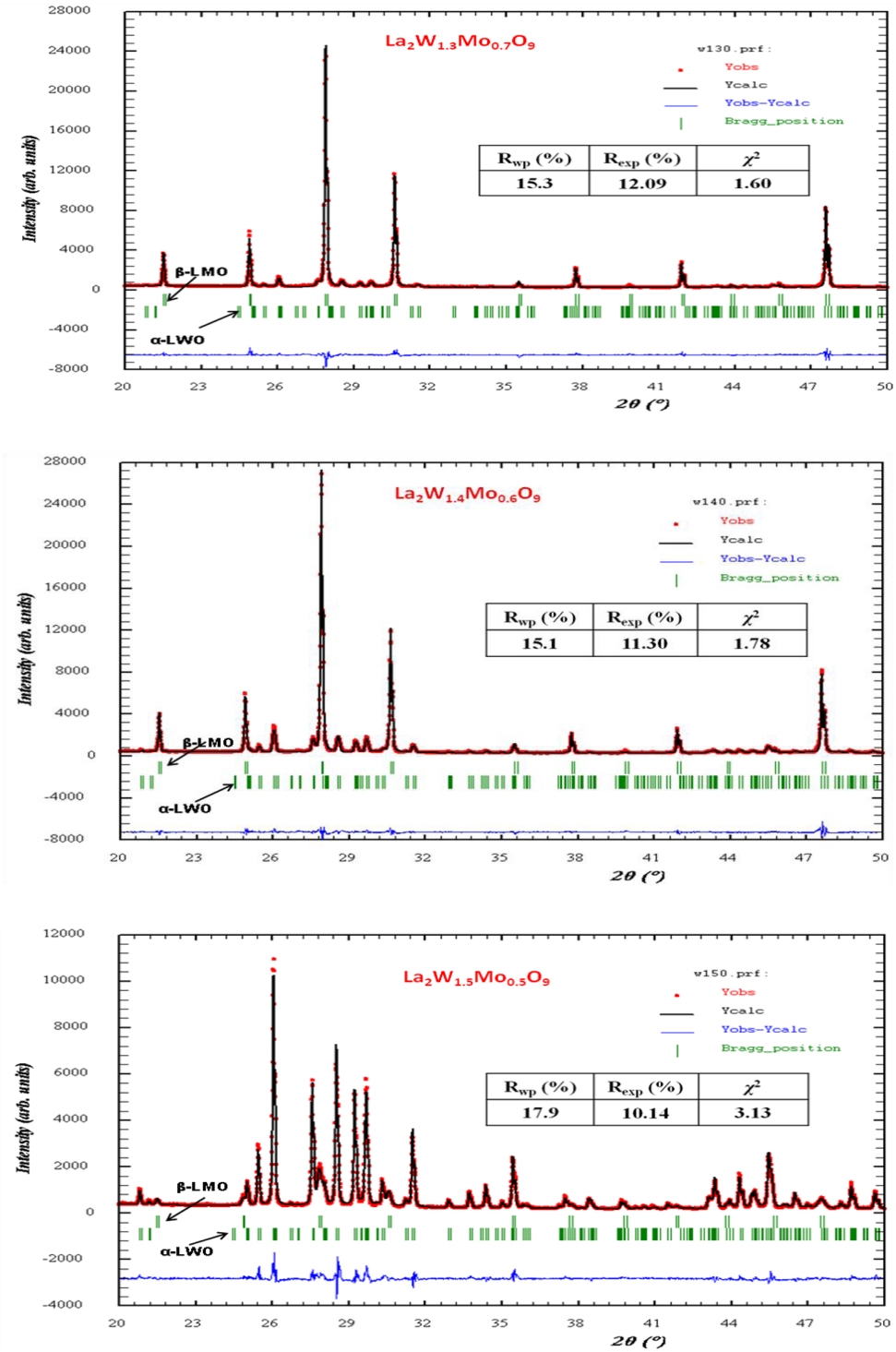

Figure 3.35: Observed (dots), calculated (lines), and difference (below) patterns at room temperature of $La_2W_yMo_{2-y}O_9$ (y=1.3-1.5) ***(HT-800-RT).*** *Vertical markers give Bragg peak positions of space group P-1 (α–form). Reliability factors of the refinement were given in inset.*

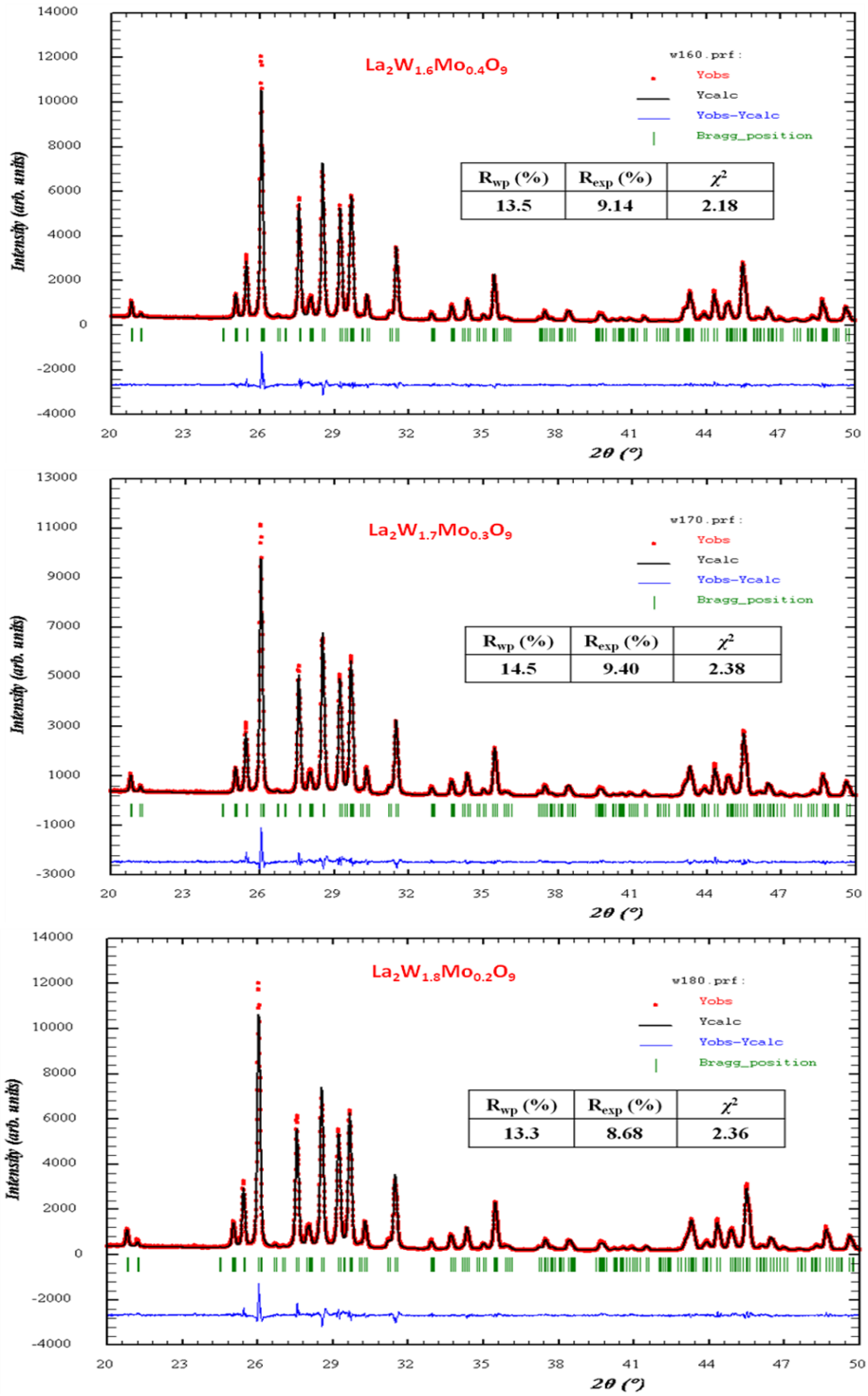

Figure 3.36: Observed (dots), calculated (lines), and difference (below) patterns at room temperature of $La_2W_yMo_{2-y}O_9$ (y=1.6-1.8) ***(HT-800-RT)****. Vertical markers give Bragg peak positions of space group $P2_13$ (β–form) and P-1 (α–form), respectively. Reliability factors of the refinement were given in inset.*

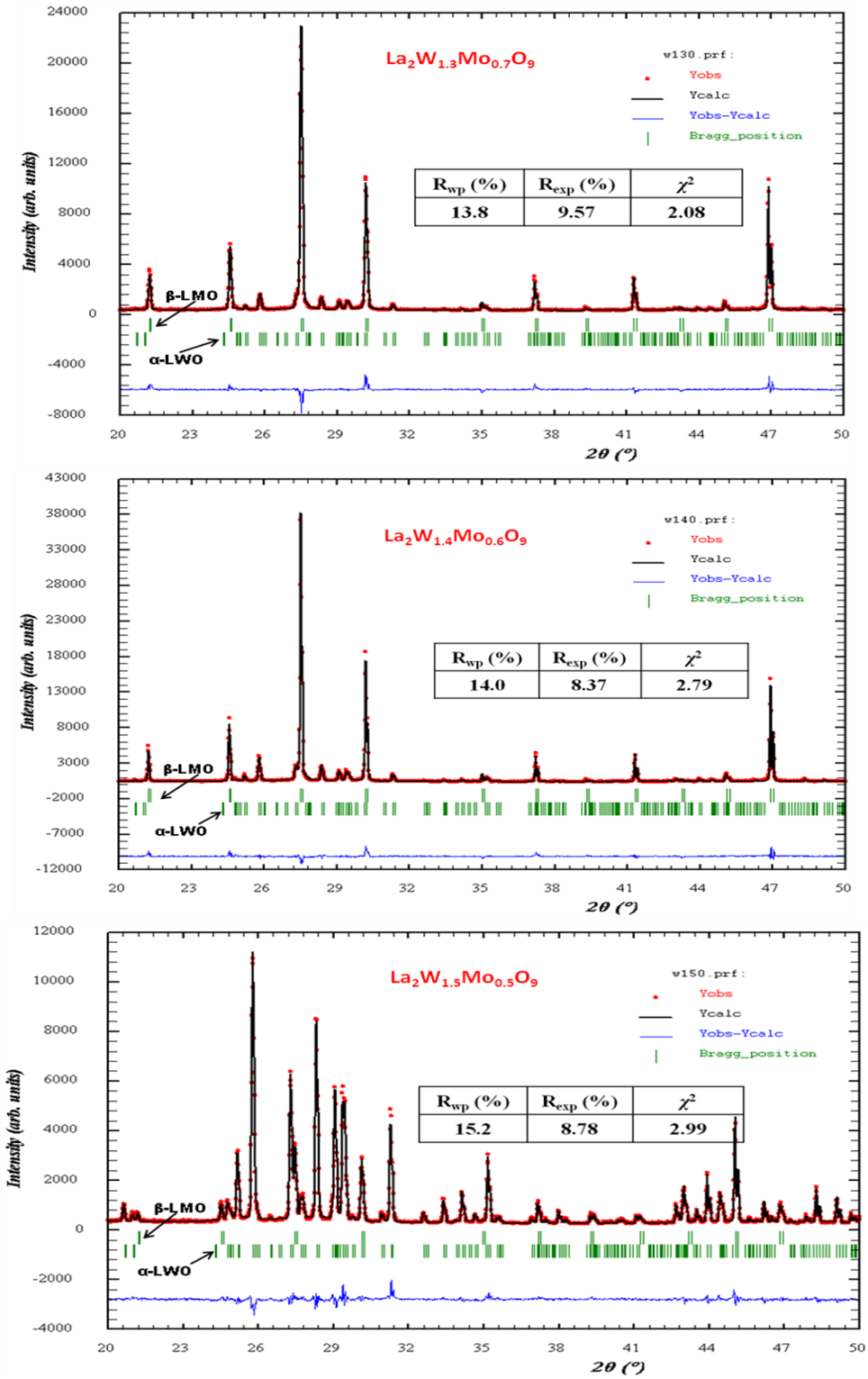

Figure 3.37: Observed (dots), calculated (lines), and difference (below) patterns collected at 700°C on $La_2W_yMo_{2-y}O_9$ (y=1.3-1.5) samples ***(HT-800-700)****. Vertical markers give Bragg peak positions of space group $P2_13$ (β–form) and P-1 (α–form), respectively. Reliability factors of the refinement were given in inset.*

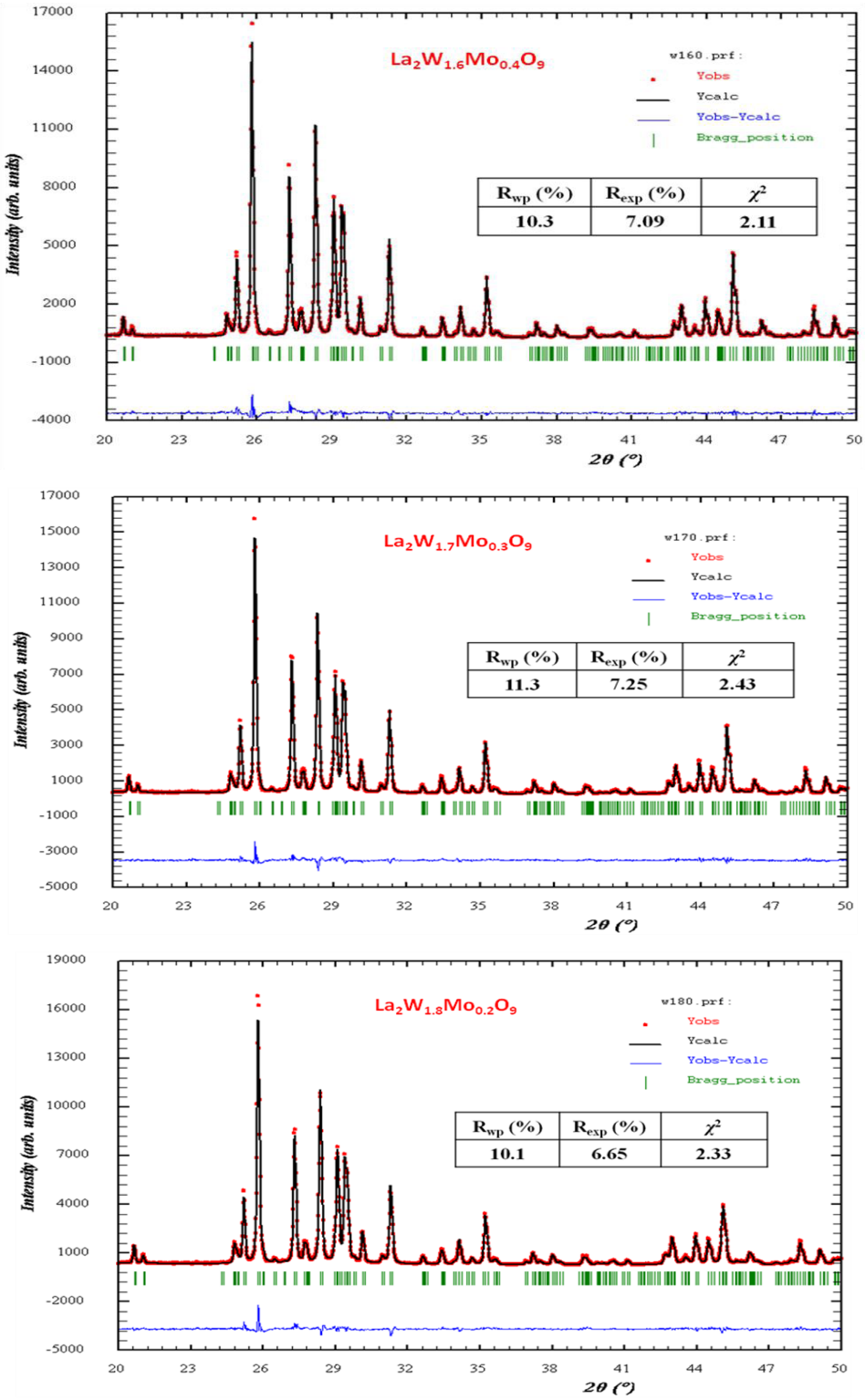

Figure 3.38: Observed (dots), calculated (lines), and difference (below) patterns collected on $La_2W_yMo_{2-y}O_9$ (y=1.6-1.8) samples ***(HT-800-700).*** *Vertical markers give Bragg peak positions of space group P-1 (α–form). Reliability factors of the refinement were given in inset.*

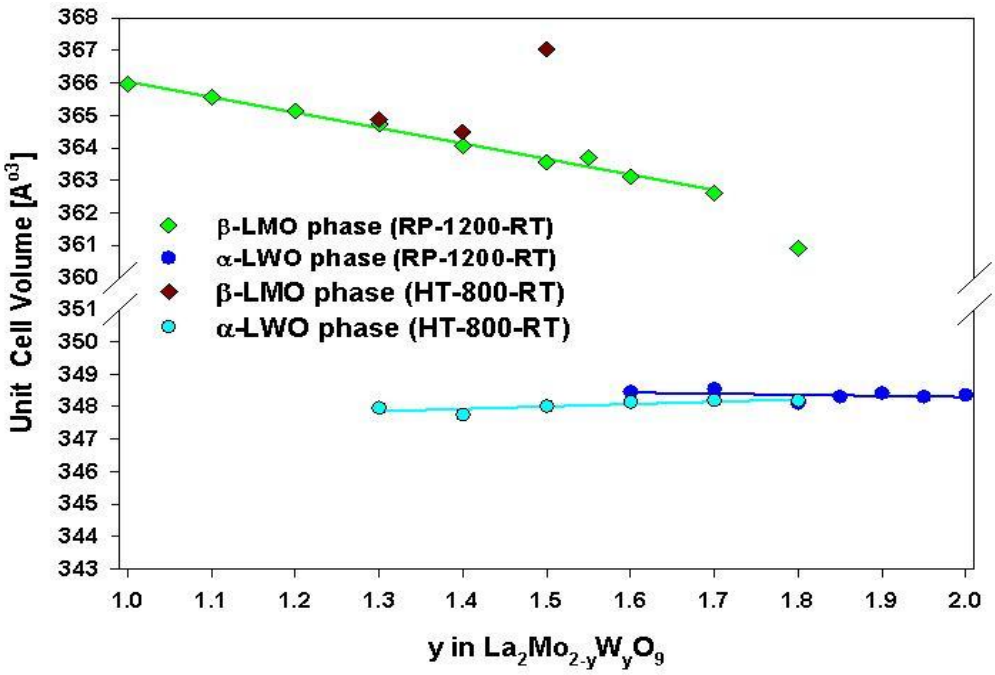

Figure. 3.39: Comparison of unit cell volume evolution of β-LMO and α-LWO phases of y = 1.0 to 2.0 compounds. Note that comparison is carried between heat treated samples ***HT-800-RT*** *and raw powders* ***RP-1200-RT****.*

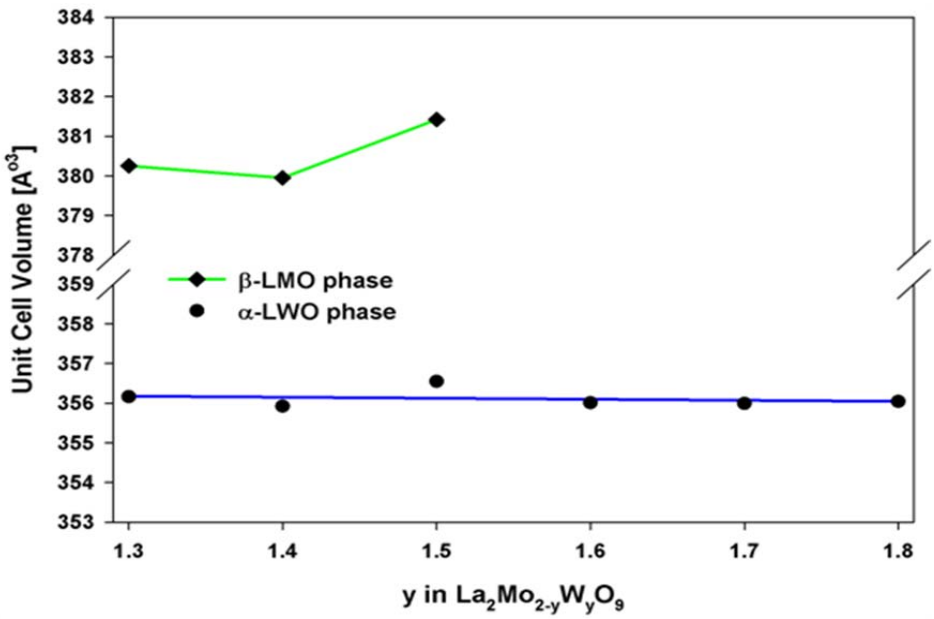

Fig. 3.40: Evolution of unit cell volume in W1.3-W1.8 compounds at 700 ^oC ***(HT-800-700)****.*

This possibility has been then tested for $1.3 \leq y \leq 1.5$ compositions by fixing the whole Mo content to the nominal content of the composition and by refining the occupation factors of Mo and W site with the following constrain: in order to balance for the enrichment in molybdenum of one phase, the second phase is depleted in molybdenum with the same magnitude. Results reported in Table 3.6, show the enrichment in tungsten of the β-LMO type phase for y = 1.3-1.4 compositions and a depletion for y = 1.5. In comparison with the cubic unit cell parameter that a single β-LMO type phase with the equivalent tungsten content would have, the cubic unit cell parameter of the β-LMO type phase determined is either very similar to that observed in Table 3.3 for mono-phasic raw powders (y = 1.3-1.4) or higher (y = 1.5) which is not consistent with the magnitude of the enrichment or of a depletion in tungsten of the phase (the higher the tungsten content the lower its cubic unit cell parameter). Sum of W and Mo SOF of β-LMO phase after the refinement do not correspond to their actual stoichiometry.

Composition	*Phase*	Cubic *Unit cell parameter*	*Atoms*	*Nominal SOF*	*Refined SOF*
W1.3	β-LMO	7.1457(1)	W	0.650	0.783(3)
			Mo	0.350	0.216(3)
	α-LWO		W1/W2	0.650	0.605(3)
			Mo1/ Mo2	0.350	0.395(3)
W1.4	β-LMO	7.1432(1)	W	0.700	0.735(2)
			Mo	0.300	0.267(2)
	α-LWO		W1/W2	0.700	0.689(2)
			Mo1/ Mo2	0.300	0.311(2)
W1.5	β-LMO	7.1598(3)	W	0.750	0.5762)
			Mo	0.250	0.426(2)
	α-LWO		W1/W2	0.750	0.808(2)
			Mo1/ Mo2	0.250	0.192(2)

Table 3.6: Change in the SOF of W1.3-W1.5 compounds ***(HT-800-RT)*** *after refinement. No change in the β-LMO phase unit cell parameter 'a' was observed before and after refinement of SOF.*

It must be noted that in their thermodynamic equilibrium state at room temperature (reached after long annealing), the compositions in the range $1.3 \leq y \leq 1.5$ are located in a border region of the phase diagram between two mono-phasic domains: a single β-LMO phase domain for $y \leq 1.2$ and a single α-LWO phase domain for $y \geq 1.6$. At room temperature, each composition located in this border region must consist in a mixture of β-LMO and α-LWO type phases having a tungsten content corresponding to compositions delineating this bi-phasic domain: between $y \approx 1.2$-1.3 for the β-LMO type phase and between $y \approx 1.575$-1.6 for the α-LWO type phase (let say β-$La_2Mo_{0.75}W_{1.25}O_9$ and α-$La_2Mo_{0.4125}W_{1.5875}O_9$). Theoretically, the molar fraction of each constituent phase of a bi-phasic domain in a phase diagram can be determined by applying the Lever Rule [21].

By considering the reverse situation, the tungsten content of the end members of this bi-phasic domain could be determined from the weight fractions in β-$La_2Mo_{0.75}W_{1.25}O_9$ and α-$La_2Mo_{0.4125}W_{1.5875}O_9$ phases obtained from the Rietveld refinement of X-ray diffraction data of $1.3 \leq y \leq 1.5$ compositions. In Figure 3.41, the amount of the β-LMO type phase within the sample decreases as the tungsten increases with a strong evolution above y =1.4. The Lever rule was then applied to each couple of compositions (y = 1.3+y = 1.4, y = 1.3+y = 1.5 and y = 1.4+y = 1.5). For each couple considered, the tungsten contents of the end members have been determined and tabulated in Table 3.7. Unfortunately, the tungsten contents are either not realistic (couple y = 1.3 + y = 1.4) or lower than the tungsten content of known bi-phasic samples (couples y = 1.3 + y = 1.5 and y = 1.4 + y = 1.5). Rietveld refined XRD patterns are given in Annex.II at the end of the thesis.

Suspecting that the tungsten content of each phase could be affected by cooling, and in a sense that it would have induced a concentration gradient, the above method for determining the limit of the bi-phasic domain was applied to weight fractions obtained from the Rietveld refinement performed on X-ray diffraction data collected in-situ at 700°C. Weight fractions and the tungsten contents of the end members are reported together in Table 3.7. Once again, the method remains non appropriate to determine these limits.

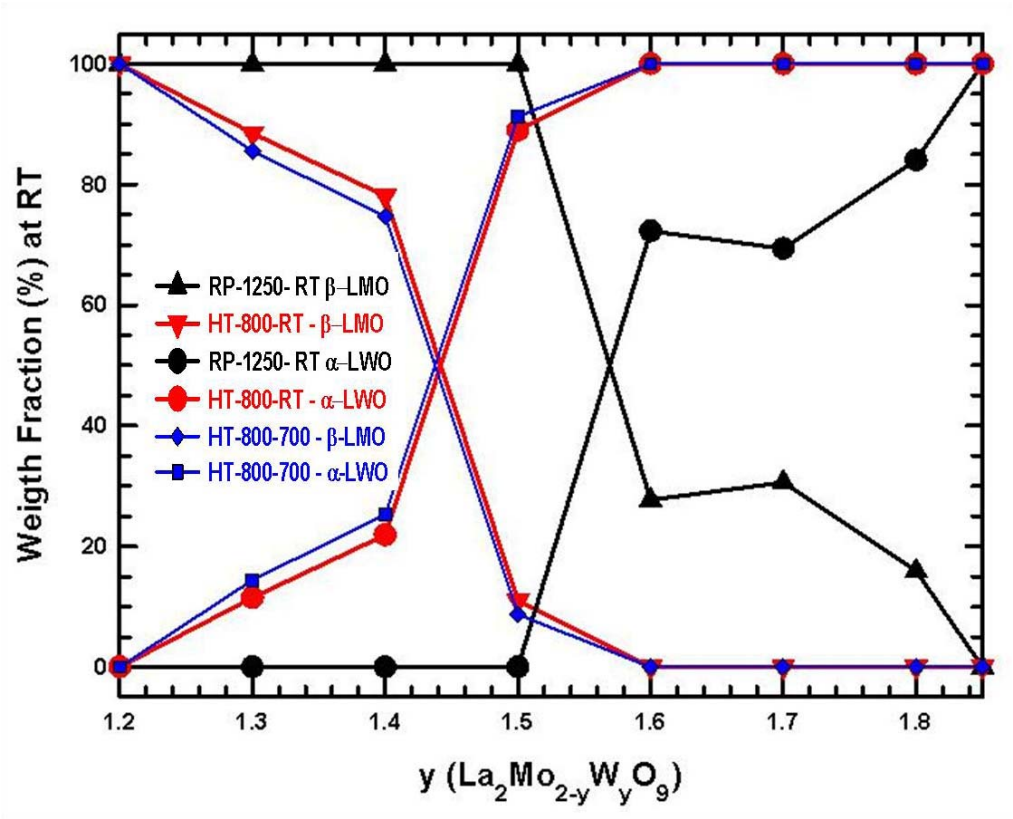

*Figure 3.41: Evolution of weight fractions of β-$La_2Mo_2O_9$ and α-$La_2W_2O_9$ type phases in raw powders **(RP-1250-RT)** and heat treated $La_2W_yMo_{2-y}O_9$ (y=1.2-1.85) powders at room temperature **(HT-800-RT)** and at 700 °C **(HT-800-700)**.*

Couple	*Limits of Bi-phasic domain at R.T*		*Limits of Bi-phasic domain at 700 °C*	
	β-LMO	*α-LWO*	*β-LMO*	*α-LWO*
W1.3 + W1.4	W1.29	W1.79	W1.171	W2.10
W1.4 + W1.5	W1.368	W1.517	W1.381	W1.513
W1.3 + W1.5	W1.29	W1.527	W1.267	W1.514

*Table 3.7: Boundary limits of bi-phasic domain calculated on heat treated W1.3-1.5 samples at R.T **(HT-800-RT)** and at 700 °C **(HT-800-700)** using the (inverse) Lever Rule.*

3.8 Conclusions

$La_2Mo_{2-y}W_yO_9$ (y = 1.0 to 2.0) oxides were synthesized by conventional solid state synthesis route. Oxides with y = 1.0, 1.1 and 1.2 were always obtained in high conducting cubic β-LMO phase. Heat treatment performed on these samples for 60 days at 700 ^oC, did not show any change in the crystal structure, suggesting β-LMO is a thermodynamic stable state for these three compounds.

Compounds from y = 1.3 to 1.575 were β-LMO phase after synthesis using a cooling rate of 5 ^oC/min, however TC-XRD and DTA has shown multiple phase transitions where triclinic α-LWO phase appears at intermediate temperatures and disappears when heated at elevated temperatures. Short annealing performed on these (y = 1.3 to 1.575) samples (800 ^oC for 96 hours) shows that the bi-phasic domain (β-LMO + α-LWO) is the stable state for these compounds at room temperature. However the limits of biphasic domain are suspected as: between W1.2←→W1.3 for β-LMO phase and between W1.575←→W1.6 for α-LWO phase. Application of (inverse) Lever rule to precise such boundary limits was delicate. This could be because of inhomogeneous W/Mo distribution within the sample (also supported by literature). TEC of W1.3 was calculated from linear regressions of two thermal domains as 15.6 x 10^{-6} $^oC^{-1}$ and 22.3 x 10^{-6} $^oC^{-1}$ in the temperature range 25 - 350 ^oC and 350 - 900 ^oC respectively.

Oxides with y = 1.6 to 1.8 were bi-phasic (β-LMO + α-LWO) when synthesized and cooling rate of 5 ^oC/min, however these compounds were in pure β-LMO form when quenched from elevated temperatures into a mixture of water and ice (from ~1250 ^oC). TC-XRD and DTA exhibit multiple phase transitions in these samples and it was observed that rate of cooling has an impact over the final phase purity of these compounds. Short term annealing (800 ^oC for 96 hours) on these samples has shown that α-LWO is a stable state for these compounds at room temperature.

For compounds from y = 1.85 to 2.0, α-LWO was thermodynamic stable state at room temperature and β-LMO phase was the stable state at elevated temperatures (above ~ 1050 ^oC). These compounds (y = 1.85 to 2.0) were always obtained in α-LWO form, irrespective of rate of cooling or quenching.

Overall it was observed that oxides from $1.0 \leq y \leq 1.2$ are in β-LMO form, and $\sim 1.3 \leq y \leq 1.8$ were metastable (bi-phasic: β-LMO + α-LWO) and $1.85 \leq y \leq 2.0$ were α-LWO phase. Considering the speculations on the boundary limits of bi-phasic domain, and all the DTA, XRD and TC-XRD results, a new phase diagram for $La_2Mo_{2-y}W_yO_9$ (y = 1.0 to 2.0) oxides is proposed (see Fig. 3.42). Inhomogeneous distribution of W is suspected in biphasic samples. It was clear that compounds above 60 mol% of W substitution (1.2<y) are not suitable for SOFC applications. It was shown that NiO does not react with $La_2Mo_{2-y}W_yO_9$ compounds, contrary to what has been claimed in the literature.

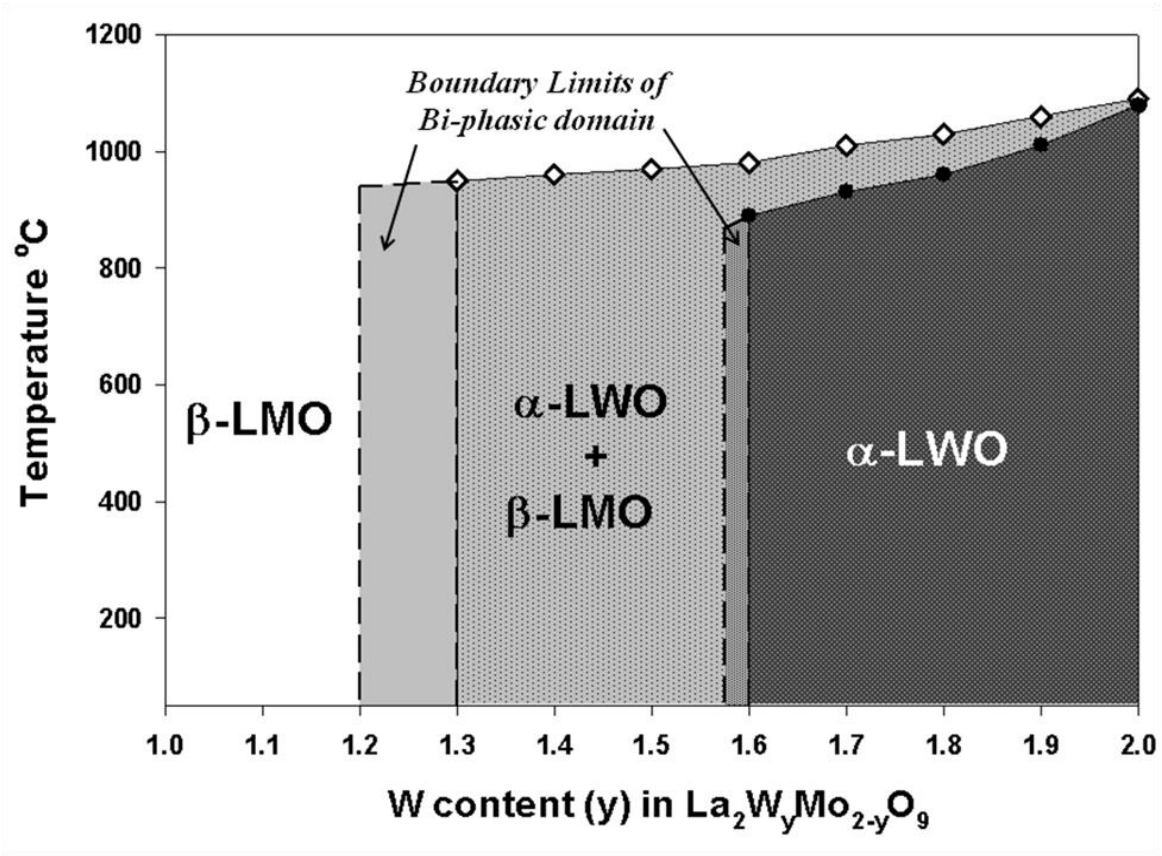

Figure 3.42: Proposed phase diagram for $La_2W_yMo_{2-y}O_9$ (y =1.0 - 2.0) oxides. Note that the boundary limits of biphasic domain are assumed to be between W1.2-W1.3 for β-LMO phase and between W1.575 –W1.6 for α-LWO phase.

3.9 References

1. J. A. Collado; M. A. G. Aranda; A. Cabeza; P. Olivera-Pastor; S. Bruque, *Journal of Solid State Chemistry* **2002,** 167, (1), 80-85.
2. G. Corbel; Y. Laligant; F. Goutenoire; E. Suard; P. Lacorre, *Chemistry of Materials* **2005,** 17, (21), 5390-5390.
3. S. Georges; F. Goutenoire; P. Lacorre; M. C. Steil, *Journal of the European Ceramic Society* **2005,** 25, (16), 3619-3627.
4. S. Georges; F. Goutenoire; Y. Laligant; P. Lacorre, *Journal of Materials Chemistry* **2003,** 13, (9), 2317-2321.
5. T.-Y. Jin; M. V. Madhava Rao; C.-L. Cheng; D.-S. Tsai; M.-H. Hung, *Solid State Ionics* **2007,** 178, (5-6), 367-374.
6. Y. Laligant; A. Le Bail; F. Goutenoire, *Journal of Solid State Chemistry* **2001,** 159, (1), 223-227.
7. D. Li; X. P. Wang; Z. Zhuang; J. X. Wang; C. Li; Q. F. Fang, *Materials Research Bulletin* **2009,** 44, (2), 446-450.
8. D. Marrero-Lopez; J. Canales-Vazquez; J. C. Ruiz-Morales; J. T. S. Irvine; P. Nunez, *Electrochimica Acta* **2005,** 50, (22), 4385-4395.
9. D. Marrero-Lopez; J. Pena-Martinez; J. C. Ruiz-Morales; D. Perez-Coll; M. C. Martin-Sedeno; P. Nunez, *Solid State Ionics* **2007,** 178, (23-24), 1366-1378.
10. P. Pinet; J. Fouletier; S. Georges, *Materials Research Bulletin* **2007,** 42, (5), 935-942.
11. W. Thepsuwan; S. Kuharuangrong, *Functionalized and Sensing Materials* **2010,** 93-94, 509-512.
12. J. H. Yang; Z. H. Gu; Z. Y. Wen; D. S. Yan, *Solid State Ionics* **2005,** 176, (5-6), 523-530.
13. Z. Zhuang; X. P. Wang; D. Li; T. Zhang; Q. F. Fang, *Journal of the American Ceramic Society* **2009,** 92, (4), 839-844.
14. G. Corbel; E. Chevereau; S. Kodjikian; P. Lacorre, *Inorganic Chemistry* **2007,** 46, 6395-6404.
15. A. Selmi; C. Galven; G. Corbel; P. Lacorre, *Dalton Trans* **2010**, (1), 93-102.
16. G. Corbel; E. Suard; P. Lacorre, *Chemistry of Materials* **2011,** 23, (5), 1288-1298.
17. G. Corbel, in: 2009.
18. G. Corbel; P. Lacorre, *Journal of Solid State Chemistry* **2006,** 179, (5), 1339-1344.
19. C. Tealdi; G. Chiodelli; G. Flor; S. Leonardi, *Solid State Ionics* **2010,** 181, (31-32), 1456-1461.
20. G. Corbel; Y. Laligant; F. Goutenoire; E. Suard; P. Lacorre, *Chemistry of Materials* **2005,** 17, (18), 4678-4684.
21. P. M. Chaikin; T. C. Lubensky, *Principles of Condensed Matter Physics*. Cambridge University Press: 1995.

Chapter 4: Cationic diffusion studies in $La_2Mo_2O_9$

4.1: Introduction 119

4.2: Experimental Setup: 120

4.3 Results & Discussions: 122

4.3.1 Surface reactions on the solution deposited $La_2Mo_2O_9$ and $La_{0.8}Sr_{0.2}MnO_{3-\delta}$ pellets: ... 122

4.3.1. 1) $La_2Mo_2O_9$ with 5 mg/cm^2 of $MnCl_2 \cdot 4H_2O$ solution deposition: 122

4.3.1.2: $La_2Mo_2O_9$ with 5 mg/cm^2 of $Sr(NO_3)_2$ solution deposition: 128

4.3.1.3: $La_{0.8}Sr_{0.2}MnO_{3-\delta}$ with 5 mg/cm^2 of $(NH_4)_6Mo_7O_{24}.4H_2O$ deposited solution: 138

4. 3.2: Cationic diffusion measurements on $La_2Mo_2O_9$ / $La_{0.8}Sr_{0.2}MnO_{3-\delta}$ pellet couples 146

4.3.2.1: XRD analysis and FIB-SIMS surface analysis on $La_2Mo_2O_9$ pellets: *146*

4.3.2.2: XRD analysis and FIB-SIMS surface analysis on $La_{0.8}Sr_{0.2}MnO_3$ pellets: *150*

4.3.2.3: FIB-SIMS depth profile analysis on $La_2Mo_2O_9$ / $La_{0.8}Sr_{0.2}MnO_3$ couples: *151*

4.3.2.4: Discussions 154

4.4: Conclusions 160

4.5: References 165

Chapter 4:
Cationic Diffusion Studies in $La_2Mo_2O_9$

4.1: Introduction

Chemical inertness between the electrolyte material and its electrode counterparts is a vital parameter for fuel cells. If reaction takes place between materials, the appearance of undesired reaction products at the interface affects the performance of the cell (i.e. decreases the overall cell potential or even puts the operation of total cell at risk). Chemical compatibility of $La_2Mo_2O_9$ (LMO) was tested against many well known and industrially accepted electrode materials. NiO anode material was found to be totally inert towards LMO and LMO derived materials, thus making Ni-LMO cermets possible anode materials [1-3]. Coming to chemical stability towards cathodes, LMO was found to be reactive with current industrially accepted materials. Chemical instability of LMO with several cathode materials, their reaction temperatures and reaction products were overviewed in chapter 1 in section 2.5. Apart from knowing the reaction products, it is important to understand the reaction mechanism and the diffusion phenomena governing it. For this, phase diffusivity of each element from one compound to the other has to be studied. The next stage would then be to find an appropriate barrier to overcome elemental diffusion.

Out of many compounds tested in mixture with LMO, $La_{0.8}Sr_{0.2}MnO_{3-\delta}$ (LSM) was found to be the least reactive compound and remaining stable in mixture with LMO below 700 ^{o}C, making it a suitable candidate for study [4]. It was found that LMO reacts with LSM and forms insulating $SrMoO_4$ phase at temperatures above 700 ^{o}C. These studies were performed on powder samples, which is not the case for SOFC applications. Here we induced reactivity between LMO with LSM pellets and attempts were made to study the cationic diffusion of elements from LMO to LSM and vice versa. We probed cationic diffusion in LMO and LSM, and investigated cross cationic diffusion between these two materials after pellets of such compositions were annealed in close contact by coupling the polished surfaces. Diffusion studies were also carried out by depositing desired cationic rich solutions on the surface of polished LMO or LSM pellets. Cationic diffusion studies were performed by SIMS measurements and XRD analysis. Similar experiments reported by other authors on zirconias, with electrode and

electrolyte materials, were discussed in chapter 1 in section 1.3.3. A brief introduction to SIMS measurements and experimentation methodology was given in chapter 2.

4.2: Experimental Setup:

High density pellets (> 95%) of LMO and LSM were prepared by pressing and sintering powders of such compositions, which were synthesized by conventional solid state synthesis process. These highly dense pellets were polished mechanically using 0.1 μm diamond particle sprays. XRD measurements were performed to confirm their phase purity at every stage (stages include: after synthesis of powders, synthesis of pellets and after polishing the pellets). Once polished pellets were ready, cationic diffusion measurements were carried out. For cationic diffusion experiments two different sample setups were used (see Fig. 4.1). First setup involves coupling pellets of LMO and LSM together. Second setup involves deposition of cationic rich solutions on LMO and LSM pellets.

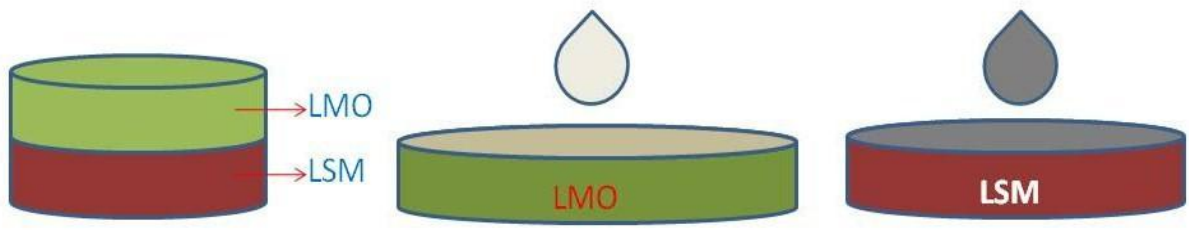

Figure 4.1: Schematic representation of cationic diffusion experiments on LSM and LMO pellets. Coupled experimental setup (left); Solution deposited experiment setup on LMO pellet with solutions of $Sr(NO_3)_2$ and $MnCl_2.4H_2O$ (two different solutions on two different LMO pellets) (middle); similar setup on LSM pellet with $(NH_4)_6Mo_7O_{24}\cdot 4H_2O$ solution (right)

In the first experimental setup, pellets of LMO and LSM were coupled together with polished surfaces facing each other. Three different measurements were performed by annealing three different couples under different conditions (different temperatures and time). The three measurement conditions were: 1) 1150 ^oC for 12 hours, 2) 1050 ^oC for 36 hours and 3) 1050 ^oC for 12 hours. These conditions were chosen to study the changes in diffusive behavior as a

function of temperature and time. All the couples went through rapid cooling after the annealing to avoid possible back diffusion or further reactions. The furnace was turned off and the door was opened.

A complex reaction process and cross cationic diffusion of all cationic species was observed in measurements involving couples of LMO/LSM pellets. Corbel *et al.* also reported a complex reaction with $SrMoO_4$ as a reaction product when powders of LMO and LSM were annealed together at elevated temperatures [4]. To clarify such complex mechanism, a second experimental setup was introduced. In this setup, solutions of $Sr(NO_3)_2$ and $MnCl_2{\cdot}4H_2O$ were deposited on polished surfaces of two different LMO pellets. These measurements were performed to study the diffusive behaviour of the individual cation Sr/ Mn in LMO. Mo rich solution $(NH_4)_6Mo_7O_{24}{\cdot}4H_2O$, was deposited on polished surface of LSM pellet to study Mo diffusion in LSM. Horita *et al.*, performed similar cation diffusion studies using SIMS techniques on solution deposited samples (where $Sr(NO_3)_2$ solution with 0.05 M amount was deposited on $La_{1-x}Ca_xCrO_3$ pellet and Sr content on such pellet was observed as 2 $mg.cm^{-2}$) [5]. In our case, all the solutions (Mn, Sr and Mo) were 0.5 M, and care was taken that amount of desired cation (Sr or Mn or Mo) is limited to 5 mg/cm^2 on the surface of pellet. Such solution deposited pellets were than dried at 80 ^oC to remove water. It was later observed that the distribution of the solution on the surface of the pellets was not homogeneous (after drying the pellets at 80 ^oC). Non-uniform layer of solution on the polished surface of the pellet was found, with high amount on certain regions of the pellets and very low on other regions. This could be because of surface tension created by solution drop applied on the surface of the pellets. Nevertheless, these pellets were annealed at 1150 ˚C for 12 hours in static air to induce diffusion of solution into samples. Similar rapid cooling process, as performed on coupled experiments was carried out on these samples (turning off the furnace and opening the furnace doors).

These samples after annealing at their respective temperatures have shown different reaction products. Reactions were followed by XRD analysis. Diffusion studies were carried by Focused Ion beam Secondary Ion Mass Spectrometry (FIB-SIMS) and Time of Flight – Secondary Ion Mass Spectrometry (TOF-SIMS). Surface imaging, mass spectrograms and depth profile studies were conducted. Secondary electron and total secondary ion detector were used for *in-situ* surface imaging. Mass spectra were obtained over a wide range of mass (from 50 –

160 amu). For mass spectra, species of Mn (55^+), Sr (84^+, 86^+, 87^+, 88^+; with isotope at 88^+ amu being of 82.5% naturally abundant), Mo (92^+, 94^+, 95^+, 96^+, 97^+, 98^+, 100^+; with isotope at 98^+ being 24.1% naturally abundant) and La (138^+, 139^+; with 0.09 and 99.91 % abundance respectively) were used. Apart from individual elements, MoO^+ and LaO^+ species were also found at amu 108^+ – 116^+ and 155^+ amu respectively. Primary ion source of Ga (in FIB-SIMS) with amu 69^+ and 71^+ was detected. Mo has 7 isotopes widely spread in the range of amu 92 - 100^+ with abundances ranging from 9.25 % to 24.1%, made it hard to detect. Depth profiling was carried out over an area of 20 x 20 μm^2 and species of La^+, Mo^+, Sr^+ and Mn^+ were focused for study. The rate of sputtering for LMO and LSM pellets were calculated as 0.36 µm/sec and 0.29 µm/sec respectively (see the section 2.6 of Chapter 2 for sputtering depth calculation procedure). For sake of clarity, results concerning the solution deposited pellets will be presented before.

4.3 Results & Discussions:

4.3.1 Surface reactions on the solution deposited $La_2Mo_2O_9$ and $La_{0.8}Sr_{0.2}MnO_{3-\delta}$ pellets:

4.3.1. 1) $La_2Mo_2O_9$ with 5 mg/cm^2 of $MnCl_2{\cdot}4H_2O$ solution deposition:

LMO pellet was covered with $MnCl_2{\cdot}4H_2O$ solution and annealed at 1150 ^oC for 12 hours. The pellet surface after annealing was analyzed by XRD, which showed presence of Mn_3O_4, $LaMnO_{3+\delta}$ and LMO phases (see the Fig. 4.2). When surface imaging of the pellet was carried out in SIMS equipment, three different kinds of surface morphologies were observed: smooth surfaced islands (A); rough textured surface (B) and fresh nucleated crystals (C) (see Fig. 4.3).

A depth profile was collected on a smooth textured island (area A) (see Fig. 4.4). Depth profile shows presence of La and Mo in these areas and no Mn was seen. Profiles of La and Mo were linear to each other and no changes were observed in their profiles until 10 µm depth. Similarities in their profiles would suggest that these areas (smooth islands) have homogeneous La and Mo content, therefore corresponding to the LMO substrate free from any deposited matter.

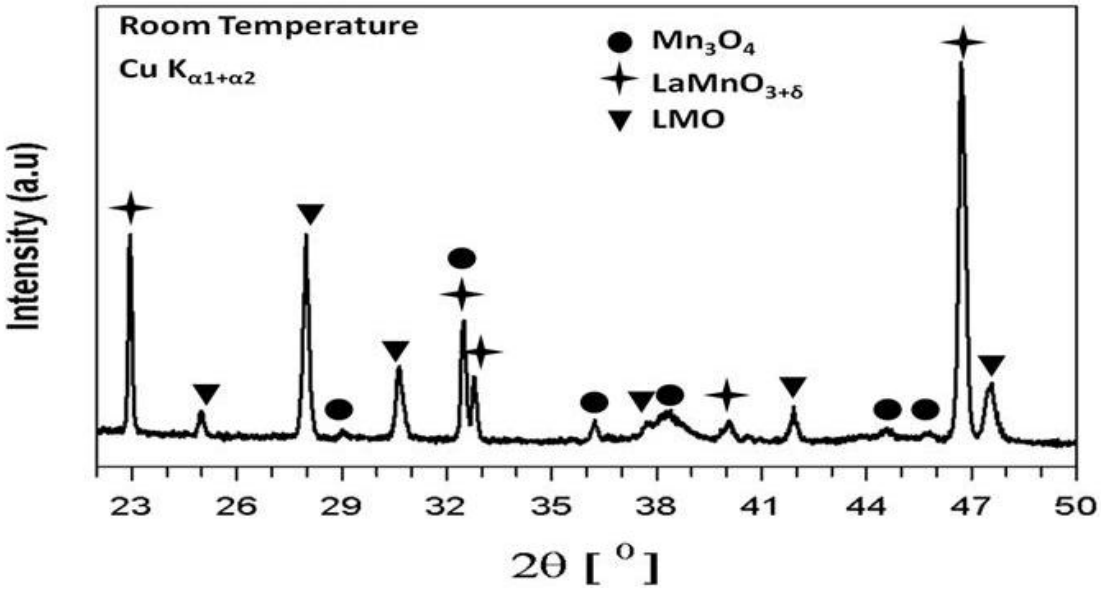

Figure 4.2: XRD pattern of LMO pellet after deposition with $MnCl_2 \cdot 4H_2O$ solution and heat treatment at 1150 ^oC for 12 hours.

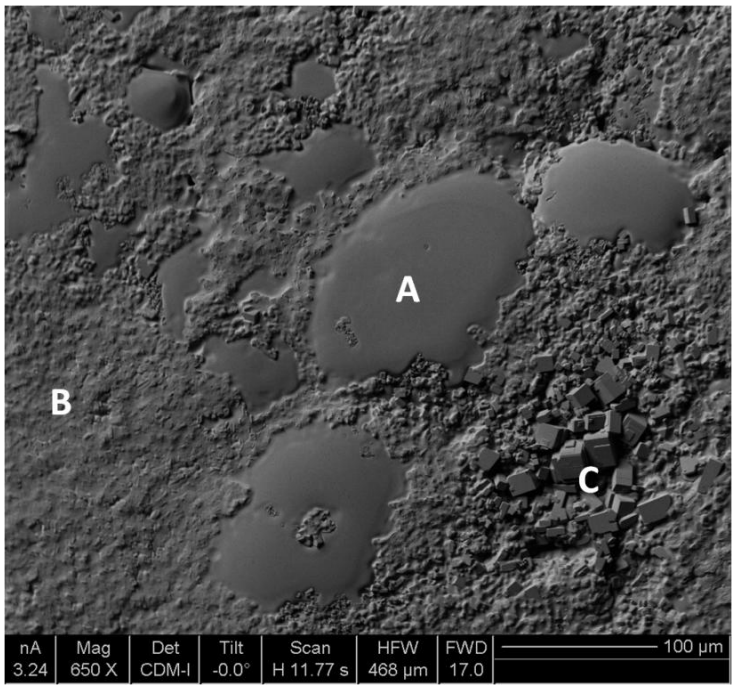

Figure 4.3: FIB-SIMS surface ion image of LMO pellet after deposition with $MnCl_2 \cdot 4H_2O$ solution. Three different surface features can be clearly noticed: the smooth surfaced islands (area A,) the rough textured area (area B), and the newly formed crystals (area C).

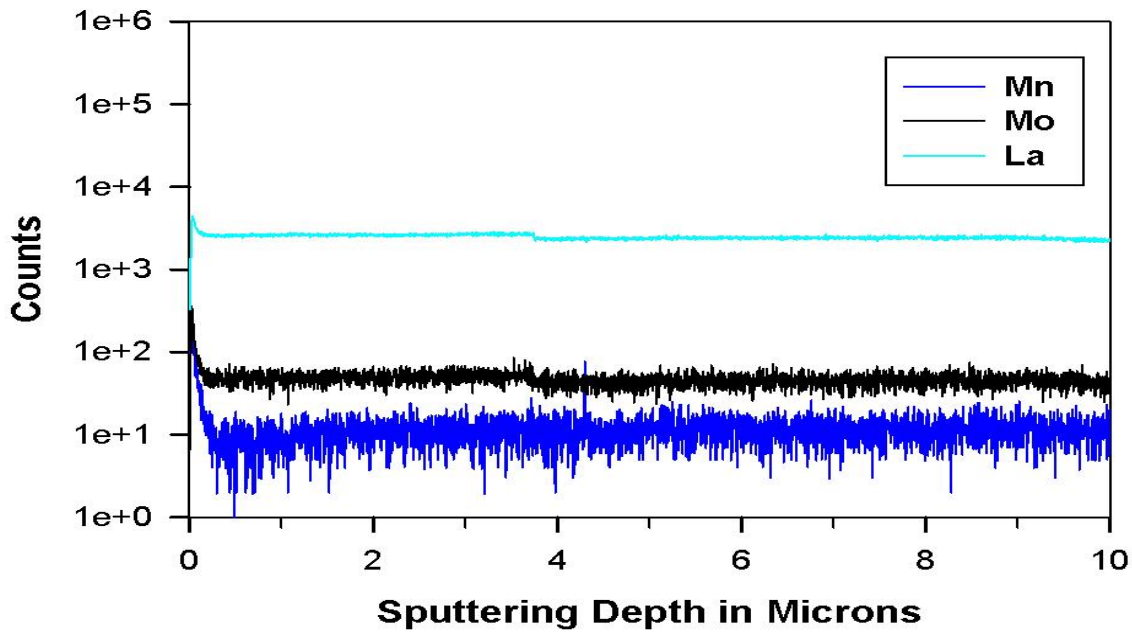

Figure 4.4: FIB-SIMS depth profile of LMO pellet collected on smooth textured area after deposition with $MnCl_2 \cdot 4H_2O$ solution. Similarity in profile of La and Mo suggest the presence of LMO and fall of Mn signal in the background shows the absence of Mn on smooth surfaced area.

As already seen on the pellet surface, areas B and C feature rough texture and nucleated crystals respectively. On both areas only FIB-SIMS mass spectrograms were collected because of high surface roughness (which would create an uneven crater formation and would lead to a huge error bar on depth profiles). On area C, nucleated crystals were observed to be oriented in indefinite direction relative to the pellet surface. This uneven distribution of crystals makes it hard to perform FIBS-SIMS depth profile.

On the FIB-SIMS mass spectra, Fig. 4.5.b, collected on newly nucleated crystals of area C, species of La^+, LaO^+ and Mn^+ were seen (apart from primary ion source Ga^+). From the XRD pattern these newly nucleated single crystals are $LaMnO_{3+\delta}$. On the XRD pattern, one observes high intense peak of $LaMnO_{3+\delta}$ at 2θ scattering angle of 47° ((2 0 0) peak), showing that these (newly) nucleated single crystals were oriented preferably with (1 0 0) direction perpendicular to pellet surface. Fig. 4.6 shows a higher resolution image of these nucleated crystals. Nucleated single crystals were seen in the middle of the rough textured surface. On FIB-SIMS mass spectra collected from the rough textured area (Area B) (see Fig. 4.5.a), La^+, LaO^+, Mo^+, MoO^+, Mn^+

and MnO^+ were seen. Apart from these species, Ga^+ origination from the primary ion source was also observed. When FIB-SIMS mass spectra and XRD are compared, it is deduced that this rough textured area is composed of LMO and Mn_3O_4 phased compounds. It obviously results from the decomposition upon annealing of $MnCl_2{\cdot}4H_2O$. In this rough textured surface, La from LMO reacts with Mn_3O_4 and forms $LaMnO_{3+\delta}$ phase.

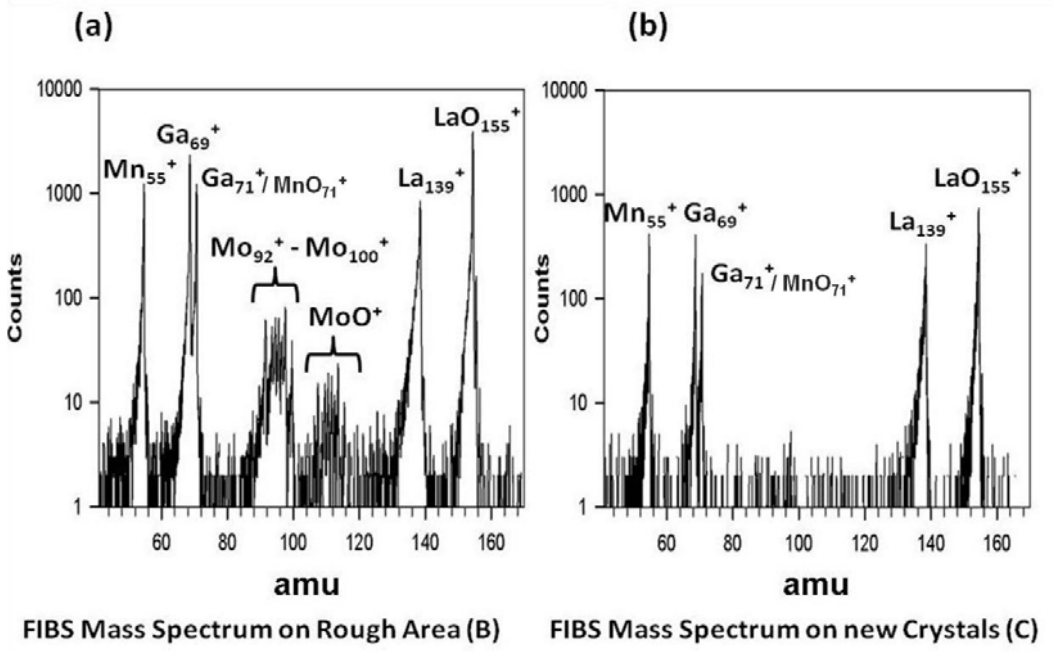

Figure.4.5. a) and b) FIB-SIMS mass spectrums of rough textured areas (area B) and new nucleated crystals on the LMO surface (area C).

This would result in a Mo rich remaining phase but no Mo rich phase was detected in the XRD pattern. We propose two hypotheses for this observation. A first hypothesis is that the La deficient/ Mo rich lanthanum molybdate phase (La:Mo $\neq$ 1) is deep under $LaMnO_{3+\delta}$ single crystals and cannot be detected by XRD. Penetration depth of X-Rays under these conditions is limited to 9.7 µm (at 50° 2θ scattering angle) and these crystals are thicker than 10 µm. Table of X-Ray penetration depths of all the reaction products found in this study are given in table 4.1. The second hypothesis results from the La_2O_3-MoO_3 phase diagram (see Fig. 4.7). It can be seen in this figure that all the Mo rich phases ($La_2Mo_3O_{12}$, $La_2Mo_4O_{15}$, $La_2Mo_6O_{21}$ and MoO_3) have a melting point below the annealing temperature 1150 ^oC. Hence there is a possibility that this Mo rich phase sublimates upon annealing. A possible reaction equation is:

$$3\ La_2Mo_2O_9 + 2/3\ Mn_3O_4 + (1/6 - \delta)\ O_2 \rightarrow 2\ LaMnO_{3-\delta} + 2\ La_2Mo_3O_{12}\uparrow$$

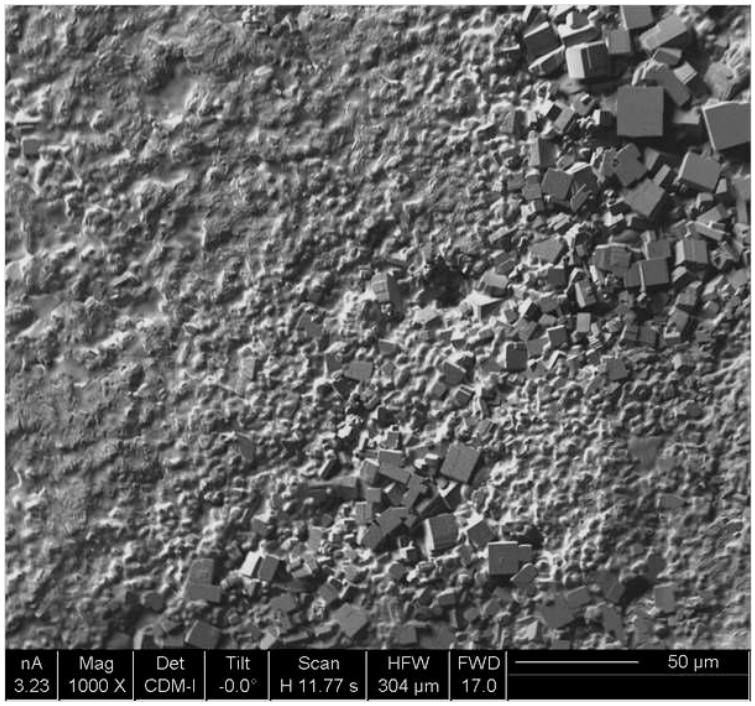

Figure 4.6: FIB-SIMS surface ion image of LMO pellet after deposition with $MnCl_2 \cdot 4H_2O$ solution and annealing at 1150 ^oC for 12 hours. Nucleation of $LaMnO_{3+\delta}$ *single crystals from LMO and Mn_3O_4 phased rough surface can be noticed.*

Compound	Density g/cm³	Penetration depth in µm at given 2θ [°]			
		20	30	40	50
SrO	6.39	12.2	17.9	23	27.5
$SrMoO_4$	4.74	15.7	23	29.5	35
LSM	6.55	4.73	6.92	8.89	10.06
LMO	5.56	6.47	9.45	12.15	14.49
MoO_3	4.69	15.36	22.4	28.8	34.4
$LaMnO_3$	6.55	4.34	6.345	8.157	9.7
Mn_3O_4	4.86	7.96	11.64	14.97	17.84
MnO	5.28	9.714	14.20	18.257	21.75

Table 4.1: X-Ray penetration depth of compounds used for this study and their reaction products are given along with their evolution with 2θ [^{o}] angle.

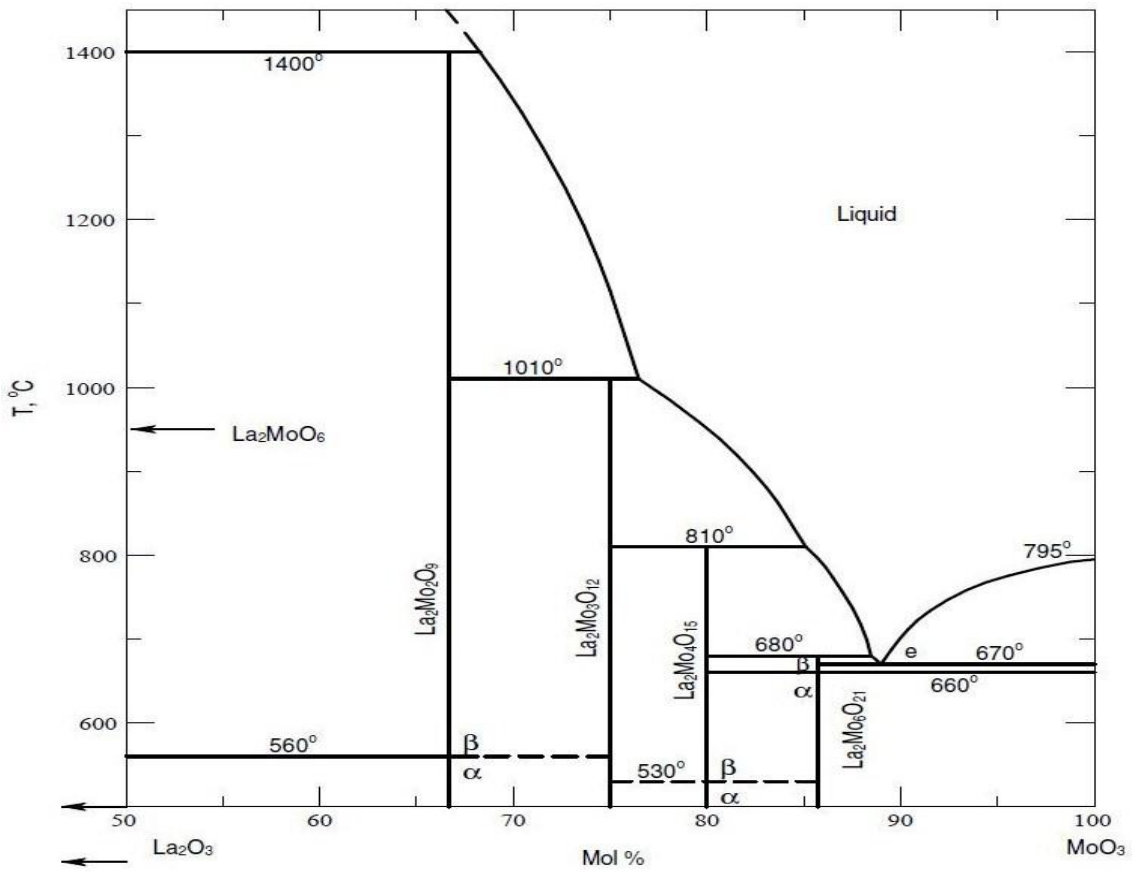

Figure 4.7: Phase Diagram of La_2O_3 – MoO_3 system. [6]

One of the goals of the experiment was to study the diffusion process of Mn in LMO pellet. In order to get the diffusion coefficient, regular amount gradient is expected. However, in this measurement non uniform reactions were observed, where La from LMO reacts with unequally formed Mn based compound and forms single crystals of $LaMnO_{3+\delta}$. Reaction between LMO and Mn_3O_4 is not complete. Appearance of such intermediate reaction products and uneven surface texture, limits any further diffusion analysis in these samples. The uneven distribution of Mn_3O_4 probably results from the fact that the deposition of $MnCl_2{\cdot}4H_2O$ solution on the surface of finely polished LMO pellet was not uniform. Pellet after deposition of Mn solution was heated at 80 ^oC to evaporate water in the solution. According to the color variation on the surface it was found that, amount of $MnCl_2{\cdot}4H_2O$ was higher at some regions on the pellet, whereas no $MnCl_2{\cdot}4H_2O$ was detected in some regions. This process has been probably governed by surface tension of the solution, amount of $MnCl_2{\cdot}4H_2O$ solution or some other uncontrolled parameters. Utilization of sputtering (RF-Sputtering) or vapour deposition process

(Pulsed vapour deposition or Chemical vapour deposition) for deposition of the Mn on surface of LMO pellet would have been advantageous. Such techniques would have achieved uniform deposition of Mn on the surface of LMO pellet; however the reaction of Mn with LMO and formation of reaction products would have been unchanged. Further studies using such deposition techniques are still in scope for Mn diffusion studies on LMO samples.

4.3.1.2: $La_2Mo_2O_9$ with 5 mg/cm^2 of $Sr(NO_3)_2$ solution deposition:

LMO pellet was covered with $Sr(NO_3)_2$ solution and was annealed for 12 hours at 1150 ^oC. The deposition method, drying of solution and annealing process were the same as mentioned earlier. After annealing, the pellet was studied by FIB-SIMS ion imaging, and the pellet appeared to have a high surface roughness. It was also observed that the material on the reaction surface was chipping out (see Fig. 4.8 for FIB-SIMS surface ion image of the pellet). Significant part of the material surface became brittle and was lost once exposed in FIB-SIMS equipment (because of ultra high vacuum in FIB-SIMS equipment: ~ 1 x 10^{-6} bar).

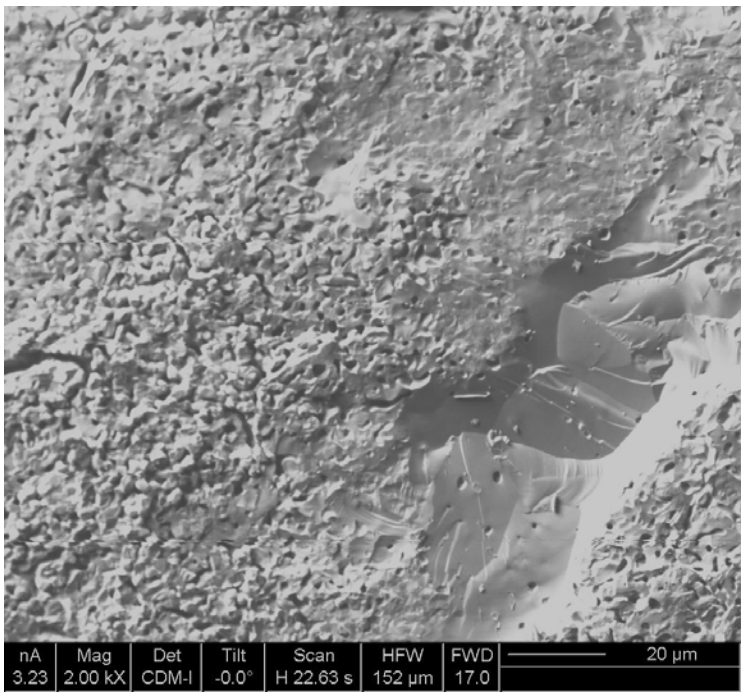

Figure 4.8: FIB-SIMS ion surface image of the LMO pellet after deposition with $Sr(NO_3)_2$ solution and annealing at 1150˚C for 12 hours.

XRD was performed on the pellet and four different phases La_6MoO_{12}, β-LMO, $SrMoO_4$ and La_2MoO_6 were observed. Pattern matching was performed on this sample with all the above phases using FullProf package. Cell parameters and cell volume of the all refined phases are in agreement with their respective standards (see Fig. 4.9 and Table 4.2); however some variations in the intensity were observed in La_6MoO_{12} and $SrMoO_4$ phases. $Sr(NO_3)_2$ solution upon annealing decomposes to SrO and reacts with Mo in LMO forming $SrMoO_4$ and Mo deficient lanthanum molybdates (like La_2MoO_6 and La_6MoO_{12}). However, when the phase diagram of $SrMoO_4$ and $La_2(MoO_4)_3$ was observed, it was realized that the solubility limit of Sr in $La_2(MoO_4)_3$ phase and solubility limit of La in $SrMoO_4$ phase is significantly high (see the Fig. 4.10). $SrMoO_4$ phase can accommodate a significant amount of La in its matrix, and $La_2(MoO_4)_3$ can accommodate high amount of Sr in its matrix and there also is a possibility for existence of intermediate solid solution (like $Sr_{0.44}La_{0.33}MoO_4$). All these compounds even share a similar tetragonal structural arrangement with little variation in unit cell parameters. This makes it very hard to determine the exact composition or content of La/Sr in $SrMoO_4$ type compound.

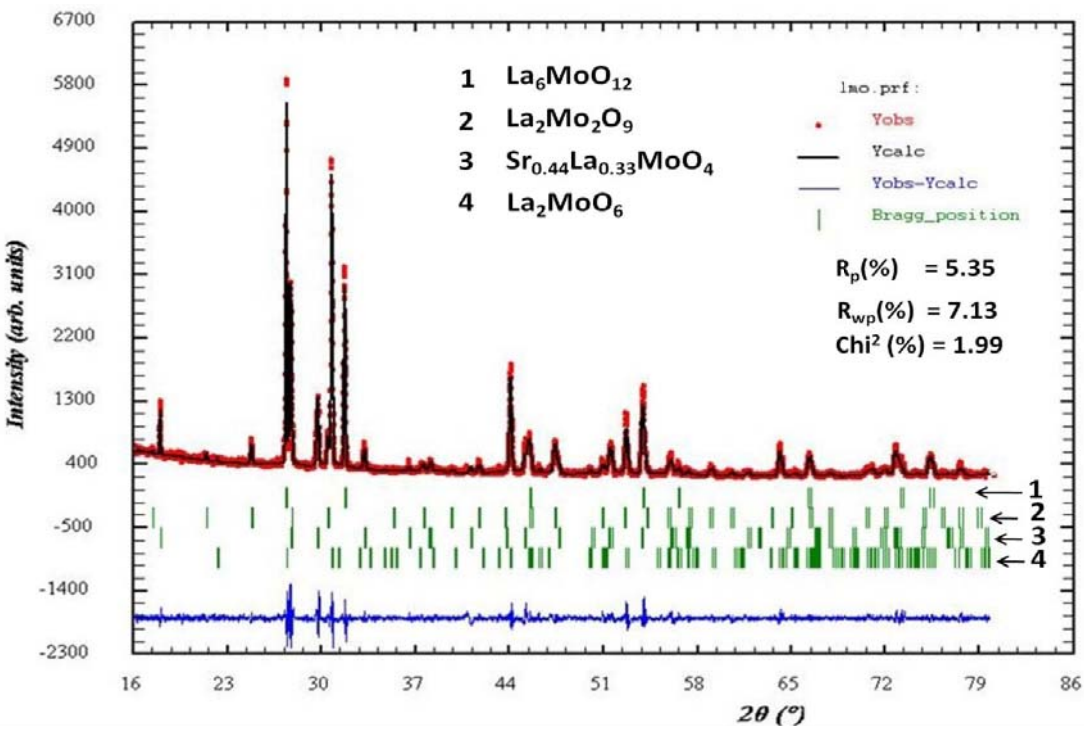

Figure 4.9: FullProf fit performed on the XRD pattern of the LMO sample which was deposited with $Sr(NO_3)$ solution and annealed at 1150˚C for 12 hours.

Phase		Standard cell parameters	Cell parameters of proposed model
La_6MoO_{12} SG = F m -3 m Ref: ICDD 00-024-1087	a = b = c (Å)	5.663	5.6348(1)
	V (Å³)	181.61	178.916(7)
β - $La_2Mo_2O_9$ SG = P 21 3 Ref: ICDD 00-028-5902	a = b = c (Å)	7.155	7.1734(3)
	V (Å³)	366.29	369.14(2)
$SrMoO_4$ SG = I 41/a Ref: ICDD 01-074-3912	a = b (Å)	5.3897(5)	5.3918(2)
	c (Å)	12.0201(8)	12.0095(4)
	V (Å³)	349.19	349.14(2)
La_2MoO_6 SG = I 41/a c d Ref: ICDD 04-009-3118	a = b(Å)	5.7970(3)	5.8049(1)
	c (Å)	32.0353(3)	31.936(1)
	V (Å³)	1076.56	1076.18(6)

Table 4. 2: Comparison of the cell parameters of the standard phases and the phases in the model proposed for LMO pellet which was annealed at 1150 °C for 12 hours after deposition of $Sr(NO_3)_2$. Standard references are taken from the International Centre for Diffraction Data (ICDD).

After annealing the LMO pellet with $Sr(NO_3)_2$ solution deposition, Sr diffuses into LMO pellet and reacts with La and Mo forming different reaction products (like $SrMoO_4$ type phases) with varying Sr and La amounts as a function of depth and there would be a gradient in the dispersion of the reaction products (with various La and Sr content) over depth. In other words there will be high amount of Sr (and low La) in a $SrMoO_4$ type phase at the surface of pellet and inside the pellet there would be low amount of Sr (and high La) in $SrMoO_4$ type phase. Since XRD always gives average information over its penetration depth, it is harder to distinguish possible existence of multiple $SrMoO_4$ type phases with different Sr and La content. XRD has shown the existence of a cubic β-LMO phase (pellet before annealing is monoclinic α-LMO). It is reported that Sr can be substituted for La in LMO and at between 2 – 7 mol% substitution, the high temperature cubic β-LMO can be stabilized down to room temperature [7, 8]. Below 2 mol% substitution of Sr, LMO adopts the monoclinic α-LMO form and above 7 mol% the resultant compound is metastable. Increase in the unit cell volume of β-LMO phase could be due to Sr incorporation in the LMO matrix and this behavior is in agreement with the literature [7].

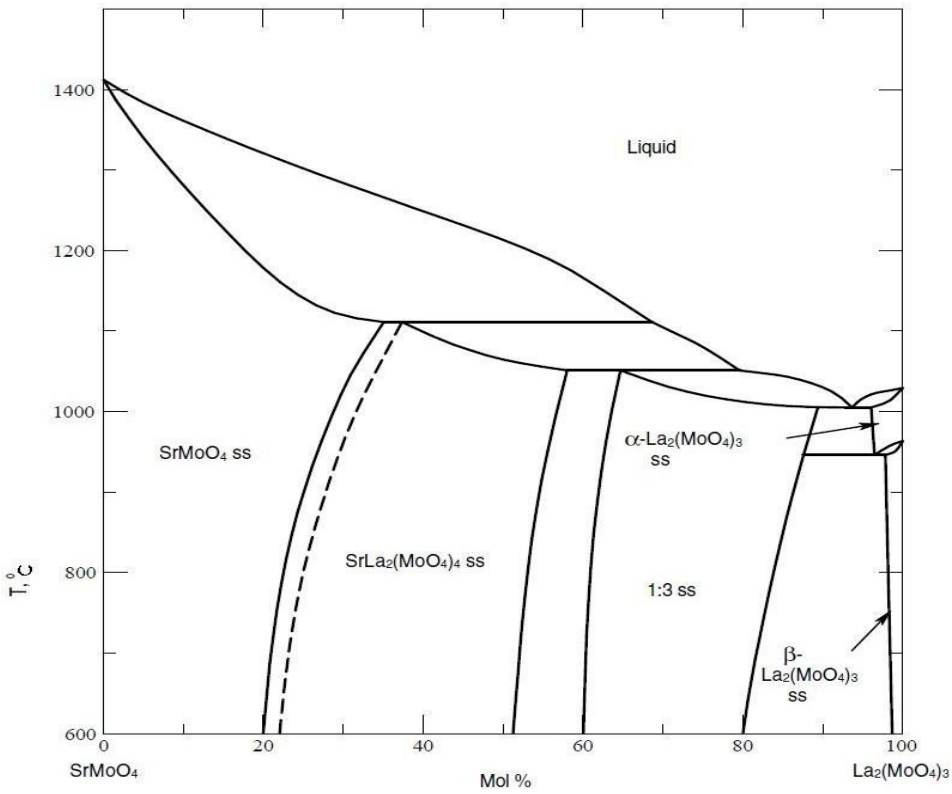

Figure 4.10: Phase Diagram of $La_2(MoO_4)_3$ and $SrMoO_4$ [9].

Further investigation of the pellet was carried by FIB-SIMS depth profile collected on this sample on 20 x 20 μm^2 area. The surface shows abundant presence of Sr on the surface of the pellet, and it shares a profile similar to Mo down to 13 µm (see Fig. 4.11). Sr and Mo profiles decrease down to 8 µm depth and remain unchanged down to 13 µm depth, below which there is a steep decrease in the Sr signal. Along with Sr and Mo, La was also seen on the surface of the pellet, which tends to gradually increase with the decrease of Sr amount down to 6µm depth, below which the La profile remains unchanged. The similarity in the profile of Sr, La and Mo down to 8 µm depth suggests that this area could be $SrMoO_4$ type material with La in $SrMoO_4$ matrix. Such possibility was discussed earlier in the thesis .

Between ~6 to 8 µm, amount of La increases, whereas amount of Sr and Mo falls down. Between ~8 to 10 µm, signals of Sr and Mo are constant and there is slight elevation in signal of La, showing that this area is rich in La. This would mean that this area between ~8 to 10 µm was

build of Mo deficient lanthanum molybdates phases (i.e. amount of La is higher than that of Mo, like La_2MoO_6 and La_6MoO_{12} phases) as observed by XRD along with $SrMoO_4$ type compounds. Between 10 µm to 13 µm in the depth profile; La, Mo and Sr signals are constant. This region could be cubic phased β-LMO, as observed by XRD. This area (10-13 µm) could be in $La_{2-x}Sr_xMo_2O_9$ phase and content of Sr could vary over the depth. After 13 µm depth, Sr signal profile changes and appears to be falling down. However Sr presence did not completely disappear. Since the crater size is 20 x 20 µm, further depth analysis could lead to superficial signals which could be caused by crater walls or uneven surface roughness at the bottom of the crater e.t.c (more information about SIMS limitations in Annex-1). To further investigate such behavior of Sr after 13 µm depth, TOF-SIMS study was carried out. A slide of the sample was cut out and polished on the inner side of the pellet (see the schematic representation of in Fig. 4.12). Later TOF-SIMS line scan was measured from the surface (Side A: reaction surface after deposition and annealing) towards bulk material. Amounts of Sr, SrO, Mo, MoO, La, LaO were studied.

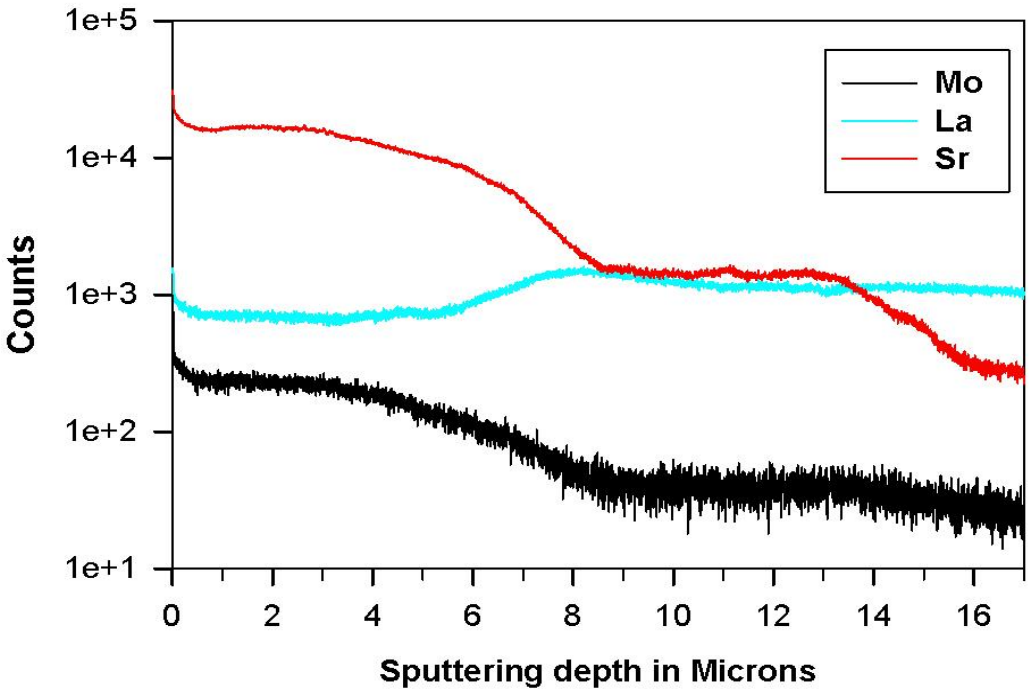

Figure 4.11: FIB-SIMS depth profile of LMO pellet after deposition with $Sr(NO_3)_2$ solution and annealing at 1150˚C for 12 hours.

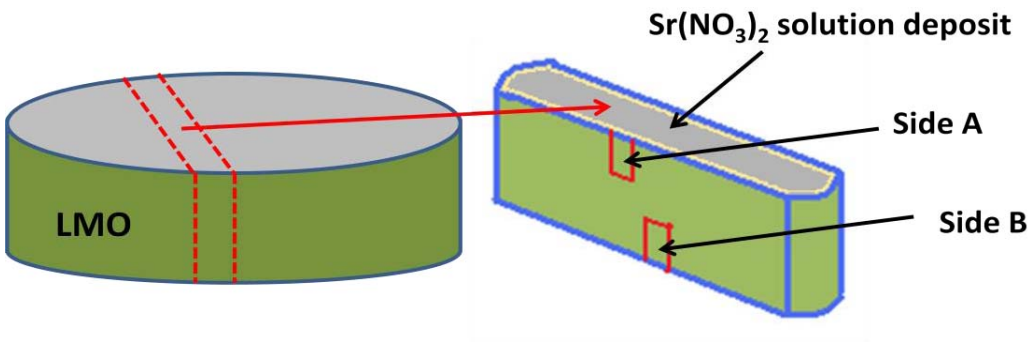

Figure 4.12: TOF-SIMS line scan setup on slide of sample cut out of LMO pellet after deposition with $Sr(NO_3)_2$ solution and annealing at 1150˚C for 12 hours.

Similar line scan study was carried on the opposite side (Side B), the side which did not undergo any solution deposition or reaction, to check for any superficial artifacts. On side A (on the side of deposition), significant amount of Sr was seen and its amount increased gradually with the depth in the pellet and later such content falls back. This presence of Sr was observed for about ~ 60 – 70 µm. On a similar line scan performed on the same area, similar behaviour of Mo was also detected. Profile of Mo and Sr were same and their similarity lasts till ~ 60 – 70 µm. After ~ 70 µm the Mo content goes linear with La signal and remain unchanged, this would mean that after ~ 70 µm LMO bulk material appears. On the TOF-SIMS image, little amount of La was seen on the surface of the pellet, and such amount increase gradually with the depth of the pellet. These results are in agreement with the FIB-SIMS depth profile results and XRD analysis. $SrMoO_4$ type phase rich in Sr and Mo with little amount of La could be present at the surface till ~ 8 µm. La amount slowly increases whereas amount of Mo and Sr decrease till ~ 8 µm. After such depth amounts of all the three elements remain unchanged. This is the depth where Sr enters in to the matrix of LMO and stabilizes it into cubic phase. $La_{2-x}Sr_xMo_2O_9$ phase exist till ~ 60 – 70 µm after which Sr disappears and LMO appears. The diffusion length of Sr^+ in LMO under the above mentioned conditions would be ~ 60 – 70 µm. See the line scan and TOF-SIMS images of side A in Fig. 4.13. Similar TOF-SIMS imaging and line scan measurements were performed on side B (the surface of pellet without any deposition). In these measurements constant Mo and La content were observed. Sr was not seen. One can notice that number of counts of Mo is less than that of La; this could be because of abundance of its

isotopes. Note that the number of counts of La and Mo cannot be compared to each other, since the signals correspond to the sputter yield rather than the actual amount of La or Mo in the sample (see Annex-1 for more information on SIMS limitations).This confirms that the pellet on the other side is pure LMO phase. See the line scan and TOF-SIMS images side B in Fig. 4.14.

From the TOF-SIMS results, profiles of La, Sr and Mo were collected as mentioned above. The ratio of Mo/La signals and Sr/La were plotted (see Fig. 4.15). From the surface of the pellet for about ~ 60 µm distance, stronger Mo signal was noticed, which levels out indicating the constant composition of bulk LMO material. Similarly Sr also show strong signal for about ~60 µm from the surface and later disappear, confirming its diffusion length in LSM for about ~60 µm. Both Mo and Sr show similar profiles indicating the reaction product at the surface of the pellet to be $SrMoO_4$ type material (even confirmed by XRD). Since the ratio of Mo/La and Sr/La profiles are not linear, it indicates that the reaction products have La in the $SrMoO_4$ lattice and that amount of Sr and La in $SrMoO_4$ type phases varies over depth. From the microstructure observed on TOF-SIMS image (see Fig. 4.13) it is evident that there is no apparent enrichment or depletion at the grain boundaries and since Sr content is gradually decreasing towards the surface of the pellet, it would be sensible to assume that this diffusion is rather bulk diffusion than grain boundary diffusion.

Unfortunately a different lattice will give different secondary ion yields and this makes quantification of any information very difficult. In addition, due to the apparent reaction between the materials this is no longer as simple as tracer ion diffusion and becomes more difficult to quantify any diffusion parameters of Sr as well as to give them any real meaning. However, using the approximated ~60 µm (at 1150 ^{o}C for 12 h) diffusion length of Sr in LMO, a diffusion coefficient, D, is estimated.

Considering D as the diffusion coefficient, L as diffusion length and t as time (in seconds); it can be stated that $\boldsymbol{L} = 2\ (Dt)^{½}$ [10]. In this measurement, diffusion length (L) of Sr was nearly as ~60 µm in LMO after annealing at 1150 ^{o}C for 12 hours (t). Using these values in above the equation, diffusion rate of Sr (D_{sr}) in LMO was estimated as ~ 2 x 10^{-10} cm^2 s^{-1}.

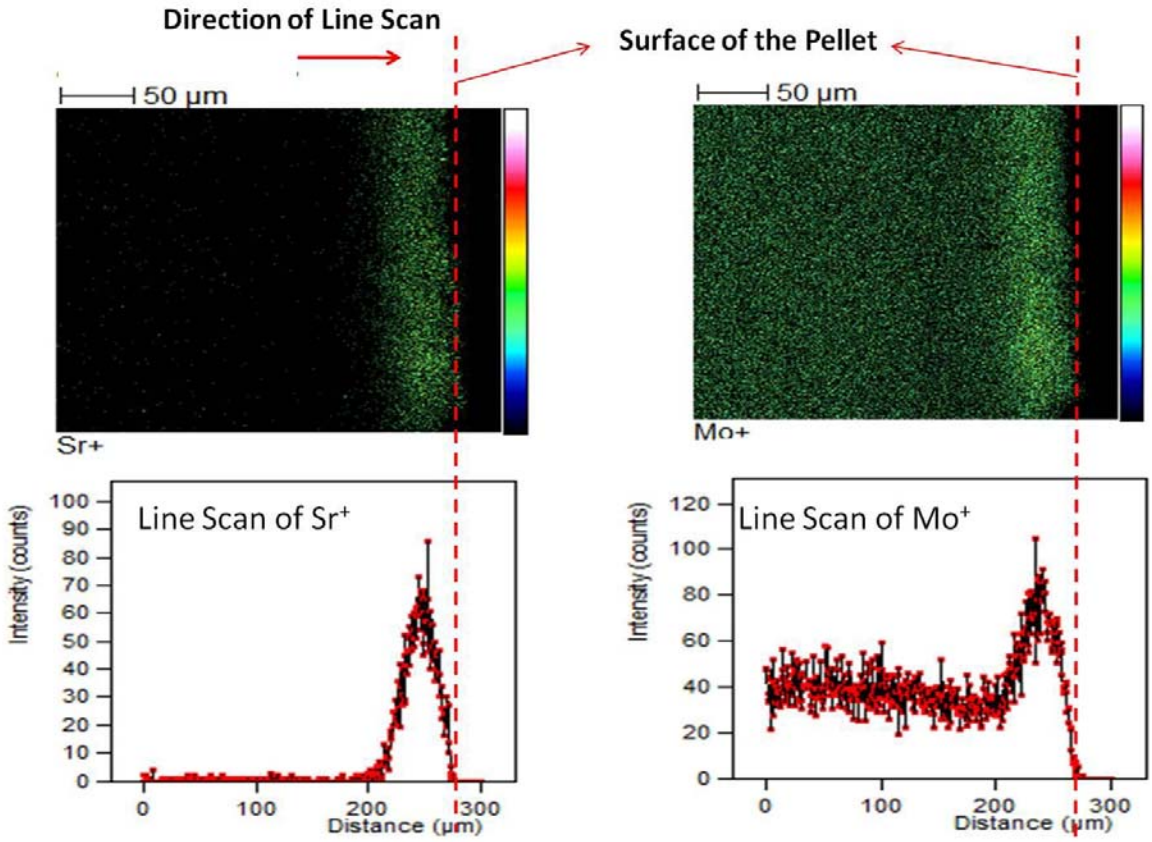

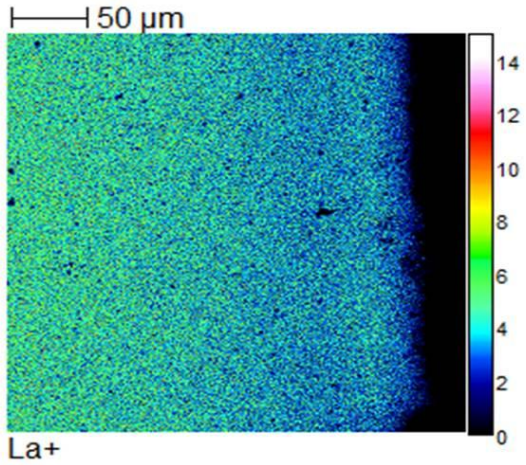

Figure 4.13: TOF-SIMS Images of LMO pellet (on side A: side of pellet where deposition was performed) after deposition with $Sr(NO_3)_2$ solution and annealing at 1150˚C for 12 hours. Images of Sr^+, Mo^+ and La^+ content can be seen. Line scan showing content of Sr^+ and Mo^+ can also be seen. Notice the similarities in the profiles of Sr^+ and Mo^+.

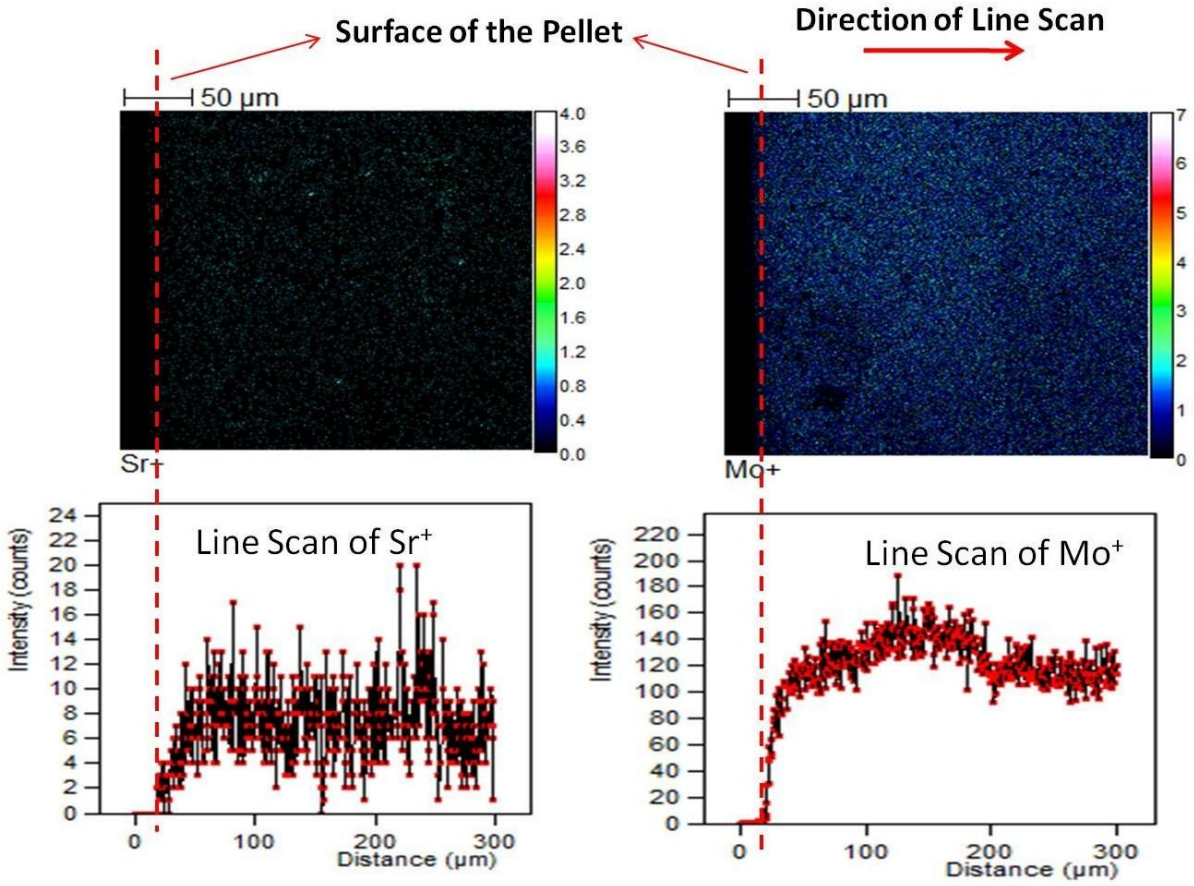

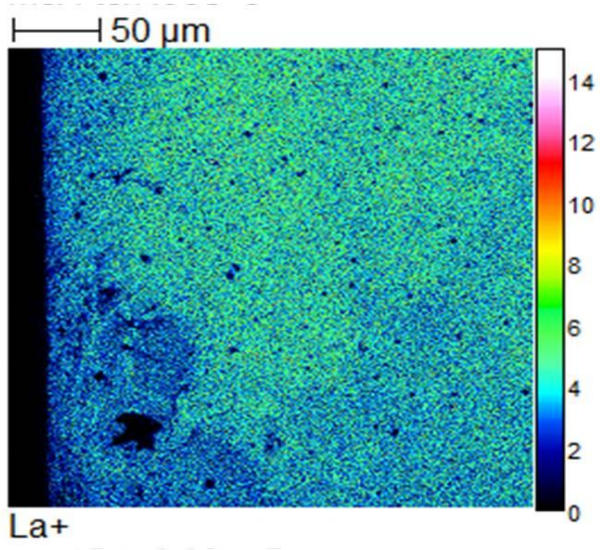

Figure 4.14: TOF-SIMS Images of LMO pellet (on side B: side of pellet where no deposition was performed) after deposition with $Sr(NO_3)_2$ solution and annealing at 1150˚C for 12 hours. Images of Sr^+, Mo^+ and La^+ content can be seen. Line scan showing content of Sr^+ and Mo^+ can also be seen where no Sr^+ was detected.

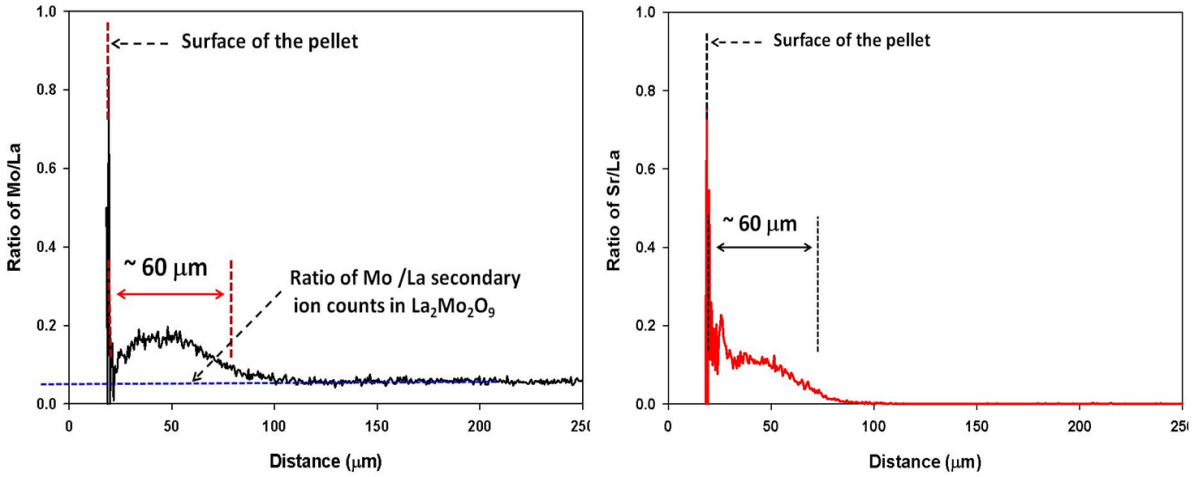

Fig.4.15: Ratio of Mo^+/La^+ (left) and Sr^+/La^+ (right) secondary ion yield signal counts as a function of distance from surface of pellet. Note that these TOF-SIMS measurements were performed on LMO pellet (on side A: side of pellet where deposition was performed) after deposition with $Sr(NO_3)_2$ solution and annealing at 1150˚C for 12 hours.

Sr diffusion coefficient in $La_{0.75}Ca_{0.25}CrO_3$ (LCC) pellet was reported to be distributed from 1 x 10^{-17} to 10^{-13} cm^2 s^{-1} in the range of 900 to 1100 ^oC [11]. Diffusion coefficient of Sr in YSZ was observed to be ranging between 1 x 10^{-16} to 10^{-15} cm^2 s^{-1} in range of 1325 to 1475 ^oC [10]. Compared to the diffusion coefficients of Sr (in LCC or YSZ) reported in the literature, our estimate of Sr diffusion coefficient as ~ 2 x 10^{-10} cm^2 s^{-1} (in LMO at 1150 ^oC) is significantly higher.

4.3.1.3: $La_{0.8}Sr_{0.2}MnO_{3-\delta}$ with 5 mg/cm^2 of $(NH_4)_6Mo_7O_{24}.4H_2O$ deposited solution:

After annealing the LSM pellet covered with $(NH_4)_6Mo_7O_{24}4H_2O$ solution for 12 hours at 1150 ^oC, sample was observed by FIB-SIMS ion imaging. The surface morphology of the pellet consists of large and small grains (see the fig. 4.16). FIB-SIMS-depth profile was collected on smaller areas (10 x 10 µm) in this sample such that the beam can be focused only on large and small grains separately. The pellet was also analyzed by XRD, and presence of LSM, Mn_3O_4 and $SrMoO_4$ type phases were detected (XRD pattern in Fig. 4.17).

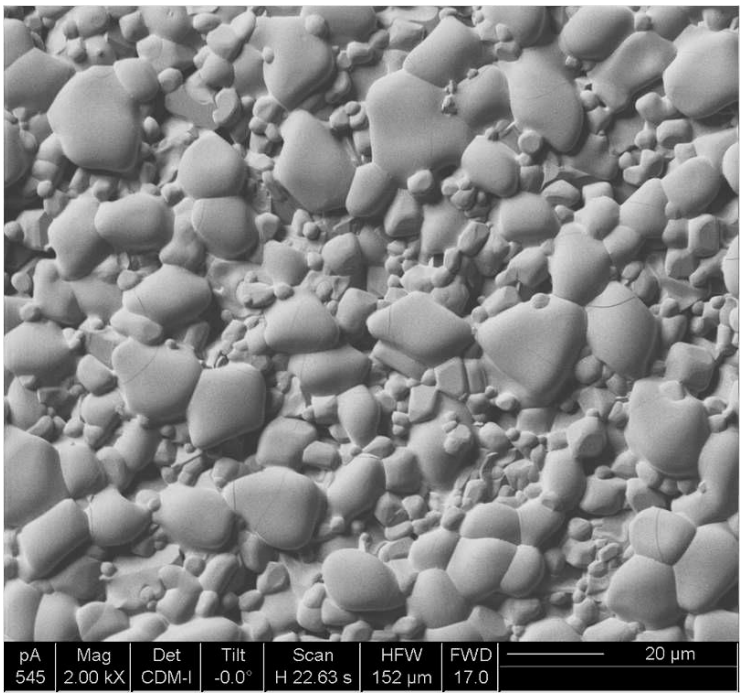

Fig.4.16: FIB-SIMS ion surface image of LSM pellet after deposition with $(NH_4)_6Mo_7O_{24}.4H_2O$ solution and annealing for 12h at 1150 ^oC.

A depth profile was collected on large grains until 18 µm depth (see the depth profile in Fig. 4.18). Considering the profiles of La, Mo, Sr and Mn detected in this sample, it was possible to divide the depth profile in to three different zones (zones A, B and C) where peculiarity of each zone was differentiated. Zone A is from the surface of the pellet till 7µm depth.

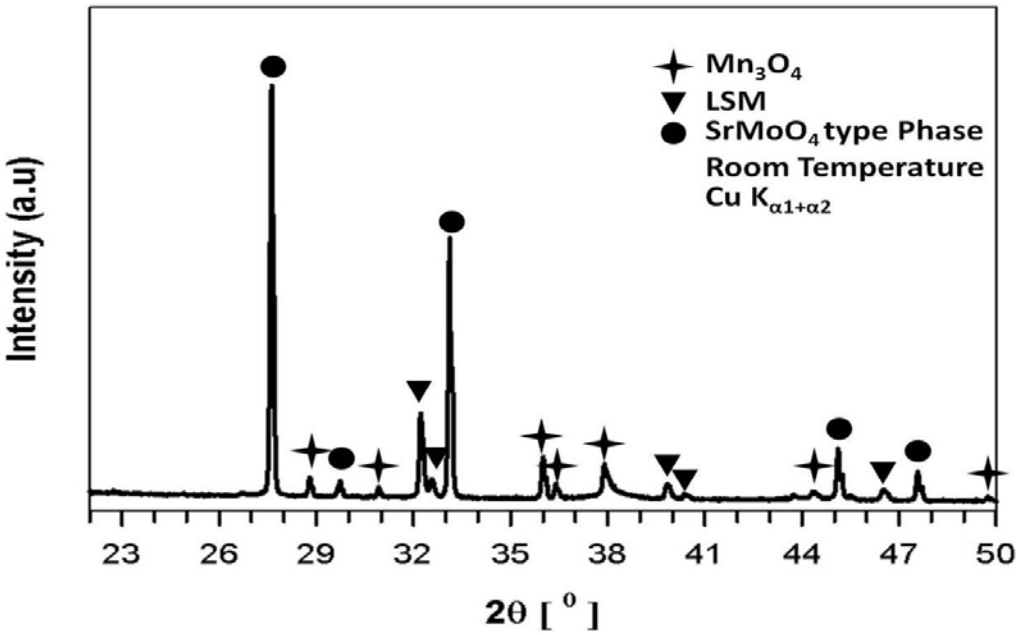

Figure 4.17: XRD pattern of LSM pellet after deposition with $(NH_4)_6Mo_7O_{24}.4H_2O$ solution and annealing for 12 hours at 1150 ^oC.

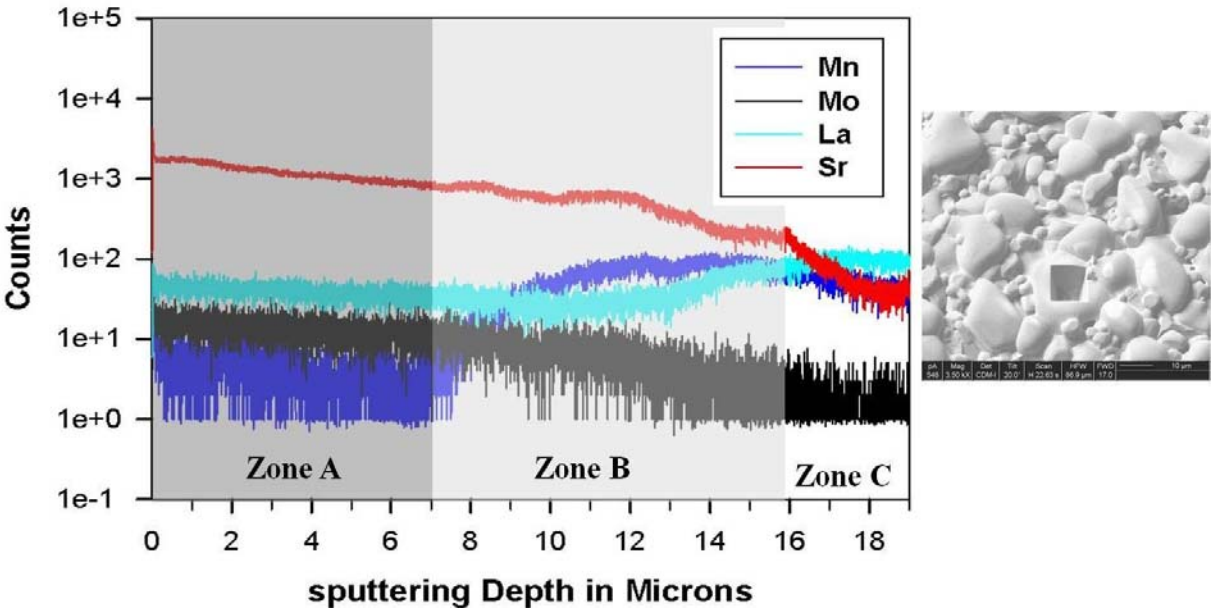

Figure 4.18: FIB-SIMS depth profile collected on a big grain formed on LSM pellet after deposition with $(NH_4)_6Mo_7O_{24}.4H_2O$ solution and annealing it for 12 hours at 1150 ^oC. Zone A, B and C can be identified along with color variation. Crater formed on the big grain after depth profiling is shown in the FIB-SIMS ion image on right side.

In zone A, signals of La, Mo and Sr were found and no Mn was detected. This zone extends down to ~7µm, then zone B starts and extends down to ~16 µm. In zone B, Mn was detected and the content of Mn gradual increases and remains constant thereafter. Elevation in La content was also noticed along with fall of Sr and Mo signals. After ~16 µm zone C starts and it appears that all the signals were constant. Close observation of the depth profile in zone C shows gradual fall of almost all the signals. Considering 10 x 10 µm crater size perturbations in signals at depths more than ~10 µm could be assumed as instrument effect. SIMS depth profile analysis is based on secondary ion yield. During depth profile measurement if the depth of crater is more than its thickness, it is likely that secondary ions which were sputtered from the surface of the sample could be obstructed by the inner walls of the crater and do not reach the mass spectrometer detector, leading to the false count and overall fall in the signals (see the section I.2 in Annex-I for limitations of SIMS experimentation). In order to have better insight in this sample TOF-SIMS line scan and surface imaging were also performed. These results will be discussed later in this section.

In the zones A and B, similarities in profiles of Sr and Mo can be seen. La was detected in zone A, with the elevation in profile in zone B. Considering the profiles of these three elements (and similarity in profiles of Sr and Mo) and XRD analysis, it can be said that the sample at the surface is most probably a $Sr(MoO_4)$ based compound with La partially substituted to Sr (as discussed in previous sections, solid solution exists between $SrMoO_4$ and $La_2Mo_3O_{12}$, see Fig. 4.10). Zone B would then correspond to LSM or Sr deficient LSM material. Reaction mechanism is discussed later in this section.

FIB-SIMS depth profile was collected on the small grains (see the fig. 4.19). In this depth profile, Mo was not detected. Sr signal was constant over the depth (from surface to ~15 µm). La content increases gradually until ~6 µm and remain unchanged. Surface of these small grains is rich in Mn, which falls gradually until ~ 6µm and later remains unchanged. Considering the XRD pattern (see Fig. 4.17), these small grains would then be Mn_3O_4 grains on top of $LaMnO_3$ / LSM phase. Note that in LSM, La is partially substituted by Sr and both $LaMnO_3$/LSM share similar structural arrangement.

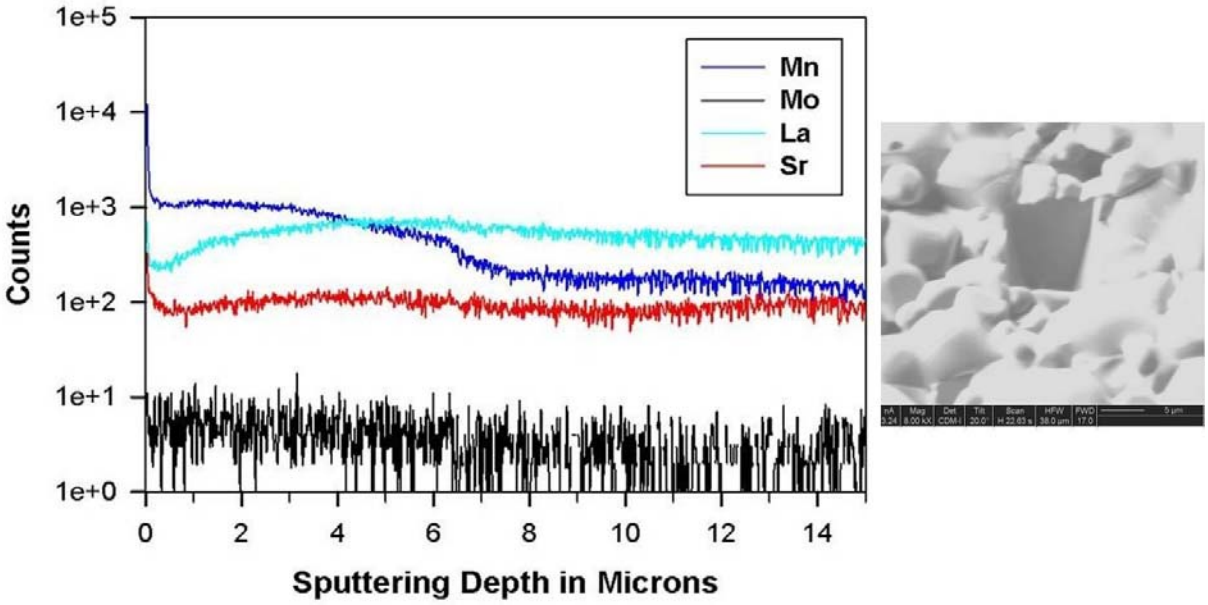

Figure 4.19: FIB SIMS depth profile collected on small grains formed on LSM pellet after deposition with $(NH_4)_6Mo_7O_{24}.4H_2O$ solution. Crater formed on the area with small grains after depth profiling is shown in the FIB-SIMS ion image on right side.

For the TOF-SIMS measurement, the pellet was sliced off radially and the inner sides of the dissected pellets were polished (as described in earlier section and as in Fig. 4.12). The surface of the pellet on which solution deposition was performed was untouched were analyzed (see Fig. 4.20). As observed by depth profile, Mn^+, La^+ amounts in TOF-SIMS measurements were low on the surface and increased with the depth of the pellet. Mo^+ was seen on the surface of the pellet and its content gradually disappeared with the depth. Mo^+ can be seen till ~50 µm. Considering this diffusion length of Mo (~50 µm at 1150 ^oC for 12 h), the bulk diffusion coefficient was estimated as ~$1.10^{-10}.cm^2s^{-1}$ (calculations were similar to those performed for Sr diffusion in LMO as in previous section) Some spots with high amount of Sr was noticed, this would be because of presence of $SrMoO_4$ type grains and Mn_3O_4 type grains as seen on the surface by FIB-SIMS ion imaging. Irregular surface roughness was also detected, which would be the result of appearance of small and big grains as noticed in FIB-SIMS ion image. However such high amount of Sr (either from presence of $SrMoO_4$ or irregular grain distribution) at the surface of the pellet gradually decreased with depth and remained constant in the bulk.

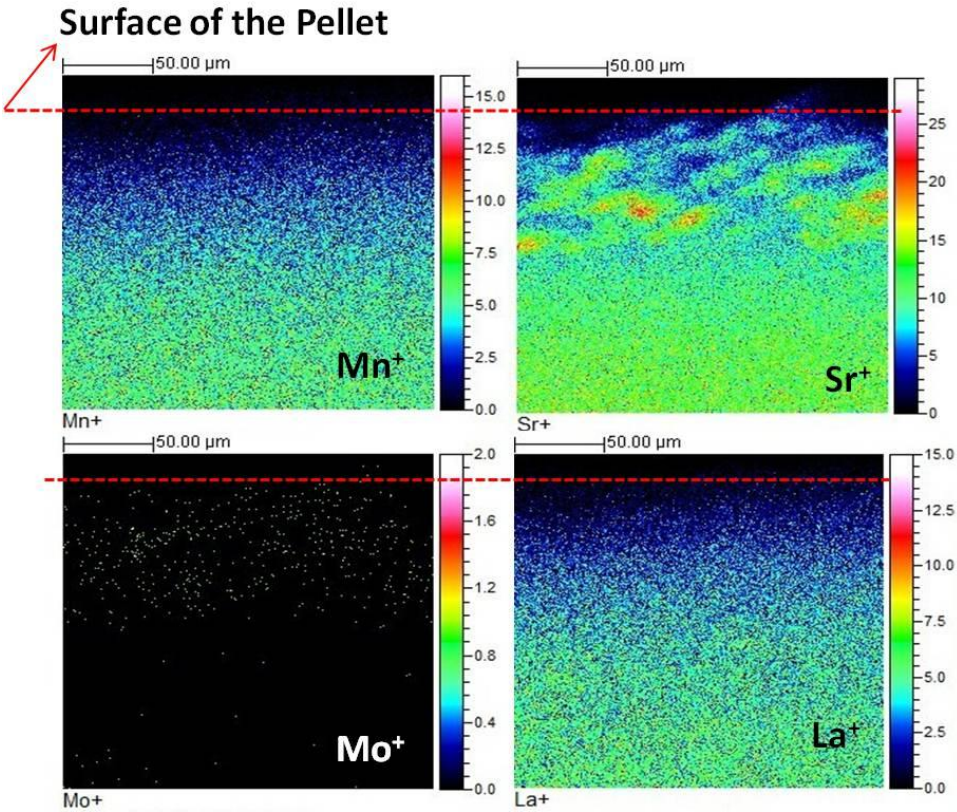

Figure 4.20: TOF-SIMS Images of LSM pellet (on the side of pellet where deposition was performed) after deposition with $(NH_4)_6Mo_7O_{24}.4H_2O$ solution and annealing at 1150˚C for 12 hours. Images of Mn^+, Sr^+ , Mo^+ and La^+ content can be seen. Depletion of signal towards the sample surface is an artifact probably caused because of sample curvature due to polishing and/or mounting of the sample.

It is well informed in the literature that substitutions made to A-site cations segregate towards the surface in ABO_3 type perovskites, yet the reason for this behavior is not understood well [12-16]. Note $(NH_4)_6Mo_7O_{24}{\cdot}4H_2O$ after annealing at high temperature decomposes into MoO_3. Sr segregated from LSM pellet towards the surface reacts with the decomposed MoO_3 to form $Sr(MoO_4)$ based material. Signals of La were also detected in FIB-SIMS depth profile. It is possible that La is present in the matrix of such $SrMoO_4$ phase, because of existence of possible solid state solution between $La_2Mo_3O_{12}$ and $SrMoO_4$ as discussed in previous section. Since both end members of this series share similar tetragonal or pseudo-tetragonal structural arrangement with slight variation in unit cell parameters, it is hard to know the exact composition. Moreover, XRD data is always averaged over penetration depth. For example, X-ray penetration depth for

$SrMoO_4$ is 15.7 µm at 2θ 20°, and is around 35 µm at 2θ 50°. The result is consistent with presence of $Sr_{1-x}La_xMoO_4$ with small amount of La at the surface (0 µm) and gradual increase of La content with depth (for example down to ~ 14 µm). On the XRD pattern, such variation of La content cannot be differentiated because of their structural similarities. X-rays penetrate the whole of 12 µm depth volume giving only averaged information.

Three hypotheses are proposed for this complex reaction mechanism. In first hypothesis: La and Sr from LSM reacts with MoO_3 and form $Sr_{1-x}La_xMoO_4$ ($SrMoO_4$ - $La_2Mo_3O_{12}$) phases. Such LSM compound which loose both Sr and La would form Mn_3O_4 type phases. In second hypothesis: Sr from LSM reacts with MoO_3 and form $SrMoO_4$ and small amount of La enters into $SrMoO_4$ matrix. Sr deficient LSM becomes imbalanced with the loss of Sr, and takes La from surrounding areas forming $LaMnO_3$ (LSM and $LaMnO_3$ share similar structural arrangement). The surrounding LSM grains which loose Sr and La to form $Sr_{1-x}La_xMoO_4$ and La to form $LaMnO_3$, form Mn_3O_4 phase. Limitations of XRD penetration depth; similarities in $SrMoO_4$ - $La_2Mo_3O_{12}$ phases and $LaMnO_3$ – LSM phases limit further analysis and a strong conclusion. Schematic representations of both the hypotheses 1 and 2 are presented in Fig. 4.21 and Fig. 22 respectively.

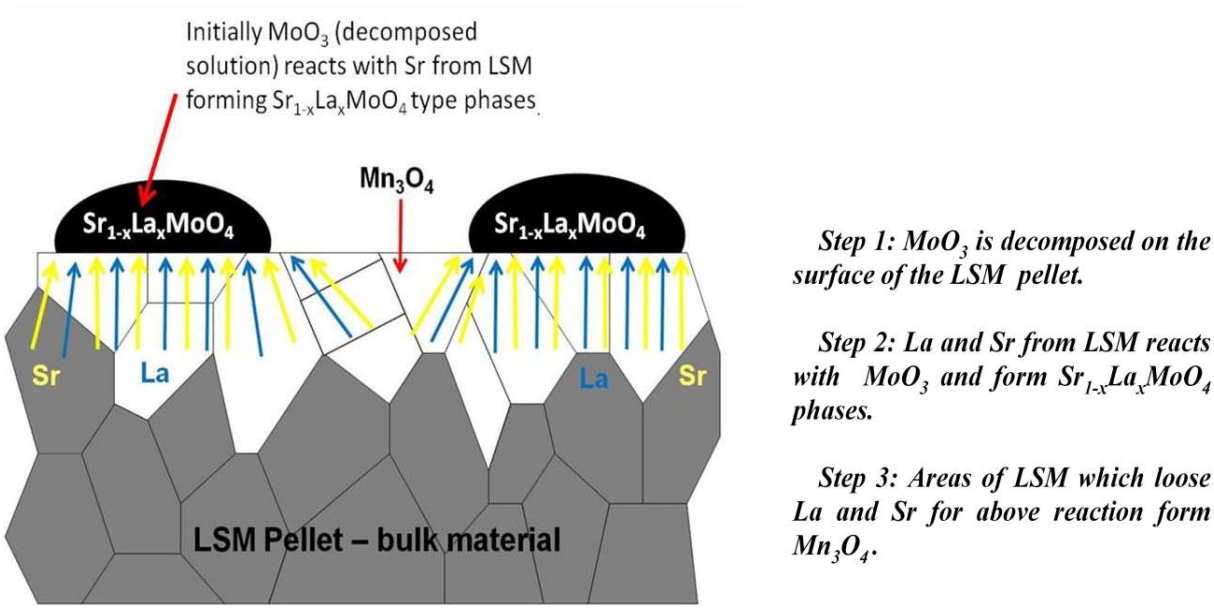

Figure 4.21: Schematic representation of hypothesis 1 for reaction mechanism (in stages) when LSM pellet is annealed after deposition with $(NH_4)_6Mo_7O_{24}.4H_2O$ solution.

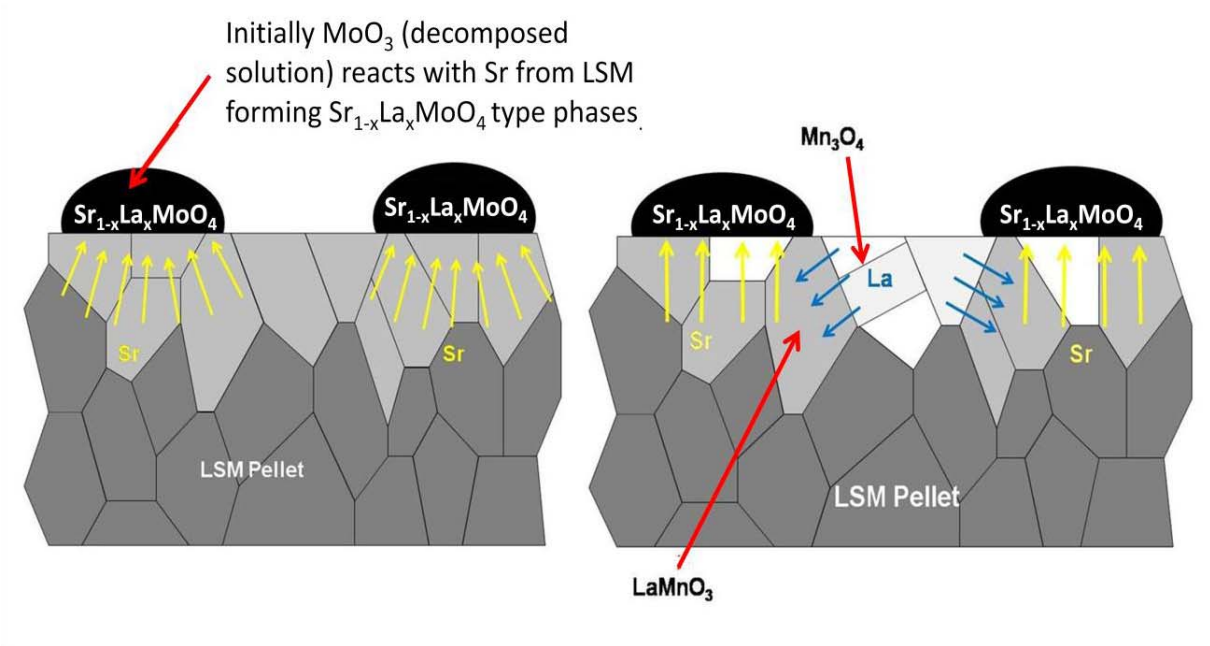

Step 1: ***MoO_3 is decomposed on the surface of the LSM pellet.***

Step2: ***Sr from LSM reacts with MoO_3 and form $Sr_{1-x}La_xMoO_4$ phases.***

Step3: ***La from surrounding area react with Sr deficient LSM to balance Sr loss and form $LaMnO_3$.***

Step4: ***Grains which loose Sr and La for $Sr_{1-x}La_xMoO_4$ and La for $LaMnO_3$ form Mn_3O_4.***

Figure 4.22: Schematic representation of hypothesis 2 for reaction mechanism when LSM pellet deposited with $(NH_4)_6Mo_7O_{24}.4H_2O$ solution and annealed for 12 hours at 1150 ^oC. Reaction mechanism is described in stages.

Third hypothesis is based on assumption of cation(s) segregation towards the surface of sample. Such a segregation behavior upon annealing is a well acknowledged phenomenon in $A_{1-x}S_xBO_3$ perovskites [12-16]. On the surface of the LSM pellet, enrichment of SrO and MnO layers was observed by Jiang *et al.*[15]. In LSM, Mn is in mixed valance state (Mn^{3+} and Mn^{4+}). It was reported that Mn^{4+}/ Mn^{3+}ratio at the surface is higher than that of bulk, and it was reported that such ratio varies with temperature (which affects the redox mechanism) [13]. One can therefore

assume that SrO and MnO migrate towards the surface of the pellet and a thin layer of $SrMnO_{3-\delta}$ growing on LSM surface. $SrMnO_{3-\delta}$ than reacts with deposited MoO_3 and forms $SrMoO_4$ type phases (along with little La). $SrMnO_{3-\delta}$ upon loosing Sr forms Mn_3O_4 grains (see Fig. 4.23). However, there could be some LSM grains on the top of the surface, where $SrMnO_{3-\delta}$ layer would have not covered and La from such grains enter the matrix of $SrMoO_4$ (not represented in the figure). Since the stoichiometry of the final reaction products are not known (Sr/La content in $Sr(MoO_4)$ or LSM phases is not known), only an averaged chemical equation for the reaction is proposed.

$$\mathbf{La_{0.8}Sr_{0.2}MnO_3 + 0.2\ MoO_3 \rightarrow 0.2\ SrMoO_4 + 0.8\ LaMnO_3 + 0.2/3\ Mn_3O_4 + 0.2/3\ O_2\uparrow}$$

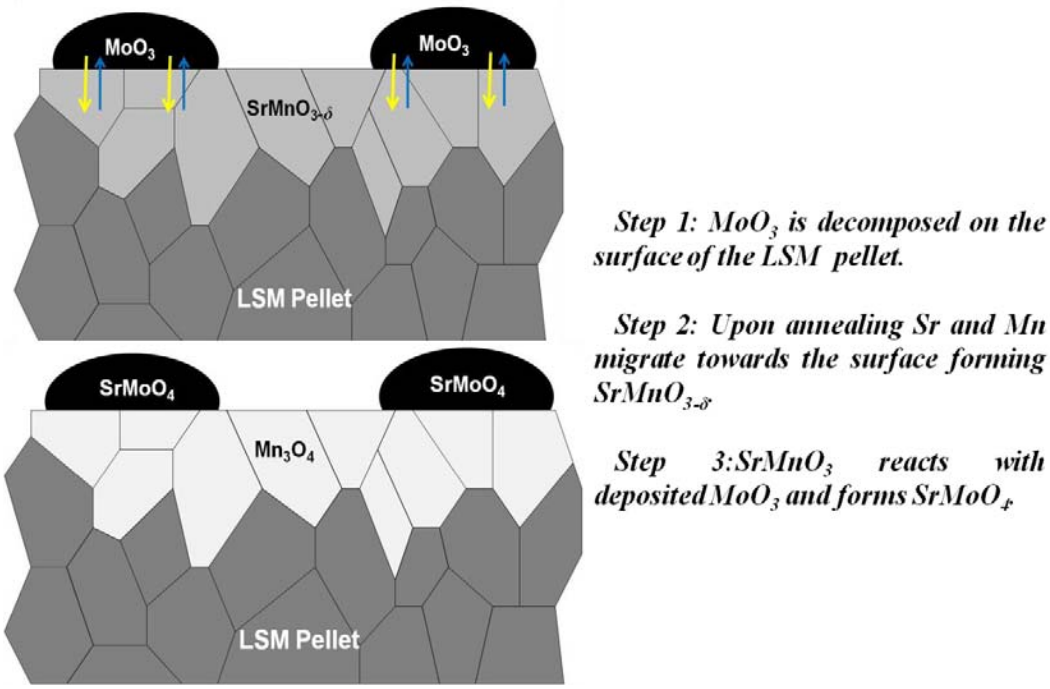

Figure 4.23: Schematic representation of hypothesis 3 for reaction mechanism when LSM pellet is annealed after deposition with $(NH_4)_6Mo_7O_{24}.4H_2O$ solution. Reaction mechanism is described as stages.

4. 3.2: Cationic diffusion measurements on $La_2Mo_2O_9$ / $La_{0.8}Sr_{0.2}MnO_{3-\delta}$ pellet couples

Different annealing measurements were performed on pellets of LSM/LMO which were coupled together on their polished faces (detailed in section 4.2). As mentioned earlier, coupled experiments were performed at different temperatures and annealing times to study their respective effects on diffusion. Three different couples were annealed at 1) 1050 ^{o}C for 12 hours, 2) 1050 ^{o}C for 36 hours and 3) 1150 ^{o}C for 12 hours (see the Fig. 4.24). After annealing, the coupled pellets were not sticked to each other and they split naturally. However, the surface topography and the darkish grey color on the surface of the LMO pellet indicated a reaction or diffusion of elements from LSM. On the LSM pellet, noticeable change in the surface roughness can be clearly identified. Because of complexity induced in the diffusion behavior, results are presented first and separate section is dedicated for discussions on reaction mechanism.

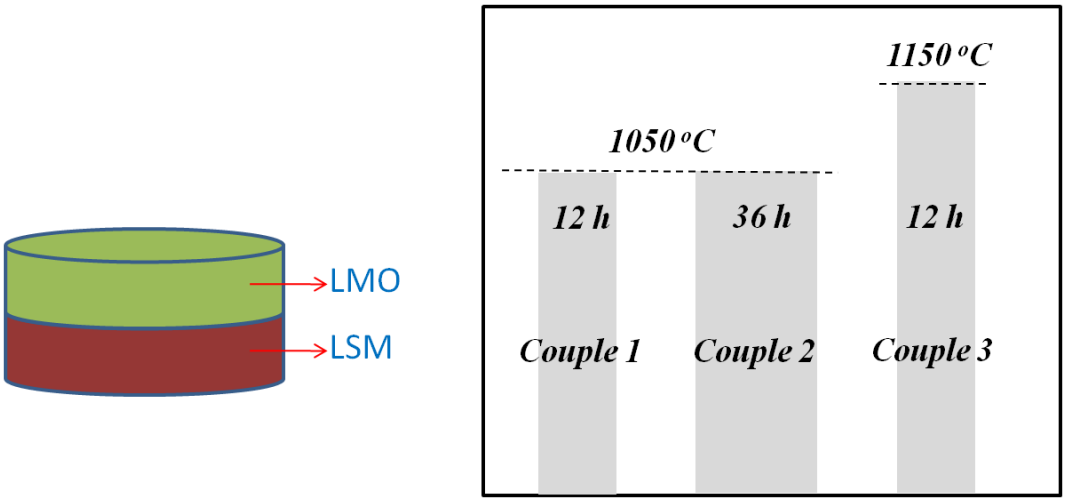

Figure 4.24: Schematic representation of LMO and LSM couple (left). Bar diagram of the heat treatment experiments on three different LMO-LSM couples (right).

4.3.2.1: XRD analysis and FIB-SIMS surface analysis on $La_2Mo_2O_9$ pellets:

As mentioned earlier, LMO and LSM pellets of the couple split naturally. On the three LMO pellets from couples annealed at 1050 ^{o}C (for 12 and 36 hours) and 1150 ^{o}C, XRD analysis has shown presence of $LaMnO_3$ /LSM phase (both the structures share similar rhombohedral

structure) (see Fig. 4.25). On the LMO pellet which was annealed at 1150 ^{o}C, another phase was also observed. The identification of this phase was delicate because of presence of only one low intensity peak at 2θ 27°. This peak can however be attributed to La_2MoO_6 phase since 2θ positioning of the peak fits with the position of the high intense peak of La_2MoO_6 phase and such phase was already observed when LMO pellet was deposited with $Sr(NO_3)_2$ and heat treated at 1150 ^{o}C for 12 hours (see section 4.3.1.2 of this chapter). Corbel *et al.*, reported appearance of La_2MoO_6 phase when powders of LMO and $La_{0.6}Sr_{0.4}Co_{0.2}Fe_{0.8}O_{3-\delta}$ were mixed and annealed at temperatures more than 800 ^{o}C [4]. Probably this phase is a high temperature reaction product of LMO with Sr substituted perovskites.

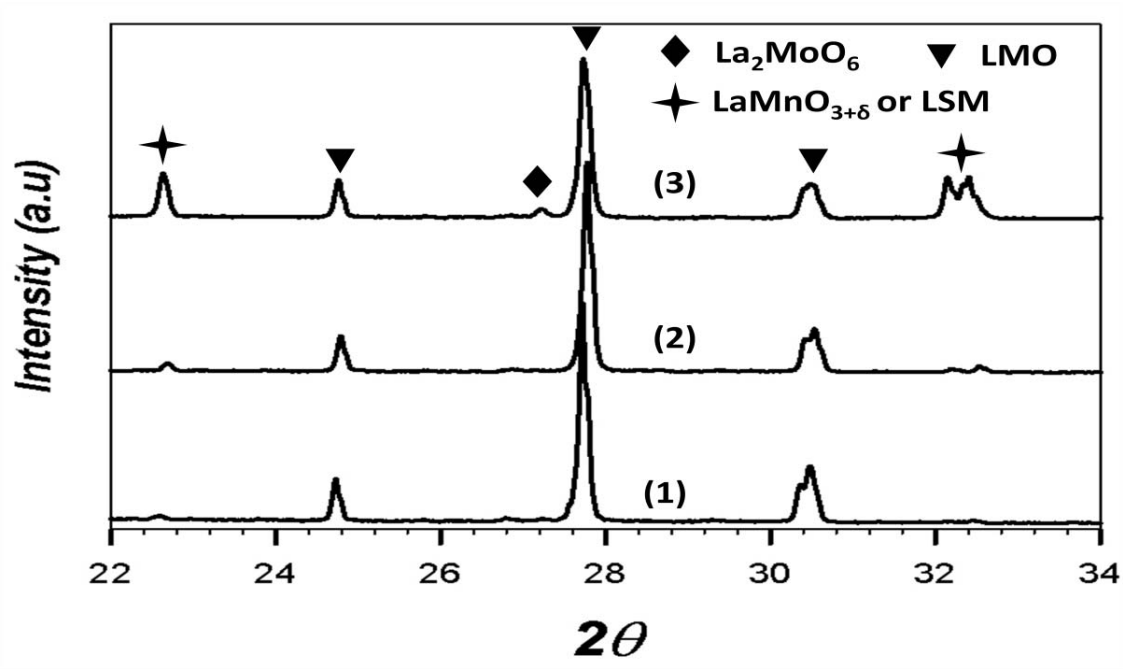

Figure 4.25: XRD patterns collected on the surface of the LMO pellets which were coupled with LSM and annealed at ***(1)****: 1050 ^{o}C for 12 hours,* ***(2)****: 1050 ^{o}C for36 hours and* ***(3)****: 1150˚C for 12 hours.*

The three LMO pellets were analyzed by FIB-SIMS surface analysis and numerous rod shaped structures were observed on the surface of all the three. In agreement with the reaction kinetics the size and number of rod like structures were higher in case of LMO pellet which was annealed at 1150 ^{o}C compared to pellet annealed at 1050 ^{o}C for 36 hours and even more when

compared to pellet annealed at 1050 ^{o}C for 12 hours. FIB-SIMS mass spectra analysis carried out on the rod like structures on the LMO pellet annealed at 1150 ^{o}C revealed that these structures were made up of La and Mn. The mass spectrum collected on these grains shows the presence of Mn^{+} (55), La^{+} (139), LaO^{+} (155) species (see the Fig. 4.26). On the other hand, another mass spectrum was collected on the area where rod shaped structures were not present. Such mass spectra does not indicate the presence of Mn^{+} (see the Fig. 4.27). Considering the XRD results and mass spectra, it can be assumed that the composition of these rod shaped structures on the LMO surface is $LaMnO_{3-\delta}$. FIB-SIMS surface image of LMO pellets which were annealed at 1050 ^{o}C for both 12 and 36 hours are given in Fig. 4.28.

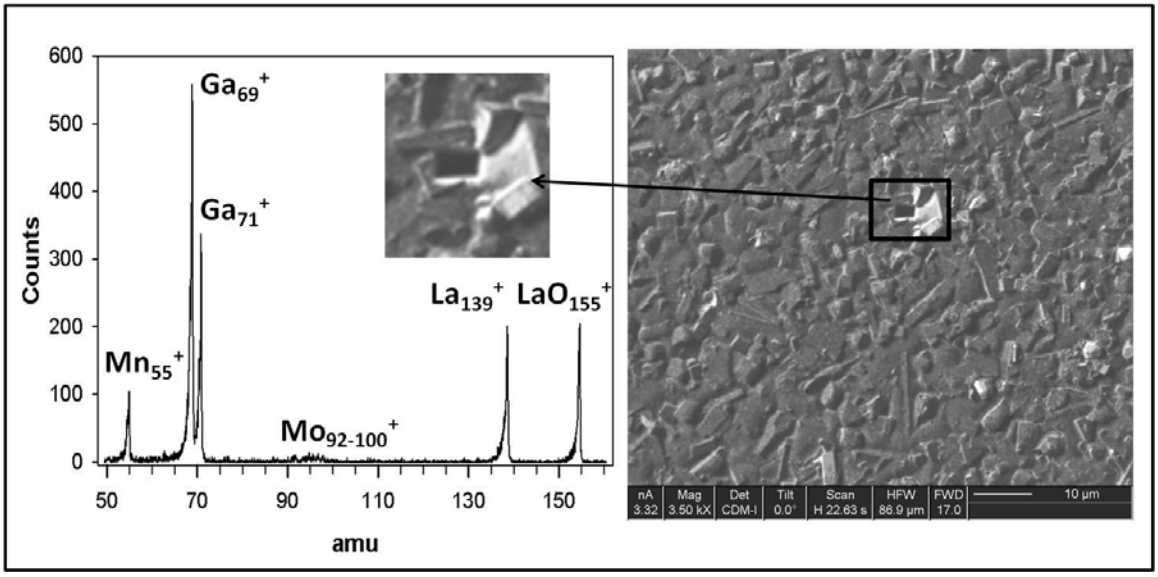

Figure 4.26: Mass spectrogram collected on the rod-shaped grains observed on the LMO sample surface which was annealed at 1150 ^{o}C for 12 h after coupling with LSM. Mn^{+} peak at 55 amu can be clearly observed. The crater formed from mass spectra is showed in the circle in the FIBS-Ion image.

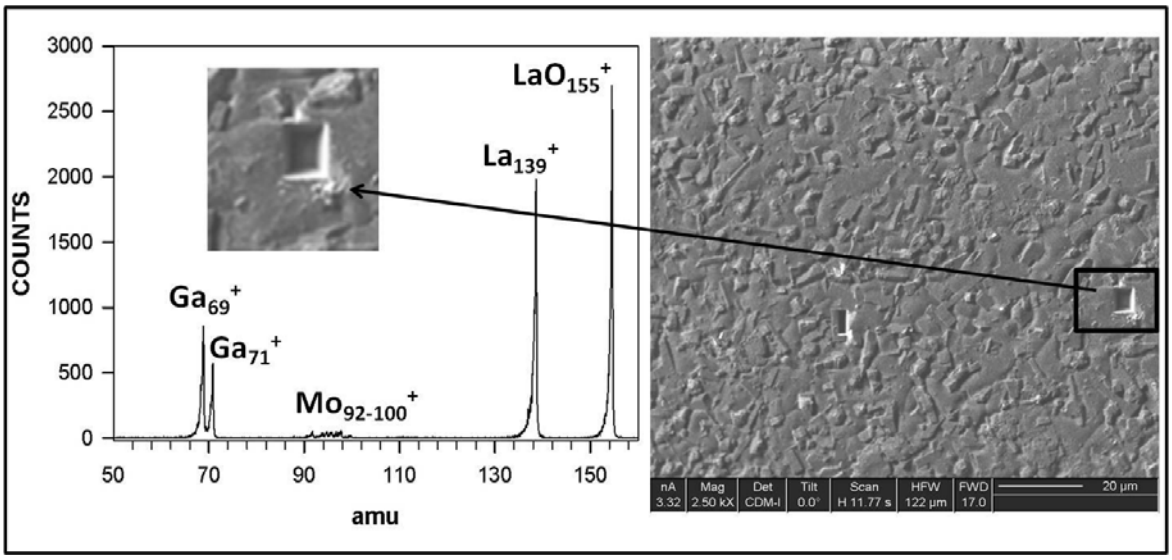

Figure 4.27: Mass spectrum collected on planar area on the LMO sample surface sample surface which was annealed at 1150 ^oC for 12 h after coupling with LSM. No Mn^+ peak at 55 amu can be seen here. The crater formed from mass spectra is showed in the circle in the FIBS-Ion image.

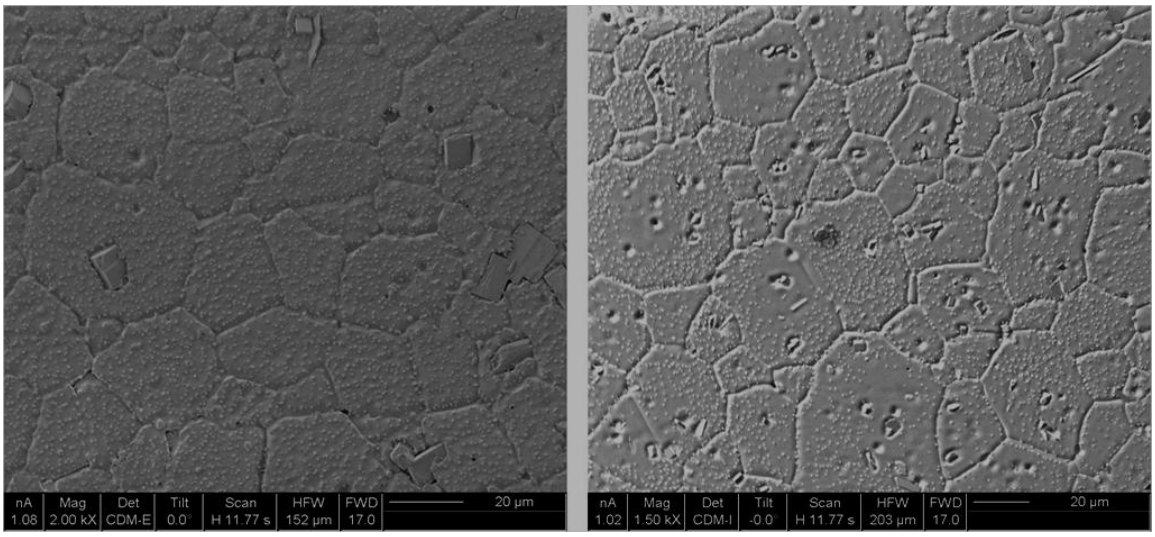

Figure 4.28: FIB-SIMS surface ion image of LMO pellet annealed at 1050 ^oC for 12 h (right). FIB-SIMS surface Electron image of LMO pellet annealed at 1050 ^oC for 36 h (left). Rod shaped $LaMnO_3$ structures can be noticed. Small dot like structures on the image are the result of Au sputtering.

4.3.2.2: XRD analysis and FIB-SIMS surface analysis on $La_{0.8}Sr_{0.2}MnO_3$ pellets:

Surface of all three LSM pellets appeared rough (to the naked eye) after the heat treatments at 1050 ^oC (for 12 and 36 hours) and 1150 ^oC (initially these pellets were mirror polished). These pellets were then analyzed by XRD, and new $SrMoO_4$ type phase was detected (see the Fig. 4.29). Possible appearance of $SrMoO_4$ type phases in these compounds was already discussed in earlier sections along with respective phase diagram (high solubility limit of La/Sr in $SrMoO_4$ and $La_2Mo_3O_{12}$). The same behavior is suspected to be reason for the variations in the intensity of the peaks (in XRD pattern) attributed to $SrMoO_4$ type phase.

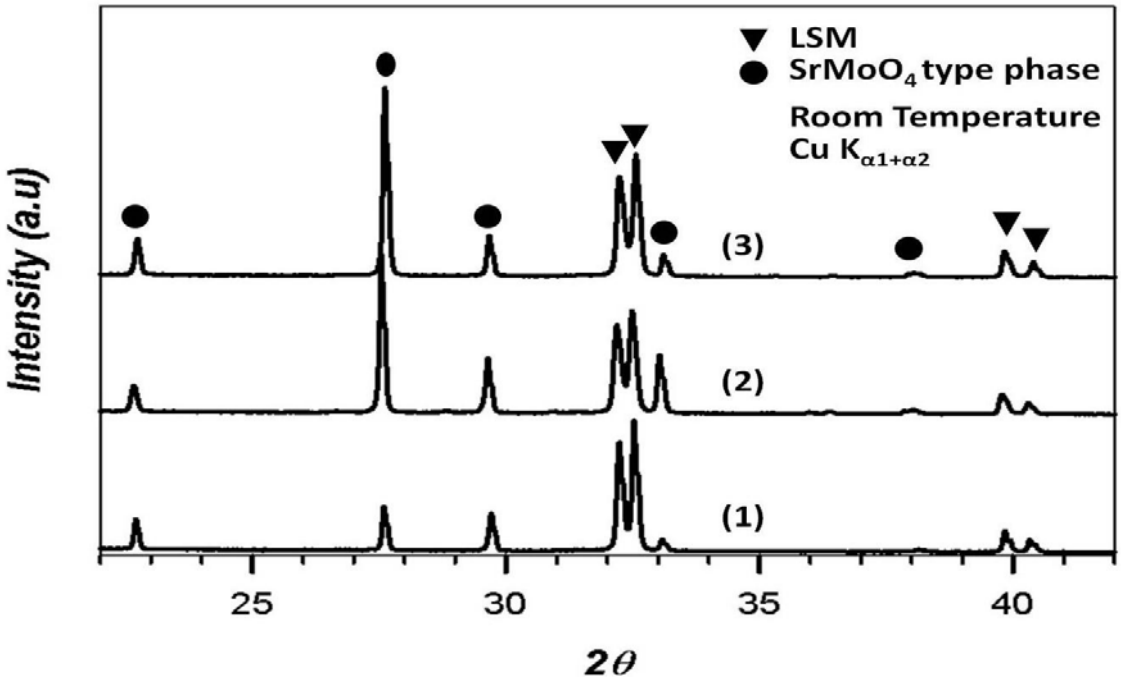

*Figure 4.29: X-ray diffraction pattern collected on the surface of the LSM pellets which was coupled with LMO and annealed at **(1)**: 1050 ^oC for 12 hours, **(2)**: 1050 ^oC for36 hours and **(3)**: 1150˚C for 12 hours.*

FIB-SIMS ion and electron images were collected on LSM pellet which was annealed at 1050 ^oC for 36 hours (see Fig. 4.30). During both the images (ion and electron) variation in the contrast was observed. When insulating material (non electronic conductive) material is exposed to electron beam, this variation is observed and this behavior is common for any electronic imaging (SEM, TEM etc...). Ion image was clear whereas electronic image was dark on some

areas. This insulating layer was attributed to $SrMoO_4$ or $SrMoO_4$ based materials (with La in the matrix) and the bright areas on the electronic image are attributed to LSM material (as observed by XRD).

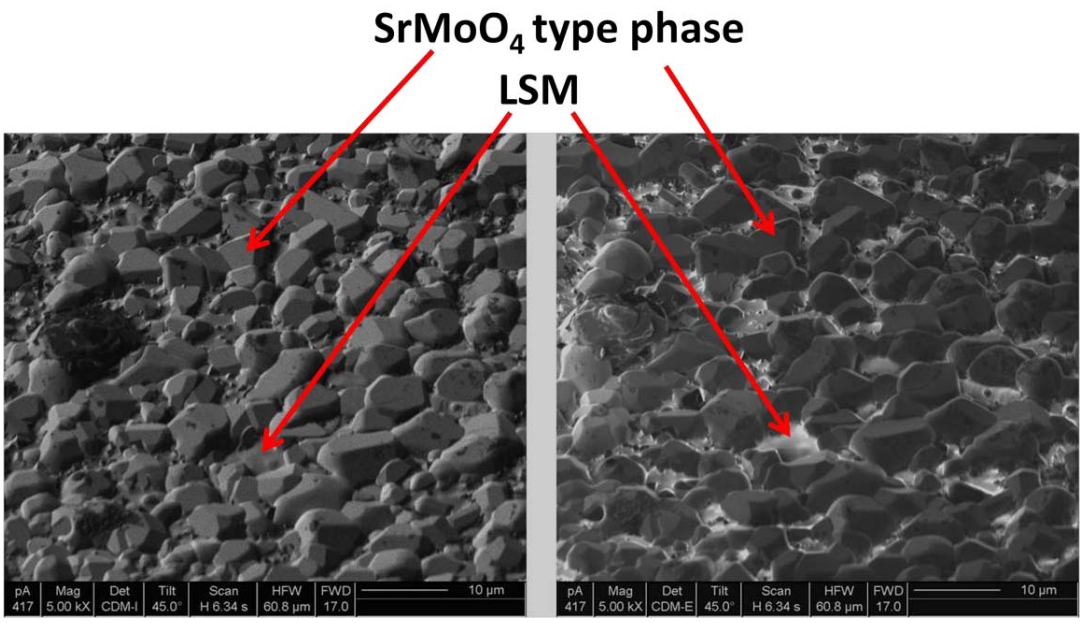

Figure 4.30: FIB-SIMS surface Ion image (left) and Electron image (right) of LSM pellet (annealing at 1050 ^{o}C for 36 Hours). This contrast in ion and surface image is because of $SrMoO_4$ type insulating phase.

4.3.2.3: FIB-SIMS depth profile analysis on $La_2Mo_2O_9$ / $La_{0.8}Sr_{0.2}MnO_3$ couples:

FIB-SIMS depth profile analysis was carried out on all the three couples on both LMO and LSM pellets (on the faces which were in contact) (see Fig. 4.31). Depth profiles were plotted in a way to ease the understanding of diffusion behavior in these samples. The line separating both the pellets is the interface at which the pellets were coupled and annealed.

On the LMO / LSM couple annealed for 12 hours at 1050 ^{o}C (see Fig. 4.31): on the LSM pellet no significant change in signals of either La^+ or Mn^+ were detected. However Mo^+ is found deep till 2 µm, which was diffused from LMO side of couple. Mo^+ share similar profile with that

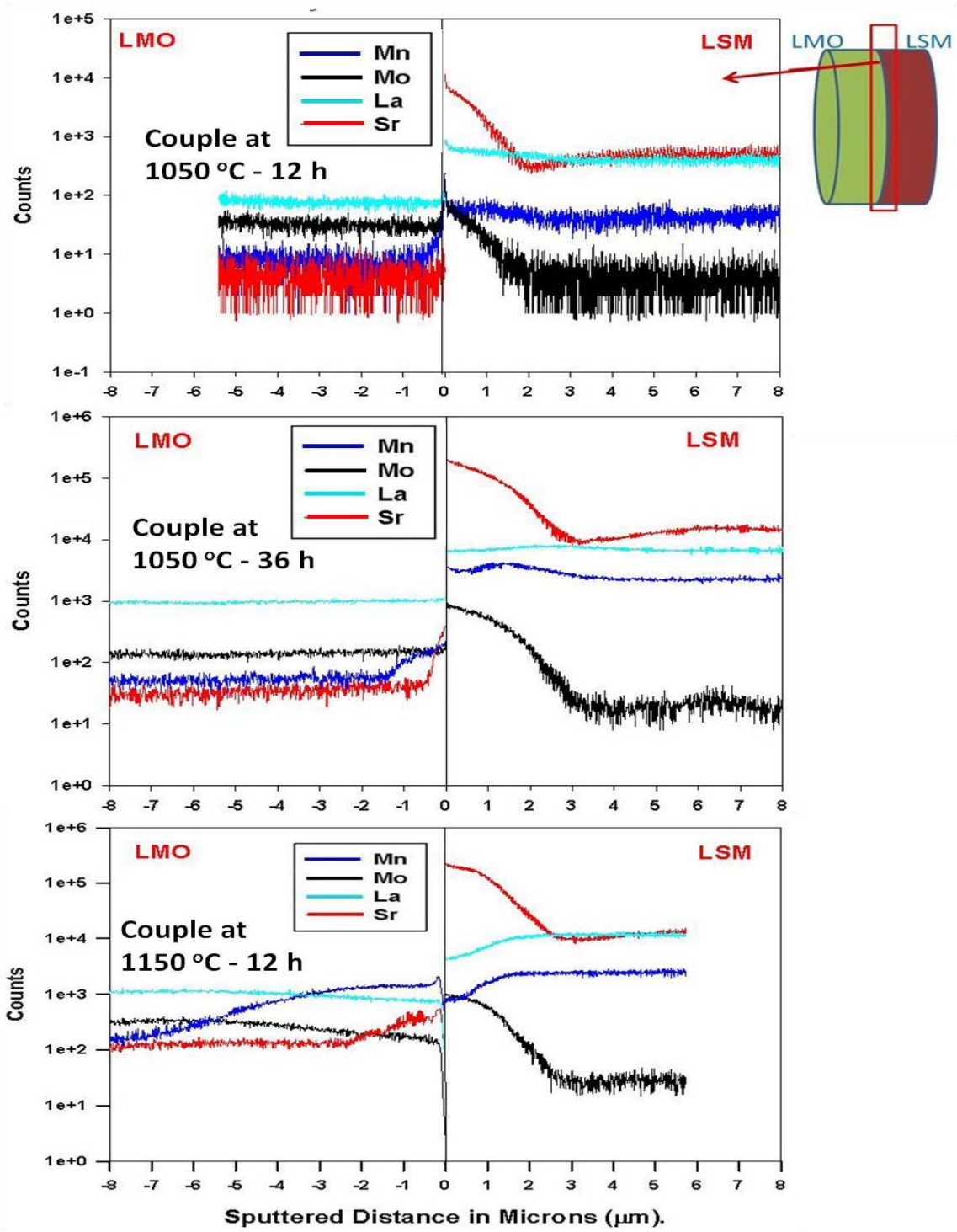

Figure 4.31: FIB-SIMS depth profile collected couples of LMO and LSM pellets which were annealed for 12 hours at 1050 °C (top), 36 hours at 1050 °C (middle) and 12 hours at 1150 °C bottom. Similarity in Sr^+ and Mo^+ profile on LSM side showing probable existence of $SrMoO_4$ type phase. On the LMO side Mn can be seen with changes in the length of diffusion.

of Sr^+. $SrMoO_4$ type phase detected by XRD was in agreement with this presence. Depth profile collected on LMO pellet does not reveal any Sr presence however almost negligible amount of Mn was noticed on the surface. No change in the profiles of La^+ and Mo^+ are noticed, this may mean that most of the surface is bulk LMO material.

For the couple annealed for 36 hours at 1050 ^oC (see Fig. 4.31): on the LSM part, Sr^+ and Mo^+ signals were seen with similar profile (till ~3 μm) defining possible presence of $SrMoO_4$ type phase. No big variation in the La^+ profile was seen, which suggest that La was present in $SrMoO_4$ type matrix. Little variation in the Mn^+ signal was noticed at the surface of profile, which remains constant after 3 μm. These results suggest that, Mo from LMO diffused towards LSM and reacted with Sr in LSM creating $SrMoO_4$ type insulating phase. Depth profile analysis of LMO pellet show presence of Mn^+ until ~1.5 μm, whereas Sr^+ signal can be seen till ~0.5 μm. No change in the profile of La^+ and Mo^+ were noticed. Presence of rod shaped $LaMnO_3$ structures on the surface of LMO pellet and Mn^+ presence until ~1.5 μm suggest that these rod shaped structures are approximately ~1.5 μm thick.

For the couple annealed for 12 hours at 1150 ^oC (see Fig. 4.31); on the LSM side of the couple, Mo^+ signal can be seen down to ~2.5 μm below surface and considering the similarities in the profile of Sr^+ and Mo^+ it can be assumed that the surface is rich in $Sr(MoO_4)$ type phase. La^+ and Mn^+ content was low at the surface which could be because of their probable diffusion towards LMO. The change in La^+ and Mn^+ profiles could also be because of the presence of higher amounts of $Sr(MoO_4)$ type phases on the surface of pellet, than deeper stabilize to constant levels. Mo^+ cannot be seen after ~2.5 – 3 μm. All the elements La^+, Mn^+ and Sr^+ get remain constant thereafter. In other words, LSM bulk material appears below ~2.5 – 3 μm depth.

On the depth profile on LMO, Mn^+ was seen down to 6 μm from the interface. Presence of rod shaped structures on LMO side of the pellet was already discussed earlier and it was also known that these rod shaped structures are rich in La and Mn and correspond to $LaMnO_3$ material. Following the appearance of Mn^+ down to ~6 μm deep, it would be sensible to assume that the rods shaped structures were present down to ~6 μm in depth. Change in Mo^+ profile in LMO pellet could be caused by Mo loss (or diffusion) towards the LSM side for formation of $Sr(MoO_4)$ type phases. La^+ signal is almost constant. Uneven distribution of rod shaped grains makes it hard to estimate the exact depth at which $LaMnO_3$ exist. Sr^+ was also seen in LMO

pellet until ~2 µm, however its amount is low. Sr could have entered into LMO matrix, which is possible as discussed in earlier sections. XRD analysis revealed that LMO was in monoclinic α-LMO form. It was reported by Gao *et al.* [7] that, when Sr substitution to La in LMO is less than 2 mol%, no change in the room temperature monoclinic structure can be detected (as discussed in section 4.3.1.2. of this chapter). This possibility of Sr diffusion in LMO cannot be overruled. Similar observations as in annealing measurement performed at 1050 ^{o}C were observed here, but with higher diffusion lengths. Explanation of the reaction mechanisms are discussed in next section.

Taking the penetration depths of Mo in LSM part of couple and Sr and Mn in LMO part of the couple (for two couples: 1050 ^{o}C for 36 h and 1150 ^{o}C for 12 h), respective diffusion coefficients were estimated using the equation $\boldsymbol{L = 2(Dt)^{1/2}}$. Respective penetration depths of elements and there estimated bulk diffusion coefficients were given in Table 4.3.

Element	*LMO/LSM Couple (1050 °C/36 h)*		*LMO/LSM Couple (1150 °C/12 h)*	
	Penetration Depth (µm)	*Diffusion Coeff. ($cm^2.s^{-1}$)*	*Penetration Depth (µm)*	*Diffusion Coeff. ($cm^2.s^{-1}$)*
Mn in LMO	**1.5**	**~4 x10^{-14}**	**6**	**~2 x 10^{-12}**
Sr in LMO	**0.5**	**~5x10^{-15}**	**2**	**~2x10^{-13}**
Mo in LSM	**3**	**~1.5x10^{-13}**	**2.5**	**~3.5x10^{-13}**

Table 4.3: Penetration depths and estimated bulk diffusion coefficients of Mn, Sr and Mo observed in LMO/LSM couples (annealed at 1050 ^{o}C /36 h and 1150 ^{o}C/12h).

4.3.2.4: Discussions

In all of the diffusion measurements concerning couples of LMO / LSM, few limitations were observed. Structural similarities between LSM and $LaMnO_3$, aswell as between $SrMoO_4$ and $La_2Mo_3O_{12}$ phases, and high solubility of La/Sr in either of the phases have to be taken into account for the interpretation. XRD data was always limited to its penetration depth, considering existence of different reaction products as the function of depth of the pellet only averaged X-ray

data was obtained. However for the reaction mechanism concerning coupled pellets we propose three hypotheses.

In first hypothesis: Cross diffusion of La from LMO and Sr from the LSM pellet takes place. Such Sr deficient LSM phase on LSM pellet would become $LaMnO_{3-\delta}$ and $La_{2-x}S_xMo_2O_{9-d}$ is formed on LMO surface. Once the samples were cooled by opening furnace doors (which cannot be considered quenching), there would be demixion of Sr forming LMO and $SrMoO_4$ type phases. This demixion phenomenon has already been observed in alkaline earth LAMOX compounds. This behavior probably occurs in LMO /LSM couples at 1050 ^oC. Whereas in couple annealed at 1150 ^oC, demixion leads to formation of La_2MoO_6 (a Mo deficient lanthanum molybdate phase), $La_{1-x}MnO_{3-\delta'}$ (a La deficient lanthanum manganate phase), $SrMoO_4$ and LMO phases. LSM grains which lost Sr towards LMO, forms $LaMnO_3$ rod shaped structures, and these structures stick to the surface of LMO pellet while cooling back (see the Fig 4.32). The reaction mechanism is stated as:

For LMO / LSM couple at 1050 ^oC:

$$\mathbf{La_{1-x}Sr_xMnO_{3-\delta} + La_2Mo_2O_9 \rightarrow LaMnO_{3-\delta'} + La_{2-x}Sr_xMo_2O_{9-x/2} \rightarrow LaMnO_{3-\delta'} + (1-x/2)\ La_2Mo_2O_9 + x\ SrMoO_4}$$

For LMO / LSM couple at 1150 ^oC:

$$\mathbf{La_{1-x}Sr_xMnO_{3-\delta} + La_2Mo_2O_9 \rightarrow LaMnO_{3-\delta'} + La_{2-x}Sr_xMo_2O_{9-x/2} \rightarrow La_{1-x}MnO_{3-\delta'} + (1-x)\ La_2Mo_2O_9 + x\ SrMoO_4 + x\ La_2MoO_6}$$

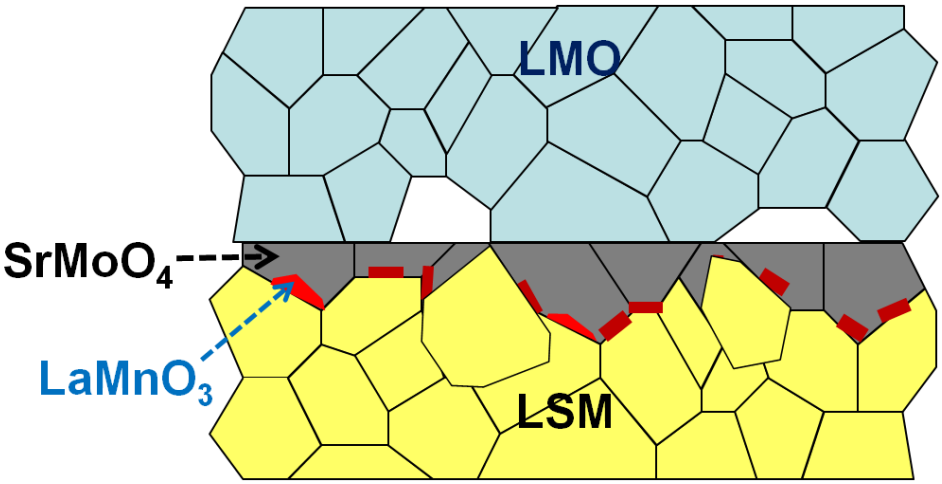

Figure 4.32: Schematic representation of reaction products observed in LMO and LSM couple.

As of the first hypothesis, $LaMnO_3$ phase has to be observed in between layers of $SrMoO_4$ and LSM, which was not consistent with the observation. To overcome this limitation another hypothesis is proposed. Second hypothesis is based upon an assumption of substituting cation(s) segregation towards the surface of sample. Such a segregation behavior upon annealing is a well acknowledged phenomenon in $A_{1-x}S_xBO_3$ perovskites [12-16] (as discussed earlier in section 4.3.1.3 of this chapter). One can therefore assume that a thin layer of $SrMnO_{3-\delta}$ grows on the LSM surface, before reaction with LMO pellet. $SrMnO_{3-\delta}$ then reacts with LMO to form $SrMoO_4$ and $LaMnO_3$ type phases. By cross diffusion of Mo and Mn through the surface $LaMnO_3$ forms rod like structures and sticks to the surface of the LMO pellet, and $SrMoO_4$ remains at the surface of LSM pellet. For couple at higher annealing temperature (1150 ^oC), $LaMnO_3$ becomes La deficient forming $La_{1-x}MnO_{3-\delta'}$ and such depleted La reacts with LMO forming La_2MoO_6 phase. Schematic representation of this mechanism can be seen in Fig. 4.33. The reaction equation would be:

Surface segregation:

LSM → Σ $SrMnO_{3-\delta}$ (surface) + **LS′M** (LS′M with slightly lower Sr amount than LSM)

Surface reaction in couples at 1050 ^oC:

$$\mathbf{SrMnO_{3-\delta} + \tfrac{1}{2}\, La_2Mo_2O_9 \rightarrow SrMoO_4 + LaMnO_3 + \tfrac{1}{4}\, O_2\uparrow}$$

Surface reaction in couples at 1150 ^{o}C:

$$SrMnO_{3-\delta} + \frac{1}{2}(1 + x)\, La_2Mo_2O_9 \rightarrow SrMoO_4 + La_{1-x}MnO_{3-\delta'} + x\, La_2MoO_6 + \frac{1}{4}\, O_2\uparrow$$

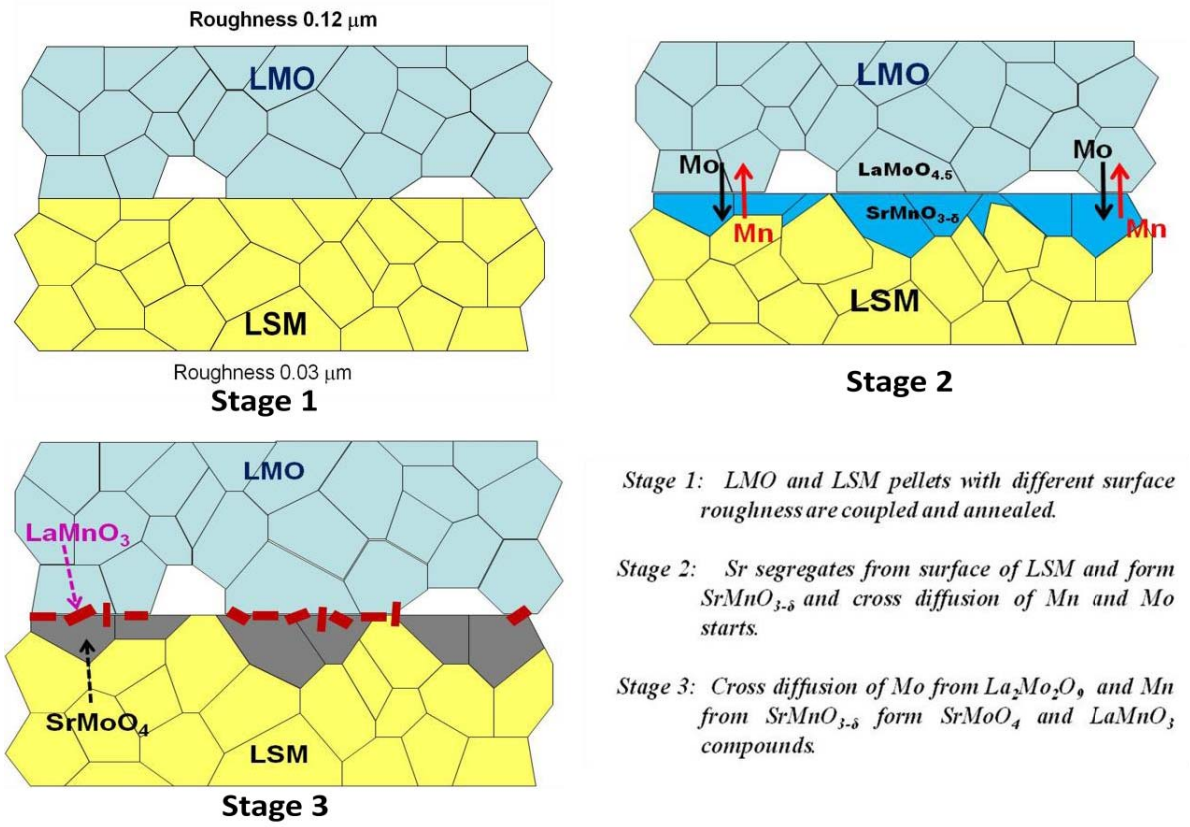

Figure 4.33: Schematic representation of hypothesis 2; a possible reaction mechanism in LSM/LMO couples

The third hypothesis is a variant of the second one without prior Sr segregation. In these couples there would be cross cationic exchange of Mn from LSM side and Mo from LMO side. Excess Sr from Mn deficient LSM reacts with diffused Mo and forms $Sr(MoO_4)$ type phase. This area on LSM pellet which lost both Sr for $SrMoO_4$ formation, and Mn for migration; turns into $LaMnO_{3+\delta}$. As both LSM and $LaMnO_3$ share the same crystallographic rhombohedral structure, it cannot be clearly differentiated by X-ray diffraction. On the other side of the couple: Mo deficient lanthanum molybdate (since LMO lost Mo towards LSM) reacts with cross diffused Mn forming $LaMnO_{3+\delta}$ (freshly nucleated rod like structures). This kind nucleation of $LaMnO_{3+\delta}$

is observed when Mn rich solution is deposited on LMO pellets. In couple at 1150 °C, $LaMnO_3$ becomes La deficient forming $La_{1-x}MnO_{3-\delta'}$ and such depleted La reacts with LMO forming La_2MoO_6 phase. Schematic representation of reaction mechanism is given in Fig. 4.34.

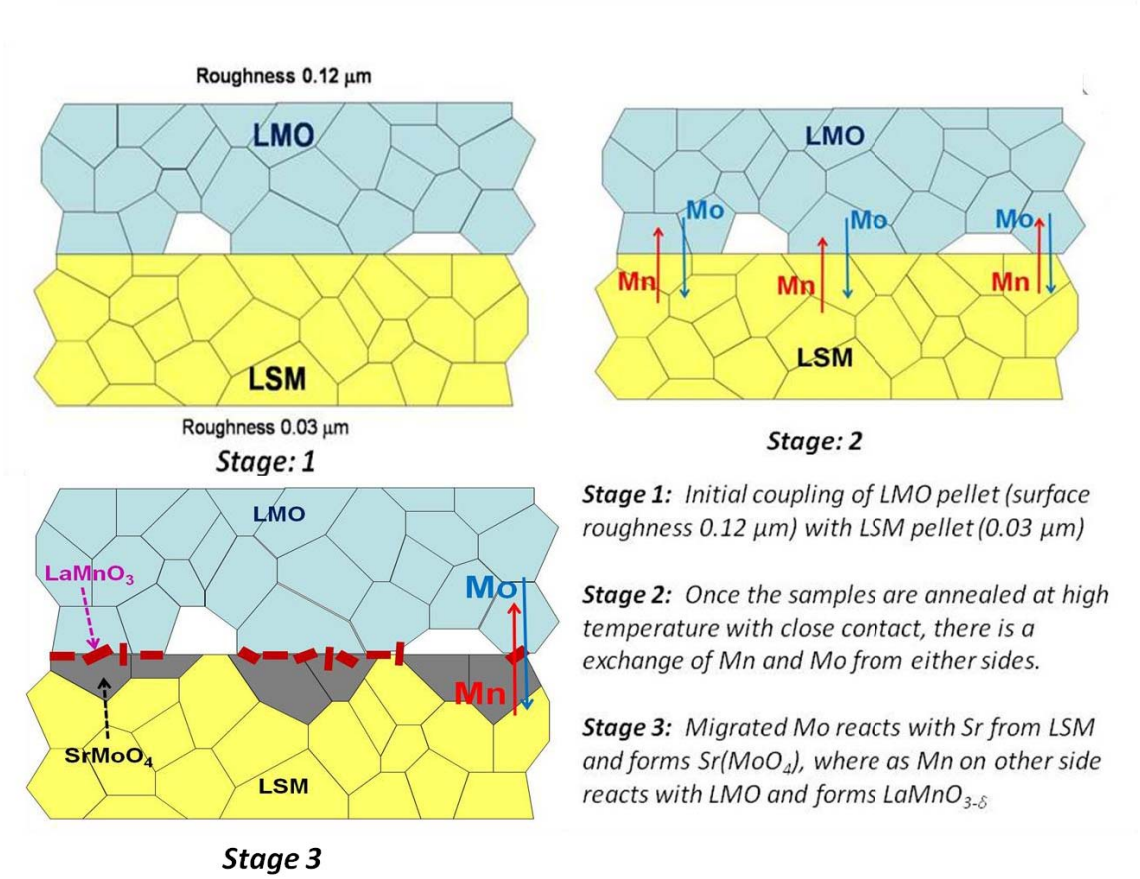

Figure 4.34: Schematic representation of possible reaction mechanism in LSM and LMO couples which were annealed at elevated temperatures (hypothesis 3).

Reaction in couples at 1050 °C:

$$\mathbf{La_{1-x}Sr_xMnO_3 + x/2\ La_2Mo_2O_9 \rightarrow LaMnO_3 + x\ SrMoO_4 + x/4\ O_2\uparrow}$$

Reaction in couples at 1150 °C:

$$\mathbf{La_{1-x}Sr_xMnO_3 + x\ La_2Mo_2O_9 \rightarrow La_{1-x}MnO_{3-\delta'} + x\ La_2MoO_6 + x\ SrMoO_4}$$

In solution deposited samples, care was taken to deposit same amount and amount of Sr and Mn on LMO pellets respectively. But when Mn rich solution was deposited on LMO pellet, there was huge amount of Mn_3O_4 (decomposed product of $MnCl_{2.4}H_2O$) left over on LMO surface which was unreacted. When $Sr(NO_3)_2$ solution was deposited on LMO pellet, there was no trace of SrO on the pellet surface. On the contrary, all the Sr is found to be reacted or deep in LMO pellet down to ~ 60 – 70 µm (as detected by TOF-SIMS line scan). In annealing measurements performed on the couples, Mn diffusion was quite limited. Mn diffusion of ~7 µm was observed on the LMO pellet which was annealed at 1150 ^{o}C. whereas on LMO pellets annealed at 1050 ^{o}C, Mn diffusion was limited to ~ 1 µm and ~0.5 µm (for 36 and 12 h respectively). This Mn seen on LMO pellets comes from rod shaped structures (see Fig. 4.35). This says the rate of reactivity of Mn with LMO is less than that of rate of reactivity Sr with LMO. In other words, $SrMoO_4$ forms more rapidly than $LaMnO_{3+\delta}$. This would be underlying reason for observation of significant amount of ($SrMoO_4$) type phased layer which was always observed on LSM side of the pellet.

Complex reactivity in these compounds, formation of undesired reaction products and cross cationic diffusion of almost all the elements in the system, create non-homogeneous surface at the interface of pellet. Even in cation rich solution deposition experiments, the same problem was encountered. This non-homogeneous surface makes it very hard to estimate the diffusion coefficient of elements into each other.

One of the main problems to study the diffusion mechanism was lack of proper interface. As mentioned already, in the coupled samples, after the heat treatment, both pellets went apart naturally. Intermediate reaction products were seen. Both surfaces have shown different surface morphologies and high surface roughness. Any diffusion study (estimated diffusion coefficients) carried to have quantitative information on such samples could have significant error scale. Apart from that, natural limitations of SIMS technique also effect in quantitative analysis of such data. For the future perspective it is suggested to use sputtering of LMO material on LSM pellet or vice versa. Many sputtering techniques can be taken into consideration (ex. RF-sputtering, CVD, PVD e.t.c). Such sputtering would generate uniform thin layers of one compound on the other and would eliminate need of proper interface.

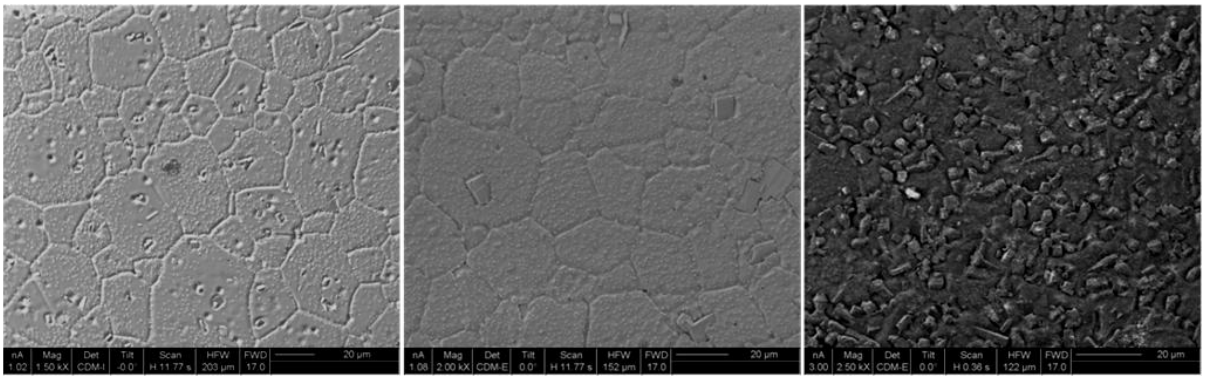

Figure 4.35: FIB-SIMS surface ion images of LMO pellets after coupling with LSM pellets and annealing (at1050 C^o for12 hrs; at 1050 ^{o}C for36 hrs; and at 1150 ^{o}C for12 hrs (from left to right)). The evolution of variation of size and the shape of the rod shaped $LaMnO_3$ formed on LMO pellets with change in reaction kinetics can be noticed.

4.4: Conclusions

The cross cation diffusion was investigated in the couples of LMO and LSM pellets. We reported the diffusive behavior of Sr, Mn when deposited on LMO pellets through solutions of $Sr(NO_3)_2$ and $MnCl_2 4H_2O$ respectively. When $(NH_4)_6Mo_7O_{24}{\cdot}4H_2O$ solution is deposited on LSM pellet, a complex reaction mechanism leading to the degradation of LSM pellet surface was observed.

In the solution deposited diffusion measurements: Penetration depth of Sr in LMO was ~ 60 µm (at 1150 ^{o}C for 12 h) and bulk diffusion coefficient of ~2 x 10^{-10} cm^2 s^{-1} at 1150 ^{o}C was estimated. Penetration depth of Mo in LSM was around ~50 µm (at 1150 ^{o}C for 12 h) and bulk diffusion coefficient of ~1 x 10^{-10} cm^2 s^{-1} at 1150 ^{o}C was estimated.

On the LMO/LSM coupled measurements after annealing, rod shaped $LaMnO_3$ grains are observed on LMO surface and $SrMoO_4$ type insulating surface is observed on LSM surface. Bulk diffusion coefficient of Mo in LSM was estimated as ~1.5x10^{-13} cm^2 s^{-1} and ~3.5x10^{-13} cm^2 s^{-1} at 1050 ^{o}C and 1150 ^{o}C respectively. Bulk diffusion coefficient of Mn in LMO was estimated as ~4x10^{-14} cm^2 s^{-1} and ~2x10^{-12} cm^2 s^{-1} at 1050 ^{o}C and 1150 ^{o}C respectively. Bulk diffusion coefficient of Sr in LMO was estimated as ~5x10^{-15} cm^2 s^{-1} and ~2x10^{-13} cm^2 s^{-1} at 1050 ^{o}C and

1150 ^{o}C respectively. The reactivity mechanism and reaction products observed in the measurements performed on LMO/LSM coupled pellets are in agreement with those observed in cation rich solution deposition measurements carried out on LMO and LSM pellets.

Bulk diffusion coefficients of Sr in both solution deposited on LMO pellet and from LSM pellet towards LMO (in LSM/LMO couple) are plotted in Fig. 4.36 and, assuming T-independent activation energy, linearly extrapolated down to lower temperatures. A standard fuel cell based on YSZ/LSM usually operates in the 900-1000°C thermal range, whereas a fuel cell based on a LAMOX electrolyte would operate in the same conditions but at a 150 °C lower temperature at least (around 750-850 ^{o}C). For comparison, diffusion coefficients of Sr in YSZ were adopted from Kilo *et al.*[10] and such diffusion coefficients (of Sr in YSZ) were extrapolated to lower temperatures. Diffusion coefficient of Sr (from LSM) into YSZ would be around ~$1x10^{-20}$ cm^2 s^{-1} at 900-1000 ^{o}C (operating temperatures of YSZ/LSM SOFC), and such diffusion coefficient would lead to penetration depth of ~10 nm/year at 900-1000 ^{o}C (YSZ/LSM operating temperatures), and using $\boldsymbol{L = 2(Dt)^{½}}$, it would lead to penetration depth of ~10 nm/year (seemingly a reasonable value since YSZ electrolyte is commonly used with LSM cathode in standard SOFC devices). which is a reasonable value and hence the use of YSZ electrolyte with LSM cathode in SOFC. Sr diffusion coefficient (from LSM to LMO) was extrapolated to be around ~$1x10^{-20}$ cm^2 s^{-1} at ~ 800 ^{o}C, the likely operating temperature of LMO based SOFC, and such diffusion value corresponds to the penetration depth of ~10nm/year. i.e. the same range as for YSZ in its operating conditions. Such a conclusion lies on several assumptions, as for instance that our estimation of diffusion coefficient is accurate enough, and that one can linearly extrapolate down to low temperature. Above all, there is the uncertainty on the measurement of Sr diffusion coefficient depending on the Sr source. An underestimation of 3 orders of magnitude (as for Sr from solution deposition) might result in an even larger underestimation at the operating temperature (depending on activation energy), which would be dramatic for Sr penetration.

Sr penetration depth estimated from the FIB-SIMS depth profiles might be largely underestimated due to the difficulty to identify the pellets surface/interface. In these conditions, is a penetration depth of ~0.5 µm of Sr at 1050 °C/36h may not be realistic. The inaccuracy in the surface position can be as high as 5 µm, as for instance, if our diffusion model is incorrect

and $SrMoO_4$ grains originally belong to the LMO pellet: these $SrMoO_4$ grains might have sticked to the LSM pellet and be pulled out during separation. A penetration depth of 5 µm instead of ~0.5 µm is an order of magnitude higher, resulting in a diffusion coefficient 2 orders of magnitude higher. Sr diffusion coefficient values would be closer to the solution deposition values, and extrapolation would give much higher value.

Let us now assume that the discrepancy between the diffusion coefficients of Sr measured from solution deposition and from LSM/LMO couple reflects a real difference due to the difference in Sr source. Since it is known that Sr tends to segregate out from LSM when cooled down, it would mean that this segregated Sr is much more likely to diffuse in the electrolyte than the bulk Sr from LSM. Since this segregated Sr is formed essentially when the cell is cooled down or heated up, its presence at electrolyte/cathode interface would be affected by the frequency of cell operating disruptions and would lead to premature ageing of the cell.

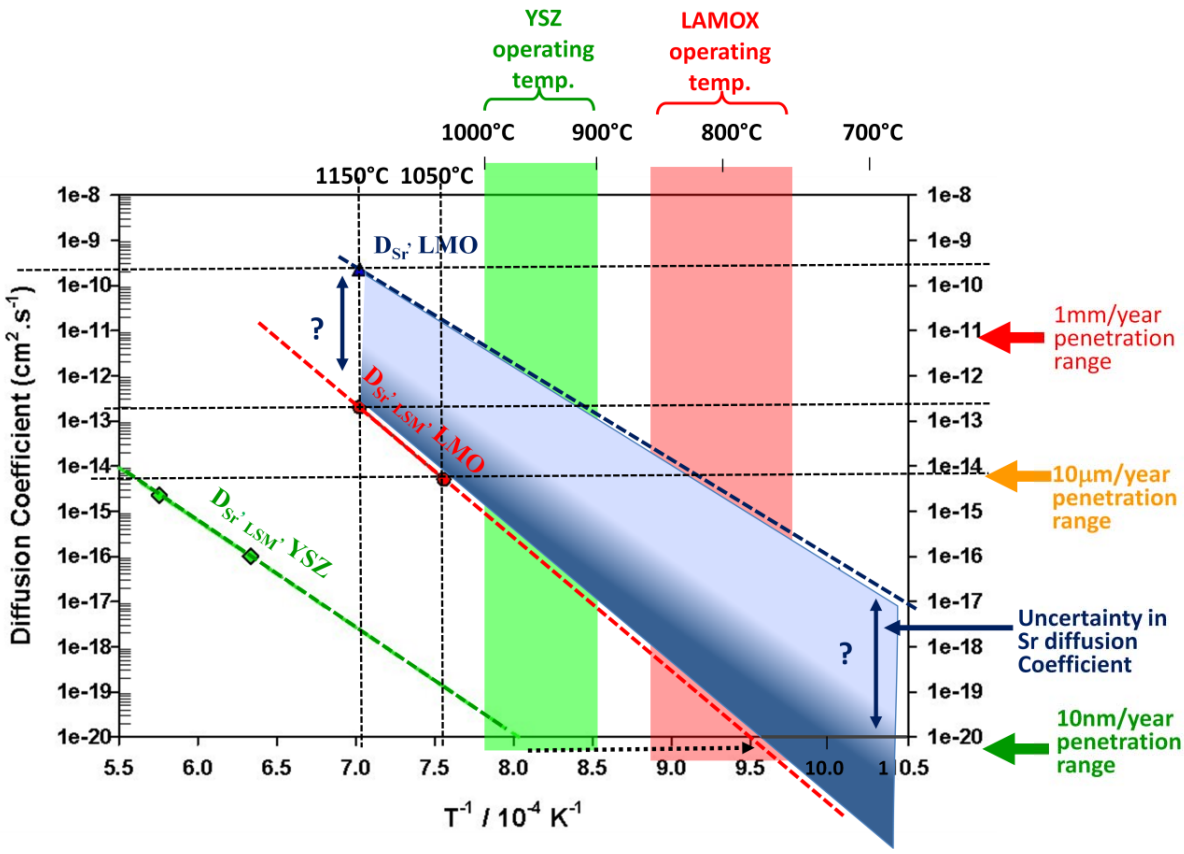

Figure 4.36: Evolution of bulk diffusion coefficients of Sr (from both LSM pellet (red line) and solution deposition (dark blue line)) in to LMO. Sr diffusion values from LSM into YSZ (green line) are adopted from Kilo et al.[10]

Corbel *et al.* [4] reported that LMO and LSM are stable under 700 °C and $SrMoO_4$ type phase appears upon further heating (around ~800 °C). It seems strange that, with a Sr diffusion kinetics as low as $1x10^{-20}$ $cm^2.s^{-1}$ (extrapolated from our measurements), such a minute effect as 10nm/year penetration depth would be detected by XRD after just 3 days. A sensible alternative would be that Mo (from LMO) diffuses more towards LSM than Sr (from LSM) towards LMO, and as a matter of fact, it was observed that estimated Mo diffusion coefficients are much higher when extrapolated towards lower temperatures (see Fig. 4.37). Penetration depth of Mo was estimated to be ~3µm/year at 800 °C. Even though Sr diffusion is low, Mo cross diffusion is higher and hence the $SrMoO_4$ layer is formed (which is problematic for fuel cell).

Note that estimated diffusion coefficient of Mn from LSM into LMO is also low at ~$1x10^{-20}$ $cm^2.s^{-1}$at 800 °C.

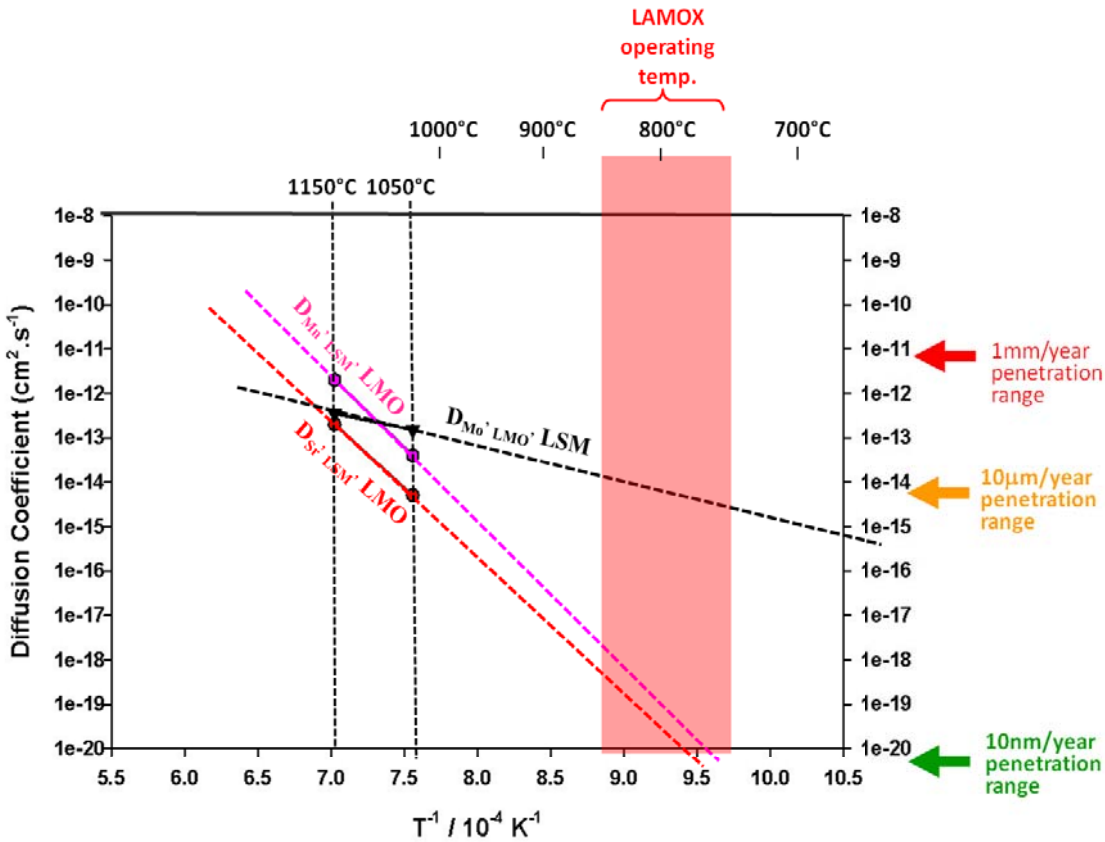

Figure 4.37: Evolution of bulk diffusion coefficients of Sr (red) and Mn (pink) from LSM to LMO and Mo (black) from LMO towards LSM.

Overall and independently from the accuracy problem on diffusion coefficient measurements, these results tend to show that the LMO/LSM couple is reactive, and that such an electrolyte/cathode association is not suitable as is for SOFC applications. However, both materials could be used with a proper buffer layer in between, so that cross cationic-diffusion of elements between LMO to LSM is stopped.

Concerning the aim of measuring accurately cationic diffusion coefficient in this particular system, high surface roughness, lack of proper interface in coupled samples and complex reactivity mechanisms make it very hard to reach. Such limitations have certainly affected the estimated diffusion coefficients reported in this work. Natural limitations of SIMS technique and XRD analysis, similarities in the structural arrangement of reaction products and parent compounds also limited the precision of diffusion study. For any further diffusion study on these samples, different sample preparation methods should be tested. Sputtering of thin layers of LMO on LSM or vice versa is suggested, from which more precise diffusion coefficients could be obtained.

4.5: References

1. G. Corbel; P. Lacorre, *Journal of Solid State Chemistry* **2006,** 179, (5), 1339-1344.
2. D. Marrero-Lopez; J. Pena-Martinez; J. C. Ruiz-Morales; D. Perez-Coll; M. C. Martin-Sedeno; P. Nunez, *Solid State Ionics* **2007,** 178, (23-24), 1366-1378.
3. C. Tealdi; G. Chiodelli; G. Flor; S. Leonardi, *Solid State Ionics* **2010,** 181, (31-32), 1456-1461.
4. G. Corbel; S. Mestiri; P. Lacorre, *Solid State Sciences* **2005,** 7, (10), 1216-1224.
5. T. Horita; M. Ishikawa; K. Yamaji; N. Sakai; H. Yokokawa; M. Dokiya, *Solid State Ionics* **1998,** 108, (1-4), 383-390.
6. E.Ya.Rode; G. V. Lysanova; L. Z. Gokhman, *Inorganic Materials* **1971,** 7, (11), 1875-1877.
7. X. M. Gao; T. M. He; Y. Shen, *Journal of Alloys and Compounds* **2008,** 464, (1-2), 461-466.
8. W. THEPSUWAN; S. KUHARUANGRONG, *Journal of Metals, Materials and Minerals* **2008,** 18, (2), 125-129.
9. V. P. Sirotinkin; A. A. Evdokimov; V. K. Trunov, *Russian Journal of Inorganic Chemistry (Eng. Tran.)* **1981,** 26, (7), 1018-1020.
10. M. Kilo, *Defects and Diffusion in Ceramics: an Annual Retrospective Vii* **2005,** 242-244, 185-253.
11. T. Horita; N. Sakai; T. Kawada; H. Yokokawa; M. Dokiya, *Journal of the American Ceramic Society* **1998,** 81, (2), 315-320.
12. J. Choisnet; N. Abadzhieva; P. Stefanov; D. Klissurski; J. M. Bassat; V. Rives; L. Minchev, *Journal of the Chemical Society-Faraday Transactions* **1994,** 90, (13), 1987-1991.
13. P. Decorse; G. Caboche; L. C. Dufour, *Solid State Ionics* **1999,** 117, (1-2), 161-169.
14. G. Horvath; J. Gerblinger; H. Meixner; J. Giber, *Sensors and Actuators B-Chemical* **1996,** 32, (2), 93-99.
15. S. P. Jiang; J. G. Love, *Solid State Ionics* **2001,** 138, (3-4), 183-190.
16. M. M. Viitanen; R. G. von Welzenis; H. H. Brongersma; F. P. F. van Berkel, *Solid State Ionics* **2002,** 150, (3-4), 223-228.

Chapter 5: LAMOX stability under Reductive Atmospheres

5.1: Introduction 169

5.2: Stability of $La_2Mo_2O_9$ under reductive atmospheres 171

5.3: Stability of $La_2Mo_2O_9$ and $La_2Mo_2O_{7-\delta}$ (amorphous 7-δ) under mild reductive conditions 179

5.4: Triggering and boosting of reduction process 184

5.5: Stability of W- substituted $La_2Mo_2O_9$ under reductive atmospheres 188

5.6: Thermodynamic stability of $La_2Mo_2O_9$ and W- substituted $La_2Mo_2O_9$ under pO_2 pressures 194

5.7: Conductivity experiments on reduced $La_2Mo_2O_9$ and reduced W-LAMOX materials 196

5.8: Conclusions 203

5.9: References 205

Chapter 5:
LAMOX stability under Reductive Atmospheres

5.1: Introduction:

$La_2Mo_2O_9$ (LMO) is not stable in reductive atmospheres, making it a non suitable candidate for electrolyte applications in conventional double chamber SOFC. H_2 or diluted H_2 when boosted to anode reacts with the electrolyte at electrolyte–anode interface and can lead to the decomposition of the material. The decomposed material affect the conductive property of the material leading to the fall in cell overall potential and could even cause total cell failure. Goutenoire *et al.* in 1999 reported partial reduction of LMO when annealed at 700 ^oC under diluted H_2 (6% H_2 + 94% N_2). LMO first reduces to $La_7Mo_7O_{30}$ (7730) phase with 1.5% Wt. oxygen loss, which on further reduction leads to the amorphisation of the material, which is observed at $La_2Mo_2O_{7-\delta}$ (7-δ) [1]. An Argentinean team reported that when LMO was annealed at 608 ^oC in 10% H_2 + 90% Ar with a flow rate of 6 L/h, the resultant compound was an amorphous phase (7-δ). No intermediate LM-7730 phase was observed [2]. XRD patterns of LMO, 7730 phase and amorphous (7-δ) phase can be seen in fig. 5.1.

Overall conductivity increase in reduced LMO was discussed in previous works, consistently with the partial reduction of Mo^{6+} [1-3]. Use of reduced LMO as an anode material for SOFC was proposed and attempted with success. It is even found that reduced LMO material is sulfur tolerant, thus giving new opportunities to explore in LAMOX family [4].

In an XPS study carried on LMO by partial substitution of Dy on La site and W on Mo site, it was found that only Mo is susceptible to reduction [5]. It is shown that W substitution to Mo in LMO not only retains its high conductive cubic β phase to room temperature, but also limits the reducibility in diluted H_2 atmospheres [6-8]. [Note: Please refer to the section 1.6 in chapter 1. Studies concerning the stability of LMO and W-substituted LMO compounds in reductive atmospheres from literature are reported].

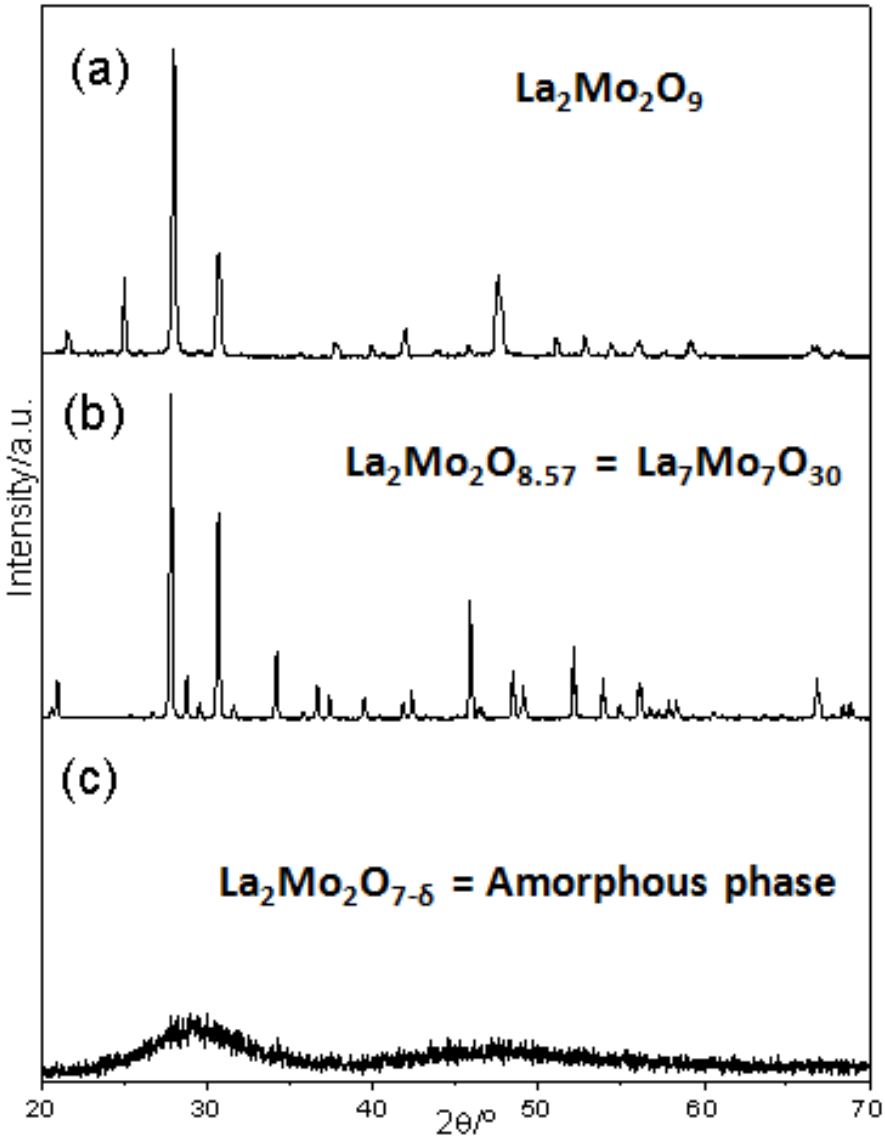

Figure 5.1: XRD patterns of (a) LMO, (b) 7730 and (c) amorphous (7-δ) phase collected at room temperature.

Not many studies were reported on the reduction behavior and reduction kinetics of LMO. In this chapter, we study the structural changes, reductive behavior, and reduction kinetics of LMO and W-substituted LMO in different reductive atmospheres. Electrical conductivities were studied as a function of reducibility, considering possible applications. Similar studies were carried on W substituted LMO compounds. Reduction studies were performed under diluted H_2,

different pO_2 pressures and ultra high vacuum (UHV) setups. Thermo-gravimetric (TGA) instruments and regular laboratory tubular furnaces were employed for this study. XRD setup was used for structural analysis.

5.2: Stability of $La_2Mo_2O_9$ under reductive atmospheres:

As a first exploring step, 1 g of LMO was annealed in TGA under N_2 + 6% H_2 at 760 ^oC for 20 hours with a flow rate of ~1.2 L/h. The resultant powder was black due to the mixed valence of molybdenum and a weight loss of 1.8% (by TGA) was observed. XRD analysis revealed that the resultant compound was in 7730 phase. When 500 mg of LMO is annealed in Ar + 5% H_2 atmosphere for 72 hours at 800 ^oC with a flow rate ~1.2 L/h, a larger weight loss was noticed (6.99 % by TGA). The sample turned amorphous and was black. XRD patterns are similar to what was shown in Fig. 5.1. Both the TGA curves are in Fig. 5.2. Difference in the profiles of TGA curves shows significant difference in reduction behavior with the change in the reduction parameters. Variations induced in the controllable parameters seem to govern not only the amount of oxygen lost, but also the path of reduction. Numerous experiments studying the reductive behavior were conducted in TGA. It is believed that the reductive behavior of LMO is quite challenging and many parameters govern such behavior. These parameters include quantity of the sample, concentration of H_2 used in diluted H_2, flow rate of gas, annealing time and temperature. Here we have discussed the results of reduction experiments on LMO performed under different controlled parameters.

In order to follow the reductive process and considering the results of the previous experiment, all the controlled parameters governing the reduction mechanism except one were kept constant. Series of measurements were performed by increasing the annealing time (varying from 0 to 48 hours for every measurement) in TGA apparatus at 760 ^oC in 10 % H_2 + 90% Ar with a flow rate 3.6 L/hr. For the measurements, batches of 300 mg of LMO sample were used and a new fresh batch was loaded for each measurement. Weight loss was measured by TGA and oxygen stoichiometry of the sample at given point was calculated, taking into reference the weight of the sample before the plateau. TGA curves of all the measurements along with the schematic representation of thermal profile can be seen in Fig. 5.3. On a TGA curve it was possible to define different zones A, B, C and D; where each zone exhibit a unique combination

of crystallographic phases and annealing time. See Fig. 5.4 for such schematic representation. Such samples in zones A, B, C and D were grouped in accordance of their structural symmetries as defined by XRD are shown in Fig. 5.5. Each zone is constituted of multiple samples. Final oxygen stoichiometry of the sample along with the nature of the crystallographic phases can be seen in Table 5.1.

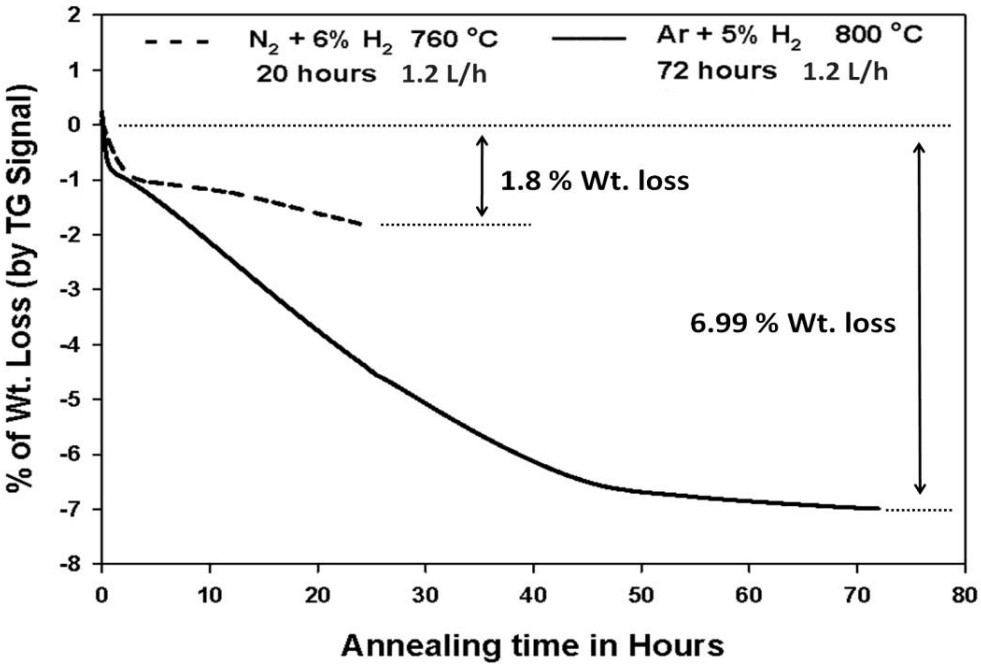

Figure 5.2: TGA curves of measurements carried on LMO sample showing the % of the Wt. loss as a function of the annealing time. Difference in the reduction profile can be identified with the change in the reduction parameters.

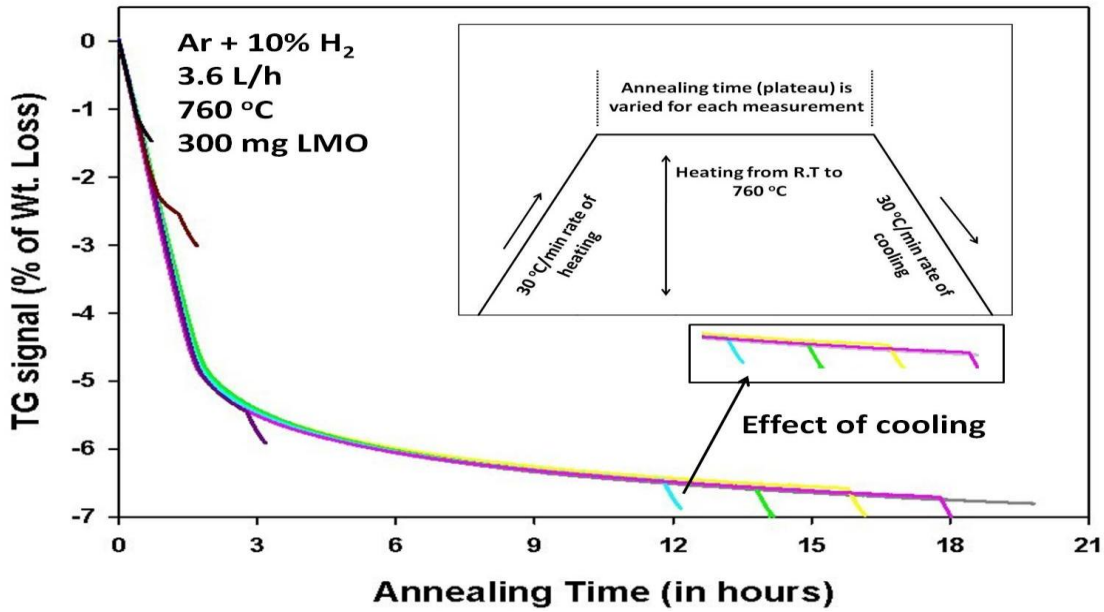

Figure 5.3: Multiple reduction measurements performed on different fraction of LMO samples which were taken from the *same batch, were displayed in above TGA curves as a function of Wt. loss % and annealing time.* The *thermal profile of* the *TGA measurement can be seen in inset. At the end of each curve, change in the slope of reduction path can be seen, which represents the sudden Wt. loss observed while cooling the sample.*

LMO sample when heated to 760 ^{o}C and cooled back immediately (without any plateau of annealing time) turned black and weight loss was also observed. XRD revealed mixture of monoclinic α - $La_2Mo_2O_9$ (LMO), 7730 and amorphous phases in this sample. Presence of these three phases was still observed when annealing time was increased to an hour (in Zone A). After further annealing till 3 hours, total disappearance of LMO phase was noticed and a mixture of 7730 and amorphous phases were observed (in Zone B). Further reduction of sample leads to amorphisation (between 3 to 18 hours of annealing). In the XRD patterns of the amorphous phase samples a bump was seen around 2θ ~29°, but no shift in the bump was noticed with the change in the oxygen content of sample bearing amorphous phase (in Zone C). In Fig. 5.6, XRD patterns of the amorphous phase are shown. When the sample was annealed over 18 hours under the above reducing conditions, appearance of metallic Mo from amorphous phase was noticed (i.e. complete reduction of Mo^{6+}).

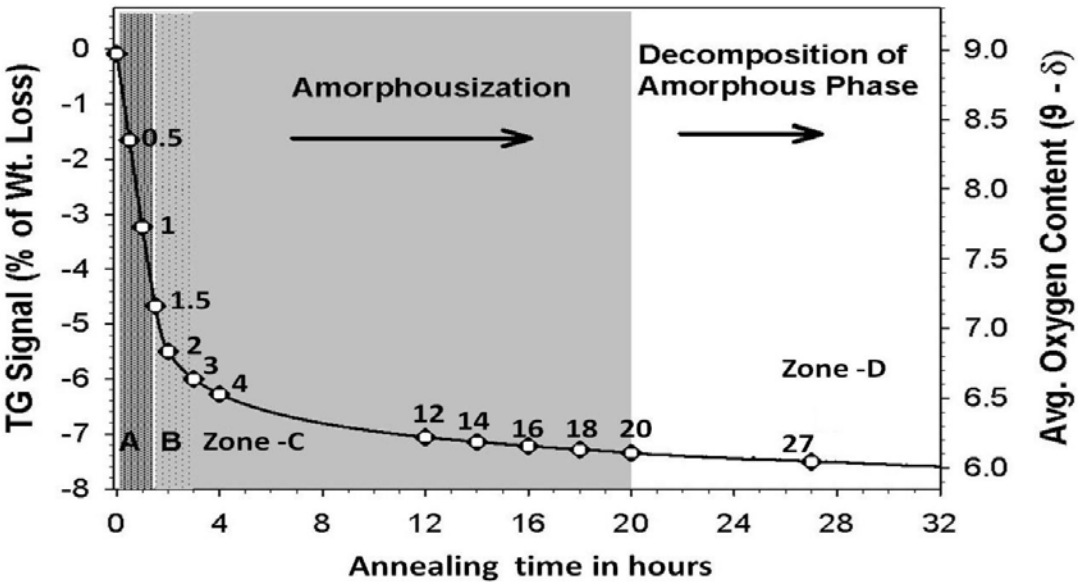

Figure 5.4: Graph showing the TGA curve of LMO when reduced in 10%H_2 + 90% Ar gas with a flow rate of 3.6L/h at 760 ^oC. Each zone A, B, C and D presented, represent a unique combination of crystallographic phases observed after different annealing times.

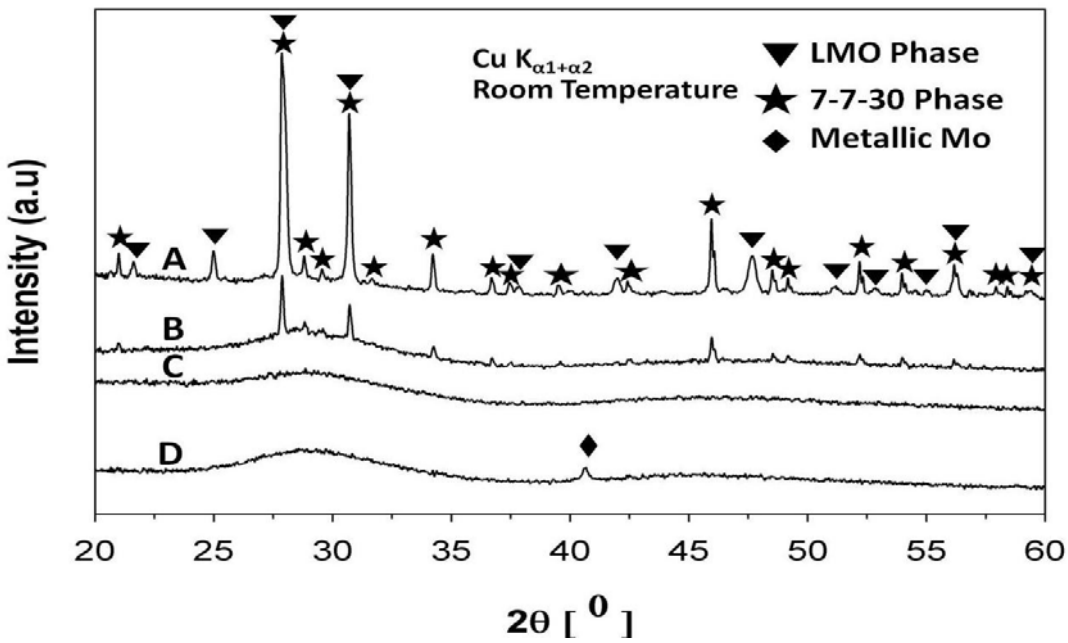

Figure 5.5: XRD patterns after reduction for 4 zones A, B, C and D. It is to be noticed that peaks at 28° and 31° 2θ share both LMO and LM-7730 phases.

Intensity of XRD peak (at 2θ ~ 40°) representing metallic Mo, increases with the increase of oxygen loss in the sample. This would be because of negligible Wt. loss observed in the sample after such reduction (in zone D). These measurements show the vulnerability of LMO towards reducing conditions.

Zones	*Annealing time (in hours)*	*Average Oxygen Stoichiometry (9-δ)*	*Final Phases observed by XRD*
A	0	8.96	LM + 7-7-30 + Amorphous
	0.5	8.35	LM + 7-7-30 + Amorphous
	1 hour	7.76	LM + 7-7-30 + Amorphous
B	1.5	7.20	7-7-30 + Amorphous
	2	6.89	7-7-30 + Amorphous
C	3	6.69	Amorphous
	4	6.59	Amorphous
	12	6.29	Amorphous
	14	6.26	Amorphous
	16	6.23	Amorphous
	18	6.20	Amorphous
D	20	6.18	Amorphous + Mo peak
	27	6.12	Amorphous + Mo peak
	36	6.06	Amorphous + Mo peak
	48	6.02	Amorphous + Mo peak

Table 5.1: The resultant phases formed when LMO was reduced in TGA at 760 °C in 10% H_2 + Ar gas with a flow rate of 3.6 L/h. Final oxygen content in the sample is also given.

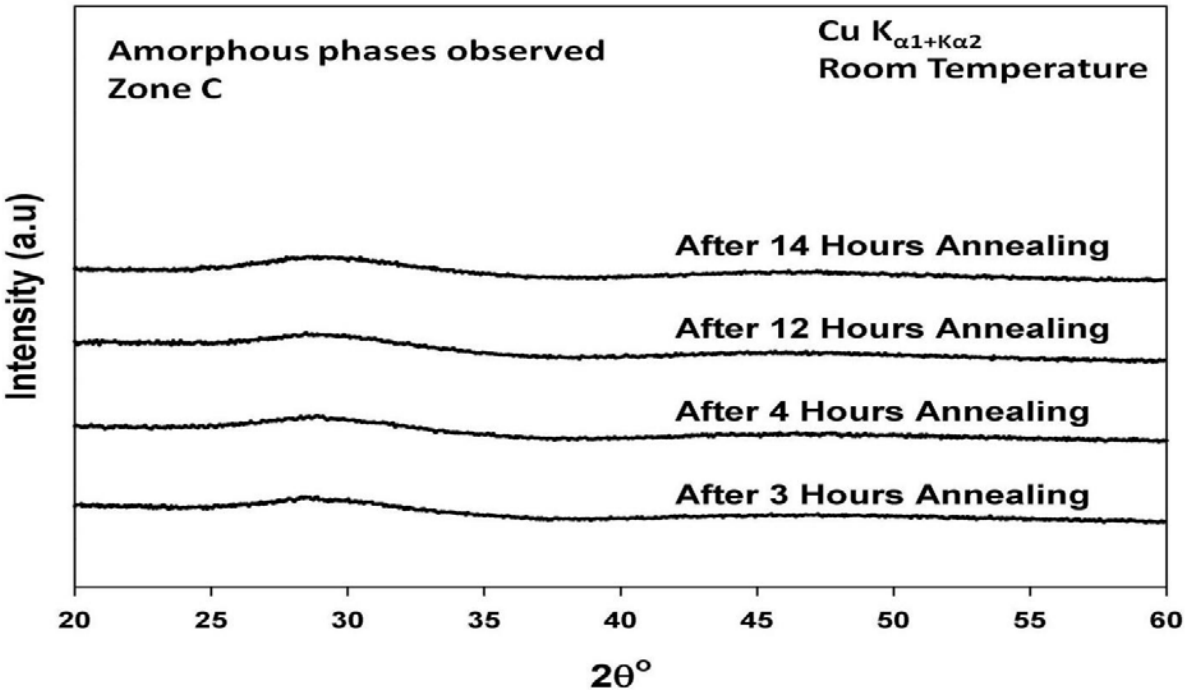

Figure 5.6: XRD patterns of amorphous phase (7-δ) oxides, when LMO was reduced in TGA at 760 °C in 10% H_2 + Ar gas with a flow rate of 3.6 L/h.

As mentioned in the introduction (section 5.1 of this chapter) and in the bibliography (section 1.6 in chapter 1), it was reported that when LMO was reduced (6% H_2 + N_2 at 700 °C) the appearance of $La_7Mo_7O_{30}$ (7730) phase is observed first, which on further reduction leads to the amorphisation of the sample (i.e. is $La_2Mo_2O_{7-\delta}$ (7-δ)) [1]. Direct transition of LMO to an amorphous phase was also reported when annealed at 608 °C under 10% H_2 + Ar with 6 L/h flow rate [2]. But here in the measurements mentioned above, we have seen the presence of all the three phases in the same sample (LMO + 7730 + 7-δ), which later tend to form an amorphous phase. It has to be noted that all the measurements were not performed in a thermodynamic equilibrium. If the samples were in thermodynamic equilibrium conditions, the presence of two phases at most can be noticed and no Wt. loss would have been observed. It can be because of inhomogeneous reduction. Initially LMO partially reduces to 7730 phase, which on further reduction leads to amorphisation. In other words reduction works as a gradient rather than uniform oxygen loss all over the annealed sample. A wide stability range of the amorphous phase (oxygen stoichiometry

6.69 to 6.183) was found. Further reduction leads to total loss of oxygen coordinated with Mo and appearance of metallic molybdenum (as seen in XRD). In addition to the change in oxygen stoichiometry, the amorphous phase seems to accommodate a non stoichiometry in cationic system. Ratio of La:Mo in LMO is 1; amorphous phase accommodates displacement in oxygen stoichiometry, which inturn effects the stoichiometry of the cations. In other words La:Mo $\neq$ 1.

In one of the above mentioned measurements, where LMO sample was annealed and cooled back from 760 ^{o}C without any plateau stage (0 annealing time), the sample was found to be already reduced (760 ^{o}C, 10% H_2 + Ar and 3.6 L/h flow rate). Change in color was observed and the sample was found to be a mixture of LMO + 7730 and 7-δ phases. A similar experiment was performed to increase the reduction kinetics. The flow rate was increased from 3.6 L/h to 6 L/h; keeping all the other parameters constant (Annealing temperature fixed to 760 ^{o}C, 10% H_2 + Ar and annealing time 0 (i.e.no plateau stage)). As soon as LMO was heated and cooled back in the TGA instrument, surprisingly the sample was found to be brown (instead of white LMO or black reduced). The Wt. loss observed was 0.53% ($La_2Mo_2O_{8.77}$). More surprisingly the sample was found to be in the high temperature cubic (β) LMO phase. The XRD pattern can be seen in Fig. 5.7. Similar behavior was noticed by our collaborators at Centro Atomico Bariloche (CAB), Bariloche, Argentina. When the stability of LMO was studied under different pO_2 pressures at 608 ^{o}C, complete crystalline high temperature cubic β phase powder was observed at 10^{-23} atm and this β phase was stable till 10^{-25} atm; which later turned to amorphous phase once the pO_2 pressures were reduced. This experiment was performed in TGA instrument, where Wt. loss was measured and oxygen content of this β-polymorph sample was calculated to be $La_2Mo_2O_{8.96}$ (9-δ = 8.96) [9]. These two experiments cannot be compared as they are in different thermodynamic conditions, however the appearance of the cubic phase $La_2Mo_2O_{8.96}$ can be acknowledged.

Appearance of a brown β-phased LMO was noticed at oxygen content 8.77 (9-δ = 8.77). Similar crystalline compound was obtained previously with oxygen content 8.96 (9-δ = 8.96). If we consider the series of TGA measurements performed on LMO, the coexistence of a mixture of LMO, 7730 and 7-δ phases was seen in few measurements (which were discussed above and presented in Fig. 5.3, 5.4, 5.5 and 5.6 and Table 5.1 of this chapter). The brown LMO (at 9-δ = 8.77) only single cubic β-phase is seen by XRD. However a slight amorphisation of a fraction of the sample cannot be ruled out, as it cannot be clearly determined by XRD analysis (considering

limitations of XRD). Inhomogeneous reduction of LMO is already discussed above. Reduced brown LMO sample (9-δ = 8.77) would already have turned cubic phase at 9-δ = 8.96, and little part of the compound could be amorphous which could not be detected by XRD (since the reduction is not homogenous). Even though all the reduction parameters are kept constant and when the flow rate is increased by 2.4 L/h different reduction behavior was noticed.

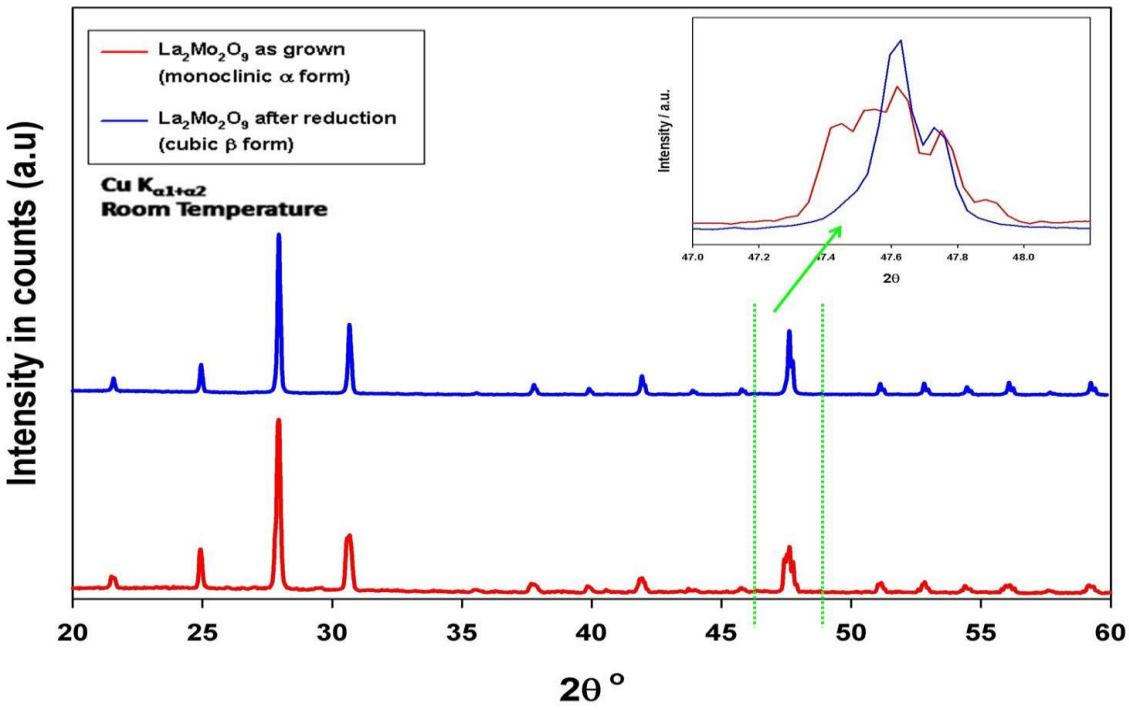

Figure 5.7: XRD patterns of LMO when synthesized (red) and after reduction (blue). LMO turns from monoclinic α to cubic β form when heated and cooled back at 760 °C in 10%H_2 + Ar gas with a flow rate of 6 L/h. XRD patterns collected at 47.5° 2θ showing cubic or pseudo-cubic (2 3 1) reflection of LMO, cubic (β) and monoclinic (α) phases are shown in inset.

5.3: Stability of $La_2Mo_2O_9$ and $La_2Mo_2O_{7-\delta}$ (amorphous 7-δ) under mild reductive conditions:

Inhomogeneous reduction behavior and extreme vulnerability of LMO towards reduction was already noticed. Despite of a small amount of oxygen loss from LMO matrix (0.04 oxygen loss per unit formulae; i.e. 9-δ = 8.96), cubic β-LMO form is retained. Heating and immediate cooling (with zero annealing time/ no plateau stage) is sufficient to partially reduce LMO into an amorphous phase (along with the mixture of the parent phase and 7730 phase). Considering such instability of LMO towards reductive conditions and inhomogeneous reduction process, before any further applications were considered, it is important to determine reduction conditions at which LMO is stable. Few measurements were performed to determine such conditions. Since it was already known that LMO is too vulnerable to reduction atmosphere of double chamber SOFC and that possible application of the amorphous phase LMO (7-δ) as sulfur tolerant MIEC anode was demonstrated [4, 10]; stability conditions of amorphous phase (7-δ) sample were then studied under mild reduction conditions.

Mild reduction conditions included usage of gas with less hydrogen concentration. The annealing time of was fixed to 12 hours 1% H_2 + N_2 with a flow rate of 3 L/h. Series of measurements were performed in TGA fixing the above mentioned parameters and increasing the temperature (from 500 to 700 ^oC for LMO; and 500 to 800 ^oC for amorphous 7-δ samples). Fresh batch of 300 mg of sample was used for each measurement. Wt. loss was measured by TGA and the phase purity of the samples after cooling down to room temperature at 30 ^oC/min, was checked by XRD analysis.

When LMO sample was annealed at 500 ^oC, no change in weight or crystal structure was observed. When the annealing temperatures were increased to 550 ^oC and 600 ^oC, sample turned to grey color. However XRD did not reveal any change in the structure and no Wt. loss was observed either. At annealing temperatures of 700 ^oC, the sample showed traces of the 7730 phase. There was a slight Wt. loss in the sample (< 0.1% Wt. loss) as seen in the Fig. 5.8 for XRD patterns. Black spots/ seeds are seen in a grey matrix of the sample. These seeds would be an indication of inhomogeneous reduction in the sample which could explain the presence of the 7730 phase as noticed in XRD (more details about these black spots will be discussed in the next

section). It was concluded that LMO is stable till temperatures less than 700 ^{o}C. See the details in Table 5.2. See the TGA curves in Fig. 5.10.

The stability of the amorphous phase LMO (LM 7-δ) was also probed under mild reduction conditions (1% H_2 + N_2, flow rate 3 L/h, annealing time 12 hours and 300 mg sample). In the measurements performed at 500 ^{o}C, 600 ^{o}C and 700 ^{o}C, no structural change is noticed by XRD and TGA revealed Wt. gain in the sample (very less Wt. gain ~ 0.2 %). No shift of the bump position in the amorphous samples was observed in the XRD patterns. At the annealing temperature of 800 ^{o}C, a weight gain was observed (~ 0.2% Wt. gain), the amorphous phase 7-δ decomposed into a mixture of La_2MoO_5, La_2MoO_6 and an unknown phase. See the Fig. 5.9 for XRD patterns. See the TGA curves in Fig. 5.11.

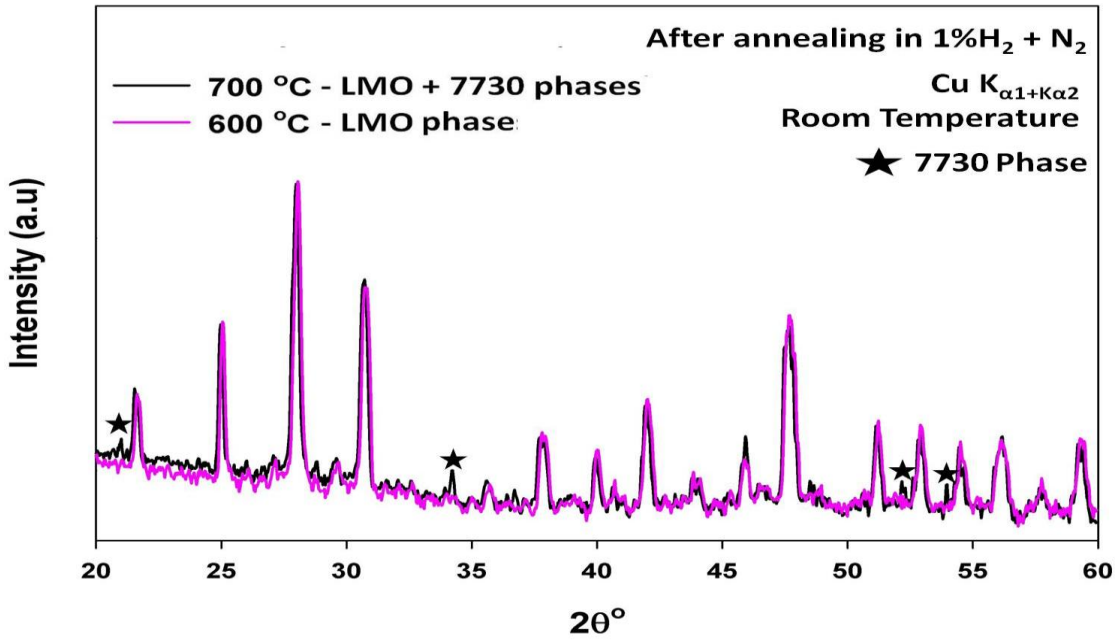

Figure 5.8: XRD patterns of LMO compounds which where annealed in 1%H_2 + N_2 atmosphere with flow of 3L/h, at 600 ^{o}C (pink) and 700 ^{o}C (black). The super structural reflections of LMO phase and the *coincidence of peak positions of LMO and 7730 phases make it difficult to differentiation. Few visible traces of 7730 phase were marked with star.*

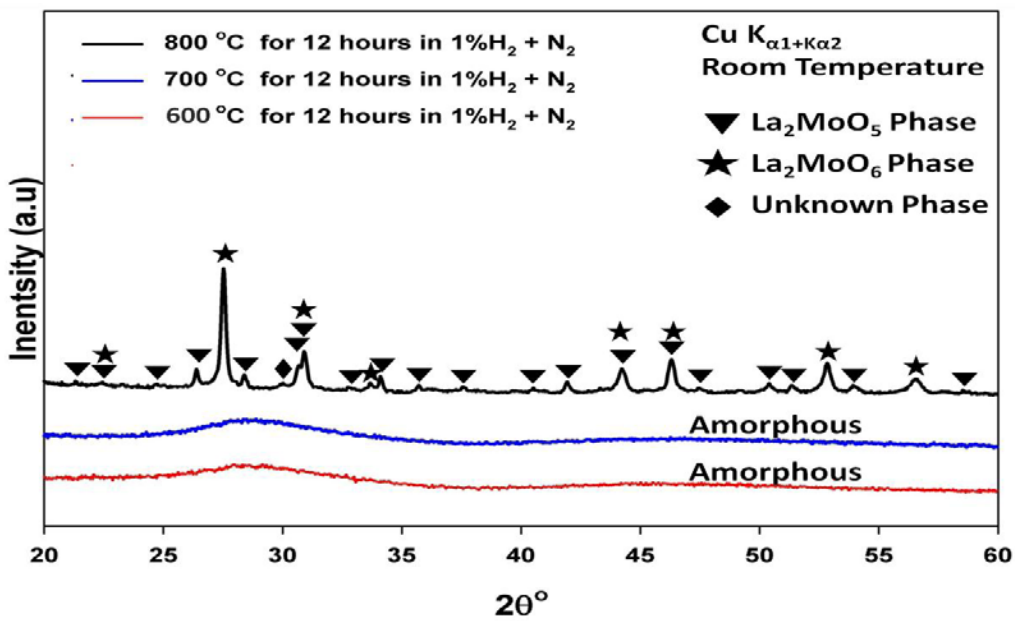

Figure 5.9: XRD patterns of amorphous (7-δ) samples when annealed in 1%H_2 + N_2 atmosphere under flow of 3L/h.

Sample	Temperature in °C	Gas (flow rate 3 L / H)	Plateau (Hours)	Nature of Phases(after reduction)	Color
$La_2Mo_2O_9$	500	N_2 + 1% H_2	12	$La_2Mo_2O_9$	White
$La_2Mo_2O_9$	550	N_2 + 1% H_2	12	$La_2Mo_2O_9$	Grey
$La_2Mo_2O_9$	600	N_2 + 1% H_2	12	$La_2Mo_2O_9$	Grey
$La_2Mo_2O_9$	700	N_2 + 1% H_2	12	$La_2Mo_2O_9$ + traces of 7730 phase	Grey with black spots matrix
$La_2Mo_2O_{7-\delta}$	500	N_2 + 1% H_2	12	amorphous	Black
$La_2Mo_2O_{7-\delta}$	600	N_2 + 1% H_2	12	amorphous	Black
$La_2Mo_2O_{7-\delta}$	700	N_2 + 1% H_2	12	amorphous	Black
$La_2Mo_2O_{7-\delta}$	800	N_2 + 1% H_2	12	La_2MoO_5 + La_2MoO_6 + Unknown phase	Black

Table 5.2: Stability of LMO and amorphous LMO (7-δ) under mild reducing conditions (1%H_2 + N_2 atmosphere under flow of 3L/h).

.

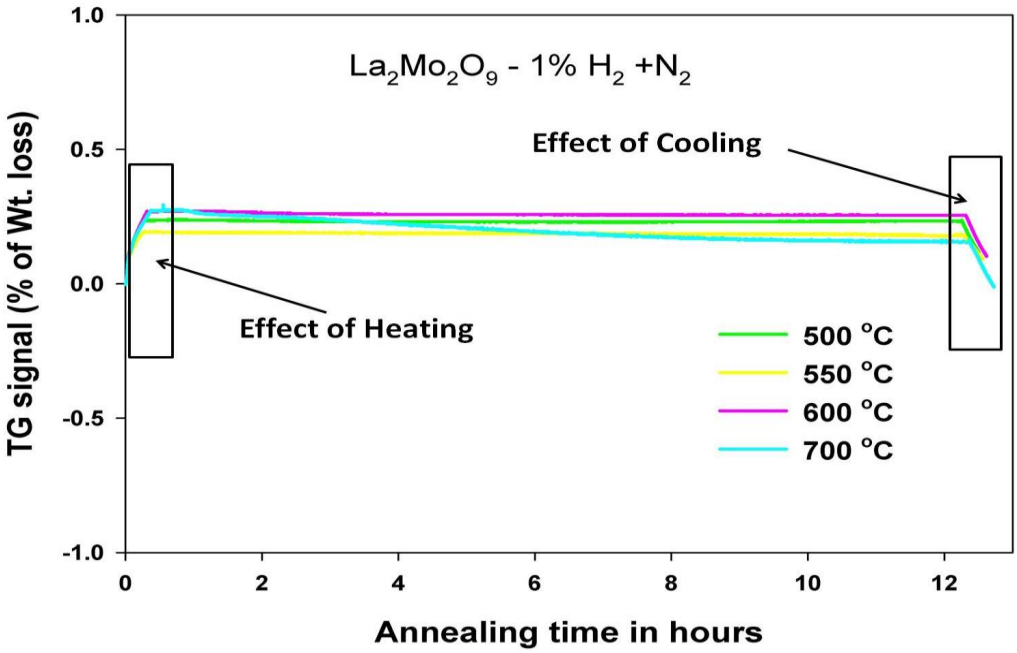

Figure 5.10: TGA curves of LMO sample when annealed in 1% H_2 + N_2 atmosphere. Weight gain and loss displayed in the boxes, is because of increase in temperature.

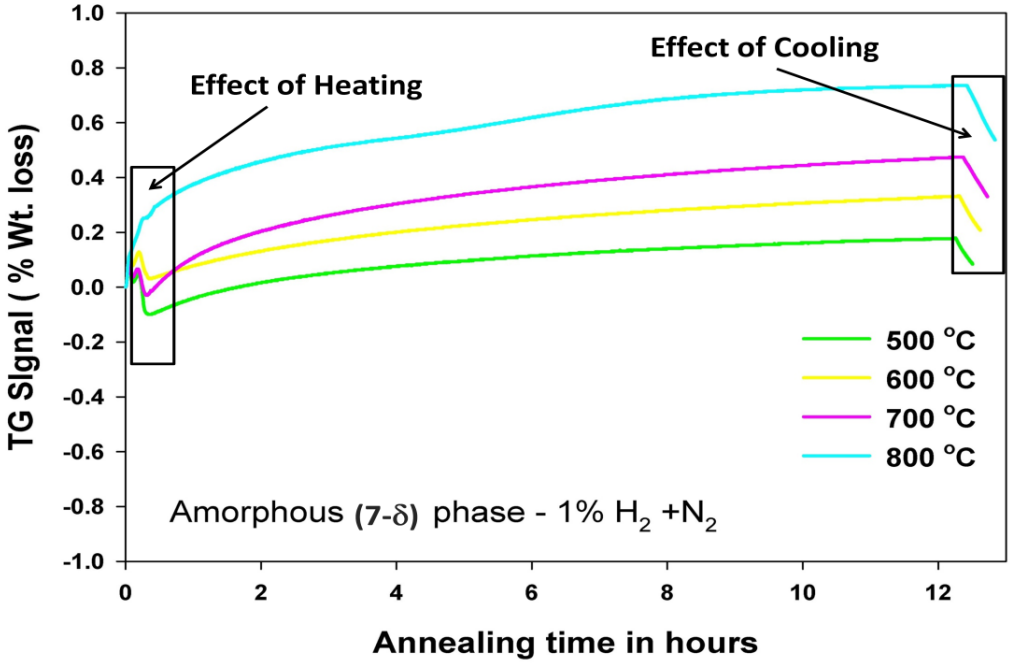

Figure 5.11: TGA curves of amorphous (7-δ) phase sample when annealed in 1% H_2 + N_2 atmosphere (at 3L/h). Weight gain and loss displayed in the boxes, is because of increase in temperature.

When the TGA curves of LMO and amorphous (7-δ) phases are compared, difference in the % Wt. gain/ loss was noticed. No change in the %Wt. gain or loss was observed in LMO samples during the measurements performed at 500, 550 and 600 ^{o}C. However, at 700 ^{o}C there was a slight fall in the Wt. signal (~ <0.1%). Whereas all the amorphous phase samples show Wt. gain, although, such % Wt. gain was very small (< ~0.2 % Wt. gain). This could be because of oxygen residue left in the commercial N_2 gas which was used to dilute H_2. LMO is stable at this partial oxygen pressure (pO_2) in the gas when annealed at 500, 550 and 600 ^{o}C. But at 700 ^{o}C such pO_2 induces reduction of LMO thereby losing oxygen from the system; however the rate of such reduction is very small. But amorphous phase is not stable in such pO_2, and it oxidizes; in other words pO_2 of 1% H_2 + N_2 is an oxidizing atmosphere for amorphous phase. It is hard to define the stoichiometry of the sample in the amorphous phase and its oxygen gain, since these amorphous phases synthesized in a tubular furnace where Wt. loss or gain cannot be precised. Moreover it is also known that the amorphous phase can accommodate a wide range of oxygen content (for amorphous phase: 9-δ = 6.69 to 6.18; see table 5.1 for more details). These measurements show the instability of LMO towards the annealing temperature (normal temperatures at which SOFC operates ~ 800-1000 ^{o}C) even though the reduction parameters were very mild (content of H_2 in the gas, flow rate of gas, annealing time (in case of SOFC, its operating time)).

5.4: Triggering and boosting of reduction process:

Considering the variations observed in the reduction behavior even with slight variation in thermodynamic conditions and inhomogeneous reduction process, it is of significant importance to understand the reduction phenomenon in these samples. In order to control the reduction phenomenon or overcome any limitations of LMO (towards reduction) and to design LMO as a possible candidate for SOFC application, one has to understand at first the triggering phenomenon which leads to reduction and how the reduction process boosts.

An unusual reduction phenomenon was accidentally observed in LMO. During a measurement in TGA (on 300 mg of LMO sample in 10% H_2 + Ar with flow of 3.6 L/h), the thermocouple has failed while in operation. The sample after this failed experiment showed an inhomogeneous mixture of dark spots within a white matrix (see the Fig. 5.12). Traces of the 7730 phase were found by XRD (which is consistent with the initial stages of measurements mentioned in table 5.1). The annealing temperature and time of the experiment were not determined because of the thermocouple failure. Numerous attempts made to reproduce this behavior were unsuccessful.

If we recall the measurement carried on a LMO sample at 700 ^{o}C under mild reduction conditions mentioned in Table 5.2 (1% H_2 + N_2, flow rate 3 L/h, annealing time 12 hours and 300 mg of LMO), similar behavior is observed. Here black spots are seen in a grey matrix instead of a white matrix. The XRD pattern showed the presence of the 7730 phase besides the parent compound even though TGA did not reveal any significant Wt. loss. This experiment is reproducible. Similar behavior is again noticed when 300 mg of LMO is heated at 650 ^{o}C and cooled back immediately at 30 ^{o}C/min (no plateau stage for annealing) under 10 % H_2 + Ar with a flow rate of ~5.1 L/h. The resultant sample was a mixture of LMO and 7730 phases with no Wt. loss. The sample showed black spots/seeds in a grey colored matrix.

Note that black spots are seen in the above mentioned three measurements around grey or white matrix and traces of a 7730 phase were detected by XRD in all of these three measurements. LMO material is normally white (beige to cream color), but the existence of grey LMO in an α-monoclinic phase was already seen before (see table 5.2). Remaining black spots

could be the areas which were prone to initial stages of reduction (since reduction in these samples is not uniform) and could be in 7730 phase.

Figure 5.12: Photograph of LMO sample when attempt to be reduce in Ar + 10% H_2 with 60 ml/min flow rate in a quartz crucible. Black spots in a white matrix can be seen.

It has to be noted first, thermodynamic equilibrium was not reached in any of these measurements. Since the sample is in a powder form and synthesized by conventional solid state synthesis route, it would be sensible to assume that it is a homogeneous mixture of various grain sizes. We assume that these black dots develop around reduction spots have a in smaller grain size and are more prone to reduction. This could be because of convection water vapour bubbles, forming around the sample and helping to get it more reduced. In the literature it was found that during oxygen isotope exchange experiments in LAMOX compounds, to enhance the oxygen surface exchange, water vapour is used and it is reported that diffusion of oxygen gas into the sample is very small in pure oxygen gas, but when wet gas is used, the exchange es boosted considerably [11]. Not only in LAMOX materials but in other ceramic oxide ion conductors and BIMEVOX materials wet atmospheres were reported to be advantageous for oxygen exchange [12-14]. A study states that LAMOX samples are stable when annealed in a dry propane:air mixture, whereas samples get reduced in wet propane:air mixture, pointing out the role of water vapor in the reduction [8, 10]. In our case, maybe the water vapour is forming in the sample and is helping

oxygen to deplete from the sample; and these black spots could be seeds for reduction. However, further studies have to be made to understand the phenomenon.

In a reduction measurement performed in a tubular furnace, 1.5 g of LMO was annealed in an alumina boat. The sample is uniformly spread in the crucible to promote homogenous reduction and measurement was performed at 760 ^{o}C for 12 hours in 10% H_2 + Ar gas with a flow of 3.6 L/h. After the measurement, the sample revealed a gradient of reduction towards the direction of the gas flow. It was possible to divide the sample into three different zones (zones A, B and C) and XRD was performed on material from each zone. Sample in zone A was mostly in LMO phase with little amorphousness in the sample, in Zone B mixture of LMO and amorphous phases were seen; in Zone C sample was mostly amorphous along with traces of the LMO phase. Schematic representation of the measurement and XRD patterns corresponding to Zones A, B and C are shown in Fig. 5.13 and Fig.5.14 respectively.

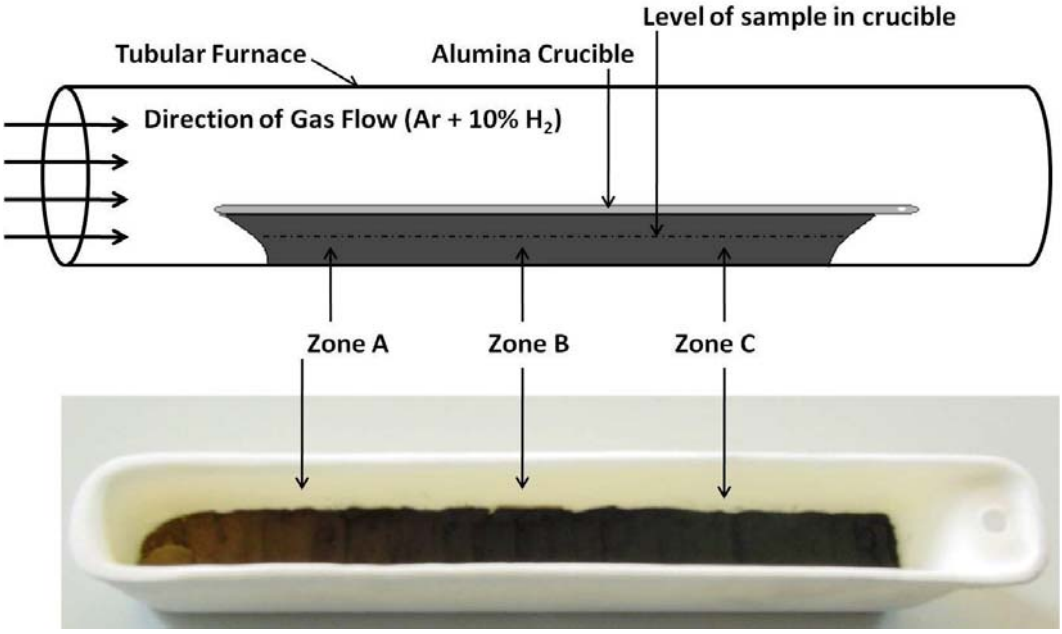

Figure 5.13: Schematic representation (above) and photograph (below) of gradient reduction observed in LMO when reduced in a tubular furnace. Reduction was performed at 760 ^{o}C in Ar + 10% H_2 gas with a flow rate of 3.6 L/h for 12 hours.

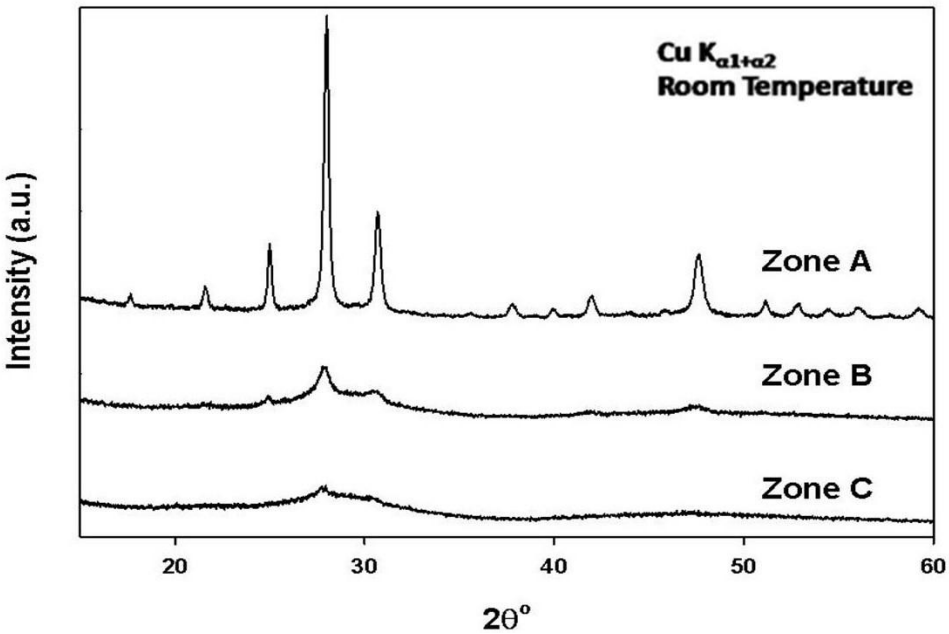

Figure 5.14: XRD patterns of zones A, B and C as mentioned in Fig. 5.11.

If we recall the results of measurements presented in the Table 5.1, intermediate 7730 phase was noticed under similar reduction conditions (no change in the reduction parameters except the quantity of the sample used (1.5 g instead of 300 mg)). Measurements detailed in Table 5.1 were carried in a TGA, whereas the measurement detailed above is carried in a tubular furnace (i.e. different setup). The absence of the 7730 phase indicates a change in the thermodynamic conditions applied and due to possible gas leaks in the system. However this reduction gradient phenomenon can be explained by the same hypothesis used to explain the black spots seen in the white matrix sample. The gas would have exchanged oxygen from the surface of the sample at zone A forming H_2O (Note: it is already described above that LMO is more prone to reduction to wet gas compared to dry gases). The wet gas (which picked up H_2O) flows over the surface of the sample at Zones B and C creating a gradient of reduction over the direction of flow. More the sample surface is exposed to gas, higher will be the surface exchange of oxygen and higher will be the formation of H_2O. More the H_2O in the gas, higher reduction of LMO was observed. This could be the reason for appearance of a reduction gradient in the direction of gas flow. Later the sample (gradient reduced) was annealed by placing the crucible in a direction opposite to gas flow for 12 hours (in direction C → A with similar reduction

conditions). The sample turned amorphous with uniform black color all over the surface. Since the Wt. loss cannot be measured in the tubular furnace, the exact stoichiometry of the sample was not known (more over it was detailed earlier that amorphous phase accommodates a wide range of oxygen non stoichiometry). Overall a complex reduction behavior is noticed in LMO materials.

5.5: Stability of W- substituted $La_2Mo_2O_9$ under reductive atmospheres:

The instability of LMO compounds towards reduction is one of its vital problems. Reports from literature and the experimental results mentioned in the above sections of this chapter have shown us the same. It was shown that when hexavalent tungsten is substituted to hexavalent molybdenum in LMO, its instability towards reductive atmospheres can be limited besides preserving its high temperature and high conductive β-form down to room temperature. An XPS study was reported where Dy is substituted to La (10 mol %) and W substitution to Mo by 50 mol %. When such compound is annealed in reductive atmospheres, oxygen loss was observed and it was stated that only Mo component in LMO is susceptible to reduction [5]. It was reported that when the compound y = 0.5 was annealed at 605 ^{o}C for 16 hours in 6% H_2 + N_2 atmosphere, oxygen loss of 0.543 per unit formulae (9-δ = 8.457) was noticed. Similar measurements were performed on compounds with y = 0.25, 0.5, 0.75, 1.0, 1.2 and 1.4. It was concluded that the reducibility in W-LMO compounds reduces with increased W-content [15]. In a study which included reduction of W-LMO compounds ($La_2Mo_{2-y}W_yO_9$) with y = 0, 0.5, 1.0 and 1.4, the compound with y = 1.4 was suggested as a suitable candidate for electrolyte application in SOFC. On the other hand, compounds with low W content were suggested for MIEC anode applications [8].

One of the main aims of this study is to explore the effects of reduction on W-LMO materials. For this study $La_2Mo_{1.5}W_{0.5}O_9$ (W0.5) and La_2MoWO_9 (W1.0) were used. All the measurements were performed in the TGA instrument using different reducing parameters and the phase purity was determined by XRD.

As a preliminary step, 300 mg of a W0.5 was annealed at 760 ^{o}C for 12 hours with 3.6 L/h flow of Ar + 10% H_2 gas. The sample was later found to be in $La_7Mo_7O_{30}$ (7730) phase. See the

TGA curve in Fig. 5.13. 1.11% Wt. loss was measured by TGA, which corresponds to an oxygen content of 8.57 (i.e. 9-δ = 8.57). When 300 mg of W0.5 sample was annealed in the TGA at 780 ^{o}C under Ar +10% H_2 with flow rate of 3.6 L/h, after 18 hours, the sample has lost 2.83% oxygen from the system (9 – δ = 8.025). XRD revealed that the sample is a mixture of 7730 and amorphous phases. See the XRD patterns in Fig. 5.16. Later a fresh batch of W0.5 compound was annealed at 800 ^{o}C for 24 hours. XRD revealed presence of amorphousness and an unknown phase. Oxygen content is calculated as 6.83 (i.e. 9-δ = 6.83) (calculated with Wt. loss of 5.65% measured by TGA). When 300 mg of W0.5 sample was annealed in TGA at 820 ^{o}C under Ar +10% H_2 with a flow rate of 3.6 L/h, after 36 hours 5.89 Wt. % was detected (9-δ = 6.96) and the sample was in mixture of amorphous and an unknown phase (the unknown phase found in this experiment is similar to that found in all the measurements performed on W0.5). TGA curves are presented in Fig. 5.15. XRD patterns corresponds to all the above experiments are shown in Fig. 5.16. Increase in temperature by 60 ^{o}C made a significant difference in the reduction profile in these compounds. Irrespective of the weight loss, difference in the path of reduction is noticed (when all the above measurements are compared).

It is known that LMO after partial reduction transforms to the 7730 phase which in turn on further reduction transforms into an amorphous phase. Further reduction of such phase completely reduces hexavalent Mo to metallic Mo. In the above experiments, the 7730 type phase of W0.5 compound was seen. When the compound is further reduced, a mixture of phases is noticed (amorphous phase + an unknown phase). Considering the resultant phases (by XRD analysis), it would be sensible to assume that the unknown crystalline phase has lower oxygen content than the 7730 phase (i.e. oxygen content less that 8.57; 9-δ < 8.57). However pure crystalline form of this unknown phase was never obtained. Attempts to reduce W0.5 to this unknown phase in single crystalline form were unsuccessful. Since the unknown phase always appears along with the amorphous phase, any information on the crystal structure cannot be determined. The results are detailed in Table 5.3.

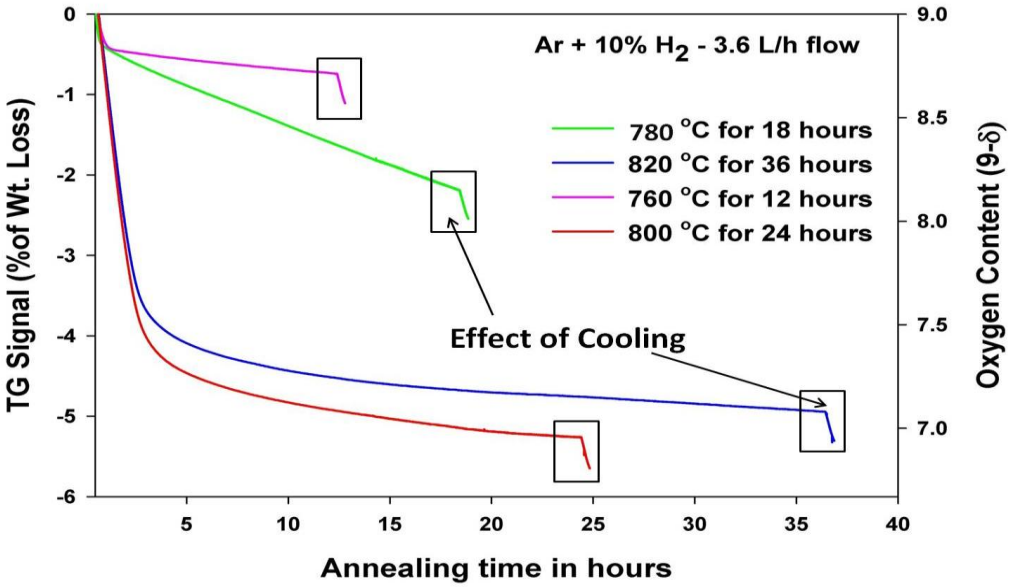

Figure 5.15: TGA curves showing reduction profiles of four different samples of W0.5, which were annealed at different temperatures. Sudden fall of TG signal was observed while cooling.

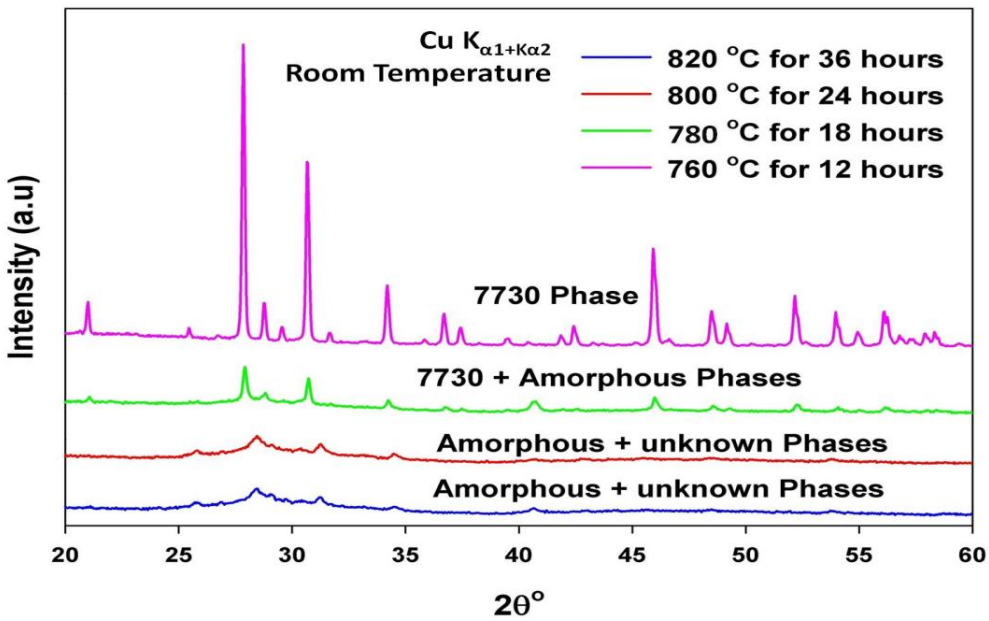

Figure 5.16: XRD patterns of W0.5 compounds after reduction. Annealings were performed in 10% H_2 + Ar with flow rate of 3.6 L/h.

Sample	Annealing Temperature °C	Time of annealing in Hours	Oxygen Stoichiometry (9-δ) after reduction	Nature of phase after reduction
W0.5	760	12	8.57	7730
W0.5	780	18	8.03	7730 + Amorphous
W0.5	800	24	6.83	Amorphous + Unknown*
W0.5	820	36	6.96	Amorphous + Unknown*

Table 5.3: TGA measurements carried on W0.5 under constant flow of Ar + 10 % H_2 at 3.6 L/h. Unknown is the similar unknown phase when all the W0.5 compounds are reduced.*

Sample	Annealing Temperature °C	Flow Rate L/h	Time of Annealing in Hours	XRD pattern of product
W0.5	718	6	24	7730 + Amorphous
W0.5	718	1.2	12	Unknown * + Amorphous
W0.5	718	1.2	48	Unknown * + Amorphous
W0.5	750	3	14	Unknown * + Amorphous
W1.0	718	6	24	β - $La_2Mo_2O_9$

Table 5.4: Reduction experiments carried on W0.5 and W1.0 in a tubular furnace under constant flow of Ar + 10 % H_2 with variation of flow rate, temperature and annealing time. Unknown is the similar unknown phase when all the W0.5 compounds are reduced.*

Batches of 300 mg of W0.5 were annealed at 718 °C in a tubular furnace in Ar + 10% H_2. Flow rate and annealing time were varied from an measurement to another. None of the

compounds after reduction were found to be a single crystalline phase. The samples were a mixture of 7730 / unknown phase along with the amorphous phase. Details of these measurements can be seen in Table 5.4. 300 mg of a W1.0 sample was annealed for 24 hours at 718 ^{o}C with a flow rate of 6 L/h in a tubular furnace. The crystal structure of sample after annealing was found unchanged (i.e. sample is still in the cubic β-LMO form). All the similar reduction conditions were applied on the W0.5 sample (all the parameters are the same and even the same tubular furnace is used). After annealing it is noticed that W0.5 is a mixture of 7730 and amorphous phases; supporting literature information that with the increase of W substitution to Mo in LMO, vulnerability towards reduction will be improved. It was reported earlier that, after a loss of 0.43 oxygen per formulae unit, turned to 7730 phase [1]. Here in these measurements it was observed that W0.5 sample also transforms to 7730 phase when 0.43 of oxygen is lost per formulae unit. It was also reported that when W0.25 compound lost 1.136 oxygen per unit formulae, the sample was able to retain its cubic β-LMO form and such structural framework can sustain such oxygen loss [15]. This is in contradiction with what was observed in our measurements, but in agreement with similar observations reported by Marrero-Lopez *et al.* [3]. It is clear from all the above mentioned measurements that reduction in LAMOX samples can be controlled by increasing W-content in LMO and is in agreement with literature [15].

W0.5 pellet (10mm ϕ) which was of 96% relative density was annealed at 608 ^{o}C for 260 hours. This measurement was performed in a TGA in Ar + 10% H_2 atmosphere with a flow rate of 6 L/h. Steady state was not achieved during measurement and no intermediate plateau was observed either. The pellet after reduction was checked by XRD and is a mixture of amorphous and an unknown phase (see the XRD in Fig. 5.17). Pellet turned black and oxygen content in the pellet after reduction was 7.53 (9-δ = 7.53). The similar reduction study was performed on an LMO pellet which was 10 mm diameter and of ~96% relative density. Flow rate, gas and annealing temperature were the same. LMO pellet after reduction was amorphous after 130 hours of reduction. Oxygen content in the sample was 6.88 (9-δ = 6.88). Although, the thermodynamic conditions applied to both pellets (W0.5 and LMO) were similar; there is a significant change in the reduction profile of both compounds. Even though W0.5 was annealed for longer time (LMO was annealed for 130 hours, W0.5 was annealed for 260 hours), W0.5 showed significant stability towards reduction atmospheres. TGA curves of both the samples can be seen in Fig: 5.18. Both measurements described above were performed at CAB, Bariloche, Argentina.

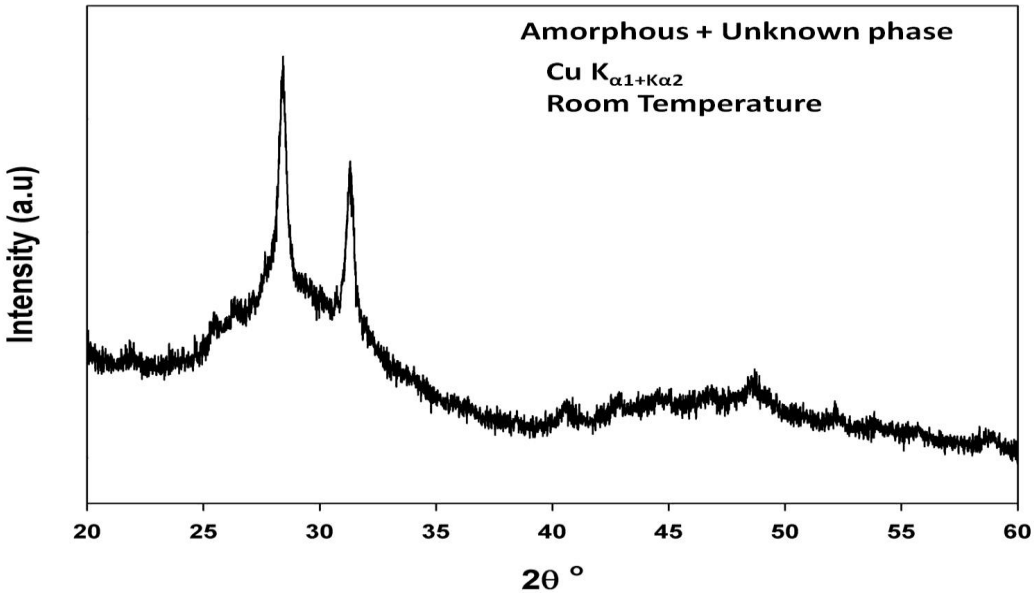

Figure 5.17: XRD pattern of W0.5 pellet (10 mm ϕ) which was annealed at 608 °C for 260 hours in Ar + 10% H_2 with a flow rate of 6 L/h.

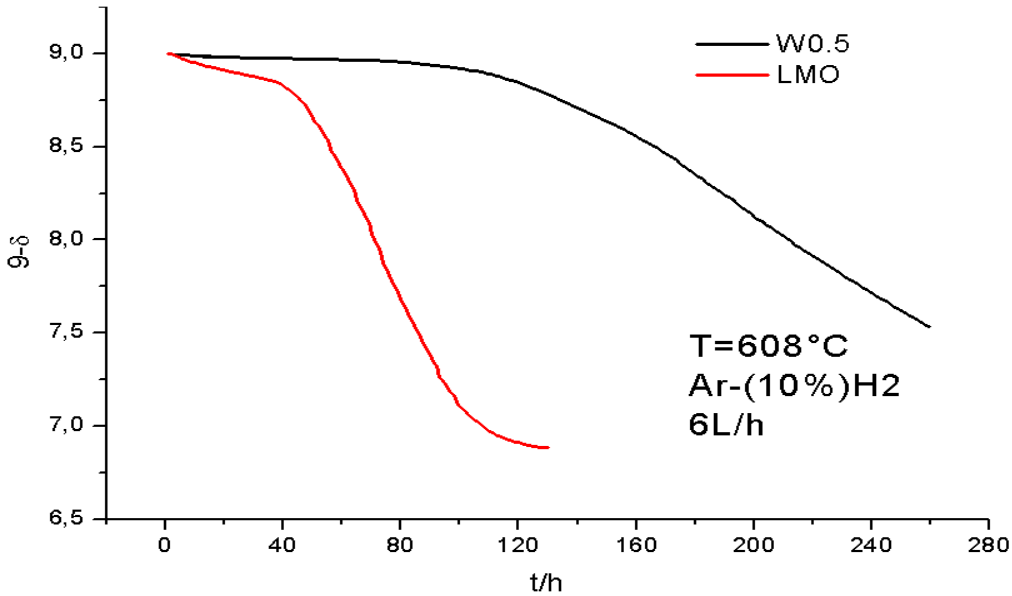

Figure 5.18: TGA curves collected on W0.5 pellet and compared against similar experiment done on LMO pellet.

5.6: Thermodynamic stability of $La_2Mo_2O_9$ and W- substituted $La_2Mo_2O_9$ under pO_2 pressures:

Numerous reduction measurements were performed on LMO and W-LMO compounds and are discussed in the above sections. It has to be noted that in neither of those measurements thermodynamic equilibrium was achieved. It is already mentioned that LMO when reduced first changes to crystalline cubic β- LMO form with loss of 0.04 oxygen per unit formulae. On further reduction 7730 phase appears and further reduction can lead to the amorphisation of the sample. Complete reduction leads to appearance of metallic Mo. Coexistence of more than two phases were seen above, and oxygen loss in the sample was still observed. This clearly tells that thermodynamic equilibrium conditions were not achieved.

It is of vital importance to study the thermodynamic stable domains of LMO and W-LMO compounds under reductive atmospheres. Such experiments have to be performed by controlling reduction parameters. In this part of the chapter we discuss isothermal measurements performed on LMO, W0.5 and W1.0 samples. 500 mg powder of each sample (LMO, W0.5 and W1.0) was annealed in TGA at 718 ^{o}C with constant gas flow of 6 L/h. pO_2 pressures were decreased to probe the reduction in the samples. By using an electrochemical oxygen pump and an electrochemical oxygen sensor, it was possible to control the pO_2 pressure of the gas. Commercially available Ar, CO_2 and Ar + H_2 gases were mixed according to the pO_2 requirement. Highest pO_2 was found to be $pO_2 = 3 \times 10^{-6}$ atm where commercial Ar was used (because of oxygen residue in the gas). Intermediate pO_2 pressures were obtained by using a CO-CO_2 mixture ($pO_2 \sim 10^{-7}$ to 10^{-18} atm). Lowest pO_2 pressures were obtained by using a mixture of Ar-H_2-H_2O ($pO_2 \leq 10^{-18}$ atm). Measurements started with Ar and pO_2 were dropped by changing the gas as chemical pump. Since the goal of these experiments is to achieve steady state (thermodynamic equilibrium conditions), it is not possible to fix the annealing time. Samples were annealed under the gas flow till a steady state was achieved. Each equilibrium point was recorded only after a constant TGA signal was measured for at least 5 hours. Once the steady state was achieved, the sample was cooled down to room temperature in the same atmosphere and the XRD was performed. These measurements were performed at CAB, Bariloche, Argentina.

The LMO powder is first annealed at 718 ^{o}C in Ar and no oxygen loss is detected by TGA. Constant oxygen content is measured till 10^{-15} atm. After five days when pO_2 of the gas is dropped down below 10^{-16} atm, abrupt fall in the oxygen content was noticed and remained constant till pO_2 10^{-22} atm (see Fig. 5.19). The loss of oxygen was calculated to be in stoichiometric value of 9-δ = 8.57. Below this pO_2 value further fall in the oxygen content is noticed and drift of the oxygen content increases with the decrease in pO_2 pressures. Reduction was continuous and no thermodynamic equilibrium sate was observed either. Wt. loss by TGA signal showed oxygen content less than 7 (i.e. 9-δ < 7; $La_2Mo_2O_{7-\delta}$). Partially reduced LMO compounds at pO_2 of 10^{-20} and 10^{-24} atm are cooled down and followed by XRD. At pO_2 of 10^{-20} atm, an oxygen loss of 0.43 (9-δ = 8.57) per formulae unit was observed and is consistent with the formation of the 7730 phase. At lower pO_2 of 10^{-24} atm an amorphous phase was obtained having an oxygen stoichiometry lower than 9-δ < 7. The amorphous phase 7-δ compound has no fixed oxygen content and loses oxygen continuously with kinetics depending on the pO_2. This experiment was performed for nearly 11 days.

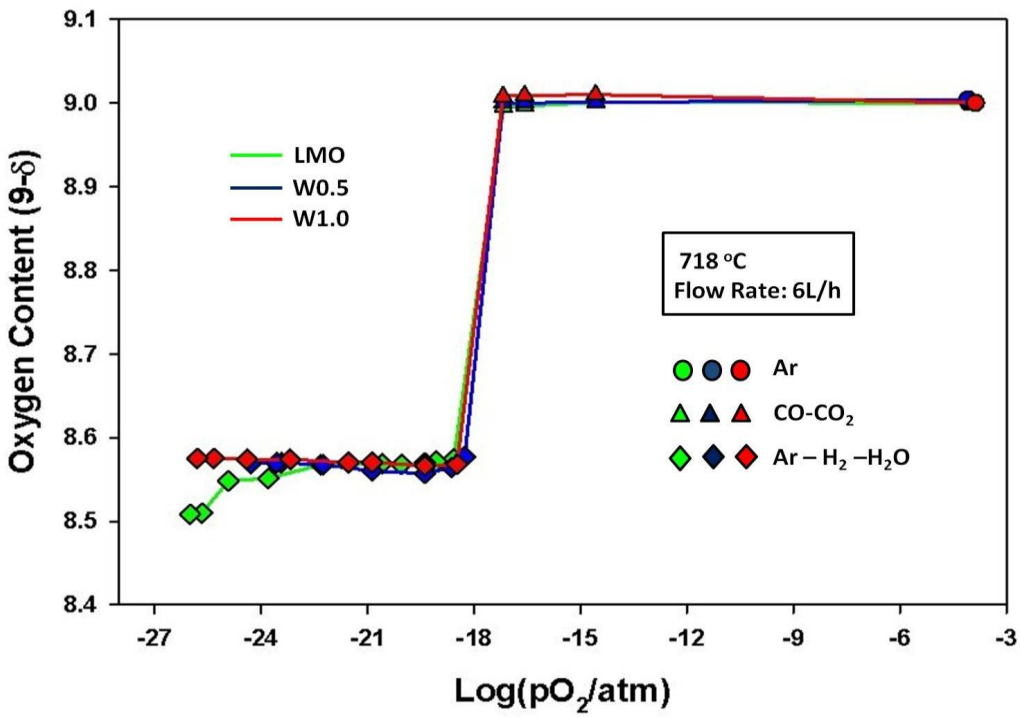

Figure 5.19: Oxygen content as a function of pO_2 at 718 ^{o}C for LMO, W0.5 and W1.0 powders.

The W0.5 sample is found to be stable in the range 10^{-5} (Ar) to 10^{-18}atm (Ar-H_2-H_2O). By decreasing pO_2, the oxygen content in the sample decreases down to 8.57 (9-δ = 8.57; 7730 phase confirmed by XRD when the sample is cooled down) and remains constant even after further decrease in pO_2. This total measurement was carried over 6 days. After the last measurement, the sample was left in dry Ar + 5%H_2 atmosphere at 718 ^oC for two hours and no change in the oxygen content was observed.

The W1.0 sample is found to be stable in the range 10^{-5} (Ar) to 10^{-18}atm (Ar-H_2-H_2O). By decreasing the pO_2, the oxygen content in the sample decreases down to 8.57 (9-δ = 8.57; 7730 phase confirmed by XRD when sample is cooled down) and remains constant even till pO_2 10^{-27} atm. Later when the sample is exposed to dry Ar + 10%H_2 for a couple of hours, no change in the oxygen content is seen. The total experiment is carried over for 8 days.

The pO_2 measurements carried on LMO, W0.5 and W1.0 demonstrate that the stability domain of the LAMOX phase does not depend on the W content. Only the reduction kinetics varies with the W content. The pO_2 limit found for the three compositions is almost identical. On the Contrary, the stability of the 7730 phase is dependent on the W substitution. The 7730 phase in LMO is stable only till pO_2 of 10^{-22} atm, which reduces to amorphous 7-δ phase, whereas in W-LMO (both W0.5 and W1.0) compounds, the 7730 phase was observed down till 10^{-27} atm.

5.7: Conductivity experiments on reduced $La_2Mo_2O_9$ and reduced W-LAMOX materials:

As discussed earlier, the reduced LMO compounds show superior conductive values than fully oxidized LMO phase. Overall conductivity increase in reduced LMO is already reported [4, 8, 10, 16, 17]. This increase in conductivity is related to the partial reduction of Mo^{6+}. Appearance of n-type conductivity in these samples makes them potential candidates as MIEC anode and bad electrolyte materials for SOFC applications. In the above sections of this chapter it was already shown that, under extreme reduction conditions, LMO reduces down to the amorphous phase and further reduction could lead to reduction of Mo^{6+} to metallic Mo. It is even seen that W substitution in LMO can limit its reducibility; however it cannot be totally eliminated. It is important to study the conductivities of the reduced LMO and W-LMO compounds before

considering their applications into SOFC. In this part of work we report electrical characterization studies carried out on the LMO and W0.5 compounds.

Electrical resistivity measurements were carried out on LMO and W0.5 samples which were over ~ 96 % relative dense. The pellets of both compositions were cut down into dense bars (8 x 3 x 2 mm) by a diamond saw. These bars were heat treated at 1000 ^{o}C and 1225 ^{o}C (LMO and W0.5 respectively). On these bars, four Pt contacts were obtained by sputtering Pt thin films. On these four contacts, Pt wires (electrodes) were joined using Pt paste and annealing subsequently at 800 ^{o}C. On two out of these four Pt electrodes (at the end of the bars), VG98 powder glass paste is applied and again heat treated at 800 ^{o}C for wetting the electrodes (electrode blockage). This method which helps to characterize only electronic conductivity (since ionic conductivity is totally blocked) was performed by four probes electrical resistivity method (more details are given in chapter 2, experimental section).

The samples were then placed in the tubular furnace setup in 6 L/h flow of Ar + 10% H_2. The resistivity measurements were performed at temperatures 608 ^{o}C and below. Immediate drop of the resistivity is found and the resistivity was practically constant thereafter for the next 144 hours (duration of measurement). This resistivity could be coming from the surface of the pellets. Reduction first occurs at the surface of the pellets and oxygen depletion from the bulk occurs later. This could be the reason for sudden displacement of resistivity appearing in initial stages of measurement. See the curves in Fig. 5.20. Arrhenius plot of the conductivity data vs. temperature is collected during 144 hours under the reducing conditions mentioned above. The resistivity measurements were performed as a function of time on cooling from 608 ^{o}C to 293 ^{o}C every 35 ^{o}C. The samples were left for 30 min at each stage before the conductivity was measured. The activation energies of both samples are calculated and found to be similar (Ea = 0.23eV). Arrhenius plot can be seen in Fig. 5.21. Both bars were ground after the experiment and XRD analysis was carried out. LMO sample was an amorphous phase (7-δ), whereas W0.5 was a mixture of an amorphous and an unknown phase (similar unknown phase to that observed in all W0.5 reduced powders).

Once the samples were cooled down to room temperature numerous cracks were noticed on both LMO and W0.5 pellets. These cracks as we believe would form

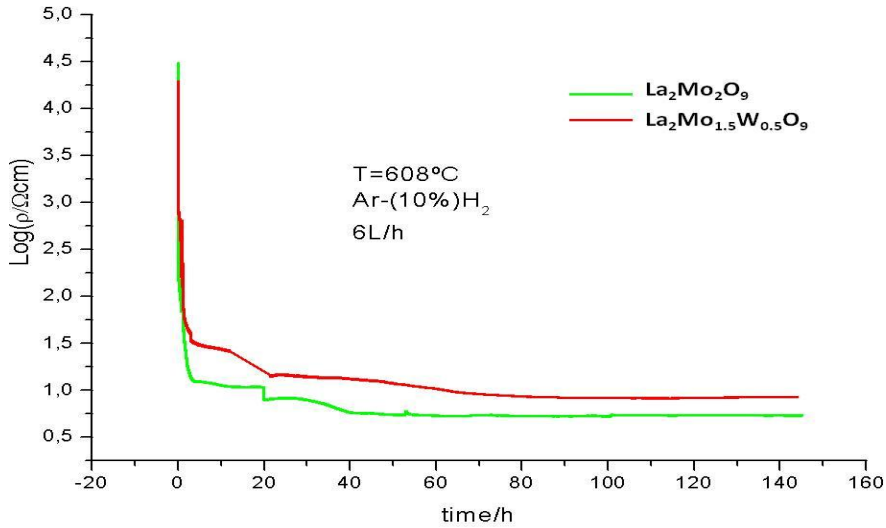

Figure 5.20: Resistivity of LMO and W0.5 compounds in Ar + 10 % H_2 (6 L/h flow rate) at 608 ^oC.

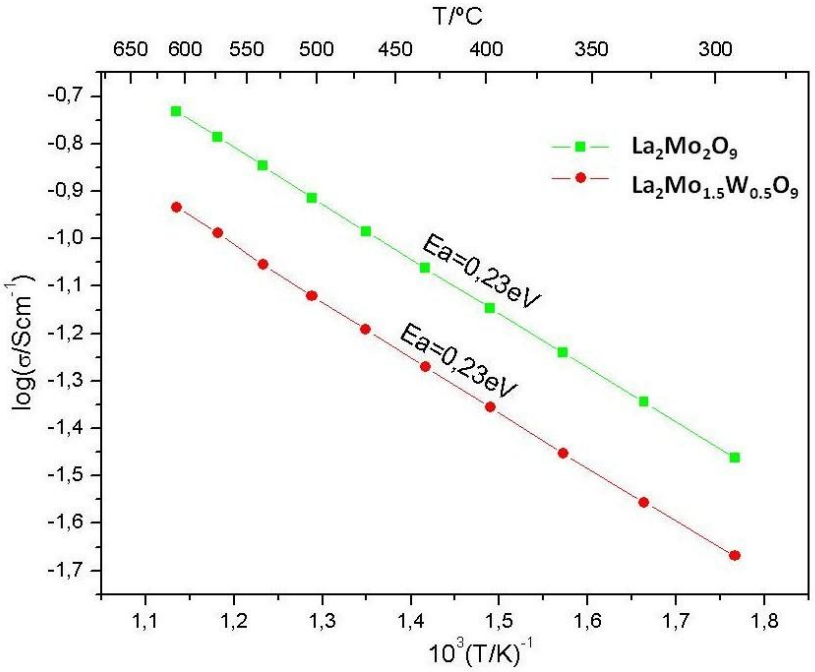

Figure 5.21: Arrhenius plot (conductivity vs. temperature) of LMO and W0.5, samples after a preliminary reduction at 608 ^oC for 144 hours under 6 L/h flow of Ar + 10 % H_2.

because of extreme reduction conditions to which the samples were exposed. SEM images of LMO bar after measurement are shown in Fig.5.22. The appearance of similar cracks in LMO was reported in literature [7, 10, 16, 18, 19]. The formation of these cracks makes it impossible to characterize the electrical properties with precision. Cracks could create a barrier for the transport of electrons, which would reflect lower conductivity values. Various approaches were attempted to resolve formation of cracks.

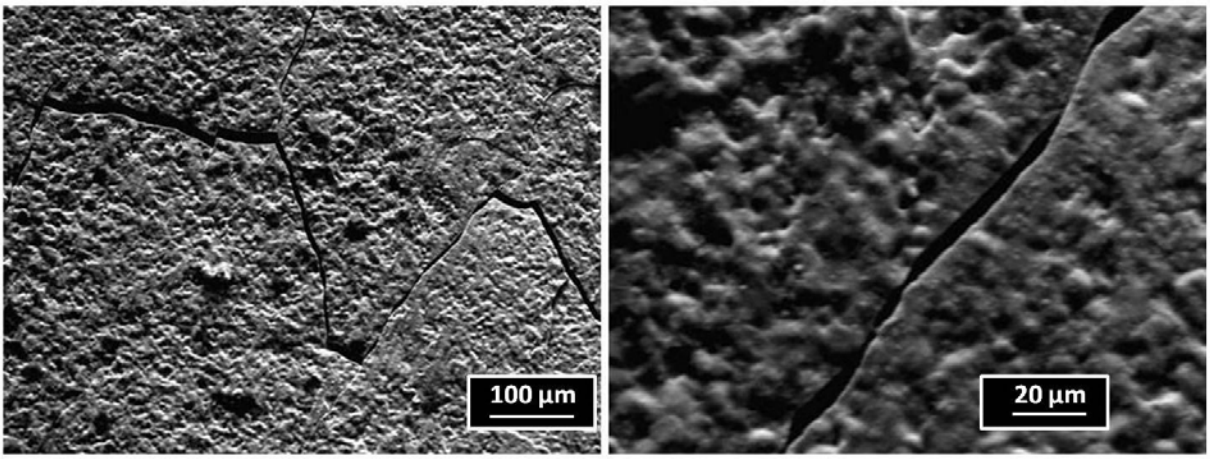

Figure 5.22: SEM images of LMO bar after reduction for 144 hours under 6 L/h flow of Ar + 10 % H_2 at 608 ^oC. Both the images show huge cracks formed on the bar.

LMO (both powder and pellet) transforms to amorphous phase (7-δ) when reduced. Pellets/bars of LMO when reduced show numerous huge cracks on the surface. One of the approaches to overcome such problem is to reduce LMO down to the amorphous phase and sinter such powder into a high dense pellet. Normally sintering of LMO takes place at temperatures near to ~1000 ^oC [20, 21]. If such amorphous powder is sintered at 1000 ^oC in static air or ambient conditions, amorphous phase sample (7-δ) would oxidize back to LMO (oxygen content = 9) [3]. If attempted to sinter in diluted H_2 atmospheres, it would further deplete more oxygen and decompose (metallic Mo appears). Studies performed in thermodynamic equilibrium states using pO_2 showed that LMO is not stable at 1000 ^oC [2]. Another approach is reducing a LMO (fully oxidized) bar gently (under mild reduction conditions for a long time). In such

attempt, a low dense LMO bar would be more effective (instead of using bar with ~ 96 % relative density as earlier). A low dense sample would limit /eliminate formation of cracks. Utilization of a low dense bar for conductivity measurement generates a similar problem as a bar with no cracks. Porosity in a less dense bar obstructs the free path of the electrons in the sample which reflects poor conductive value. Ideal case would be to perform electrical characterization on a bar with high relative density and free of cracks.

In such attempt to synthesize crack free pellets, two batches of LMO pellets (one with high density ~98 % relative density and other with low relative density 75%) were taken. Both batches were cut into bars of very small thickness (50 – 1000 μm) and were reduced under very mild reducing conditions in tubular furnace. Ar + 10% H_2 was used for reduction with a flow rate of 1.2 L/h. The temperature was first increased to 400 ^{o}C with the rate of increase 2 ^{o}C/min. From 400 ^{o}C, temperature was increased to 600 ^{o}C with the rate of heating 0.03 ^{o}C/min. After 96 hours of annealing, the samples were cooled back to room temperature with the rate of cooling 2 ^{o}C/min. Few bars from each batch were ground to follow phase purity by XRD. Samples in both batches were found to be amorphous. Bars which were initially 98% dense showed cracks, but very less compared to what we have seen in above mentioned measurement. Low dense bars (~75 % relative dense) show almost no cracks (very few cracks with very small width). SEM images of gently reduced low dense LMO bars are shown in Fig. 5.23.

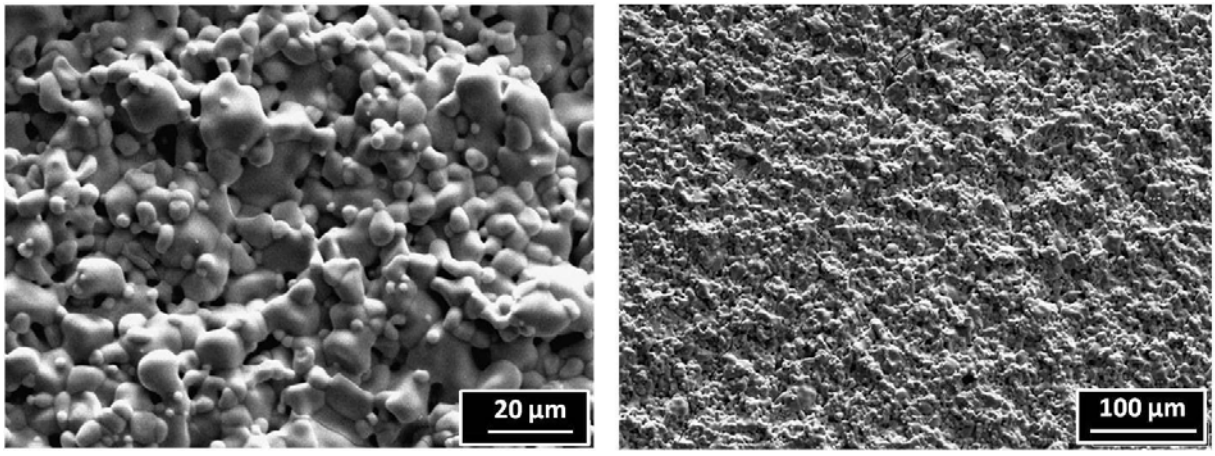

Figure 5.23: SEM images of a low dense LMO bar (~75 %) which was reduced to amorphous phase (7-δ) under very mild reduction conditions.

Thus obtained low dense bar (8 x 1 x 1 mm) with negligible cracks were selected for electrical resistivity experiments (4 probes electrical resistivity method; more details were given in chapter 2, experimental section). Four Pt electrodes were painted on the bar, Pt wires were sealed to each electrode using the same Pt paste. Sample was then annealed at 800 ^{o}C for 30 min under ultra high vacuum (UHV) to dry the Pt paste used for sticking the electrodes. The conductivity measurements were performed under UHV (~ 1 x 10^{-6} bar) from 279 ^{o}C to 760 ^{o}C every 50 ^{o}C. The sample was annealed at each temperature for 30 minutes before the conductivity was measured. The thermal evolution of conductivity is plotted and a pseudo activation energy of 0.25 eV was calculated from the slope of such curve. Arrhenius plot can be seen in Fig. 5.24. Sample was ground after the measurement and is observed to be in amorphous phase (7-δ). Conductivity values observed in porous non cracked bars is higher than that of the cracked one.

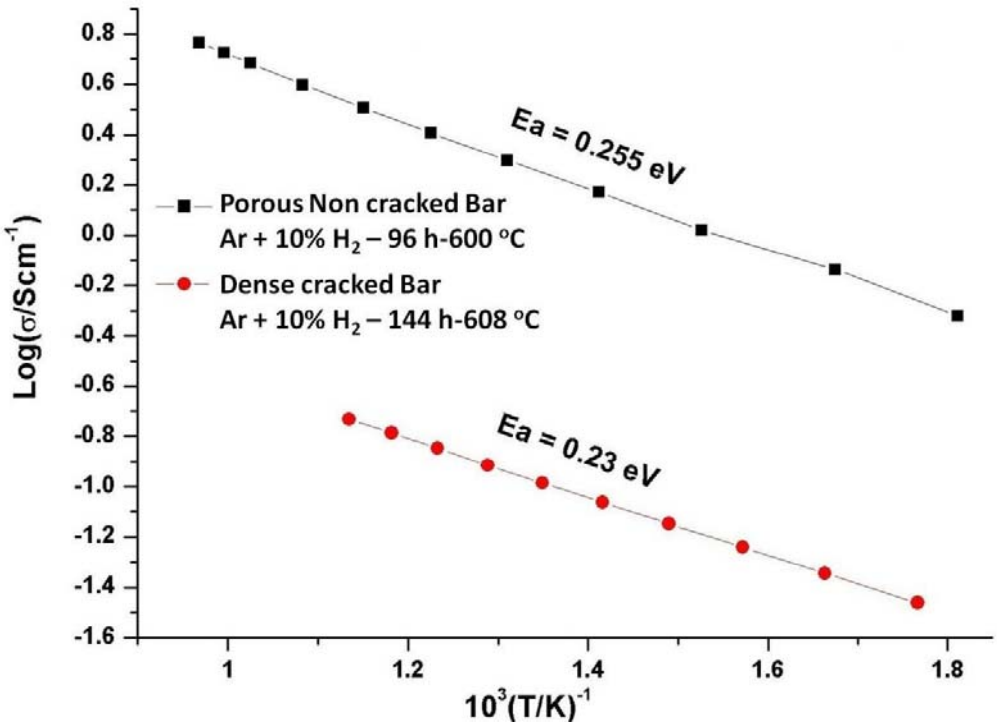

Figure 5.24: Thermal evolution of conductivity for LMO bars which were reduced in different conditions. Porous non cracked bar (black-squares) was obtained by reducing low dense LMO bar at 600 ^{o}C for 96 hours under very mild conditions (1.2 L/h). Dense cracked bar (red-circles) was obtained by reducing at 608 ^{o}C for 144 hours in Ar + 10 % H_2 flow, 6 L/h .

In an approach to synthesize high dense and crack free samples for electrical measurements, an intermediate reduced phase 7730 was also considered. Stability limits of 7730 phase were already known (reported earlier in this report). Plan was to sinter high dense 7730 phase pellets and reduce them gently to amorphous phase to obtain crack free samples. 7730 phase powders of LMO sample were synthesized (annealing 300mg of sample for 13 hours in Ar + 10% H_2 at 710 ^oC with gas flow rate of 1.2 L/h). These samples were fired in UHV (~1 x 10^{-6} bar) at 1000 ^oC. This firing was performed in UHV to avoid possible oxidation if annealed in ambient temperatures or Ar and to avoid further reduction in the sample if annealed in diluted H_2 atmospheres. Sample after annealing showed good density; however XRD revealed $La_5Mo_3O_{16}$ and $La_5Mo_6O_{21}$ impurities in agreement with the literature [2]. Several attempts to synthesize 7730 phase high dense pellet were unsuccessful. Attempts to synthesize LMO and 7730 phase high dense crack free samples are still in progress. These conductivity experiments were also performed at CAB, Bariloche, Argentina.

5.8: Conclusions:

Here in this work we report studies carried out on the stability of LMO and amorphous (7-δ) samples under very mild reducing conditions. It was found that LMO is stable at temperature less than 700 ^{o}C and the amorphous phase is stable under 800 ^{o}C when N_2 + 1% H_2 gas is used (performed only for 12 hours). Stability and phase transformations occurring in LMO compound when annealed at different times are reported (at 760 ^{o}C in Ar + 10% H_2 atmosphere with 3.6 L/h flow rate). Transformation of LMO to amorphous phase was observed, which on further reduction leads to the appearance of a fraction of metallic molybdenum. All the three LMO, 7730 and amorphous phases were observed in one sample, depending on the reducing conditions applied (annealing time and temperature, reductive atmosphere, flow rate of gas, quantity of the sample used).

During such stability measurements, LMO was heated at 760 ^{o}C (Ar + 10% with 6 L/h) and immediately cooled back (no annealing/ plateau stage). Resultant compound $La_2Mo_2O_{8.77}$ was brown. In spite of partial reduction, the high temperature cubic β-LMO was retained.

Unusual reduction phenomenon is reported where black spots are seen in a white matrix powder. Reasons underlying this phenomenon were not clear but a hypothesis is proposed. It is believed that black spots are the areas in the sample which were more reduced than the other parts. Inhomogeneous reductive behavior is also reported. Gradient of reduction over the sample in alumina boat is observed (exhibiting O_2 depletion with the gas contact) and respective phase transformation is analyzed by XRD.

Reductive behavior of W0.5 is studied using TGA and laboratory tubular furnaces. 7730 phase of W0.5 (powder sample) was synthesized in TGA with Ar + 10% H_2 gas. It is shown that reducibility in LMO can be limited by substitution of W^{6+} to Mo^{6+}; thus confirming the results reported in the literature. In a measurement performed on W0.5 and W1.0 (powder samples), where all the reduction parameters were kept constant, it was found that W1.0 is more stable than W0.5. TGA study performed on W0.5 and LMO pellets showed that LMO is more vulnerable to reduction than W0.5.

TGA in controlled oxygen partial pressures atmospheres were performed on LMO, W0.5 and W1.0 (shown in Fig. 5.17). LMO was found to be stable till 10^{-17} atm, later which reduces to

7730 and is stable till 10^{-22} atm. Further fall in pO_2 leads to amorphisation of the sample with no stable oxygen stoichiometry. Stability limits of 7730 phase for W0.5 and W1.0 were defined, see the curves in Fig. 5.19. It was observed that the stability domain of the $La_2Mo_{2-y}W_yO_9$ phases does not depend on the W content; only the reduction kinetics varies with the W content. pO_2 limit found for the three compositions is almost identical. On the contrary, the stability of 7730 phase was found to be dependent on W substitution.

Resistivity experiments were performed on LMO and W0.5 pellets. It was observed that most of the resistivity arises from the surface of the pellet (in the initial stages of reduction) and falls back immediately as soon as the surface is in equilibrium with the atmosphere. LMO surface once exposed to reductive atmosphere, exhibits n-type conductivity and it is postulated that n-type electronic conductivity arises from partial reduction of hexavalent Mo^{6+} to a mixture of Mo^{6+} and Mo^{5+} (for 7730 phase) and Mo^{3+} and Mo^{4+} (for the amorphous (7-δ) phase), becoming MIEC and displays superior conductivity than its fully oxidized sample). On these dense pellets (both LMO and W0.5) on which cracks have appeared, pseudo activation energy was found to be 0.23 eV.

Synthesis of amorphous phase (7-δ) pellet with no cracks was achieved (by mild reducing conditions) and conductivity experiments were carried on such sample. Superior conductivity value with a pseudo activation energy of 0.255 eV is reported. It has to be acknowledged that for a material to be potential anode in SOFC, sufficient porosity is necessary (for free mobility of oxygen ions and hydrogen); however the true conductivity values of the potential compound are to be well studied and this is subjected to the availability of such non-cracked and high dense sample. Attempts to synthesize reduced, high dense and non cracked LMO and W-LMO compounds have to be carried out. Much higher conductivity values can be expected in such samples. Moreover level of electronic conductivity has to be improved in order to make W substituted LAMOX suitable as anode materials for dual chamber SOFC.

Local structure analysis of the amorphous reduced phase (7-δ) sample is impossible by XRD, and for this purpose use of Extended X-ray Absorption Fine Structure (EXAFS) is desirable. The oxidation states of molybdenum could be reached through X-ray Absorption Near Edge Structure (XANES) or Electron paramagnetic Resonance (EPR) measurements.

5.9: References:

1. F. Goutenoire; R. Retoux; E. Suard; P. Lacorre, *Journal of Solid State Chemistry* **1999,** 142, (1), 228-235.
2. J. Vega-Castillo; L. Mogni; G. Corbel; P. Lacorre; A. Caneiro, *International Journal of Hydrogen Energy* **2010,** 35, (11), 5890-5894.
3. D. Marrero-Lopez; J. Canales-Vazquez; J. C. Ruiz-Morales; J. T. S. Irvine; P. Nunez, *Electrochimica Acta* **2005,** 50, (22), 4385-4395.
4. X. C. Lu; J. H. Zhu, *Journal of the Electrochemical Society* **2008,** 155, (10), B1053-B1057.
5. T.-Y. Jin; M. V. Madhava Rao; C.-L. Cheng; D.-S. Tsai; M.-H. Hung, *Solid State Ionics* **2007,** 178, (5-6), 367-374.
6. G. Corbel; Y. Laligant; F. Goutenoire; E. Suard; P. Lacorre, *Chemistry of Materials* **2005,** 17, (21), 5390-5390.
7. S. Georges; M. Salaun, *Solid State Ionics* **2008,** 178, (37-38), 1898-1906.
8. J. Jacquens; D. Farrusseng; S. Georges; J. P. Viricelle; C. Gaudillere; G. Corbel; P. Lacorre, *Fuel Cells* **2010,** 10, (3), 433-439.
9. J. E. Vega-Castillo; U. K. Ravella; G. Corbel; P. Lacorre; A. Caneiro; , *(in progress)*.
10. J. Jacquens. Stabilite, reactivite et Performances de conducteurs par ions oxyde de la famille LAMOX comme elements de coeur de pile a combustible SOFC mono-chamber. Universite du Maine, Le Mans, 2010.
11. S. Georges; S. J. Skinner; P. Lacorre; M. C. Steil, *Dalton Transactions* **2004**, (19), 3101-3105.
12. N. Sakai; K. Yamaji; T. Horita; Y. P. Xiong; H. Kishimoto; H. Yokokawa, *Journal of the Electrochemical Society* **2003,** 150, (6), A689-A694.
13. R. N. Vannier; R. J. Chater; S. J. Skinner; J. A. Kilner; G. Mairesse, *Solid State Ionics* **2003,** 160, (3-4), 327-334.
14. R. N. Vannier; S. J. Skinner; R. J. Chater; J. A. Kilner; G. Mairesse, *Solid State Ionics* **2003,** 160, (1-2), 85-92.
15. S. Georges; F. Goutenoire; Y. Laligant; P. Lacorre, *Journal of Materials Chemistry* **2003,** 13, (9), 2317-2321.
16. D. Marrero-Lopez; J. C. Ruiz-Morales; P. Nunez; J. C. C. Abrantes; J. R. Frade, *Journal of Solid State Chemistry* **2004,** 177, (7), 2378-2386.
17. P. Pinet; J. Fouletier; S. Georges, *Materials Research Bulletin* **2007,** 42, (5), 935-942.
18. S. Georges; R. A. Rocha; E. Djurado, *Journal of Physical Chemistry C* **2008,** 112, (9), 3194-3202.
19. M. Goel; E. Djurado; S. Georges, *Solid State Ionics* **2011,** 204-205, (0), 97-103.
20. S. Georges; F. Goutenoire; P. Lacorre; M. C. Steil, *Journal of the European Ceramic Society* **2005,** 25, (16), 3619-3627.
21. D. Marrero-Lopez; J. Canales-Vazquez; J. C. Ruiz-Morales; A. Rodriguez; J. T. S. Irvine; P. Nunez, *Solid State Ionics* **2005,** 176, (23-24), 1807-1816.

Summary and Conclusion

$La_2Mo_2O_9$ (LMO) is a pure and fast oxide ion conductor in air, and its use as SOFC fuel cell core material (as electrolyte or anode material) was debated. LMO undergoes a phase transition around ~580 ^oC and it was reported that W substitution to Mo in LMO can suppress this phase transition. It was known that LMO reacts at various temperatures with standard cathode materials used in SOFC applications and it was reported that $La_{0.8}Sr_{0.2}MnO_{3-\delta}$ (LSM) is the least reactive compound. It was also known that LMO reduces under atmospheres with low pO_2 and W substitution to Mo in LMO can limit its reducibility. Recently reduced amorphous phase $La_2Mo_2O_{7-\delta}$ (7-δ) was proposed as a performing sulfur-tolerant MIEC anode material for SOFC applications. The aim of this study is to understand the thermal stability of W substituted LMO compounds in air (to choose optimum composition for SOFC applications), study the reactivity of LMO/LSM (to understand the diffusion behavior of individual elements in these compounds and thereby possibly limit/control such reaction mechanism) and to study the reductive behavior of LMO and W-LMO compounds and optimize the suitable candidate for SOFC anode application. The results of this study as summarized below are presented in the three main chapter of my thesis manuscript.

$La_2Mo_{2-y}W_yO_9$ (y = 1.0 to 2.0) oxides were synthesized by conventional solid state route and their thermal stability was studied using X ray diffraction (XRD), temperature controlled XRD and differential thermal analysis. Multiple quenching experiments and long term heat treatments were performed to probe their thermal behavior. It was observed that oxides with $1.0 \leq y \leq 1.2$ are in high conducting cubic β-LMO form and thermodynamically stable over long term annealing (60 days at 700 ^oC). At higher W content $1.3 \leq y \leq 1.8$, the β form is metastable in nature. A partial or full release of metastability of this β form was observed upon further heating (β-LMO + α-LWO for $y \leq 1.575$ and α-LWO for $y \geq 1.6$). Compounds with $1.85 \leq y \leq 2.0$ are always in low conducting triclinic α-LWO phase, irrespective of heat treatments and synthesis conditions. Inhomogeneous distribution of W is suspected in the biphasic samples. A phase diagram for $La_2Mo_{2-y}W_yO_9$ (y = 1.0 to 2.0) oxides was proposed. It was even seen that NiO does not react with $La_2Mo_{2-y}W_yO_9$ compounds,

contrary to what has been claimed in the literature. Overall it was clear that compounds above 60 mol% of W substitution (1.2 < y) are not suitable for SOFC application as an electrolyte.

A reaction was probed between pellet couples of LMO/LSM by annealing such couples (two couples were annealed at 1050 ^{o}C for 12 and 36 hrs, and a third one at 1150 ^{o}C for 12 hrs), and such reaction mechanism was studied using Secondary Ion Mass Spectrometry (FIB-SIMS and TOF-SIMS; surface analysis, mass spectrometry, depth profiles and line scan) and XRD. After the reaction, it was found that Mn from LSM migrates towards LMO and forms $LaMnO_3$ rod shaped grains on its surface. Whereas Mo from LMO diffuses towards LSM and forms insulating $SrMoO_4$ type phases on the surface of LSM. Multiple hypotheses for such reaction mechanism were formulated. To understand the diffusive behavior of individual cations, Sr and Mn rich solutions were deposited on two different LMO pellets and Mo solution was deposited on LSM pellet and such solution deposited pellets were annealed at 1150 ^{o}C for 12 hrs. Mn solution decomposition was observed to be forming $LaMnO_{3-\delta}$ single crystals on the surface of LMO pellet. Penetration depth of Sr in LMO was approximated at ~60 to 70 μm and Mo in LSM was nearly ~50 μm. Multiple reaction products were observed in solution deposited measurements ($LaMnO_3$, La_6MoO_{12}, La_2MoO_6, β-LMO and $SrMoO_4$ type phases) and possible reaction mechanisms are proposed. From the LSM/LMO pellet couples, diffusion coefficient of Sr and Mn (from LSM pellet) into LMO was estimated as $1x10^{-20}$ cm^2 s^{-1} in the LAMOX fuel cell operating temperature range (~800 ^{o}C), and in the same temperature range, diffusion coefficient of Mo (from LM)) into LSM was estimated to be $1x10^{-15}$ cm^2 s^{-1}. Even though diffusion rate of Sr is small, fast diffusion of Mo towards LSM leads to the formation of $SrMoO_4$ type phases at the interface and appearance of this new phase is problematic for fuel cell. It is clear that LMO/LSM are highly reactive and such electrolyte/cathode couple is not suitable for SOFC applications and an buffer layer between both components has to be used in order to realize LMO/LSM couple for fuel cell applications.

Third part of this study deals with the stability of LMO and W-LMO compounds under reductive atmospheres. Thermogravimetric analysis, XRD and tubular furnace setups were used with different diluted H_2 gases and controlled pO_2 pressures as reductive atmosphere. Resistivity measurements were performed using four wire method. Structural changes from LMO to $La_7Mo_7O_{30}$ (7730), amorphous phase and partial decomposition of amorphous phase to metallic Mo were observed as a function of oxygen loss in the system

and it was observed that the amorphous phase can accommodate a wide range of oxygen stoichiometry (from 7-δ = 6.69 to 6.20). Cubic β-LMO phase, brown colored sample was obtained for the first time when LMO was reduced to $La_2Mo_2O_{8.77}$. Inhomogeneous reduction behavior was observed in LMO and such behavior is assumed to be boosted by water vapour. When similar reduction conditions were employed on LMO, $La_2Mo_{1.5}W_{0.5}O_9$ (W0.5) and La_2MoWO_9 (W1.0), it was observed that LMO is more vulnerable to reduction compared to W0.5, which is further more reductive compared to W1.0. It was observed that LMO reduces to 7730 phase at 10^{-17}atm (at 718 ^oC), which further reduces to amorphous (7-δ) when pO_2 is dropped to 10^{-22} atm, and the sample keeps on reducing with further fall in pO_2, without reaching thermodynamic stability. Stability limits of W0.5 and W1.0 were also determined (at 718 ^oC by decreasing pO_2). It was observed that the stability domain of the $La_2Mo_{2-y}W_yO_9$ phases does not depend on the W content; but only the reduction kinetics vary with the W content. The pO_2 limits for all three compounds were identical. On the contrary, the stability limit of the 7730 phase was found to be dependent on W substitution. Resistivity measurements showed significant increase in conductivity (higher conductivity than for the fully oxidized sample) and it was clear that this increase is due to the appearance of an n-type conductivity arising from partial reduction in LMO of hexavalent Mo^{6+} to a mixture of Mo^{3+} and Mo^{4+}. Amorphous phase (7-δ) pellets were synthesized without cracks under mild reduction conditions, and on these samples, despite their porosity superior conductivity was measured (>1 S/cm at 1000 K) with a pseudo activation energy of 0.255eV.

Overall, it is clear that n-type conductivity arises in $La_2Mo_2O_9$ and W-substituted LMO, because of the partial decomposition of hexavalent Mo. Appearance of electronic conductivity makes this compound a mixed ionic and electronic conductor (MIEC) and there arises a possible utilization of LAMOX materials as MIEC anode in SOFC applications. Presuming thermal and chemical compatibilities between reduced lanthanum molybdate MIEC and LAMOX based electrolyte material, a novel LAMOX based fuel cell could be possible. Reduced amorphous (7-δ) has shown conductivity >1 S/cm at 1000 K with a pseudo activation energy 0.255 eV, which is satisfactory for a MIEC anode; however there were some stability issues. Under thermodynamic equilibrium conditions, it was shown that LMO was in amorphous (7-δ) phase at 10^{-22} atm (718 ^oC), and the sample keeps on reducing. Even though further reduction would increase electronic conductivity in the sample, one has to study the limits of reduction for an understanding of the system.

Perspectives

LAMOX materials show significant potential towards applications in high end technologies like SOFC, oxide ion separation membranes e.t.c; however substantial work has yet to be realized to meet requirements for such applications.

In this thesis work, rough estimate of $La_2W_yMo_{2-y}O_9$ (y = 1.0-2.0) phase diagram was given and it was shown that compounds with W substitution above 60 mol% (above W1.2) are not suitable for SOFC electrolyte applications. This conclusion was drawn after testing stability of W1.2 for 60 days at 700 ^{o}C. Further long term heat treatment measurements at higher temperature (say for a year at 800 ^{o}C or higher) has to be performed to verify its thermal stability. In W-LMO samples with W content more than y = 1.2, inhomogeneous distribution of W was suspected. Possible inhomogeneity of the W distribution has to be verified in samples with W content less than 60 mol%. The effect of long term heat treatment on W-inhomogeneous distribution and its possible incidence on conductivity are to be studied.

Cationic diffusion studies carried on LMO and LSM show that these samples are highly reactive and our current results point towards a high diffusivity of at least one element (Mo). In order to control/block such cationic diffusivity, a buffer layer is necessary and appropriate materials for such buffer layer are to be researched. Since it is known that ceria based materials do not react with LMO, research on buffer materials made of ceria would be worthy studying. Apart from that, it would be necessary to obtain more accurate diffusion coefficients and for this purpose, homogenous and better quality surface/interface would be necessary. Sputtering of thin layers of LMO on LSM or vice versa could be advantageous.

Conductivity values of amorphous reduced phase (7-δ) observed in our measurements were good but should be improved. Higher level of electronic conductivity would be necessary in order to improve the performance of such materials as MIEC anode for dual chamber SOFC. Elaboration of high compact and crack-free pellets of amorphous reduced phase (7-δ) has to be achieved in order to obtain the bulk conductivity values of these compounds. Conductivity higher than 1 S/cm are expected from such high density reduced samples. Since in our measurements, only electronic conductivity is studied, ionic conductivity of reduced LMO (the

amorphous phase) has to be studied to validate real conductivity and possible application of reduced LMO as MIEC materials. Long term stability studies of reduced LAMOX materials in low pO_2, possibly in a SOFC operating device, would be necessary in order to determine if a stable equilibrium can be reached for given oxygen content in the amorphous phase. We have observed that amorphous phase upon further reduction leads to partial decomposition into metallic molybdenum, and such decomposition need not be worrisome, since it should increase electronic conductivity in this new type of cermet phase. A new field of studies opens up with the determination of the compositional extension of La:Mo>1 reduced amorphous phases, their conducting properties and thermal stability. Local structure analysis of amorphous reduced phased (7-δ) sample is impossible by XRD, and for this purpose utilization of Extended X-ray Absorption Fine Structure (EXAFS) is desirable. Oxidation states of molybdenum could be reached through X-ray Absorption Near Edge Structure (XANES) or Electron paramagnetic Resonance (EPR) measurements.

Annex

I.1: Instrument effects in Differential Thermal Analysis (DTA):

As reported in chapter 3, numerous compounds were synthesized in $La_2W_yMo_{2-y}O_9$ series with (y = 1 to 2.0). Thermal behavior of these compounds was studied by TC-XRD and DTA analysis. In the DTA patterns of several compounds a variation in the TG signal resembling an endothermic event (a phase transition) was observed around ~980 ^oC. Such even registered by DTA was verified by performing HT-XRD analysis on the sample, and it was concluded that such variation in the TG signal was an instrument artifact and such perturbation does not represent any phase transition in the compounds.

In order to confirm this artifact, empty Pt crucibles were heated in DTA unit from room temperature to 1175 ^oC at 10 ^oC/min and cooled back to room temperature immediately at the same rate in air flow of 100 ml/min. This measurement conditions were similar to those used for W-LMO samples. A perturbation in the TG signal was observed at ~ 980 ^oC, confirming this behavior as an artifact (see Fig. I.1).

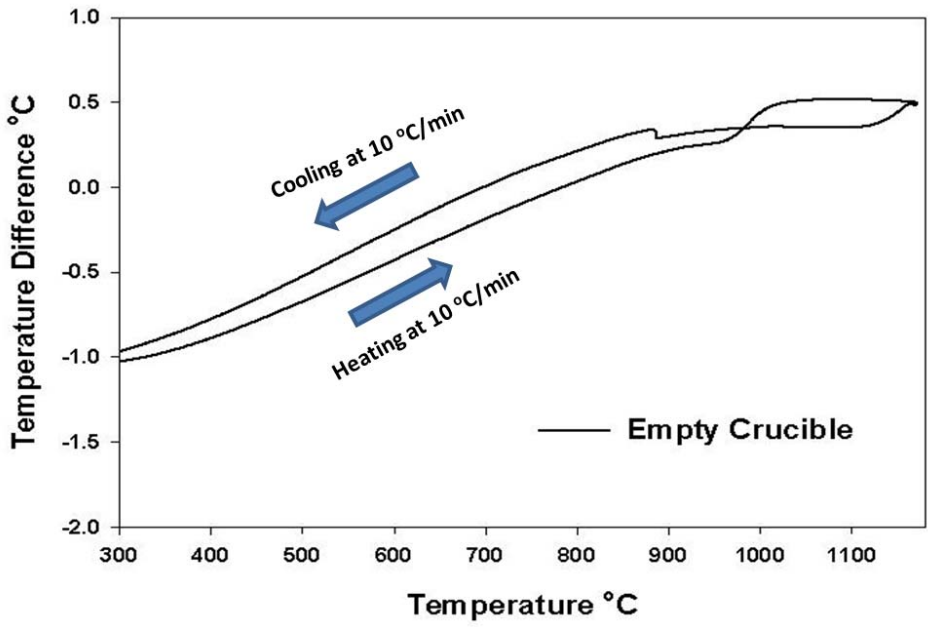

Figure I.1: DTA pattern collected on empty Pt crucibles showing perturbations at ~980 ^oC.

Reason for such perturbation is unknown; however it is believed that an unknown component) of DTA unit (alumina crucible holding arms or inner chamber walls e.t.c) was contaminated by some volatile material. Since same DTA instrument is being used by all the teams in our laboratory and some of them work with volatile materials, it is possible for the instrument to be contaminated (one team works on Li based materials and another team work on F based materials). To overcome this limitation of DTA and to confirm any abnormal behavior observed in the DTA patterns, thermal behavior of all the samples was studied by TC-XRD analysis aswell.

I.2: Limitations of Secondary Ion Mass Spectrometry (SIMS) analysis:

In SIMS analysis a high energy primary beam is collimated, focused and directed onto the surface of the sample. When the beam is rastered on the surface of the sample, material erodes or sputters from the surface. Thus obtained sputtered material is called secondary ions. Secondary ions constitute of positive or neutral or negatively charged ions, and secondary ions are mixture of different types of ions, and such variation in mixture depends on the composition of the sample. Secondary ions which were sputtered from the sample surface are transferred to another column under UHV, where the ions are separated by their mass. It is here secondary ions are counted by detectors of mass spectrometer.

SIMS collects information on the number of secondary ions, of a given mass, emitted by sample (for ex. specific count of Sr^+ (amu = 88), or La^+ (amu = 139) e.t.c). The data obtained is the number of counts, the interval of time used to take the count and the depth of the crater which was the result of sputtering (in depth profiles). Thus obtained data allows correlation of secondary ion counts made with the changes in the material and allows tracking such changes as the function of depth in the material. Using this information, profile of a specific secondary ion (identified by the mass) is plotted. If a line scan is performed instead of depth analysis, correlation of the length of line and the respective secondary ion yield (in counts) are profiled. This information is entirely qualitative. Sputter yield or secondary ion yield of one type of ion need not be similar to other and they cannot be compared. In a material system with multiple components sputter yield typically varies with the composition. It is well known that the

secondary ion yield changes with the atomic composition, chemical state, crystallographic orientation and other attributes. These sample dependent variables are called matrix effects.

In the SIMS measurements performed in this thesis work, specific cation rich solution was deposited on surface of LMO and LSM pellets. As an example, Sr is deposited on the surface of the LMO pellet and diffusion of Sr is induced into LMO pellet by annealing the pellet. Concentration of Sr on the surface of the pellet will be higher and such concentration diminishes with the depth into bulk. It was later observed that Sr can enter into LMO matrix (by partially substituting La) or can react with Mo in LMO and form $SrMoO_4$ type phases. In the section 4.3.1.2 of chapter 4, different possibilities for the existence of Sr and La (with different Sr:La ratios) in $SrMoO_4$ was explained. In this measurement two different Mo deficient lanthanum molybdate phases (La_2MoO_6 and La_6MoO_{12}) were observed by XRD. During SIMS depth profiling signals of Sr^+, La^+, Mo^+ were collected and it has to be noted that these compositions would have been spread at different layers of depth in the pellet. Also note that here the secondary ion yield of La^+ from La_2MoO_6 or La_6MoO_{12} or LMO or $SrMoO_4$ type phases will be different to each other and quantitative information of such yield would not be sensible, however the overall changes in the profile of La^+ count can be taken into account. This behavior is same for Sr^+ and Mo^+ signals aswell. Similar interpretation has to be considered for other measurements where Mn is deposited on LMO pellet or Mo is deposited on LSM pellet or LSM/LMO coupled pellet measurements.

In most of the samples on which depth profiles were carried out, the surface of the crater will not be uniform. The surface roughness of the bottom of the crater will be remarkably high when compared to surface roughness at the top of sample surface. Variations caused by the secondary ion yield and the relative density of the pellet could be factors leading such behavior (because of micro and macro porosity). It is generally recommended to have samples with relative density higher than 95 %. All pellets used for cationic diffusion studies and SIMS analysis in this thesis work had relative density higher than 95 % (LMO and LSM), and inspite of high density, surface roughness of the bottom of the crater was found to be significantly higher. Crater formed after depth profile analysis on LMO pellet is shown in Fig. I.2. This phenomenon would have been caused by micro porosity and variation in secondary ion yield.

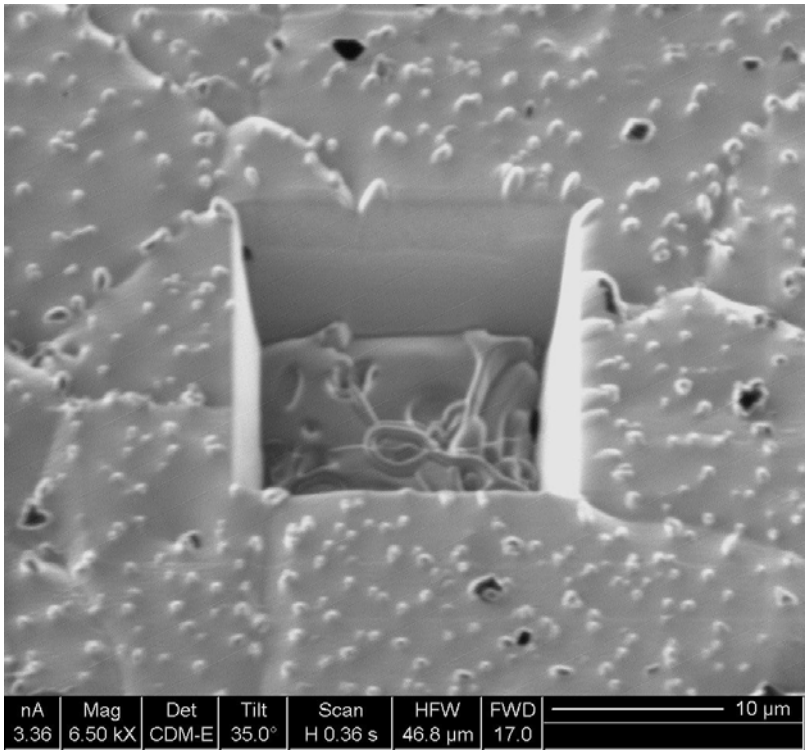

Figure I.2: FIB-SIMS depth profile of LMO pellet which was coupled with LSM pellet and annealed at 1150 ^{o}C for 12 Hrs. A (20 x 20 µm) crater and high surface roughness at the bottom of the crater are clearly visible. Small dot like structures on the surface of LMO pellet comes from Au coating.

During the SIMS depth profile analysis, the signals of all the elements gradually fall after certain depth. Consider a crater with thickness w, and a depth profile was performed on this crater till d. If d/w > 1 depth, there will be fall in the count of all the secondary ion yield signals. During depth profile measurement if the depth of crater is more than its thickness, it is likely that secondary ions which were sputtered from the surface of the sample could be obstructed by the inner walls of the crater (see Fig. I.3). Secondary ions which were struck to the crater wall do not reach the mass spectrometer detector and lead to appearance of low secondary ion yield (artifact). This phenomenon causes false count and overall fall in the signals. This behavior is observed in most of our SIMS measurements, where depth of the crater was high than its thickness.

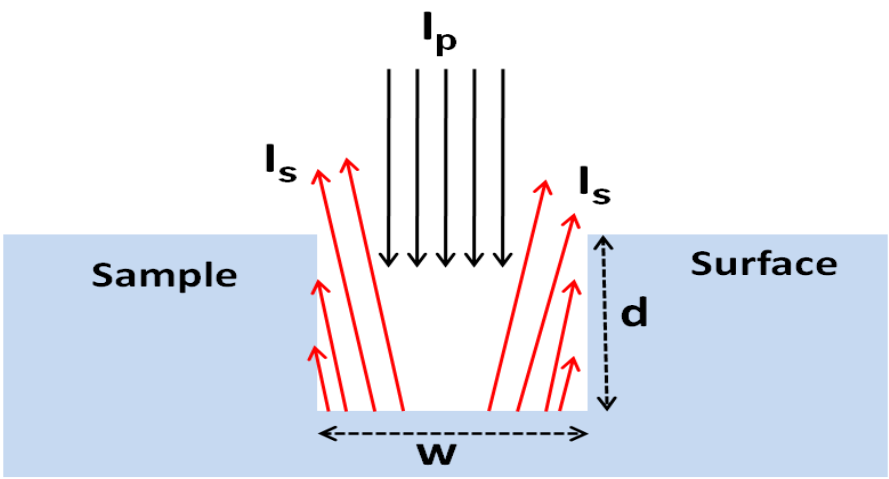

Figure I.3: Schematic representation of SIMS depth profiling limitation caused by crater walls. When primary ions I_p are bombarded over the surface of the sample, sample erodes into secondary ions I_s and forms a crater. If the depth of the crater 'd' is more than width of crater 'w', the secondary ions hit the inner walls of the crater, leading to the false count in the signals.

II. W-substituted $La_2Mo_2O_9$ XRD Analysis:

Several compounds $La_2W_yMo_{2-y}O_9$ (y = 1 to 2.0) were synthesized under different conditions (details were presented in Chapter 3). All these compounds were first synthesized by cooling from their relative synthesis temperatures at 5 ^oC/min, where it was found that samples from W1.0 to W1.575 were in cubic β-LMO form and compounds from W1.6 to W1.8 were biphasic and W185 to W2.0 were in triclinic α-LWO form. On all the single phase samples Rietveld analysis was performed and the results were shown and discussed in section 3.7 of Chapter 3. Here the Rietveld refinement of all the XRD patterns will be presented. Reliability factors (R_{wp} (%), R_{exp} (%), and χ^2) are provided in their respective patterns. Note that the background was taken into account while defining reliability factors. Patterns of the samples from W1.0 to W2.0 which were synthesized by cooling at 5 ^oC/min are shown in Fig. II.1 - Fig. II. 14.

W1.0, W1.1 and W1.2 were heat treated at 700 ^oC for 60 days to study their stability and found that these three samples were always β-LMO phase irrespective of heat treatments. On

these three samples Le-Bail fitting is performed and respective patterns are shown in Fig. II.5 to Fig. II.17.

Samples from W1.3 to W1.8 were heat treated at 800 °C for 4 days (96 hours). After heat treatments, samples from W1.3 to W1.5 were observed to be bi-phasic. On these samples XRD patterns were collected at room temperature and thermal diffractometry was performed at 700 °C by TC-XRD aswell. On all patterns both at R.T and at 700 °C, Rietveld analysis was performed and relative results were discussed in section 3.7 of Chapter 3. Note that W1.25 and W1.5875 was used as the boundary limits of the bi-phasic domain (β-LMO + α-LWO phases) and attempts were made to extrapolate the theoretical values of such bi-phasic domain using (inverse) Lever rule. Here the Rietveld analysis patterns of these compounds are presented (see Fig II. 18 to Fig. II.20 for patterns at room temperature and Fig. II. 21 to Fig. II. 23 for patterns at 700 °C). Unit cell parameters of the compounds after the refinement were given in Table II.1 and II.2 for patterns collected at R.T and 700 °C respectively. All the refined parameters of W1.3 and W1.7 for raw powders, W1.4 and W1.7 thermodynamic stable (heat treated) compounds at R.T and at 700 °C are given in Table II.3 to II.7 respectively.

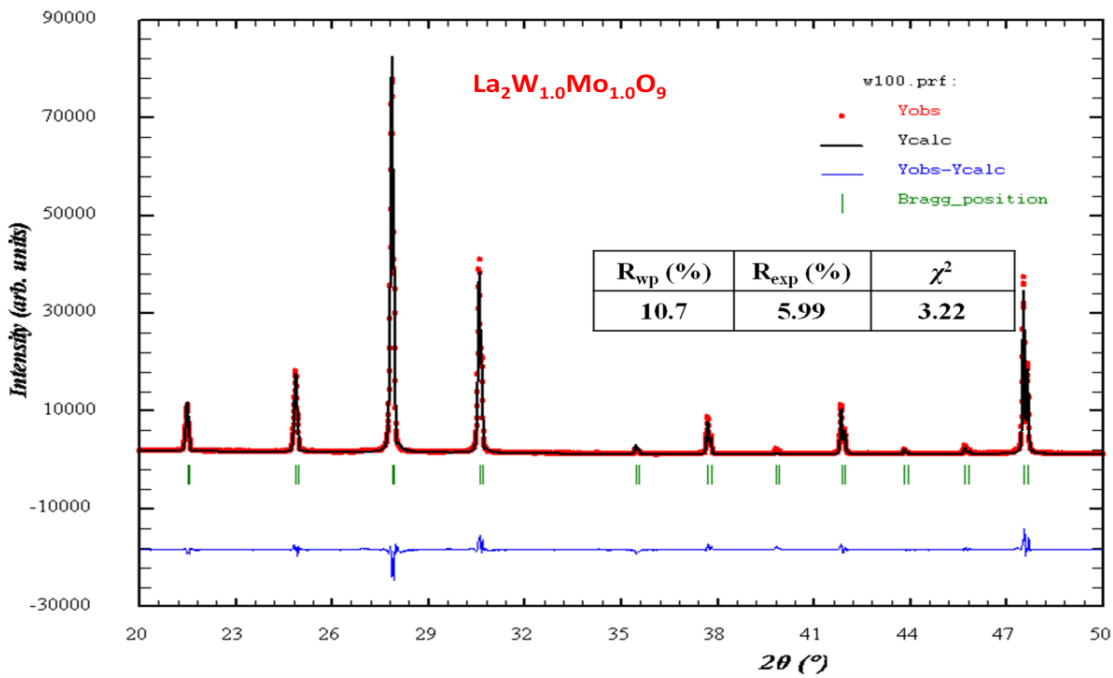

Figure II.1: Rietveld refined XRD pattern of cubic β-LMO phase W1.0 compound (space group $P2_13$). Synthesized by cooling at 5 °C/min.

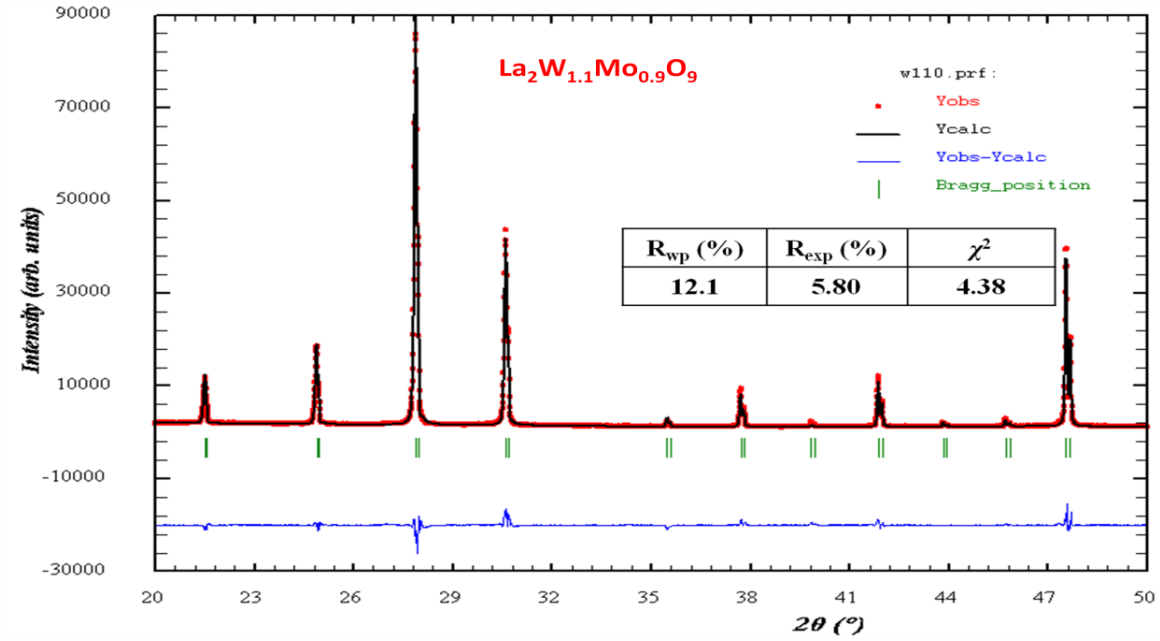

Figure II.2: Rietveld refined XRD pattern of cubic β-LMO phase W1.1 compound (space group $P2_13$). Synthesized by cooling at 5 °C/min.

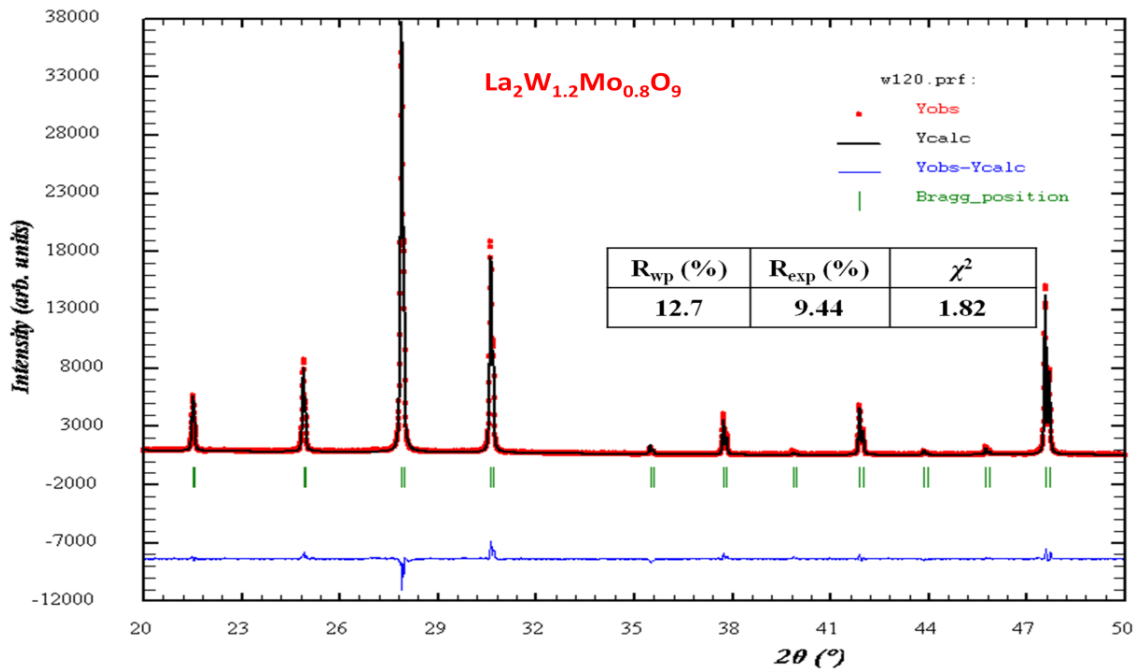

Figure II.3: Rietveld refined XRD pattern of cubic β-LMO phase W1.2 compound (space group $P2_13$). Synthesized by cooling at 5 °C/min.

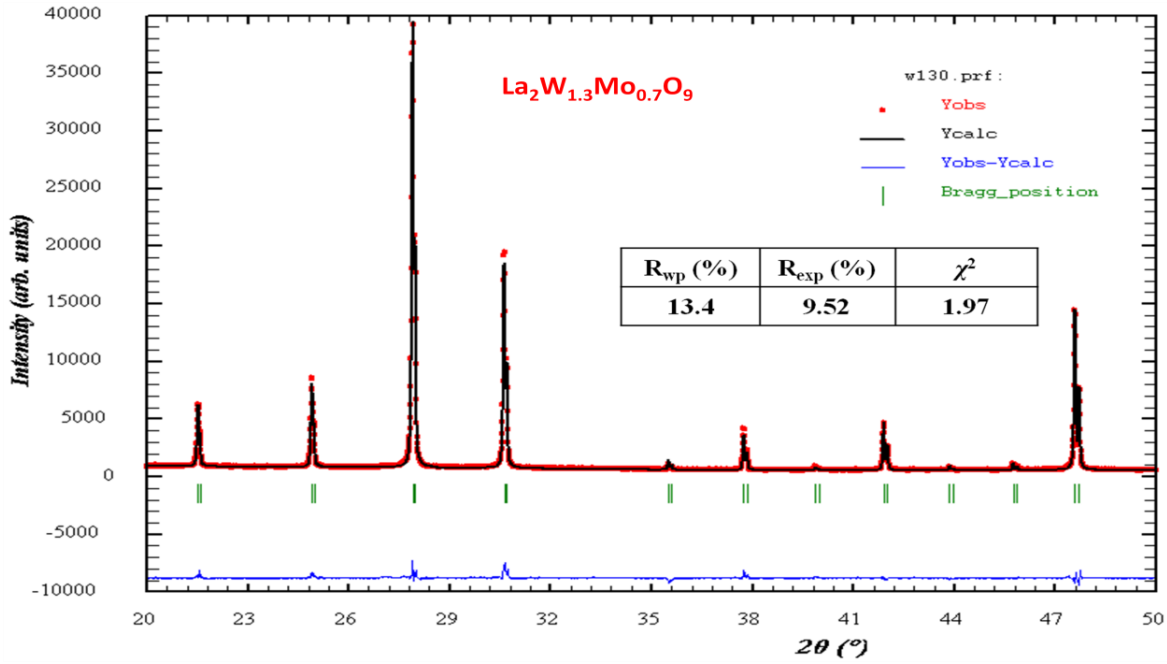

Figure II.4: Rietveld refined XRD pattern of cubic β-LMO phase W1.3 compound (space group $P2_13$). Synthesized by cooling at 5 °C/min.

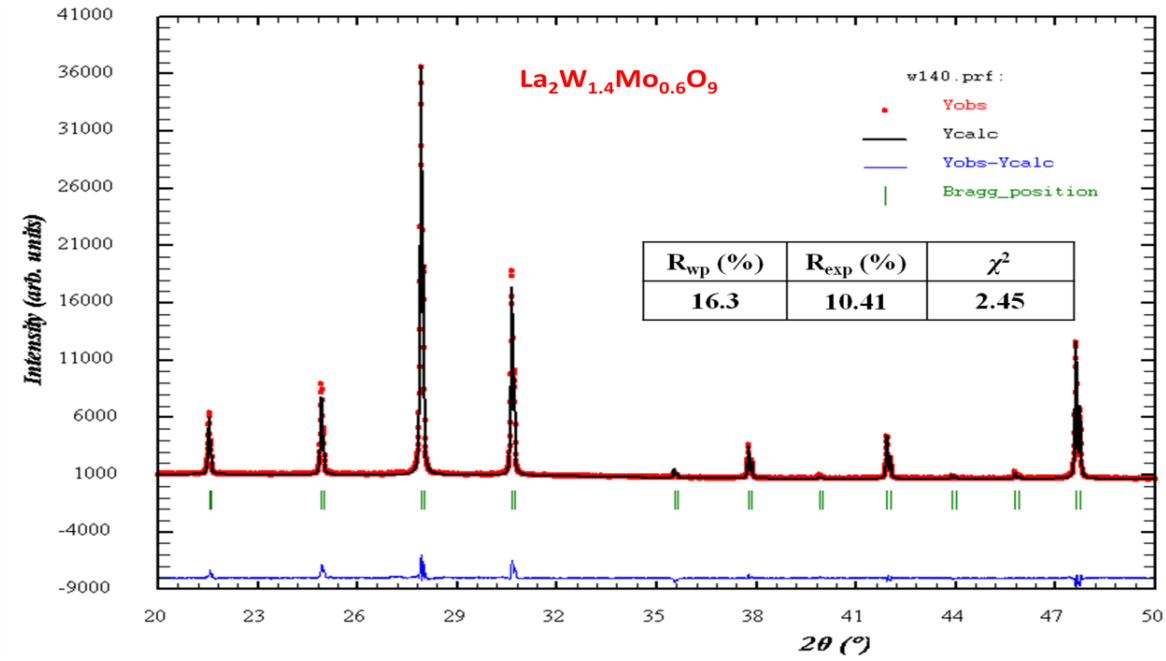

Figure II.5: Rietveld refined XRD pattern of cubic β-LMO phase W1.4 compound (space group $P2_13$). Synthesized by cooling at 5 °C/min.

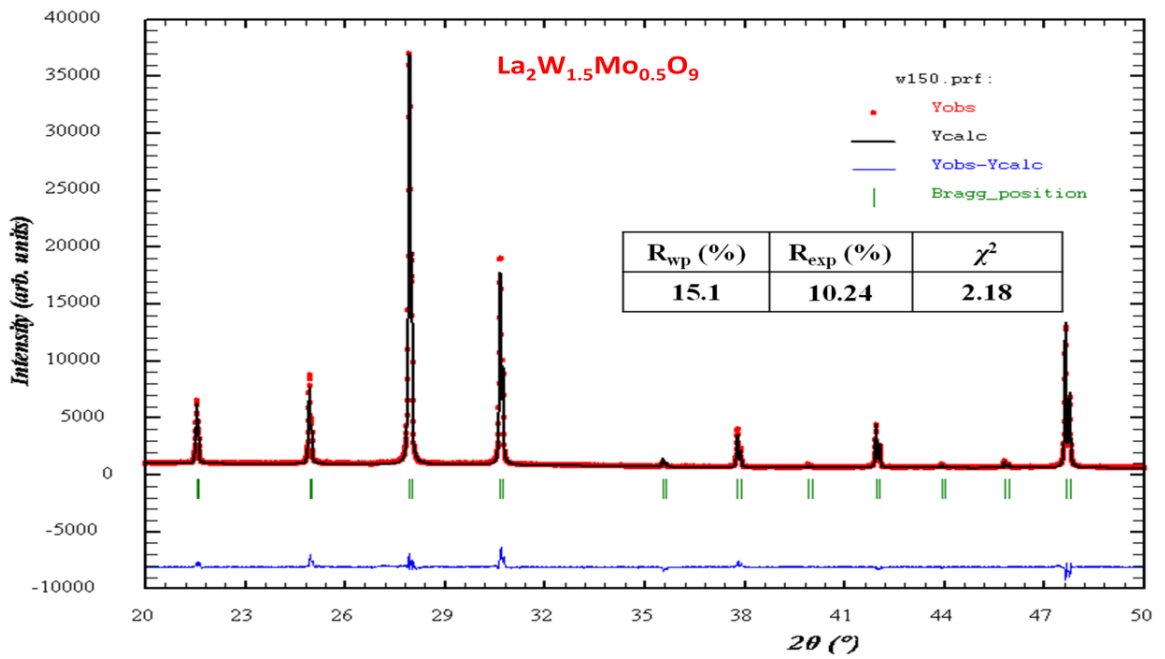

Figure II.6: Rietveld refined XRD pattern of cubic β-LMO phase W1.5 compound (space group $P2_13$). Synthesized by cooling at 5 °C/min.

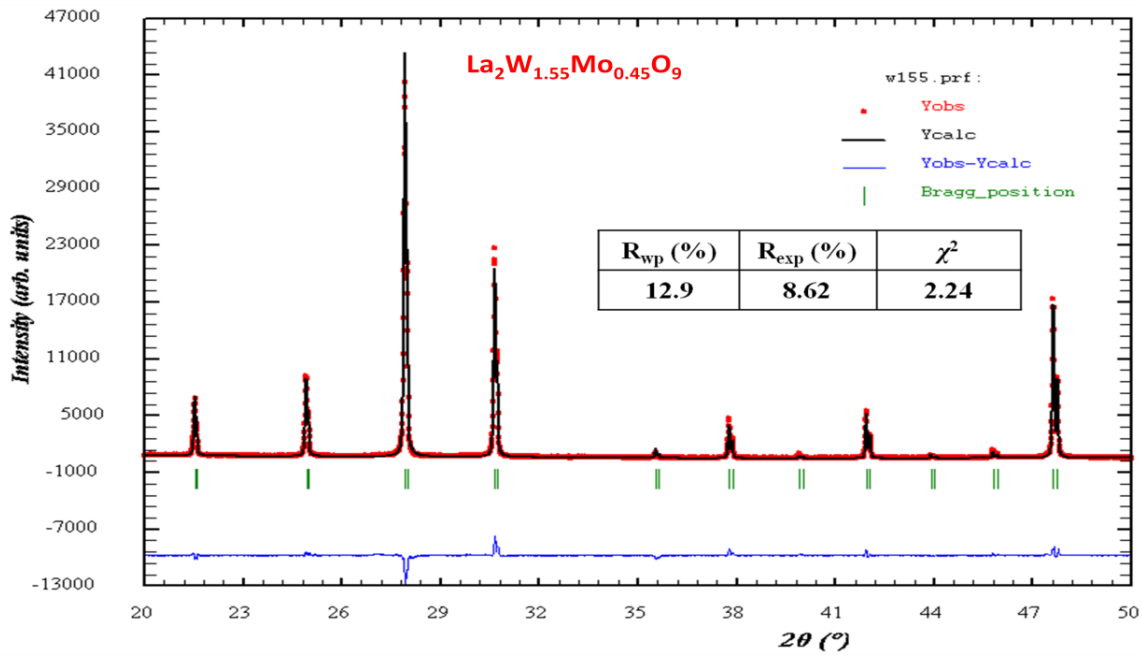

Figure II.7: Rietveld refined XRD pattern of cubic β-LMO phase W1.55 compound (space group $P2_13$. Synthesized by cooling at 5 °C/min.

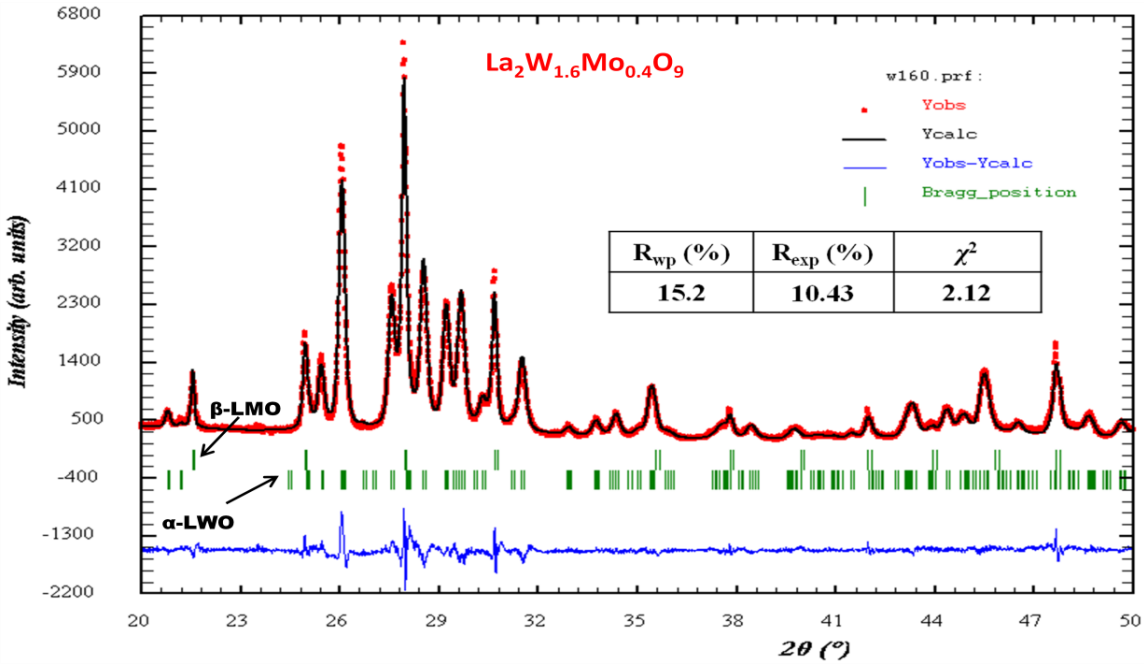

Figure II.8: Rietveld refined XRD pattern bi-phasic W1.6 compound (space group $P2_13$ and 1), which was Synthesized by cooling at 5 ^{o}C/min.

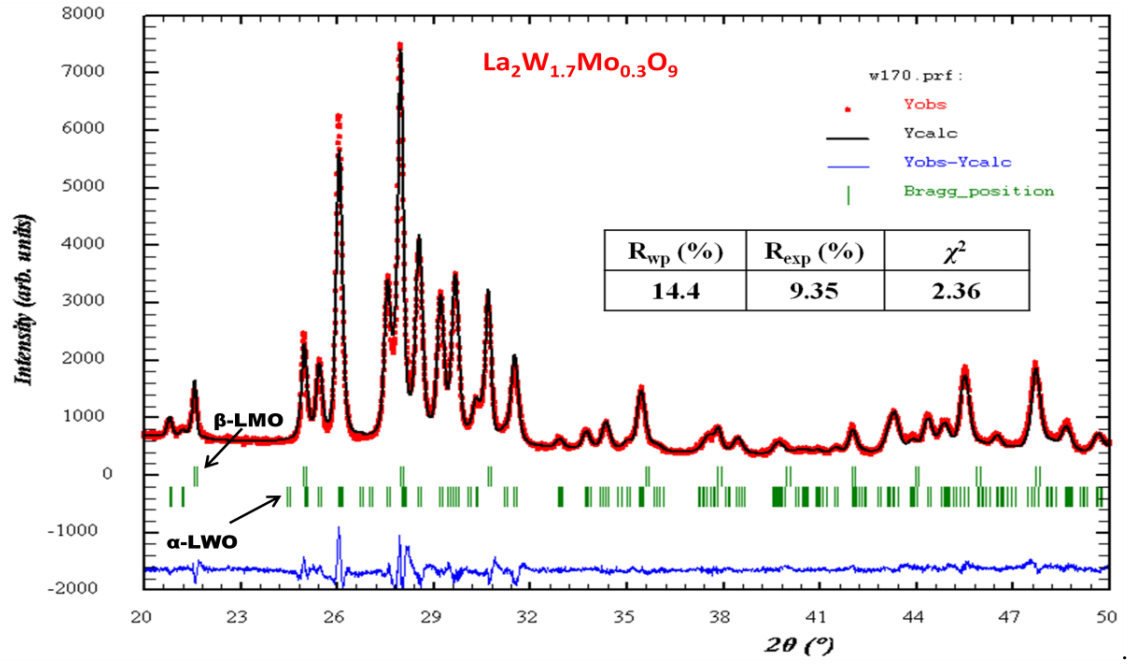

Figure II.9: Rietveld refined XRD pattern bi-phasic W1.7 compound (space group $P2_13$ and 1), which was Synthesized by cooling at 5 ^{o}C/min.

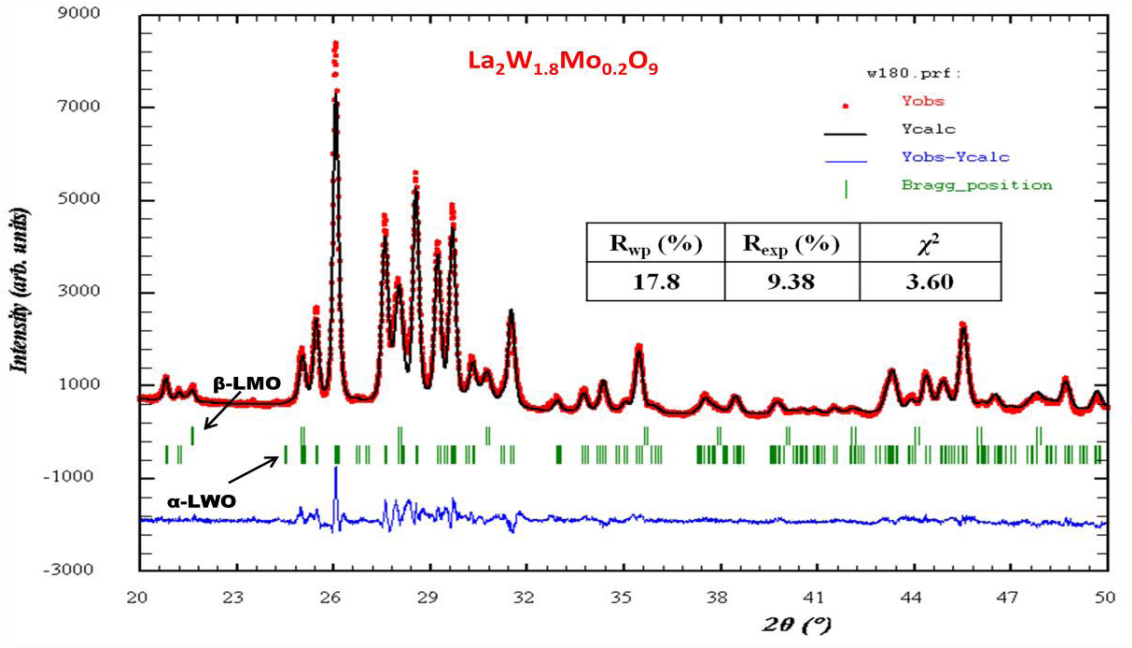

Figure II.10: Rietveld refined XRD pattern bi-phasic W1.8 compound (space group $P2_13$ and 1), which was Synthesized by cooling at 5 °C/min.

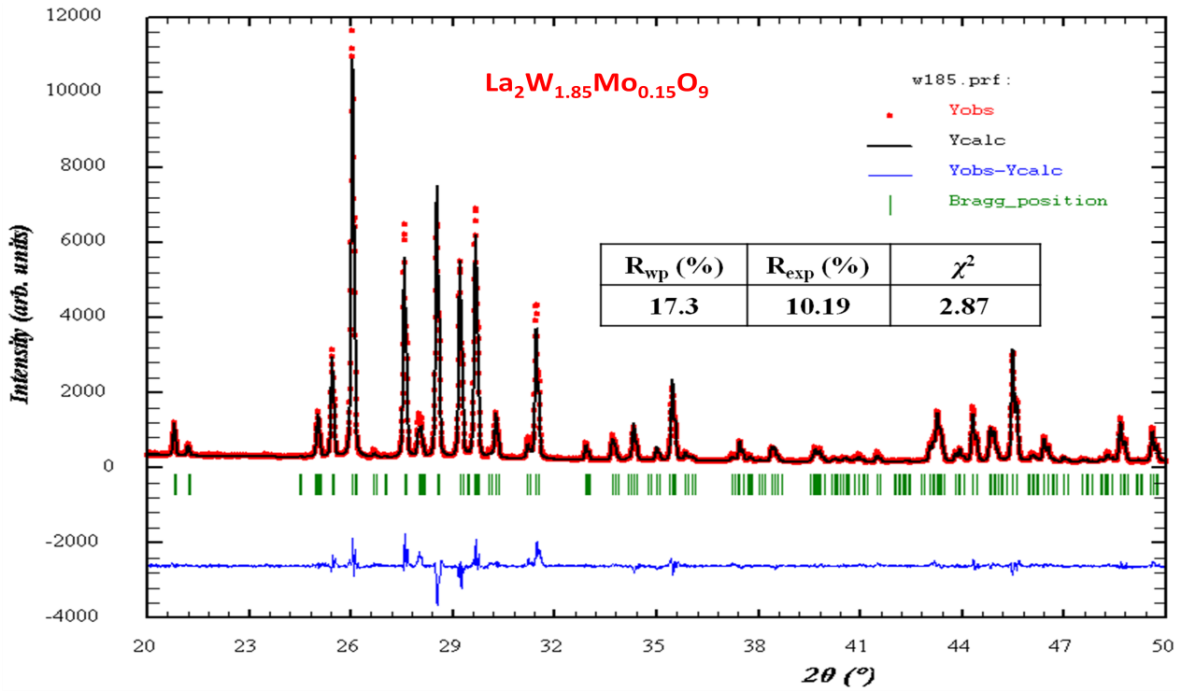

Figure II.11: Rietveld refined XRD pattern of triclinic α-LWO phase W1.85 compound (space group 1). Synthesized by cooling at 5 °C/min.

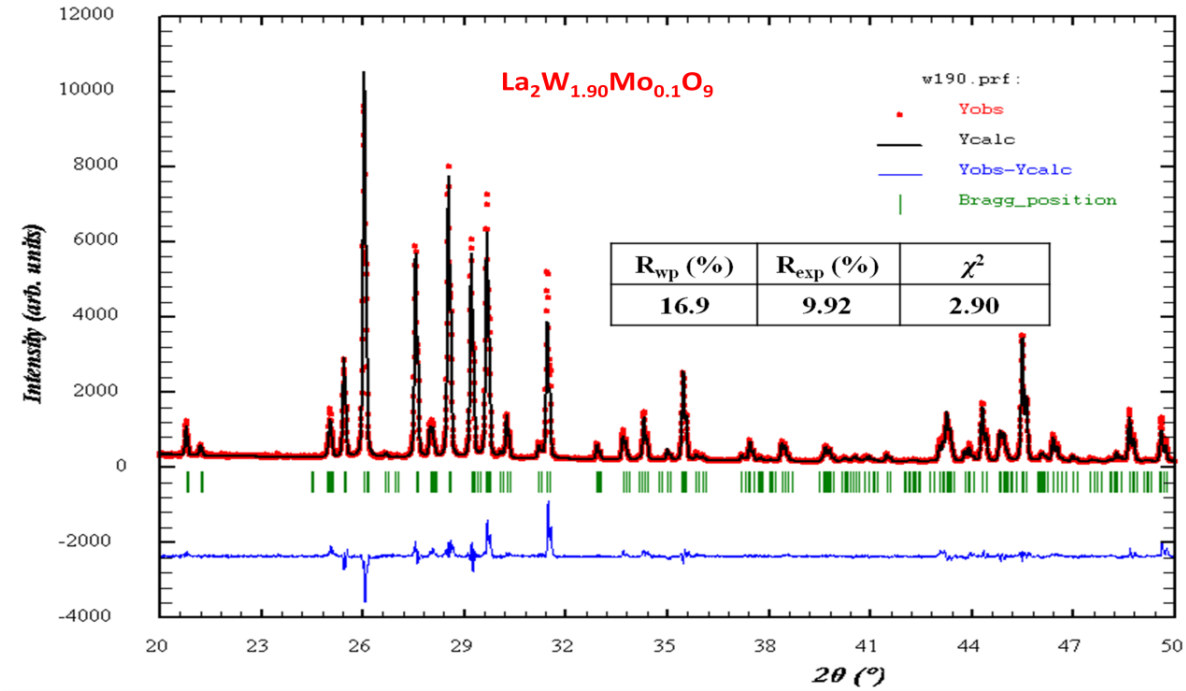

Figure II.12: Rietveld refined XRD pattern of triclinic α-LWO phase W1.9 compound (space group 1). Synthesized by cooling at 5 °C/min.

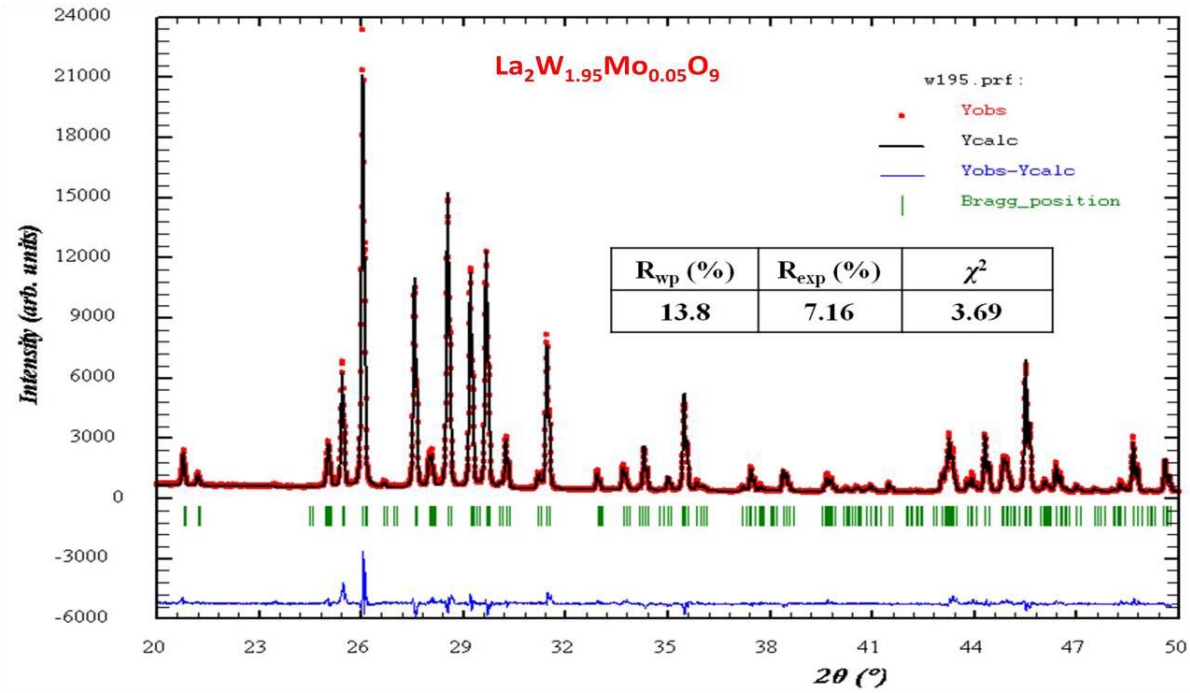

Figure II.13: Rietveld refined XRD pattern of triclinic α-LWO phased W1.95 compound (space group 1). Synthesized by cooling at 5 °C/min.

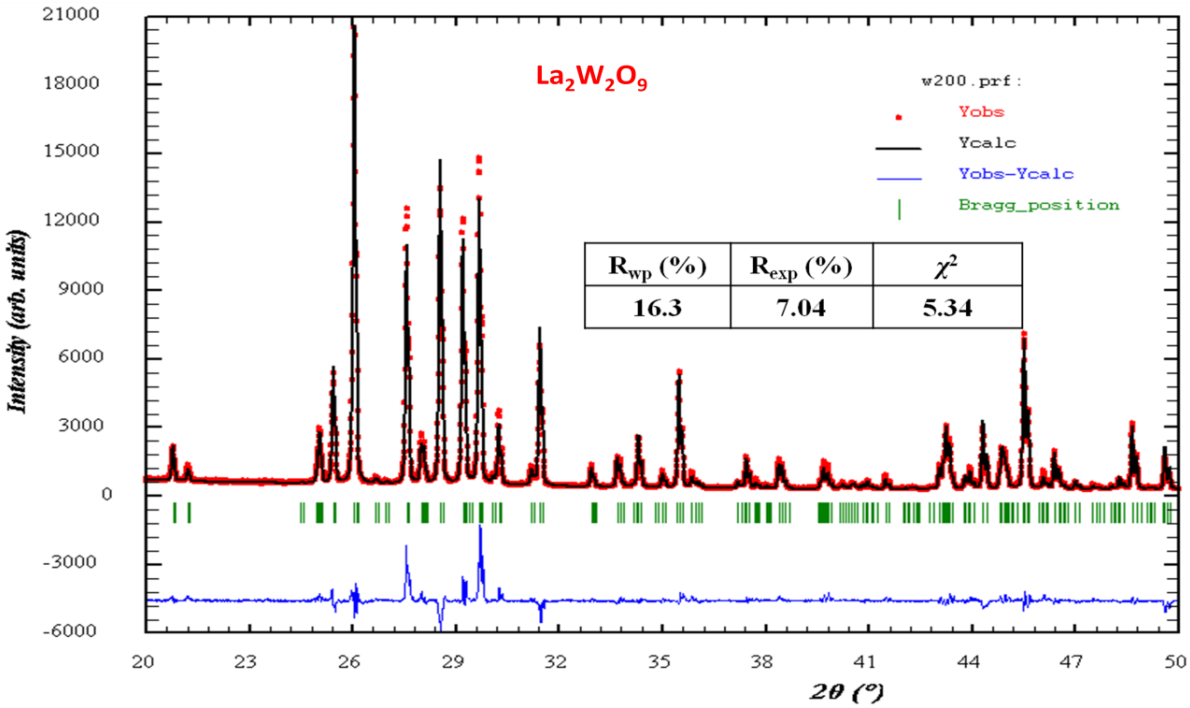

Figure II.14: Rietveld refined XRD pattern of triclinic α-LWO phase W 2.0 compound (space group 1). Synthesized by cooling at 5 °C/min.

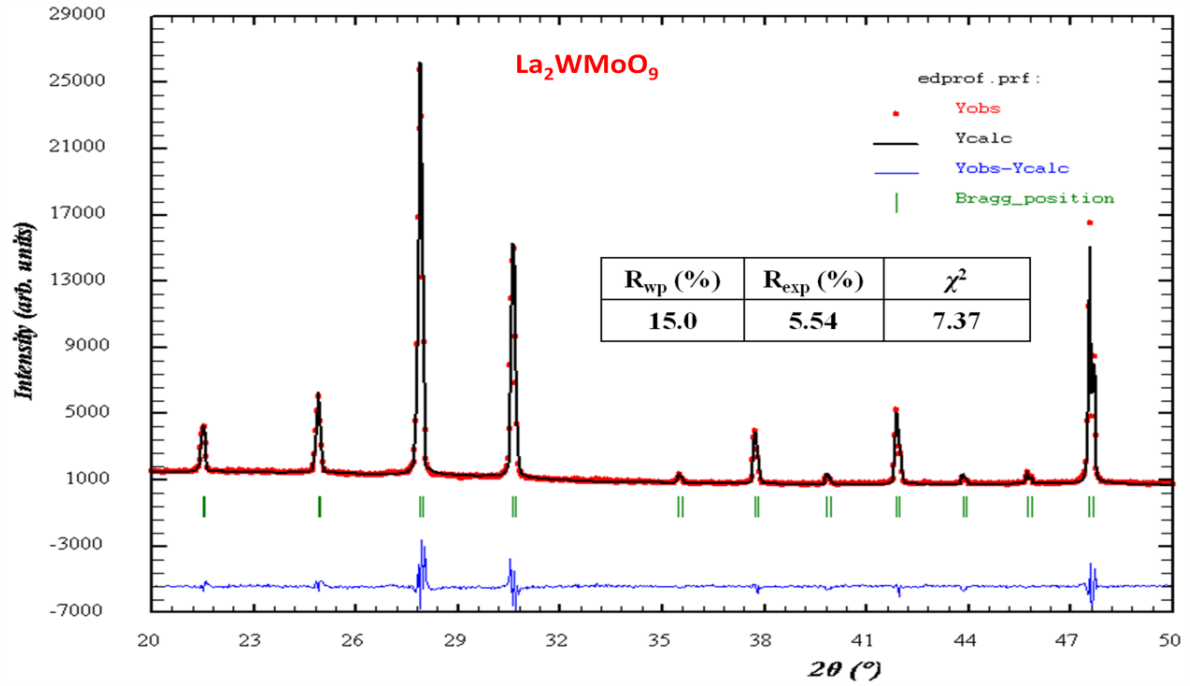

Figure II.15: Le-Bail fitting of XRD pattern of cubic β-LMO phase W1.0 compound (space group $P2_13$). Sample heat treated at 700 °C for 60 days.

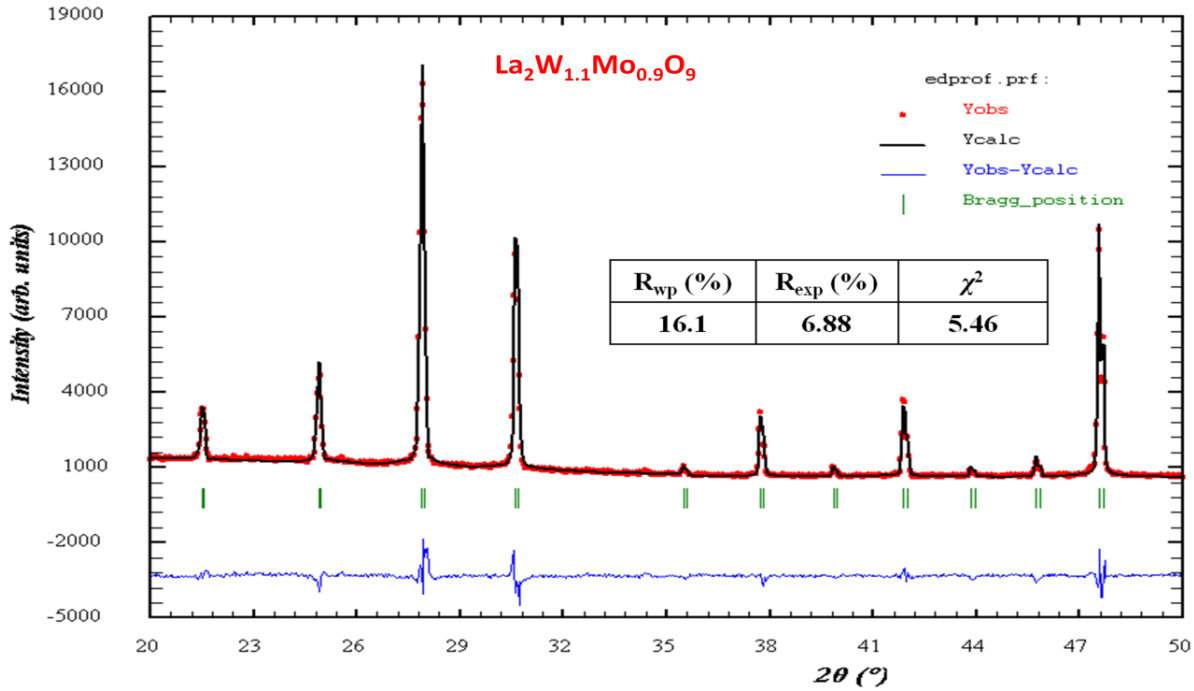

Figure II.16: Le-Bail fitting of XRD pattern of cubic β-LMO phase W1.1 compound (space group $P2_13$). Sample heat treated at 700 °C for 60 days.

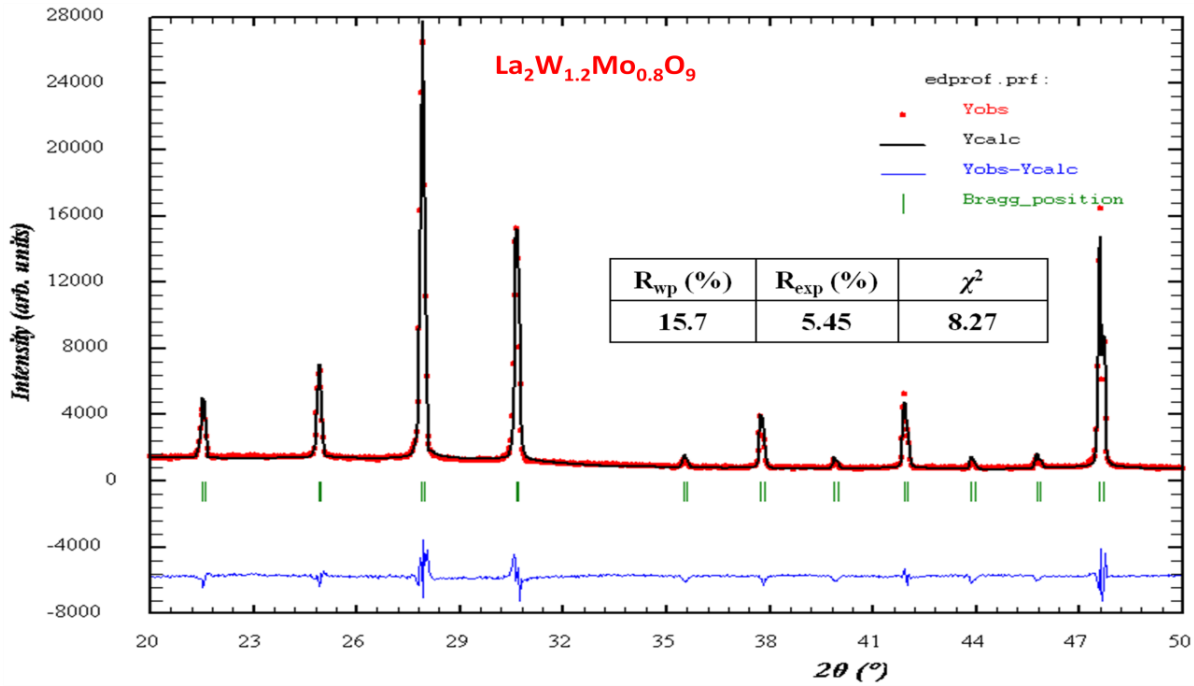

Figure II.17: Le-Bail fitting of XRD pattern of cubic β-LMO phase W1.2 compound (space group $P2_13$). Sample heat treated at 700 °C for 60 days.

(y) in $La_2W_yMo_{2-y}O_9$	Phase	Cell Parameters						Single Cell Volume V [Å]³	Wt. Fraction of phases (%)
		a [Å]	b [Å]	c [Å]	α°	β°	γ°		
1.3	β-LMO	7.1457(1)	7.1457(1)	7.1457(1)	90	90	90	364.870(5)	89.0(3)
	α-LWO	7.2491(4)	7.2807(3)	7.0448(3)	96.384(5)	94.682(5)	70.513(5)	347.95(3)	11.0(1)
1.4	β-LMO	7.1432(1)	7.1432(1)	7.1432(1)	90	90	90	364.487(6)	78.9(2)
	α-LWO	7.2403(2)	7.2855(2)	7.0459(2)	96. 384(2)	94.692(2)	70.483(2)	347.75(1)	21.1(1)
1.5	β-LMO	7.1598(3)	7.1598(3)	7.1598(3)	90	90	90	367.03(2)	11.4(1)
	α-LWO	7.2515(1)	7.2797(1)	7.0456(1)	96.383(1)	94.725(1)	70.499(1)	348.01(1)	88.6(2)

Table.II.1: Unit cell parameters and Wt. fractions (%) calculated by Rietveld refinement on R.T XRD patterns of W1.3-W1.5 compounds, applying (inverse) Lever rule and using W1.25 and W1.5875 as boundary limits for the bi-phasic domain. Note that these compounds were pre-heat treated at 800 °C for 96 Hrs.

(y) in $La_2W_yMo_{2-y}O_9$	Phase	Cell Parameters						Single Cell Volume V [Å]³	Wt. Fraction of phases (%)
		a [Å]	b [Å]	c [Å]	α°	β°	γ°		
1.3	β-LMO	7.2447(1)	7.2447(1)	7.2447(1)	90	90	90	380.253(6)	85.7(4)
	α-LWO	7.2789(3)	7.3445(3)	7.1155(3)	96.387(4)	94.750(4)	70.607(4)	356.16(3)	14.3(3)
1.4	β-LMO	7.2428(1)	7.2428(1)	7.2428(1)	90	90	90	379.951(7)	74.7(3)
	α-LWO	7.2725(2)	7.3460(2)	7.1151(2)	96.371(2)	94.731(2)	70.609(2)	355.92(2)	25.3(3)
1.5	β-LMO	7.2522(2)	7.2522(2)	7.2522(2)	90	90	90	381.42(2)	8.7(1)
	α-LWO	7.2825(1)	7.3459(1)	7.1175(1)	96.365(1)	94.756(1)	70.621(1)	356.54(1)	91.3(9)

Table.II.2: Unit cell parameters and Wt. fractions (%) calculated by Rietveld refinement on the XRD patterns of W1.3-W1.5 compounds (collected at 700 °C), applying (inverse) Lever rule and using W1.25 and W1.5875 as boundary limits for bi-phasic domain. Note that these compounds were pre-heat treated at 800 °C for 96 Hrs.

Atom	Position Co-ordinates	B_{iso}Å^2	Occupancy
La	x = y = z = 0.8543(7)	4.36(1)	1
W/Mo	x = y = z = 0.1666(6)	5.34(2)	0.5/0. 5
Cell parameters – Space group – $P2_13$			
a= b = c = 7.1527(1) Å V = 365.907(3)Å^3	$\alpha = \beta = \gamma = 90°$	R_{wp} (%)– 10.7 R_{exp} (%) – 5.99 χ^2 – 3.22	

Table.II.3: Unit cell parameters and cationic positions of W1.3 raw powder at R.T.

Atom	Position Co-ordinates	Occupancy
La 1	x 0.8514(3) y 0.7381(5) z 0.1553(6)	1
La 2	x 0.5839(6) y 0.7289(5) z 0.6258(5)	1
W1/Mo1	x 0.6438(1) y 0.2078(9) z 0.8443(3)	0.925/0.075
W2/Mo2	x - 0.0625(4) y 0.2716(5) z 0.2803(3)	0.925/0.075
Cell parameters – Space group – $P1^-$		
a -7.2533(1) Å b -7.2888(1) Å c -7.0470(1) Å V - 348.309(9)Å^3	α - 96.3779(6)° β - 94.7162(6)° γ - 70.3547(9)°	R_{wp} (%)– 17.3 R_{exp} (%) – 10.19 χ^2 – 2.87

Table.II.4: Unit cell parameters and cationic positions of W1.85 raw powder at R.T.

Phase	Atom	Position Co-ordinates	B_{iso}Å^2	Occupancy
β– LMO phase	**La**	x = y = z = 0.8542(1)	4.36(1)	1
	W /Mo	x = y = z = 0.1654(2)	5.34(2)	0.7/0.3
	Cell parameters – Space group – $P2_13$			
	a = b = c = 7.1432(1) Å V = 364.488(6)Å^3		α = β = γ = 90 º	
α– LWO phase	**La 1**	x 0.8533(6) y 0.7398(7) z 0.1541(7)	-	1
	La 2	x 0.5757(9) y 0.7416(8) z 0.6292(8)	-	1
	W1/Mo1	x 0.6460(4) y 0.2068(6) z 0.8399(6)	-	0.7/0.3
	W2/Mo2	x - 0.0626(8) y 0.2722(5) z 0.2821(8)	-	0.7/0.3
	Cell parameters – Space group – $P1^{-}$			
	a -7.2403(2) Å b -7.2856(2) Å c -7.0460(2) Å V - 347.75(1)Å^3		α - 96.385(2)º β - 94.692(1)º γ - 70.483(2)º	
R_{wp} (%)– 15.1 R_{exp} (%) – 11.3 χ^2 – 1.78				

Table.II.5: Unit cell parameters and cationic positions of W1.4 which was heat treated at 800 ^oC for 96 hours at R.T .

Atom	Position Co-ordinates	Occupancy
La 1	x 0.8484(4) y 0.7430(3) z 0.1581(7)	1
La 2	x 0.5820(6) y 0.7311(9) z 0.6264(2)	1
W1/Mo1	x 0.6456(6) y 0.2044(1) z 0.8445(4)	0.85/0.15
W2/Mo2	x -0.0628(5) y 0.2700(1) z 0.2812(0)	0.85/0.15
Cell parameters – Space group – P1̄		
a -7.2498(1) Å b -7.2850(1) Å c -7.0485(1) Å V - 348.19(1)Å³	α - 96.3782(9)° β - 94.7105(8)° γ - 70.3919(8)°	R_{wp} (%)– 14.5 R_{exp} (%) – 9.4 χ^2 – 2.38

Table.II.6: Unit cell parameters and cationic positions of W1.7which was heat treated at 800 °C for 96 hours at R.T.

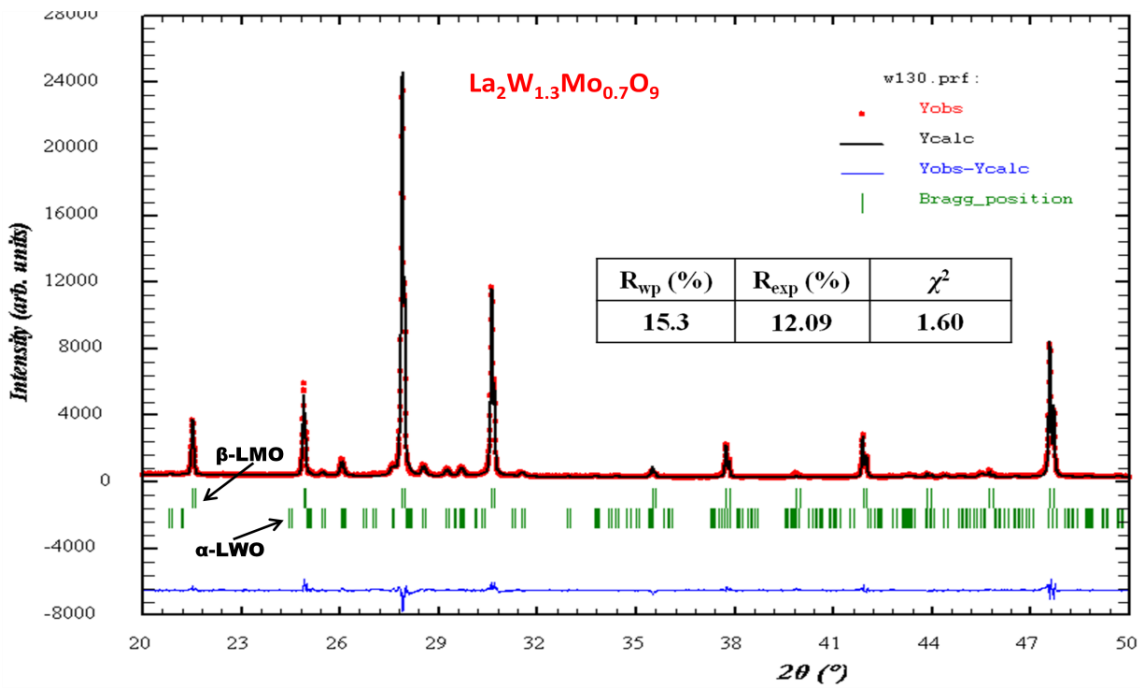

Figure II.18: Rietveld refined of the XRD pattern for bi-phasic W1.3 compound at R.T, which was heat treated at 800 °C for 96 hours. Reliability factors of the refinement were given in inset.

Phase	Atom	Position Co-ordinates	B_{iso}Å^2	Occupancy
β – LMO phase	La	x = y = z = 0.8524(4)	4.36(1)	1
	W /Mo	x = y = z = 0.1682(8)	5.34(2)	0.7/0.3
	Cell parameters – Space group – $P2_13$			
	a = b = c = 7.2428(1) Å V = 379.951(7)Å^3		α = β = γ = 90 º	
α – LWO phase	La 1	x 0.8552(9) y 0.7424(0) z 0.1506(6)	-	1
	La 2	x 0.5748(4) y 0.7379(8) z 0.6328(6)	-	1
	W1/Mo1	x 0.6419(6) y 0.2047(4) z 0.8399(1)	-	0.7/0.3
	W2/Mo2	x -0.0603(2) y 0.2723(3) z 0.2830(4)	-	0.7/0.3
	Cell parameters – Space group – $P1^-$			
	a -7.2725(2) Å b -7.3460(2) Å c -7.1151(2) Å V – 355.92(2)Å^3		α - 96.371(2)º β - 94.731(2)º γ - 70.609(2)º	
R_{wp} (%)– 14.0 R_{exp} (%) – 8.37 χ^2 – 2.79				

Table.II.7: Unit cell parameters and cationic positions of W1.4 which was heat treated at 800 ^oC for 96 hours at 700 ^oC.

Atom	Position Co-ordinates	Occupancy
La 1	x 0.8522(6) y 0.7436(5) z 0.1587(5)	1
La 2	x 0.5779(1) y 0.7321(6) z 0.6292(7)	1
W1/Mo1	x 0.6452(3) y 0.2032(0) z 0.8461(3)	0.85/0.15
W2/Mo2	x -0.0653(4) y 0.2709(9) z 0.2829(5)	0.85/0.15
Cell parameters – Space group – P1̄		
a -7.2774(1) Å b -7.3455(2) Å c -7.1140(2) Å V - 355.99(1)Å³	α - 96.365(1)° β - 94.7437(9)° γ - 70.5638(8)°	R_{wp} (%)– 11.3 R_{exp} (%) – 7.25 χ^2 – 2.43

Table.II.8: Unit cell parameters and cationic positions of W1.7which was heat treated at 800 °C for 96 hours at 700 °C.

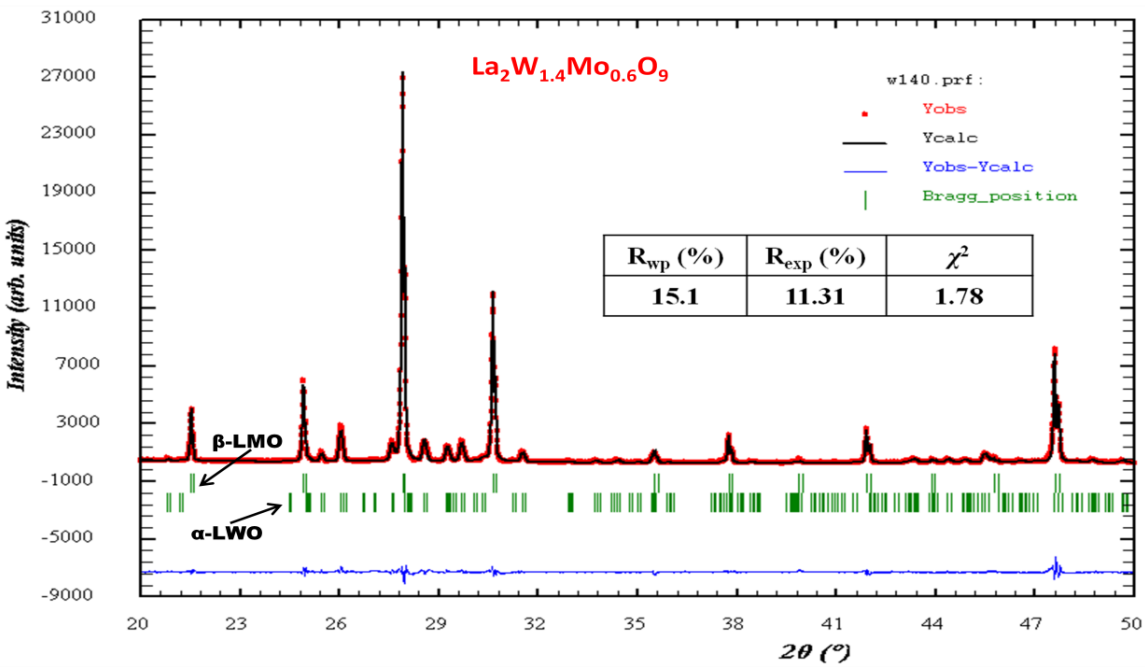

Figure II.19: Rietveld refined of the XRD pattern for bi-phasic W1.4 compound at R.T, which was heat treated at 800 °C for 96 hours. Reliability factors of the refinement were given in inset.

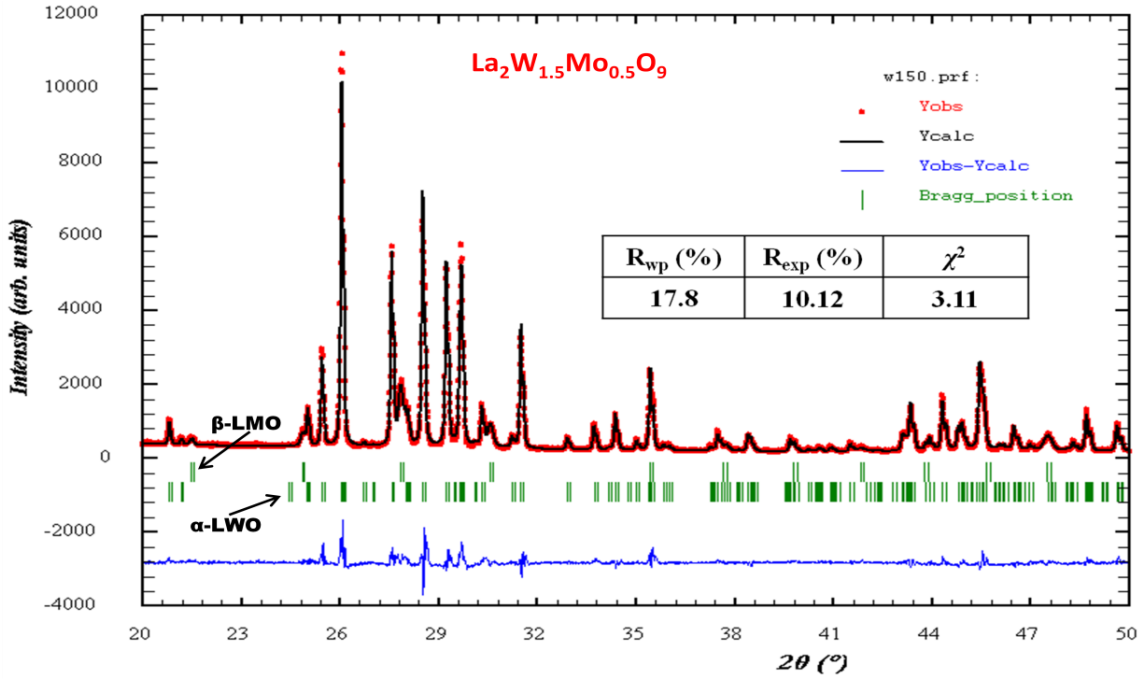

Figure II.20: Rietveld refined XRD pattern bi-phasic W1.5 compound at R.T, which was heat treated at 800 °C for 96 hours. Reliability factors of the refinement were given in inset.

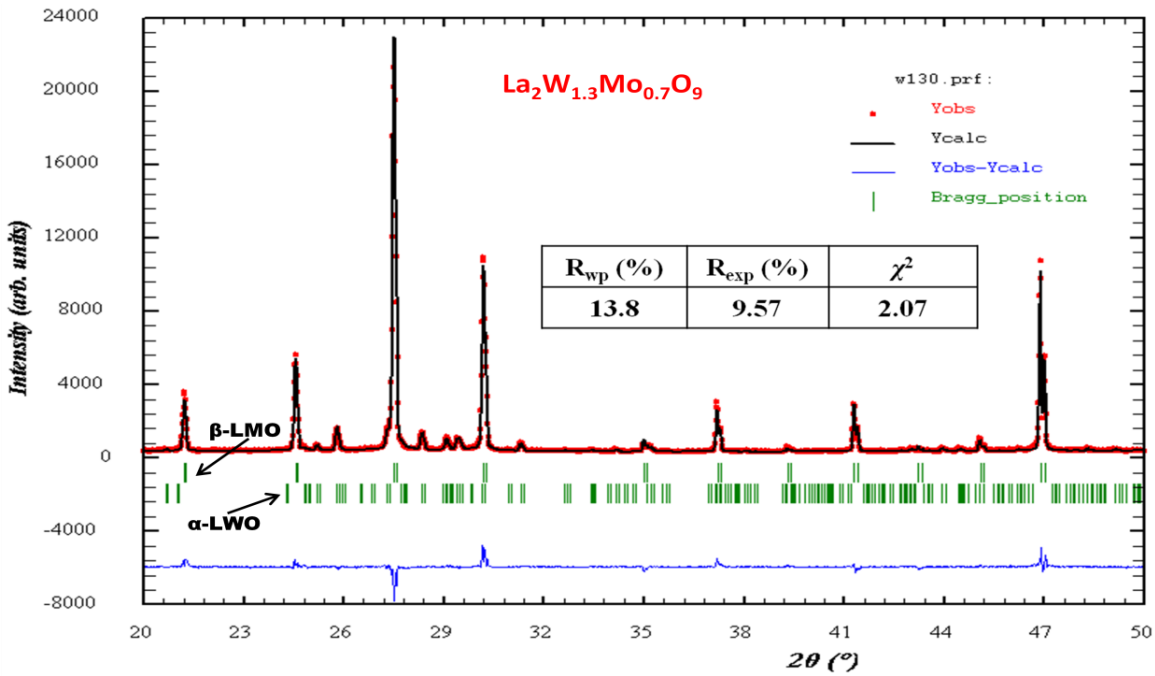

Figure II.21: Rietveld refined XRD pattern bi-phasic W1.3 compound at 700 °C, which was heat treated at 800 °C for 96 hours. Reliability factors of the refinement were given in inset.

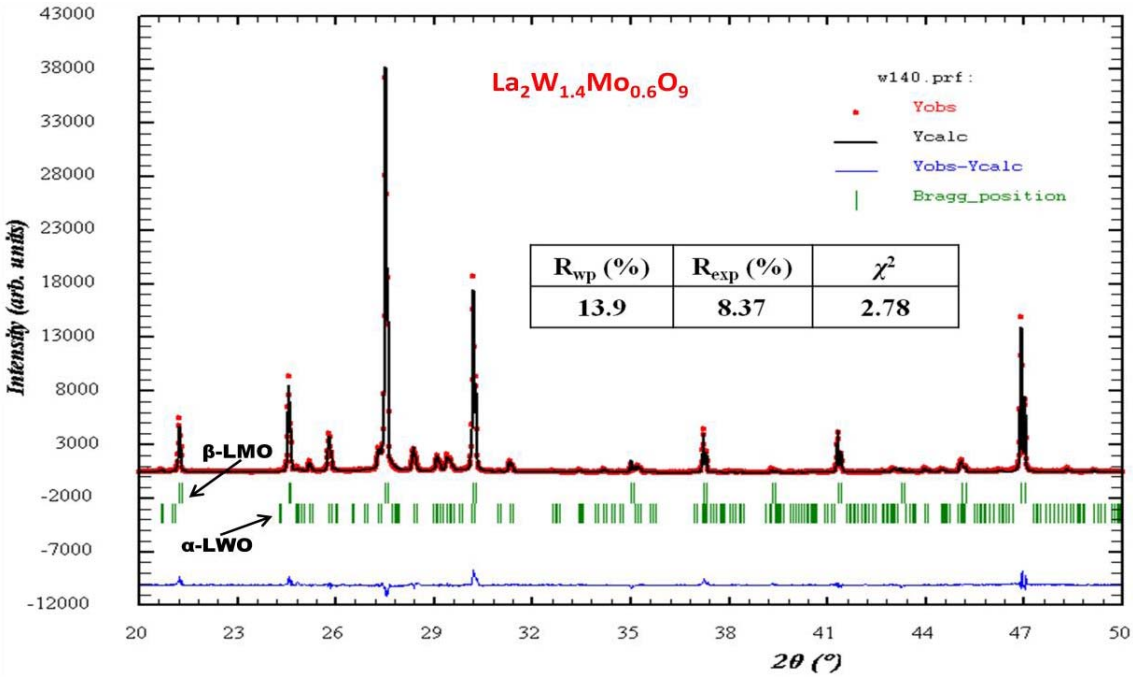

Figure II.22: Rietveld refined XRD pattern bi-phasic W1.4 compound at 700 °C, which was heat treated at 800 °C for 96 hours. Reliability factors of the refinement were given in inset.

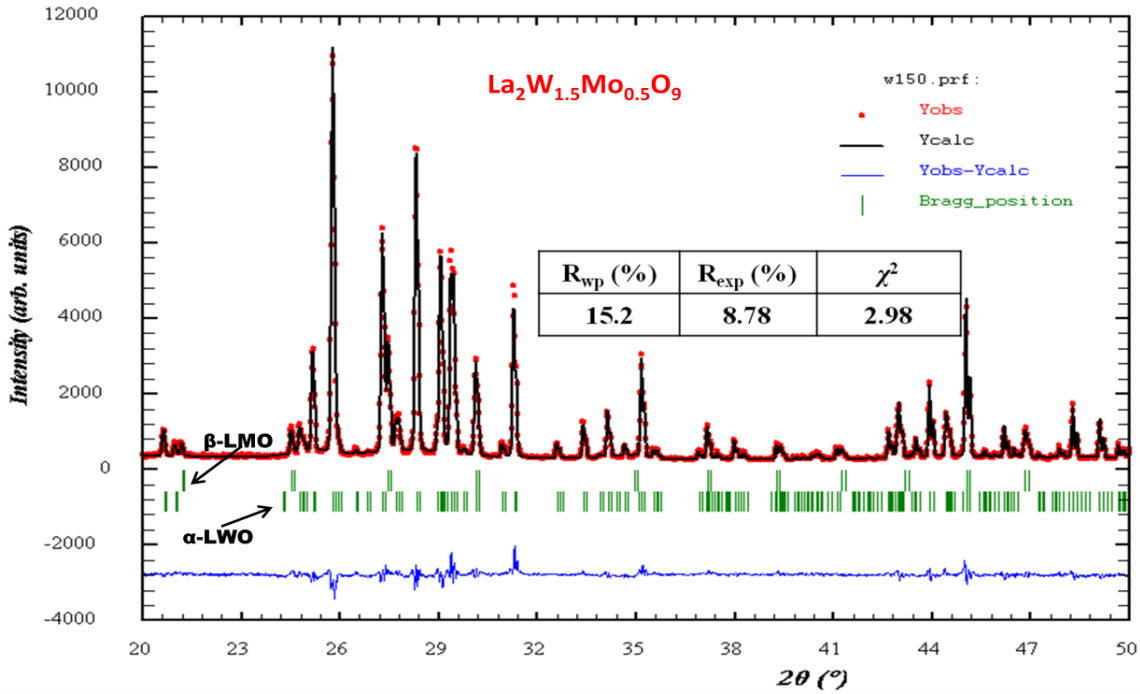

Figure II.23: Rietveld refined XRD pattern bi-phasic W1.5 compound at 700 °C, which was heat treated at 800 °C for 96 hours. Reliability factors of the refinement were given in inset.

Résumé

Les oxydes $La_2Mo_{2-y}W_yO_9$ ($1,0 \leq y \leq 2,0$) ont été obtenus par voie de synthèse solide-solide et caractérisés par diffraction des rayons X (température ambiante et en température) ainsi que par analyse thermique différentielle. Un diagramme de phase de ce système est proposé. Les phases thermodynamiquement stables à température ambiante sont : pour $1,0 \leq y \leq 1,2$ une solution solide de type β-$La_2Mo_2O_9$ (cubique); pour $1,3 \leq y \leq 1,575$ un domaine biphasique de phases de type β-$La_2Mo_2O_9$+ α-$La_2W_2O_9$ et pour $1,6 \leq y \leq 2,0$ une solution solide de type α-$La_2W_2O_9$. Dans le domaine biphasique, une distribution inhomogène du tungstène est suspectée. Il est clair que les composés à teneur en tungstène supérieure à y=1,2 ne conviennent pas pour utilisation en piles à combustibles à oxydes solides.

Des études de diffusion cationiques par SIMS ont été menées sur des couples $La_2Mo_2O_9$ (LMO)/$La_{0.8}Sr_{0.2}MnO_{3-\delta}$ (LSM) après leurs recuits à haute température. Des cristaux de $LaMnO_3$ en forme de barreau ont été observés sur les pastilles de LMO et la croissance d'une phase de type $SrMoO_4$ a été constatée sur la pastille LSM. Des hypothèses expliquant les mécanismes possibles de diffusion sont présentés. Les coefficients de diffusion en volume du strontium et du manganèse dans LMO et du molybdène dans LSM sont estimés proches respectivement de $1x10^{-20}$ $cm^2.s^{-1}$ et $1x10^{-15}$ $cm^2.s^{-1}$ à 800°C. Des études similaires de diffusion ont été menées par dépôts de solutions riches en cations manganèse et strontium sur des pastilles de LMO et d'une solution riche en cation molybdène sur une pastille de LSM. Après recuit, la formation de cristaux de $LaMnO_3$ au niveau de la zone de dépôt de la solution de manganèse a été observée. Les coefficients de diffusion du molybdène dans LSM et du strontium dans LMO semblent être beaucoup plus importants -proches de $1\text{-}2x10^{-10}cm^2.s^{-1}$ à 1150°C- que ceux obtenus lors des mesures sur couple LMO/LSM. De par leur réactivité, le couple LMO/LSM ne semble pas adapté pour une application dans le domaine des piles à combustible, sauf si une couche tampon appropriée les sépare.

Les stabilités de LMO et de LMO dopé tungstène ont été étudiées sous atmosphères réductrices. Suivant le taux de perte en oxygène, des changements structuraux successifs ont été observés : de phase LMO à $La_7Mo_7O_{30}$(7730), phase amorphe réduite $La_2Mo_2O_{7-\delta}$ et décomposition partielle sous forme de molybdène métallique. Le domaine de stabilité de $La_2Mo_{2-y}W_yO_9$ sous faible pression de O_2 ne semble pas dépendant du taux de tungstène alors que la cinétique de réduction, elle, évolue avec y. En revanche, la limite de stabilité de la phase 7730 apparait dépendante du taux de tungstène. La phase réduite amorphe existe sur un large domaine de stœchiométrie en oxygène (7-δ de 6,69 à 6,20), cependant sa stabilité *vs*. P_{O2} reste à démontrer. Les mesures de résistivité conduites sur un échantillon amorphe de $La_2Mo_2O_{7-\delta}$ de faible compacité et sans fissure ont montré une augmentation significative de la conductivité (> 1 $S.cm^{-1}$ à 1000 K) vis-à-vis de $La_2Mo_2O_9$, avec une pseudo-énergie d'activation de 0.255eV. Il a été supposé qu'une conductivité électronique de type n résulte de la réduction partielle des cations Mo^{6+} en Mo^{3+} et Mo^{4+}.

Mots clés : $La_2Mo_2O_9$, LAMOX, $La_2Mo_2O_9$ substitué par le tungstène, SOFC, électrolyte, MIEC, anode, diagramme de phase, métastabilité, réductibilité, diffusion cationique, diffraction des RX, pression partielle de O_2, $La_{0.8}Sr_{0.2}MnO_{3-\delta}$, SIMS.

Summary

$La_2Mo_{2-y}W_yO_9$ (y = 1.0 to 2.0) oxides were synthesized by conventional solid state route and studied by XRD, TC-XRD and DTA. A phase diagram of the series was proposed. The thermodynamically stable phases at room temperature are: for 1.0≤ y ≤1.2 a cubic β-$La_2Mo_2O_9$ type solid solution, for 1.3≤ y ≤1.575 a biphasic mixture of β-$La_2Mo_2O_9$ type + α-$La_2W_2O_9$ type phases, and for 1.6≤ y ≤2.0 a triclinic α-$La_2W_2O_9$ type solid solution. Inhomogeneous distribution of W is suspected in the biphasic samples. It is clear that the compounds above y =1.2 are not suitable for SOFC applications.

Cationic diffusion studies were performed using SIMS on $La_2Mo_2O_9$ (LMO)/$La_{0.8}Sr_{0.2}MnO_{3-\delta}$ (LSM) annealed couples. Rod shaped $LaMnO_3$ grains were observed on LMO pellet and $SrMoO_4$ type phases were seen to be growing on LSM pellet. Hypotheses for possible reaction mechanisms are presented. Bulk diffusion coefficients of Sr and Mn in LMO and of Mo in LSM are extrapolated to be around $1x10^{-20}$ $cm^2.s^{-1}$ and $1x10^{-15}$ $cm^2.s^{-1}$, respectively, at 800°C. Similar diffusion studies were performed by depositing Mn and Sr cation rich solutions on LMO pellets and Mo rich solution on LSM pellet. Mn solution was observed to be forming, upon annealing, $LaMnO_3$ single crystals on the surface of the LMO pellet. Mo in LSM and Sr in LMO diffusion coefficients appear to be much higher than in LMO/LSM couple experiments, namely around $1\text{-}2x10^{-10}cm^2.s^{-1}$ at 1150°C. Because of the reactivity, LMO/LSM couple is not desirable for SOFC applications, unless an appropriate buffer layer separates them.

The stability of LMO and W-LMO was studied under reductive atmospheres. Successive structural changes from LMO to $La_7Mo_7O_{30}$ (7730), an amorphous reduced phase $La_2Mo_2O_{7-\delta}$, and partial decomposition to metallic Mo were observed as a function of oxygen loss. The pO_2 stability domain of $La_2Mo_{2-y}W_yO_9$ did not appear to change with W content, but the reduction kinetics varied with y. At reverse, the stability limit of the 7730 phase was found to be dependent on W content. The amorphous reduced phase can accommodate a wide range of oxygen stoichiometry (7-δ from 6.69 to 6.20), but its stability *vs.* pO_2 is questioned. Resistivity measurements performed on a low compacity crack-free amorphous $La_2Mo_2O_{7-\delta}$ sample showed significant increase in the conductivity (> 1 $S.cm^{-1}$ at 1000 K) relative to $La_2Mo_2O_9$, with a pseudo activation energy 0.255eV. It is postulated that n-type electronic conductivity arises from partial reduction of hexavalent Mo^{6+} to a mixture of Mo^{3+} and Mo^{4+}.

Key words: $La_2Mo_2O_9$, LAMOX, W substituted $La_2Mo_2O_9$, SOFC, electrolyte, MIEC, anode, phase diagram, metastability, reducibility, cationic diffusion, XRD, pO_2 , $La_{0.8}Sr_{0.2}MnO_{3-\delta}$, SIMS.